THEORY AND RESEARCH IN SCIENCE AND MATHEMATICS II

EDITORS: PROF. DR. HASAN AKGÜL
DOÇ. DR. MEHMET YÜKSEL

gece kitaplığı

İmtiyaz Sahibi / Publisher • Yaşar Hız

Genel Yayın Yönetmeni / Editor in Chief • Eda Altunel

Kapak & İç Tasarım / Cover & Interior Design • Gece Kitaplığı

Editörler / Editors • Prof. Dr. Hasan Akgül

Doç. Dr. Mehmet YÜKSEL

Birinci Basım / First Edition • © Aralık 2020

ISBN • 978-625-7319-08-9

Gece Kitaplığı / Gece Publishing

Türkiye Adres / Turkey Address: Kızılay Mah. Fevzi Çakmak 1. Sokak Ümit Apt. No: 22/A Çankaya / Ankara / TR

Telefon / Phone: +90 312 384 80 40

web: www.gecekitapligi.com

e-mail: gecekitapligi@gmail.com

Baskı & Cilt / Printing & Volume

Sertifika / Certificate No: 47083

Theory and Research in Science and Mathematics II

EDITORS

Prof. Dr. Hasan Akgül
Doç. Dr. Mehmet YÜKSEL

gece kitaplığı

CONTENTS

Chapter 1

PHOTODYNAMIC THERAPY WITH PHTHALOCYANINES: A FIGHT AGAINST CANCER

(VIEWS FROM THE RECENT LITERATURE)

Barbaros AKKURT[1]
Altuğ Mert SEVİM[2]

1 Lecturer, PhD, Istanbul Technical University, Mustafa Inan Library, Maslak 34469, Sariyer, Istanbul.
2 Assoc. Prof., Istanbul Technical University, Faculty of Science and Letters, Department of Chemistry, Maslak 34469, Sariyer, Istanbul.

PART A: Comprehensive photodynamic therapy studies

These studies contain sophisticated antitumoral experiments in which phthalocyanines are actually used as a photosensitizer. They represent the superior part of the science and they should be contacted by the authors of other, non-comprehensive studies to see if the synthesized compounds in the latter show surprising behavior.

Authors chemically coupled heptamethylphthalocyanine (a near-infrared fluorescent dye) referred to as IR-780 and cabazitaxel, a chemotherapeutic drug based on paclitaxel. Then, the authors evaluated the potential value in castration-resistant prostate cancer. Tumor-bearing mouse xenograft models were used in the distribution, antitumoral effect, and safety of the drug. The authors state that the drug was efficiently absorbed by DU145 and PC-3 cells and the coupled molecule has a significantly stronger cytotoxicity than the counterparts. Therefore, the new synthetic drug obtained by chemical coupling of two entities has potential applications in the diagnosis and treatment (Zheng et al., 2020).

As a new class of cancer therapy, near-infrared photoimmunotherapy is based on the coupling of mAb to a phthalocyanine, the product therefore coined as IR700, and then NIR light irradiation is applied along with molecular-targeted fluorescence imaging. NIR light is applied upon the tumoral cell, and the obtained conjugate causes a target-selective and rapid death of the cell and necrosis is what happens at the end. HER2-positive cancer cell lines were tested for the antitumoral effect of near-infrared photoimmunotherapy with trastuzumab conjugated to IR700. It is important to state here that some cancer cells do not die and undergo regrowth after near-infrared photoimmunotherapy in an in vivo model; this is partly because mAb-IR700 conjugate are distributed heterogeneously in the tumor (Nishimura et al., 2020).

Treatment options for malignant pleural mesothelioma (MPM) are very limited. Molecular targeted therapy for malignant pleural mesothelioma is not available for now; new targeted therapeutic options are welcome. Near-infrared photoimmunotherapy is a recent application of antibodies' specific properties directed to the tumoral cell and the toxicity of the photoabsorber is combined with NIR-light exposure. Nishinaga et al. developed an antibody–photosensitizer conjugate having a phthalocyanine dye. In a flank model, in vivo near-infrared photoimmunotherapy caused a significant reduction in both tumoral volume and the activity of luciferase. In an MPM orthotopic mouse model, phototherapy targeting podoplanin (PDPN)-targeted NIR-PIT gave way to a significant antitumoral effect. Authors suggest that phototherapy targeting podoplanin-targeted near-infrared-photoimmunotherapy is a recent treatment for malignant pleural mesothelioma, showing great promise. (Nishinaga et al., 2020).

Ahmadi and co-workers, in their review article, reported the effect of the composition of liposomes on the release of encapsulation under ultrasound (US). The synthesis of liposomes based on dioleoyl phosphatidyl ethanolamine and hydrogenated soy phosphatidylcholine was reported. They also reported chloroaluminum(III) phthalocyanine tetrasulfonic acid as the near-infrared fluorochrome drug model. AlPcS4 was found to be included, in an efficient manner, in both liposomes, and this was confirmed with concentration-dependent fluorescent quenching. The liposomes were stable in serum and they did not give out any fluorescent signal. When 1.1 MHz ultrasound was applied, dioleolyl phosphatidyl ethanolamine-based liposomes led to ca. 40% drug release after 1 min and hydrogenated soy phosphatidylcholine was less active, only leading to about 20% drug release. The in vivo studies led to the conclusion that ultrasound application caused the release of the fluorescent phthalocyanine from the first type of liposome and a fluorescent signal intensity ($P < 0.05$) increased for 100%, where for the latter type, no signal enhancement was obtained. The study therefore describes the ultrasound-triggered release of the fluorescent phthalocyanine (Ahmadi et al., 2020).

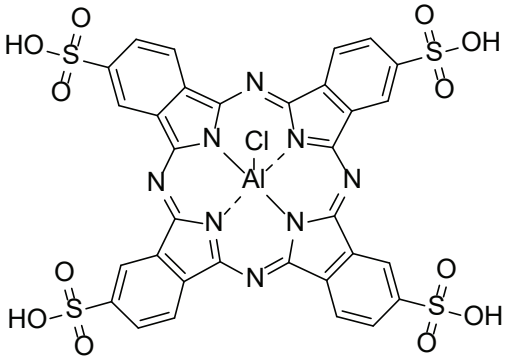

Figure 1. *The structure of chloroaluminum(III) phthalocyanine tetrasulfonic acid.*

Photodynamic therapy (PDT), is an innovative and non-invasive form of the therapy of cancer, based on the photodynamic effect. The authors determined intracellular uptake, singlet oxygen production, and in vitro photodynamic potential of the nanosystem against pancreatic cancer cells, in which the nanosystem included cetixumab, peripherally octakis (tert-butylphenoxy) substituted zinc(II) phthalocyanine, and mesoporous silica nanoparticles. The quantum yield of the complex was found as 0.60 in toluene solution. The authors tested the dark phototoxicity and the photoxicity at different light fluences of several concentrations of the zinc complex by using pancreatic cells. No dark toxicity was present and the zinc complex alone showed a mild photodynamic activity, yet when included in silica nanoparticles, the phototoxic effect in the presence of

Cetuximab was much greater. EGFR receptor-expressing pancreatic cells are excellent targets for this nanomolecular vehicles. (Er et al., 2018).

Photochemical reactions usually have dramatic effects on the physical properties of molecules in a reaction. In the study by Sato et al., the authors demonstrated that NIR light induces a release from axial position, and this alters dramatically the hydrophilicity of a SiPc (IR700) dye, ultimately leading to conjugate's shape change hence its tendency for aggregation in aqueous solution. The authors proposed that this photochemistry causes a major mechanism of cellular death along with NIR-PIT, which is considered as an efficient cancer therapy that is targeted in a molecular manner.

When the binding of antibody-IR700 conjugate has effected, NIR light activation causes physical changes in the shape of antibody-antigen complexes, and this in turn provides physical stress in the cellular membrane; the transmembrane water flow increases, leading to a burst of the cell and necrosis (Sato et al., 2018).

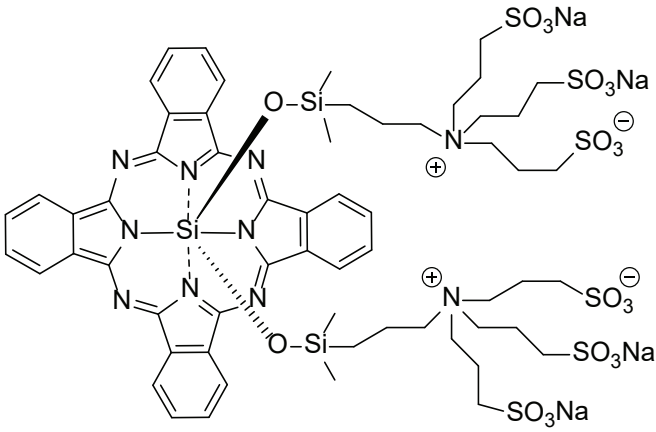

Figure 2. *The structure of silicon phthalocyanine.*

Considerable attention has been gained from multifunctional phototheranostic nanoparticles, which are prepared from photosentisizing molecules and they are successfully used in tumoral phototherapies. Photothermal activity (PTT) is more encountered than photodynamic therapy (PDT) in self-assembled photosensitizing nanoparticles, in which the latter is greatly restricted. Wang and their colleagues prepared substituted zinc phthalocyanine molecules which are capable of performing PTT and PDT at the same time with 650 nm irradiation. They obtained an outstanding therapeutic effect due to the synergistic action of PTT and PDT, in which substituted ZnPc particles behave as effective and safe cancer treatment agent in clinical research (Wang et al., 2019).

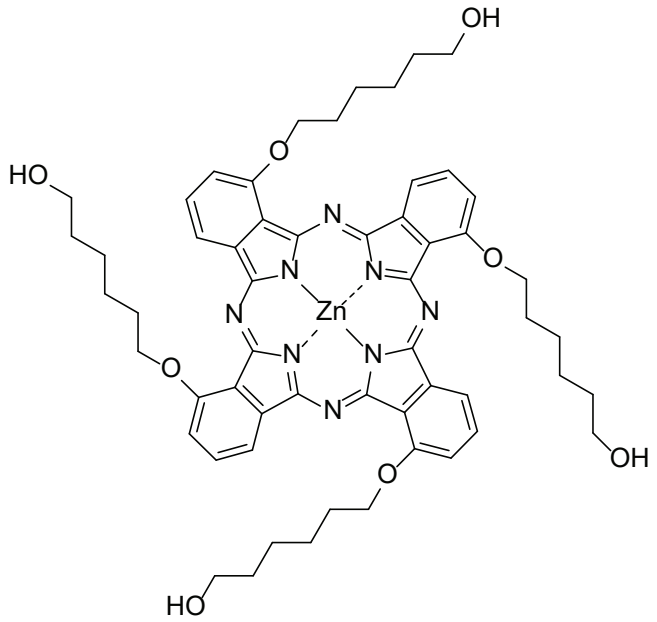

Figure 3. *The structure of non-peripherally substituted zinc phthalocyanine.*

In a review by Roguin et al., the researchers mention of photodynamic therapy applications, exhaustively using zinc phthalocyanine derivatives and they have not yet been approved as photosensitizers for clinical therapy. The authors gave physicochemical properties of ZnPc derivatives, biological results of them in the in vitro and 3D cultures, chicken chorioallantoic membranes, and tumor-bearing mice. All these media constitute of more complex models. The authors also mention of combined therapy cases including zinc phthalocyanines and their clinical trials that are currently available (Roguin et al., 2019).

Nanodrugs which are capable of performing more than one task are highly desired in the treatment of cancer. There are few examples of two-dimensional nanomaterials in the form of coordination nanosheets. Authors propose phthalocyanine-based coordination nanosheets in which the photoactive entity is manganese(II) phthalocyanine tetracarboxylic acid and hyaluronic acid is coated on their surface, forming a nanosheet structure abbreviated as MnPc@HA. The near-infrared photothermal effect, along with photothermal conversion, had an efficiency of about 73% and this value is superior to those reported in the literature. MnPc@HA nanosheets are capable of enduring high drug-loading capacity for curcumin, a chemotherapeutic agent (Zeng et al., 2019).

Elevated glutathione (GSH) levels are responsible for hindering targeted therapeutic efficiency. Wei and their co-workers studied on a non-symmetrical zinc phthalocyanine, whose brief name was ZnPc-C8-

Len, and they coupled lenvatinib (a VEGFR inhibitor) to it through an alkyl chain in a hope that multidrug resistance was reversed and enhanced antitumoral therapy was achieved. With irradiation, ZnPC-C8-Len produces reactive oxygen species that depleted intracellular glutathione and causing apoptotic cellular death. ZnPc-C8-Len had fluorescent features and the changes could be monitored in vivo, making it possible to decide when to apply the therapy (Wei et al., 2019). From a chemist's viewpoint, the molecule ZnPc-C_0-Len is not possible to occur as the amide counterpart of the molecule is not capable of acting as an amine, whereas the other molecules' formations are feasible.

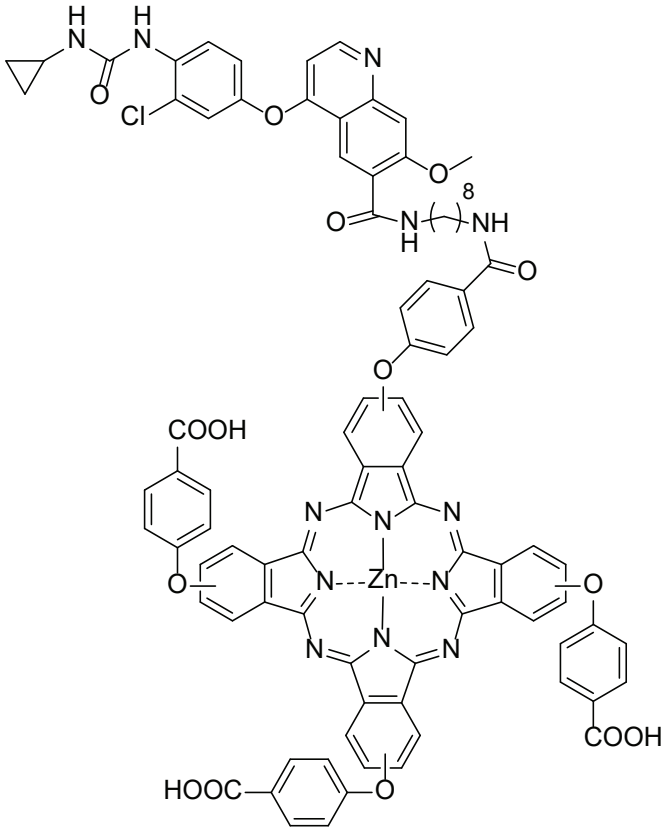

Figure 4. *The structure of ZnPc-C8-Len.*

Because telomerase plays a crucial role in the unlimited proliferation of cancer cells, inhibiting this enzyme is a promising method, by stabilizing G-Quadruplex DNAs by guest molecules in a host-guest fashion. To see if a compound is eligible as a telomerase inhibitor, it is necessary to assess whether this compound is selective for quadruplex DNA over the duplex one. In the study by Ramos et al., tetrapyrrolic compounds having four or eight quaternized groups were reviewed, because they are considered as G-Quadruplex stabilizing ligands. It was concluded that a balance

exists between the numbers and positions of the quaternized groups in the phthalocyanine; it is an important asset for selecting G-Quadruplex structures over duplex DNA. A phthalocyanine structure reported by Ramos et al., having four or eight peripheral positive charges, led to a high selectivity and affinity for G-Quadruplex over duplex DNA and aggregated in the nuclei of UM-UC-3 bladder cancer cells (Ramos et al., 2019).

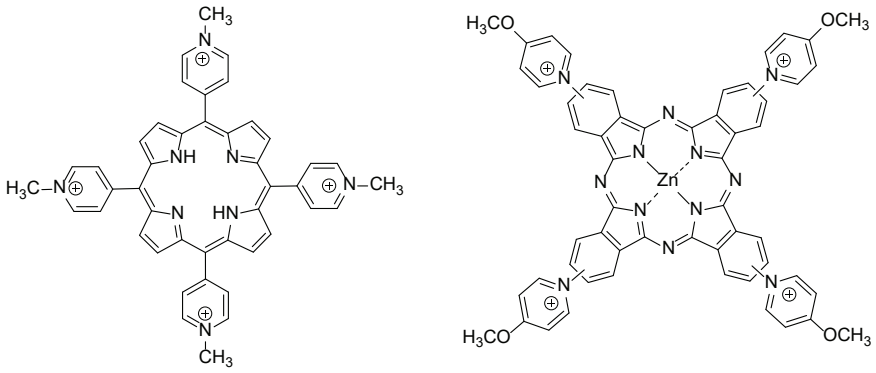

Figure 5. *Methoxypyridinium phthalocyanine.*

Non-symmetrical cobalt phthalocyanines with two sulfonic acid sodium salt entities were interacted with calf thymus DNA and there were two types of DNA binding. $CoPcS_2$ was found to bind to the phosphate end of DNA and formed aggregates on the periphery of the DNA helix. In this interaction, DNA played the role of a matrix and the number of stacking interactions increased. The second type of cobalt-DNA interaction takes some time to manifest itself. Cobalt's coordination sphere allows some atoms from DNA to coordinate to the metal ion and the whole structure is reorganized. The minor groove of DNA is not affected from the interaction. The N7 guanine, the most important part of the DNA, is unaffected, therefore the intercalation model is completely excluded. The phthalocyanines' planes showed an orientation that was normal to the DNA's axis. DNA's rigidity did not change after the interaction as suggested by the optical anisotropy and intrinsic viscosity of DNA (Kasyanenko et al., 2019).

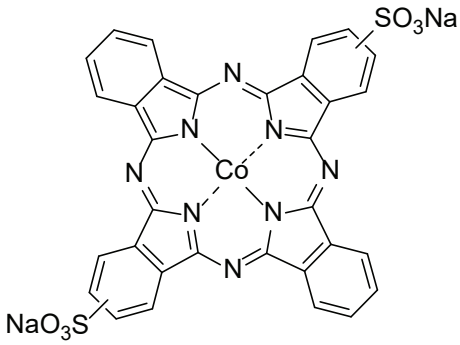

Figure 6. *Cobalt phthalocyanine disulfonic acid disodium salt.*

For photodynamic therapy (PDT), self assembly of phototheranostic nanobodies are of great importance along with many advantages. A novel method was designed for size-tunable self-assembly of nano-sized photosensitizers for PDT. A silicon(IV) phthalocyanine and biotin formed a conjugate in which the size was governed by Cremophor EL surfactant. The particle size of the prepared nanostructures also dominates the fluorescence and generation of reactive oxygen species (ROS). Tumoral over-expressing biotin receptors cause disassembly of the nanostructures and the quenching be recovered. Self-assembly structures were capable of invading HepG2 cells in a biotin-receptor pathway and biotin-receptor-triggering fluorescent recovery was obtained in a scope of cells. In the nanochemical series, the smallest member managed to provide the highest photocytotoxicity, improved intracellular fluorescence, highest ratio for reactive oxygen species, the best localization in the subcellular scale, tumor targeting in vivo, and the best photodynamic efficiency. (D. Li et al., 2019).

For photodynamic therapy, phthalocyanines are considered to have good potential, however their poor solubility, high aggregation tendency, and low specificity to tumors are key problems that must be solved for successful applications. The authors have synthesized a biotin-containing silicon(IV) phthalocyanine molecule to be a water-soluble photosensitizer capable of tumor-targeting. Axial ligation decreased the aggregative behavior of Pcs. In vitro experiments provided the information that the compound accumulates successfully in biotin receptor-positive HeLa cells. Since it is water-soluble and does not aggregate much, the compound was recommended for a xenograft tumor model. In vivo imaging and tissue distribution studies revealed that the compound selects, predominantly, the tumor cells in a tumor-bearing mice model (tolerable signals coming from the vicinity of the cell exist). In vivo, under irradiation, the compound was successful in depressing the progression of the tumor. A 14-day treatment showed that the volumes of tumor were smaller than the beginning size (K. Li et al., 2019).

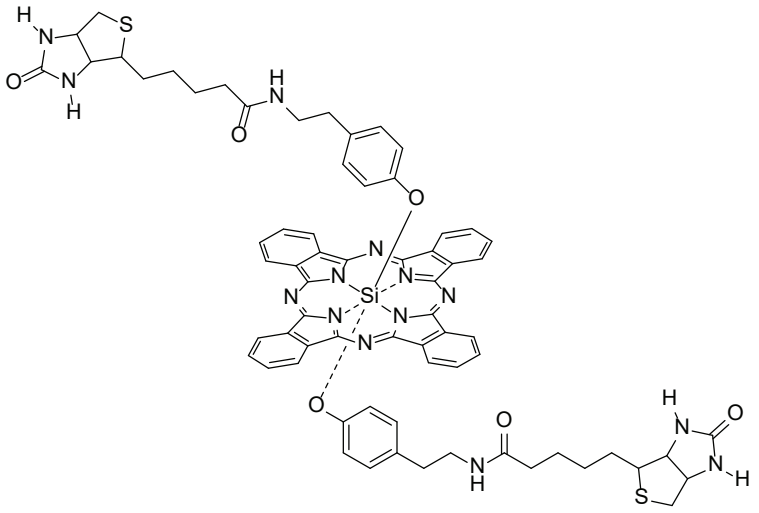

Figure 7. *Biotin-containing silicon(IV) phthalocyanine.*

Matlou and colleagues investigated the photodynamic therapy activity of cinnamic acid-containing zinc and indium phthalocyanines and they coupled the carboxylic acid bond to amino-functionalized magnetic nanoparticles. In terms of triplet and singlet oxygen quantum yields, non-symmetrical ZnPc displayed a better performance than the symmetrical analogues. When the phthalocyanine contained amino-functionalized magnetic nanoparticles, the triplet quantum yield was seen to increase. The complexes displayed an increased in-vitro phototoxicity against MCF-7 cells when the authors increased the drug concentration. At a concentration of 80 μg/mL, the conjugates gave a higher singlet oxygen quantum yield and their cytotoxic effects on cancer cells were higher in the presence of light (Matlou et al., 2019).

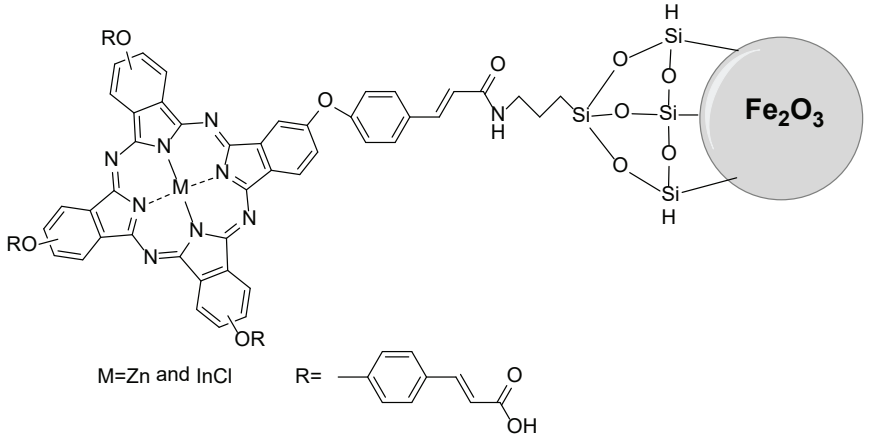

Figure 8. *Cinnamic acid-containing zinc and chloroindium phthalocyanines and their chemical linkage to amino-functionalized magnetic nanoparticles.*

Authors describe the last five-year history of phthalocyanines and discuss about designing these macrocycles for medicinal applications. This literature is a good starting point for those who want to learn more about the latest discussions on Pcs in PDT (X. Li et al., 2019).

The problem of delivering poorly soluble drugs in the diagnosis and treatment of cancer cells could be solved by the application of multifunctional nanodots. The authors applied a cryodesiccation-driven crystallization approach for preparing the nanocrystallites of water-insoluble photosensitizer (ZnPc). When the surface was modified with nanodots along with Pluronic F127 and folic acid, the resulting complex gains excellent water-solubility. Under near-infrared photoexcitation at 808 nm, the nanodots showed the production of singlet oxygen (Ding et al., 2019).

Yu and colleagues (2019) used zinc phthalocyanine for targeted photodynamic therapy and they used a tumor-directing entity and epidermal growth factor receptor (EGFR) binding peptide for the coupling required. As a result, the biocompability and tumoral selectivity increased. This phthalocyanine-peptide conjugate was investigated in terms of its biotoxicity, photophysical properties, cellular uptake, and in vivo biodistribution. Cells like A431 which over-express EGFR were more vulnerable to the Pc's effects, but low-EGFR-expressing tumoral cells like human breast adenocarcinoma MCF7 have little cellular uptake. When the authors administered the compound to the A431-tumor-bearing mice, the compound, namely Pc-GE11 conjugate, led to a much higher tumoral accumulation than the non-targeted control. According to the results, Pc-GE11 conjugate is a good candidate for targeted photodynamic therapy and bioimaging (Yu et al., 2019).

Chloroaluminum phthalocyanine tetrasulfonic acid ($AlPcS_4$) is a synthetic aromatic macrocycle. Since it could be activated with a far red light, it can penetrate deeply into the tissue, along with its low photo-bleaching and high quantum yields and it is also stable. Pulmonary cancer has a ratio of 1 to 5 in all cancer-related deaths worldwide. Crous et al. explored the photochemical properties of chloroaluminum phthalocyanine tetrasulfonic acid, its uptake into pulmonary cancer, intracellular localization of it and the photodynamic application on the cancer (A549 cells were employed). ClAlPc tetrasulfonic acid was reported to be a robust molecule, localizing in the intracellular organelles, including mitochondrion and lysosomes. PDT application revealed that cellular death increased and cellular proliferation and viability decreased. Under in vitro conditions, the photosensitizer proved to be effective, but photodynamic efficacy also relies upon tumor vasculature and tumor-specific accumulation also must be considered when a clinical application is being planned. Photodynamic

therapy could be taken into account as an adjunct therapy, until standard protocols for a number of tumoral types with a relevant photosensitizer is validated (Crous et al., 2019).

Nitrogen monoxide (NO) generation is important, especially when it is combined to photobiomodulation and photodynamic therapy. Negri et al. stated that photobiomodulation, as combined with photodynamic therapy, could be a beneficial option of cancer treatment. The authors used two ruthenium compounds, namely ruthenium(II) phthalocyanine and trans(nitrosyl)(nitro)(phthalocyaninato) ruthenium, and around 660 nm in the UV-Vis spectrum there was a band. 0.5 μM ruthenium (nitrosyl)(nitro) (phthalocyanine) compound caused the light irradiation at the Q band reduce viable A375 (human melanoma) cells to ca. 50% against the control being ruthenium phthalocyanine. Between singlet oxygen and nitric oxide, there possibly might a synergistic effect. In a combination of these compounds, PDT at 660 nm and PBM at 850 nm caused more photocytotoxicity. A possible explanation was that PBM increased the cellular metabolism (that is, production of ATP), and consequently, RuPc compounds are being taken inside the cell and apoptosis was more efficient. In the field of photodynamic therapy, metal-based photosensitizes, as combined with light therapy, seems to introduce an advanced field. (Negri et al., 2019).

The general insolubilities of phthalocyanines poses a complexity in the applications of them. Lu et al. provided a way for solubilizing the ZnPc and a mixed micellar structure was introduced. They employed sodium deoxycholate as the first and D-alpha tocopheryl polyethylene glycol succinate as the second micellar structures. The phthalocyanine, which is highly hydrophobic, reside in the hydrophobic part of the micelles, through a supramolecular self-assembly. A series of mixed micellar architectures containing ZnPc at the core were prepared and their physicochemical properties, drug release characters, photostabilities, photodynamic activities, and cellular viability. Irradiated by a 650-nm red laser, the ZnPc-loaded micellar structure produced singlet oxygen with 1,3-diphenylisobenzofuran as the probe.

The mixed micellar organizations had higher singlet oxygen quantum yields than the control compound (ZnPc), and three of them in the series had very promising singlet oxygen generation ability. The micellar structure was stable in terms of photodynamic therapeutic timescale, along with a small amount of photobleaching effect was observed after 20 minutes of irradiation. A sustained release profile was suggested for the mixed micellar structure's in vitro drug release behavior. At the same concentration, the mixed micellar structure was found to be more toxic than unbonded zinc phthalocyanine against A549 cells (Lu et al., 2019).

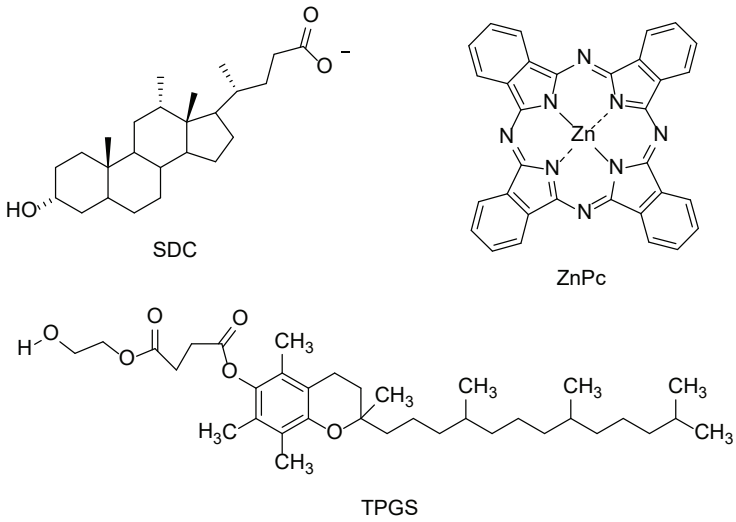

Figure 9. *Structures of SDC, TPGS, and ZnPc.*

PART B: STUDIES, WHICH MAY PROCEED TO COMPREHENSIVE PHOTODYNAMIC THERAPY AFTER SOME EFFORT

These reports contain some basic measurements of synthesized compounds which will guide to sophisticated experiments of cancer therapy, given the opportunity. There are many studies like those cited below, and they, we believe, deserve further study after a good collaboration.

At the peripheral and non-peripheral positions, the researchers prepared piperidin-containing phthalocyanines and they then quaternized the products, leading to water-soluble molecules. When they irradiated the compounds, they led to significant cleavage effects against plasmid DNA. The phthalocyanine derivatives with non-peripheral substitution were more successful in terms of cleaving the DNA, in the presence of a series of oxidizing agents. The mentioned compound was suggested as a potent photosensitizer for photodynamic therapy due to its potential to damage DNA with irradiation applied (Özel et al., 2019).

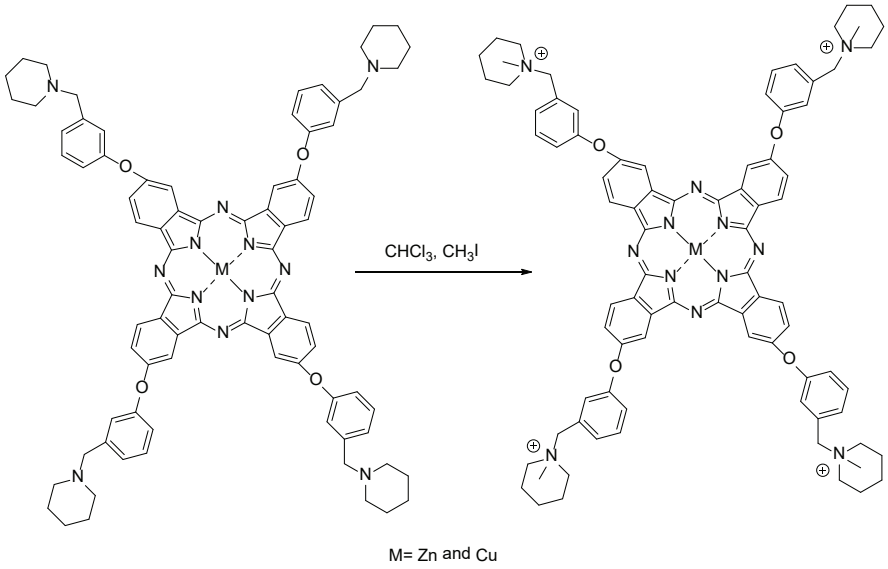

Figure 10. *Piperidin-containing phthalocyanines and their quaternized forms.*

Yalazan and coworkers examined tosylated 4-morpholinoaniline-bearing tetrasubstituted phthalocyanines at peripheral positions and their behaviors as anticancer agents. They prepared metal-free, copper, zinc, cobalt(II), and magnesium phthalocyanines. ZnPc, CoPc, and MgPc were accepted into more advanced PDT applications, say oncologic and molecular biologic studies like pBR322 plasmid DNA cleavage on agarose gel electrophoresis. ZnPc was reported to cleave pBR322 plasmid DNA with irradiation. An MTT assay towards human colorectal (HCT-116) and cervical (HeLa) cells was conducted with ZnPc, allowing to investigate its cytotoxic/phototoxic properties. Cellular viabilities for ZnPc against HCT-116 was 73 ± 1.6% and against HeLa was 65 ± 5.5% at 100 mM concentration, with applied irradiation (Yalazan et al., 2020).

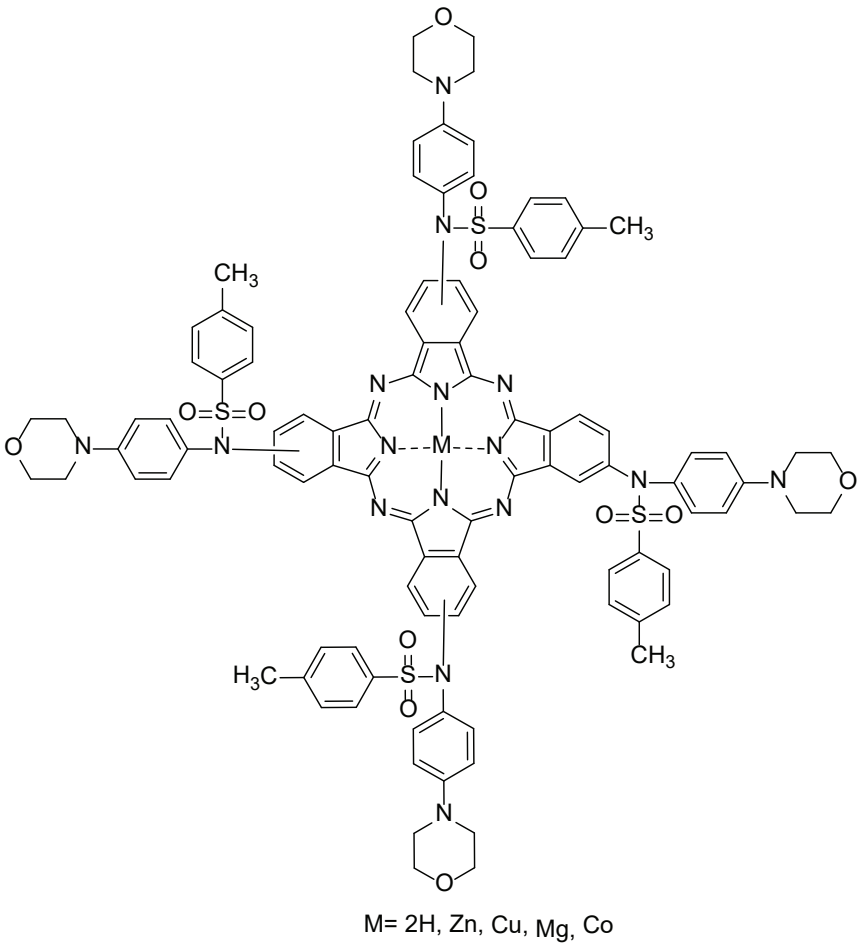

Figure 11. *Structures of tosylated 4-morpholinoaniline-bearing tetrasubstituted phthalocyanines.*

A study by Şen et al. provides a report about phthalocyanines having benzimidazole units and their unmetallated, zinc, chloroindium(III), and chlorogallium(III) phthalocyanines were prepared. Their photodynamic efficacies and photophysicochemical properties were studied in dimethyl sulfoxide. The metal-free phthalocyanine presented a higher fluorescent quantum yield and its fluorescent lifetime was also higher than that of the metallophthalocyanines investigated. Chloroindium(III) phthalocyanine, in the phthalocyanine series studied, yielded the highest values of singlet oxygen (ΦΔ) and triplet state quantum yield (ΦT) (Sen et al., 2019).

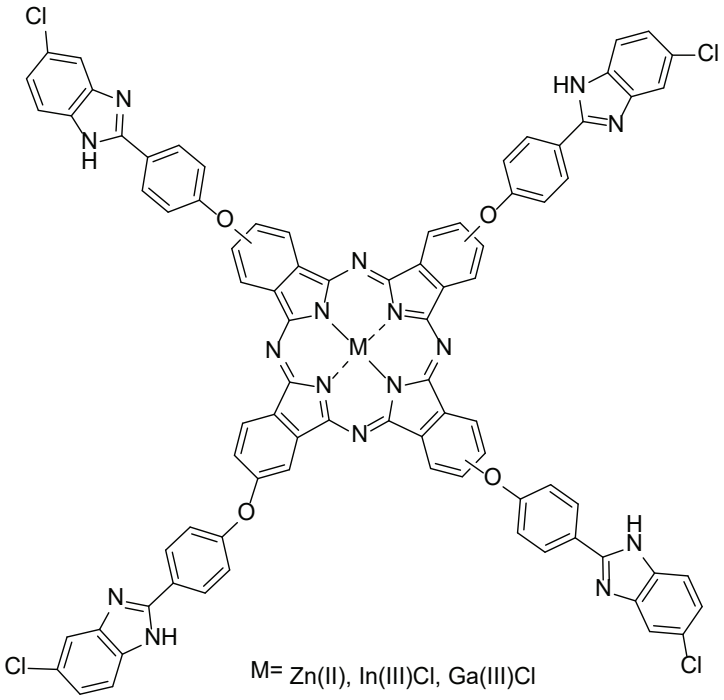

Figure 12. *Phthalocyanines having benzimidazole units.*

Şen and Nyokong synthesized a novel silicon(IV) phthalocyanine bearing, at axial positions, a palladium(II)-Schiff base complex. This silicon(IV) phthalocyanine was assayed for its photophysical and photochemical properties and its dimethylsulfoxide solution was subjected to UV-Vis absorption, fluorescence spectrophotometry, quantum yield of singlet oxygen, quantum yield at triplet state, and excited state lifetimes. The complex's very low fluorescent behavior led to an efficient intersystem crossing, high triplet lifetimes, and high singlet oxygen quantum yields. The compound displayed excellent photodynamic activity, along with a 99.94% reduction percentage and 3.26 as a log red value (Sen & Nyokong, 2019).

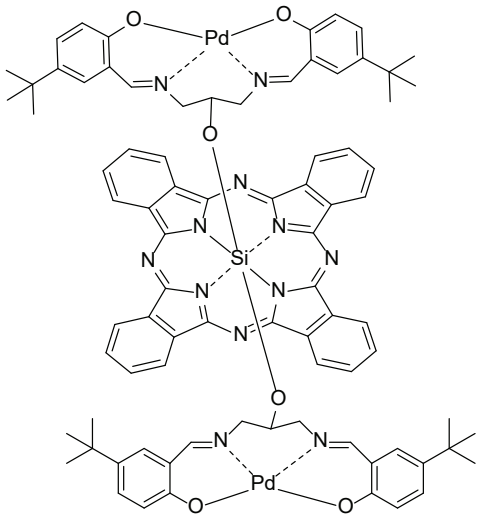

Figure 13. *A silicon(IV) phthalocyanine bearing two palladium(II)-Schiff base complexes at axial positions.*

A study by Demirbaş et al reported the preparation of a novel peripherally triazole-substituted ZnPc phthalocyanines synthesized from four different precursors. Using comparative method in calculating the fluorescence quantum yields is common in this type of studies and fluorescence quenching properties of the studied phthalocyanines was reported. In addition, photodegradation quantum yields of the complex was reported. Singlet oxygen quantum yields of the compounds were calculated via the comparative method in the presence of 1,3-diphenylisobenzofuran as the quenching entity. The quantum yield values of the complex was in the range of 0.8 – 0.85 and the compared unsubstituted ZnPc's quantum yield was 0.67. The compound with a tolyl group as the substituent proved the highest singlet oxygen quantum yield and this high value is very rare (Demirbaş et al., 2019).

A Bulgarian-Turkish collaboration yielded a paper in which Aliosman et al. prepared an octasubstituted zinc phthalocyanine containing 4-tyrosylamidophenyl substituents at the periphery and introductory photodynamic activity tests were conducted. The team also prepared the tetrasubstituted phthalocyanine and unsubstituted ZnPc for comparison. Absorption, fluorescence, and singlet oxygen photochemistry, photostability, and in vitro phototoxicity were investigated. The team obtained an improved photophysicochemical result for the substituted ZnPc complexes. The octasubsituted ZnPc molecule is more advantageous since its water solubility is greater, possibly leading its way to more sophisticated PDT tests (Aliosman et al., 2019).

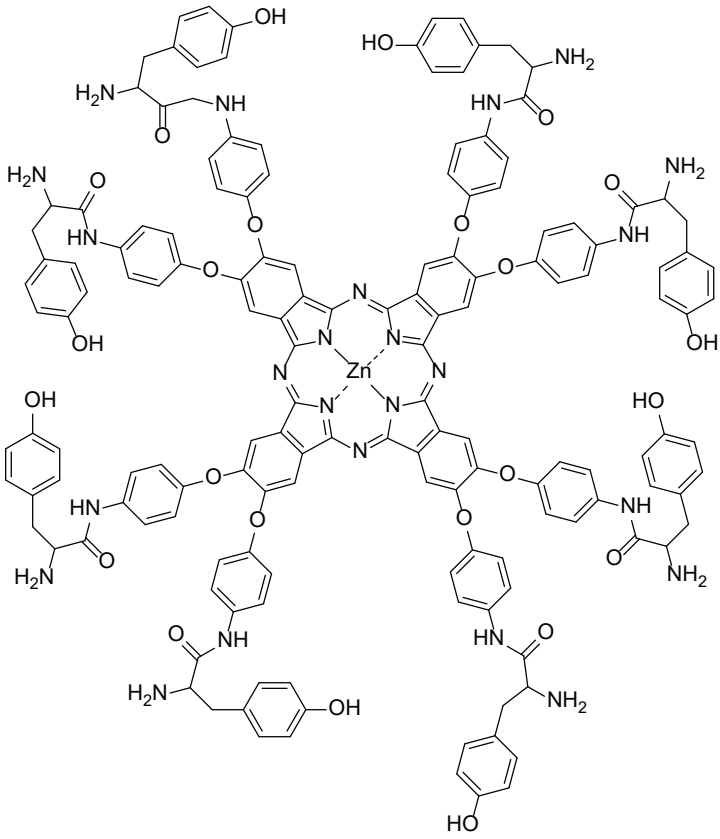

Figure 14. *Octasubstituted zinc phthalocyanine containing 4-tyrosylamidophenyl substituents.*

Aluminum octacarboxyphthalocyanine and nanoparticles were studied together to see the interaction between them. When phthalocyanine molecules are adsorbed on the nanoparticle, yet only to a certain limit, the non-radiative energy transfer efficiency was seen to be increased. When the number of phthalocyanine molecules are increased further, their concentration resulted in a decrease of its sensitized fluorescence due to the dimerization of dye molecules on the nanoparticle surface. When subjected to infrared irradiation, phthalocyanine molecules in the hybrid complex generated singlet oxygen. The observed effects are of interest in regard to the targeted search for new components of efficient third generation hybrid photosensitizers (Gvozdev et al., 2019).

In the work by Köksoy et al., the novel phthalonitrile precursor compounds having 7-oxy-3-(p-thiomethylphenyl) coumarin substituents and their corresponding peripheral/nonperipheral phthalocyanines with zinc and chloroindium metals at the core were synthesized and purified. The photochemical and photophysical properties of the complexes were

examined in dimethylformamide solutions (Köksoy et al., 2019).

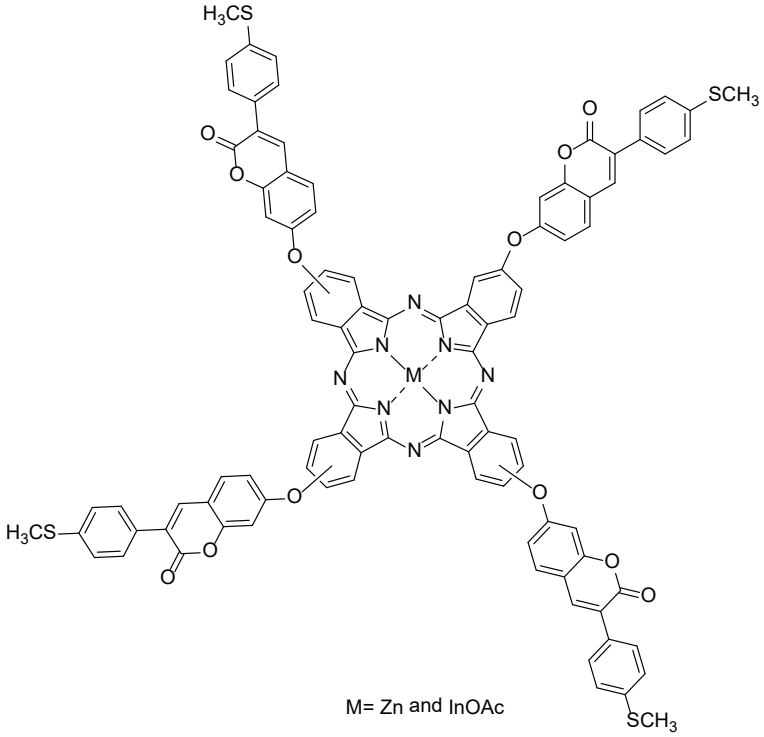

Figure 15. *Zinc and acetatoindium phthalocyanines containing (methylsulfanyl) coumarin moieties at peripheral positions.*

Majeed et al. have prepared four carbazole-containing phthalocyanines and performed their essential spectral characterizations. Owing to the charge transfer effect and prolonged excited state lifetime of 5 ns and high singlet quantum yield of 0.825 were obtained (Majeed et al., 2019).

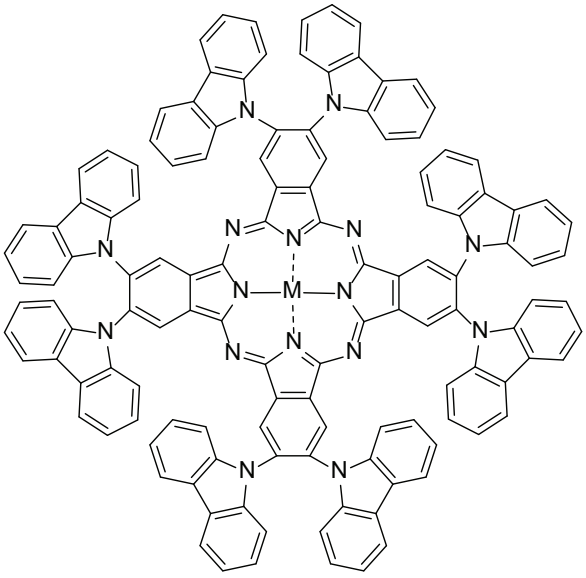

Figure 16. *Carbazole-containing phthalocyanines.*

Keleş et al. worked about pyridine-containing silicon(IV) phthalocyanine, and its naphthalocyanine counterpart, along with their quaternized, water-soluble derivatives. The cytotoxicity, DNA interaction, topoisomerase inhibitory property, and antitumoral effect against five carcinoma cell lines were examined. Among the five carcinoma cells, the CC50 values of the water-soluble compounds were determined as 2.15-52.97 μM.

Against the carcinoma cell lines, the water-soluble silicon phthalocyanine compound displayed the SI values of 4.51, 1.43, and 3.66, respectively. With flow cytometry, A549 cells suffered cellular cycle arrest and water-soluble silicon phthalocyanine and naphthalocyanine compounds led to cellular cycle arrest at G0/G1 phase. The water-soluble silicon phthalocyanine is active against pulmonary, breast, and melanoma cancer lines with high selectivity (Keleş et al., 2019).

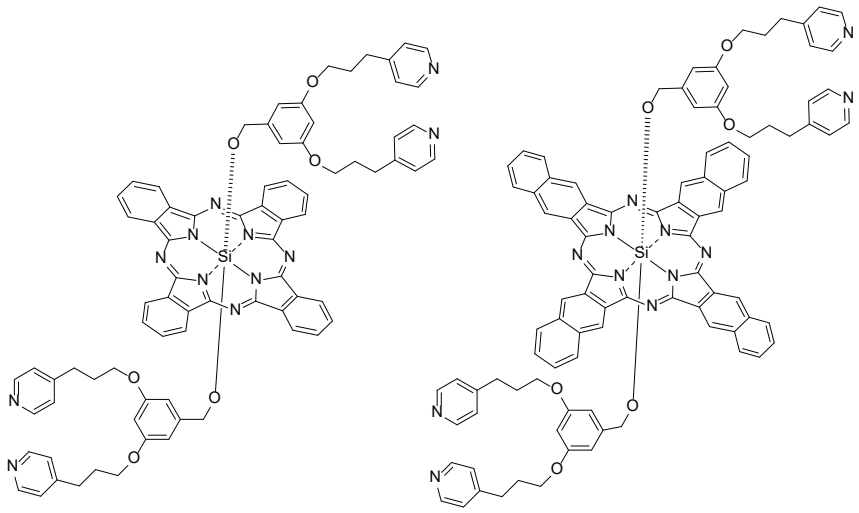

Figure 17. *Pyridine-containing silicon(IV) phthalocyanine.*

CONCLUSION

There are two main types of studies in the literature. One of them uses phthalocyanines as active agents for singlet oxygen generation and diminishing tumor volumes, while the other type of studies investigates photophysical and photochemical properties of phthalocyanine derivatives as candidates for real antitumor studies. We hope that the endeavors and molecules synthesized in the latter reach the former, therefore the library of molecules increase in the fight against cancer.

REFERENCES

Ahmadi, A., Hosseini-Nami, S., Abed, Z., Beik, J., Aranda-Lara, L., Samadian, H., Morales-Avila, E., Jaymand, M., & Shakeri-Zadeh, A. (2020). Recent advances in ultrasound-triggered drug delivery through lipid-based nanomaterials. *Drug Discovery Today*, S1359644620303834. https://doi.org/10.1016/j.drudis.2020.09.026

Aliosman, M., Angelov, I., Mitrev, Y., Iliev, I., Durmuş, M., & Mantareva, V. (2019). Novel Zn(II) phthalocyanine with tyrosine moieties for photodynamic therapy: Synthesis and comparative study of light-associated properties. *Polyhedron*, *162*, 121–128. https://doi.org/10.1016/j.poly.2019.01.029

Constantin, C., Lupu, A.-R., Fertig, T. E., Gherghiceanu, M., Pop, S., Ion, R.-M., & Neagu, M. (2019). Unveiling Ga(III) phthalocyanine-a different photosensitizer in neuroblastoma cellular model. *Journal of Cellular and Molecular Medicine*, *23*(2), 1086–1094. https://doi.org/10.1111/jcmm.14009

Crous, A., Dhilip Kumar, S. S., & Abrahamse, H. (2019). Effect of dose responses of hydrophilic aluminium (III) phthalocyanine chloride tetrasulphonate based photosensitizer on lung cancer cells. *Journal of Photochemistry and Photobiology B: Biology*, *194*, 96–106. https://doi.org/10.1016/j.jphotobiol.2019.03.018

Demirbaş, Ü., Bayrak, R., Dilber, G., Menteşe, E., & Akçay, H. T. (2019). Novel triazole substituted phthalocyanines showing high singlet oxygen quantum yields. *Journal of Luminescence*, *206*, 199–204. https://doi.org/10.1016/j.jlumin.2018.10.051

Ding, H., Cai, Y., Chen, J., Lu, T., Wen, W., Nie, G., & Wang, X. (2019). Cryodesiccation-driven crystallization preparation approach for zinc(II)-phthalocyanine nanodots in cancer photodynamic therapy and photoacoustic imaging. *Microchimica Acta*, *186*(4), 237. https://doi.org/10.1007/s00604-019-3286-z

Er, Ö., Colak, S., Ocakoglu, K., Ince, M., Bresolí-Obach, R., Mora, M., Sagristá, M., Yurt, F., & Nonell, S. (2018). Selective Photokilling of Human Pancreatic Cancer Cells Using Cetuximab-Targeted Mesoporous Silica Nanoparticles for Delivery of Zinc Phthalocyanine. *Molecules*, *23*(11), 2749. https://doi.org/10.3390/molecules23112749

Gvozdev, D. A., Lukashev, E. P., Gorokhov, V. V., & Pashchenko, V. Z. (2019). Photophysical Properties of Upconverting Nanoparticle–Phthalocyanine Complexes. *Biochemistry (Moscow)*, *84*(8), 911–922. https://doi.org/10.1134/S0006297919080078

Kasyanenko, N. A., Tikhomirov, R. A., Bakulev, V. M., Demidov, V. N., Chikhirzhina, E. V., & Moroshkina, E. B. (2019). DNA Complexes with

Cobalt(II) Phthalocyanine Disodium Disulfonate. *ACS Omega*, *4*(16), 16935–16942. https://doi.org/10.1021/acsomega.9b02300

Keleş, T., Barut, B., Özel, A., & Biyiklioglu, Z. (2019). Synthesis of water soluble silicon phthacyanine, naphthalocyanine bearing pyridine groups and investigation of their DNA interaction, topoisomerase inhibition, cytotoxic effects and cell cycle arrest properties. *Dyes and Pigments*, *164*, 372–383. https://doi.org/10.1016/j.dyepig.2019.01.044

Köksoy, B., Durmuş, M., & Bulut, M. (2019). Potential photosensitizer candidates for PDT including 7-oxy-3-thiomethylphenyl coumarino-phthalocyanines. *Inorganica Chimica Acta*, *498*, 119137. https://doi.org/10.1016/j.ica.2019.119137

Li, D., Wang, X.-Z., Yang, L.-F., Li, S.-C., Hu, Q.-Y., Li, X., Zheng, B.-Y., Ke, M.-R., & Huang, J.-D. (2019). Size-Tunable Targeting-Triggered Nanophotosensitizers Based on Self-Assembly of a Phthalocyanine–Biotin Conjugate for Photodynamic Therapy. *ACS Applied Materials & Interfaces*, *11*(40), 36435–36443. https://doi.org/10.1021/acsami.9b13861

Li, K., Dong, W., Liu, Q., Lv, G., Xie, M., Sun, X., Qiu, L., & Lin, J. (2019). A biotin receptor-targeted silicon(IV) phthalocyanine for in vivo tumor imaging and photodynamic therapy. *Journal of Photochemistry and Photobiology B: Biology*, *190*, 1–7. https://doi.org/10.1016/j.jphotobiol.2018.09.001

Li, X., Zheng, B.-D., Peng, X.-H., Li, S.-Z., Ying, J.-W., Zhao, Y., Huang, J.-D., & Yoon, J. (2019). Phthalocyanines as medicinal photosensitizers: Developments in the last five years. *Coordination Chemistry Reviews*, *379*, 147–160. https://doi.org/10.1016/j.ccr.2017.08.003

Lu, X., Zhu, W., Chen, T., Peng, Q., Yu, C., & Yang, M. (2019). Exploration of photophysical and photochemical properties of Zinc phthalocyanine-loaded SDC/TPGS mixed micelles. *Chemical Physics Letters*, *735*, 136737. https://doi.org/10.1016/j.cplett.2019.136737

Majeed, S. A., Ghazal, B., Nevonen, D. E., Nemykin, V. N., & Makhseed, S. (2019). Spectroscopic and TDDFT studies on the charge-transfer properties of metallated Octa(carbazolyl)phthalocyanines. *Dyes and Pigments*, *170*, 107593. https://doi.org/10.1016/j.dyepig.2019.107593

Matlou, G. G., Oluwole, D. O., & Nyokong, T. (2019). Evaluation of the photosensitizing properties of zinc and indium tetra cinnamic acid phthalocyanines linked to magnetic nanoparticles on human breast adenocarcinoma cells. *Journal of Luminescence*, *205*, 385–392. https://doi.org/10.1016/j.jlumin.2018.09.054

Meng, T., Qin, Q.-P., Chen, Z.-L., Zou, H.-H., Wang, K., & Liang, F.-P. (2019). High in vitro and in vivo antitumor activities of Ln(III) complexes with mixed 5,7-dichloro-2-methyl-8-quinolinol and 4,4′-dimethyl-2,2′-bipyridyl chelating ligands. *European Journal of Medicinal Chemistry*, *169*, 103–110. https://doi.org/10.1016/j.ejmech.2019.02.066

Negri, L. B., Martins, T. J., da Silva, R. S., & Hamblin, M. R. (2019). Photobiomodulation combined with photodynamic therapy using ruthenium phthalocyanine complexes in A375 melanoma cells: Effects of nitric oxide generation and ATP production. *Journal of Photochemistry and Photobiology B: Biology*, *198*, 111564. https://doi.org/10.1016/j.jphotobiol.2019.111564

Nishimura, T., Mitsunaga, M., Ito, K., Kobayashi, H., & Saruta, M. (2020). Cancer neovasculature-targeted near-infrared photoimmunotherapy (NIR-PIT) for gastric cancer: Different mechanisms of phototoxicity compared to cell membrane-targeted NIR-PIT. *Gastric Cancer*, *23*(1), 82–94. https://doi.org/10.1007/s10120-019-00988-y

Nishinaga, Y., Sato, K., Yasui, H., Taki, S., Takahashi, K., Shimizu, M., Endo, R., Koike, C., Kuramoto, N., Nakamura, S., Fukui, T., Yukawa, H., Baba, Y., K. Kaneko, M., Chen-Yoshikawa, T. F., Kobayashi, H., Kato, Y., & Hasegawa, Y. (2020). Targeted Phototherapy for Malignant Pleural Mesothelioma: Near-Infrared Photoimmunotherapy Targeting Podoplanin. *Cells*, *9*(4), 1019. https://doi.org/10.3390/cells9041019

Özel, A., Demirbaş, Ü., Barut, B., & Kantekin, H. (2019). The novel water soluble peripherally and non-peripherally tetra piperidine substituted phthalocyanines: Synthesis, characterization, DNA cleavage properties. *Journal of Molecular Structure*, *1186*, 325–332. https://doi.org/10.1016/j.molstruc.2019.03.047

Ramos, C., Almeida, S., Lourenço, L., Pereira, P., Fernandes, R., Faustino, M., Tomé, J., Carvalho, J., Cruz, C., & Neves, M. (2019). Multicharged Phthalocyanines as Selective Ligands for G-Quadruplex DNA Structures. *Molecules*, *24*(4), 733. https://doi.org/10.3390/molecules24040733

Roguin, L. P., Chiarante, N., García Vior, M. C., & Marino, J. (2019). Zinc(II) phthalocyanines as photosensitizers for antitumor photodynamic therapy. *The International Journal of Biochemistry & Cell Biology*, *114*, 105575. https://doi.org/10.1016/j.biocel.2019.105575

Sato, K., Ando, K., Okuyama, S., Moriguchi, S., Ogura, T., Totoki, S., Hanaoka, H., Nagaya, T., Kokawa, R., Takakura, H., Nishimura, M., Hasegawa, Y., Choyke, P. L., Ogawa, M., & Kobayashi, H. (2018). Photoinduced Ligand Release from a Silicon Phthalocyanine Dye Conjugated with Monoclonal Antibodies: A Mechanism of Cancer Cell Cytotoxicity after Near-Infrared Photoimmunotherapy. *ACS Central Science*, *4*(11), 1559–1569. https://doi.org/10.1021/acscentsci.8b00565

Sen, P., Managa, M., & Nyokong, T. (2019). New type of metal-free and Zinc(II), In(III), Ga(III) phthalocyanines carrying biologically active substituents: Synthesis and photophysicochemical properties and photodynamic therapy activity. *Inorganica Chimica Acta*, *491*, 1–8. https://doi.org/10.1016/j.ica.2019.03.010

Sen, P., & Nyokong, T. (2019). A novel axially palladium(II)-Schiff base complex substituted silicon(IV) phthalocyanine: Synthesis, characterization, photophysicochemical properties and photodynamic antimicrobial chemotherapy activity against Staphylococcus aureus. *Polyhedron*, *173*, 114135. https://doi.org/10.1016/j.poly.2019.114135

Wang, Z., Gai, S., Wang, C., Yang, G., Zhong, C., Dai, Y., He, F., Yang, D., & Yang, P. (2019). Self-assembled zinc phthalocyanine nanoparticles as excellent photothermal/photodynamic synergistic agent for antitumor treatment. *Chemical Engineering Journal*, *361*, 117–128. https://doi.org/10.1016/j.cej.2018.12.007

Wei, G., Huang, L., Jiang, Y., Shen, Y., Huang, Z., Huang, Y., Sun, X., & Zhao, C. (2019). Lenvatinib-zinc phthalocyanine conjugates as potential agents for enhancing synergistic therapy of multidrug-resistant cancer by glutathione depletion. *European Journal of Medicinal Chemistry*, *169*, 53–64. https://doi.org/10.1016/j.ejmech.2019.02.065

Yalazan, H., Barut, B., Ertem, B., Yalçın, C. Ö., Ünver, Y., Özel, A., Ömeroğlu, İ., Durmuş, M., & Kantekin, H. (2020). DNA interaction and anticancer properties of new peripheral phthalocyanines carrying tosylated 4-morpholinoaniline units. *Polyhedron*, *177*, 114319. https://doi.org/10.1016/j.poly.2019.114319

Yu, L., Wang, Q., Wong, R. C.-H., Zhao, S., Ng, D. K. P., & Lo, P.-C. (2019). Synthesis and biological evaluation of phthalocyanine-peptide conjugate for EGFR-targeted photodynamic therapy and bioimaging. *Dyes and Pigments*, *163*, 197–203. https://doi.org/10.1016/j.dyepig.2018.11.055

Zeng, K., Xu, Q., Ouyang, J., Han, Y., Sheng, J., Wen, M., Chen, W., & Liu, Y.-N. (2019). Coordination Nanosheets of Phthalocyanine as Multifunctional Platform for Imaging-Guided Synergistic Therapy of Cancer. *ACS Applied Materials & Interfaces*, *11*(7), 6840–6849. https://doi.org/10.1021/acsami.8b22008

Zheng, Y., Hou, G., Zhang, G., Lan, T., Yuan, J., Zhang, L., Yan, F., Wang, F., Meng, P., Dun, X., Li, X., Chen, G., Zhu, Z., Wei, D., He, W., & Yuan, J. (2020). The near-infrared fluorescent dye IR-780 was coupled with cabazitaxel for castration-resistant prostate cancer imaging and therapy. *Investigational New Drugs*, *38*(6), 1641–1652. https://doi.org/10.1007/s10637-020-00934-1

Chapter 2

TAILORING OF MICROSTRUCTURAL AND OPTICAL PARAMETERS FOR SPIN-COATED ZNO FILMS USING ULTRASONICATED SOLUTION

Saliha ILICAN[1]
Gökhan SAVAROĞLU[2]

1 Saliha ILICAN, Department of Physics, Science Faculty, Eskisehir Technical University, 26470 Eskisehir, Turkey, silican@eskisehir.edu.tr
2 Gokhan SAVAROGLU, Department of Physics, Science and Arts Faculty, Eskisehir Osmangazi University, 26480 Eskisehir, Turkey, gsavarog@ogu.edu.tr

INTRODUCTION

Zinc oxide (ZnO), an n-type semiconductor with a wide optical band gap of about 3.3 eV at room temperature, has high optical transmittance and low electrical resistivity [1, 2]. It is also an environmentally friendly material. Thanks to these superior features, it is a very popular material with a wide range of applications, especially in varistor, solar cell, sensor, photodiode and transistor applications [3-10]. It is possible to enhance the physical properties of ZnO, such as electrical, optical, morphological, magnetic or mechanical properties, by using different growth parameters or by doping a suitable element. ZnO films can be produced by using various methods, which are requiring vacuum or not, in accordance with the place and purpose of use. These methods include both expensive systems [11-13] and low-cost solution methods like electrodeposition [14], spraying [15], chemical bath deposition [16] and sol-gel [17, 18]. However, the quality of the films produced using solution methods is generally poor, and consequently films with the desired physical properties are not always obtainable. In film production stage, as well as the method-dependent film deposition parameters, the solution parameters play also an important role in film quality. Therefore, the properties of solution play very important role in production of high-quality ZnO film.

Ultrasounds are sound waves that have frequencies outside the human hearing threshold limits (between 20 kHz and 1 GHz). Since it does not harm the living tissue and creates heat and pressure in the applied area, it is widely used in both medical and diagnostic fields. In the industrial field, it is used in powdering metals, removing rodents from the environment, preparing very fine particle solutions, drying foods, sterilizing milk and much more [19-25]. If high-intensity ultrasound waves are applied to a liquid, they create physical, chemical and biochemical effects in the environment in which it advances depending on the amplitude and frequency of the ultrasound waves applied. [26-28]. Low frequency (20 kHz-100 kHz) and high intensity power ultrasound waves create cavitation as it progressives in a medium. Cavitation, as soon as ultrasound waves cause dilution of the particles in the medium, a void-shaped interrupt occurs. This void is filled with saturated vapor of the medium. During compression, the vapor condenses, and the cavity is disrupted by the effect of increased pressure. When the compression ceases, shock waves occur in the surrounding liquid, which evaporates rapidly in the medium. As a result of this phenomenon called cavitation, over 1000 atm pressure and a large energy are released. This energy heats the area of the bubbles and causes chemical reactions. In cavitation

bubbles, a very high temperature (about 5000 K) and pressure (estimated 500 MPa) occurs in their structures at the time of explosion. Temperature, frequency and amplitude are the most important parameters affecting cavitation. While ultrasound waves are progressing in a medium, it progresses by performing compression and relaxation. In a few acoustic cycles, bubbles form, develop and rise. This bubble rise provides energy to the nucleation process as early as possible. Nucleation occurs at the lowest super-saturation, where crystallization occurs, where re-dissolution occurs in the suspension.

In the available literature, there are many studies where solutions are prepared by sol-gel method to produce ZnO films [9, 17, 29-32]. In these studies, silicone or glass substrates were used to produce films, and dip coating or spin-coating techniques were preferred. Recent years, there have been also a few studies in which the prepared solutions were sonicated with ultrasound waves before they were coated onto substrate [33-36]. In these studies, the sonication time applied to the solutions prepared using ultrasonic water bath was kept constant and preferred as 30 minutes or 1 hour. Sarip et al. [37] reported that the solutions were obtained by sol-gel method using different precursors (zinc nitrate hexahydrate and zinc acetate dehydrate), and then sonication process was used different durations (0, 30s, 90s and 120s) to the prepared solutions. They produced ZnO films using spin-coating. As substrate, they used glass substrates seeded ZnO by chemical bath deposition method. They suggested that the ZnO films produced by their process have good c-axis orientation and optical properties.

In the present study, ultrasound waves were applied to the solutions at different durations, prepared via sol-gel method. Then, ZnO films were produced using these solutions by spin-coating technique. It was investigated how sonication duration affects the structural, morphological and optical properties of the produced films. In particular, microstructural, optical and dispersion parameters were studied in detail.

EXPERIMENTAL

All the used chemicals were commercially purchased and directly used without any further purification. The solutions were prepared by the sol-gel method. Zinc (II) acetate dihydrate ($Zn(CH_3COO)_2.2H_2O$; ZnAc; %99.999 purity; Sigma-Aldrich), 2-Methoxyethanol ($C_3H_8O_2$; MEt; ≥99.9% purity; Sigma-Aldrich) and monoethanolamine ($NH_2(CH_2)_2OH$; MEA; ≥99% purity; Merck) were used as starting salt, solvent and stabilizer, respectively. Solution (0.5M), used for producing the ZnO film, was prepared by using ZnAc salt, MEt solvent and MEA stabilizer.

To obtain a clear, transparent and free of precipitate solution, the prepared solutions were stirred separately in a magnetic stirrer at 60 °C during 2 hours, then heater was turned off and stirring continued about 1 hour until it dropped to room temperature. Lastly, ultrasound waves were applied without-waiting to the prepared solution. Sonication was applied to 10 ml of mixture in a glass vessel using a 20 kHz 700 W ultrasonic horn (QSONICA Q700 Sonicators) at an amplitude of 50% (700 W) for 1, 5 and 15 minutes. The during of sonication process, the temperature was maintained constant at 296.15 K, using a cooling jacket. The schematic sonication set-up is given in Fig. 1.

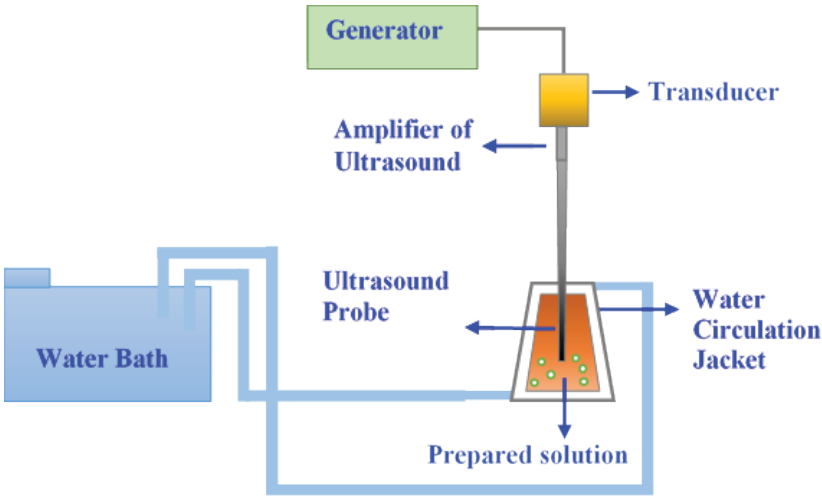

Figure 1. The schematic ultra-sonication set-up.

After the solutions (with and without sonication) were prepared, film production stage was immediately began. The chemically cleaned borofloat substrate (about 1x1 cm) was placed on the sample holder of the spin-coater (LAURELL WS-400B-6NPP/LITE), dripped from the prepared solution to a sufficient amount of substrate, and then it was spun at spin speed of 3000 rpm during 30 s. The coated wet substrate was dried at 300 °C during 10 min in a tube furnace after each coating. The spin coating−drying process was repeated ten times to obtain a 10-layer film. For better crystallization, ZnO film was annealed at a temperature greater than the preheating temperature. In order to prevent possible cracks on the film surface, the film was kept in the furnace for 20 minutes, until the temperature increased from 300 °C to 600 °C without removing the film in the furnace after preheating. Finally, the film was annealed by keeping

the temperature of 600 °C during 60 min, and the film was removed from this furnace when the temperature dropped to room temperature.

In order to check the crystalline phase and crystallite orientation of the produced ZnO films were carried out using BRUKER D8 Advance X-ray powder diffractometer equipped with $Cu_{K\alpha}$ radiation (λ=1.54059 Å). Measuring interval of X-ray diffraction (XRD) measurement was $30^o \leq 2\theta \leq 60^o$, scan speed was $0.02^o s^{-1}$ at a divergent slit of 0.5 mm width. The XRD sample-holder was rotated 15 rpm during measurements. The surface uniformity was investigated by the roughness analysis of the atomic force microscopy (AFM) images of the produced ZnO films performed with Park Systems XE-100 model AFM. The surface roughness parameters were determined by the XEI version 1.7.1 software. The transmittance and diffuse reflectance spectra of the produced ZnO films were performed by SHIMADZU 2450 spectrophotometer in the wavelength range of 300-800 nm. Before taking the transmittance measurements, the background was taken using a pre-cleaned blank borofloat glass substrate. A barium sulfate ($BaSO_4$) powder was used as a reference while performing diffuse reflectance measurements.

RESULTS AND DISCUSSION

Structural Parameters

Crystal structure analysis was determined by the XRD data of the produced ZnO films. XRD patterns of these films are displayed in Fig. 2.

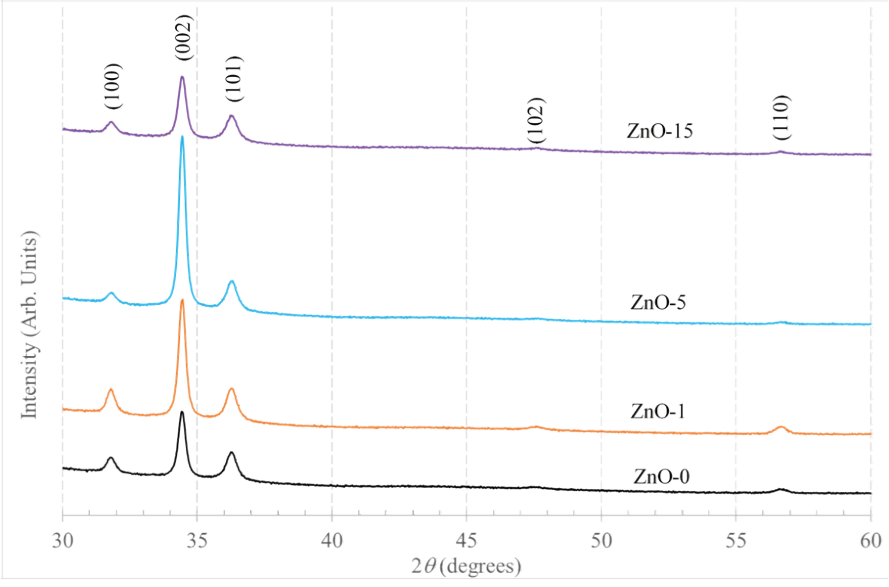

Figure 2. X-ray diffraction patterns of the ZnO films.

The XRD peaks belong to ZnO hexagonal wurtzite within Zincite-type structure (JCPDS-ICDD card Pdf number: 036-1451). Depending on the sonication duration, peak intensity and widths have changed a little. The observed 2θ values match to (*100*), (*002*), (*101*), (*102*) and (*110*) diffraction planes for ZnO. Obviously, increasing the duration of sonication is useful to significantly enhancement the crystalline quality of ZnO film. However, high sonication duration (15 min) deteriorates the crystalline quality again.

For all ZnO films, the angle of diffraction (2θ) and lattice spacing (d) of the phases specified along with the related (hkl) planes are given in Table 1. Structural parameters such as texture coefficient (TC_{hkl}), lattice constants (a and c), Zn-O bond length (L), O-Zn-O dihedral angles (α and β), volume of the unit cell (V), strain (ϵ_z), stress (σ_c), average crystallite size (D_{ave}), and dislocation density (δ) values can be calculated using XRD spectrum data. The XRD data of ZnO films were analyzed using the Diffrac.EVA software program.

Table 1. 2θ, d, γ, D_{ave} and δ values of the produced ZnO films.

Film Code	*(hkl)*	*2θ (degree)*	*d (Å)*	*γx 10^{-3} (radian)*	*D_{ave} (nm)*	*δx10^{-4} (nm^{-1})*
ZnO-0	(100)	31.762	2.8164	5.059	30	11.14
	(002)	34.411	2.6054			
	(101)	36.247	2.4775			
	(102)	47.610	1.9094			
	(110)	56.599	1.6256			
ZnO-1	(100)	31.772	2.8155	4.902	31	10.46
	(002)	34.412	2.6053			
	(101)	36.242	2.4778			
	(102)	47.621	1.9089			
	(110)	56.611	1.6253			
ZnO-5	(100)	31.786	2.8143	4.797	32	10.01
	(002)	34.414	2.6052			
	(101)	36.245	2.4777			
	(102)	47.634	1.9084			
	(110)	56.656	1.6241			
ZnO-15	(100)	31.792	2.8138	5.478	28	13.06
	(002)	34.416	2.6050			
	(101)	36.251	2.4773			
	(102)	47.649	1.9079			
	(110)	56.638	1.6245			

The preferential growth orientation belonging to the crystal structure is determined by following expression [38]:

$$TC_{hkl} = \frac{I_{hkl} / I^{S}_{hkl}}{n^{-1} \sum_{n} I_{hkl} / I^{S}_{hkl}}$$

where I_{hkl}, I^{s}_{hkl} and n denote peak intensity corresponding to (hkl) planes, the reference peak intensity of the randomly oriented crystallites and the number of the diffraction peaks taking into account, respectively. TC_{hkl} values for five peaks were calculated using I^{s}_{hkl}, of 57, 44, 100, 23 and 32 (according to the 36–1451 JCPDS-ICDD card) for the (*100*), (*002*), (*101*), (*102*) and (*110*) peaks, respectively. Fig. 3 displays the calculated TC_{hkl} values of the produced ZnO films. As can be seen from this figure, TC_{002} is greater than 2 for all the films. As the sonication time increases, the TC_{002} value also increases. However, a long sonication time (15 min), causes the lowering of TC_{002} values. The best crystallizing film is ZnO-5.

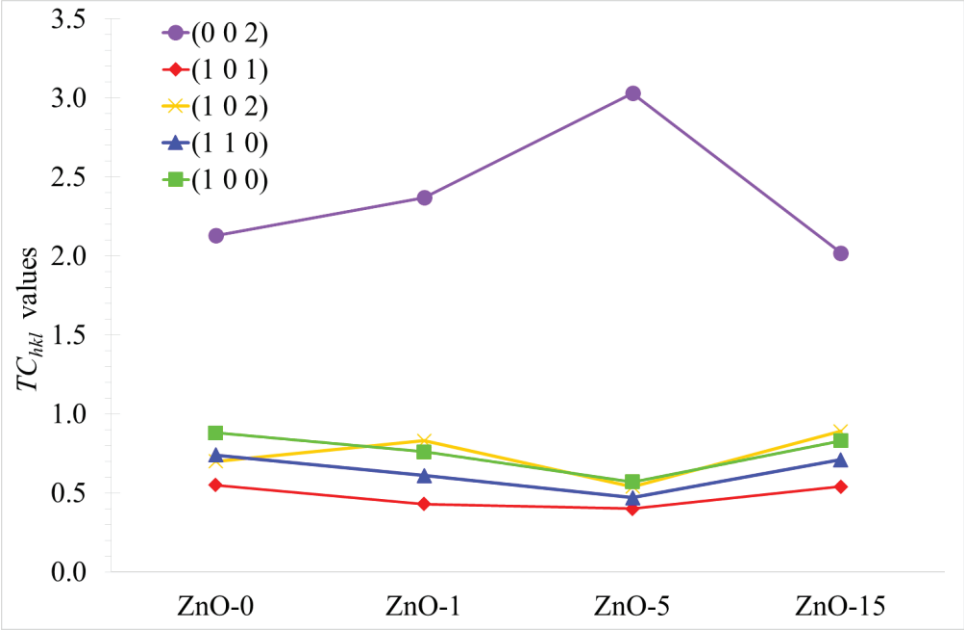

Figure 3. The calculated TC_{hkl} values of the produced ZnO films.

To calculate the lattice constants of the films, formed in hexagonal structure, the following equation [39] was used

$$\frac{1}{d^2_{hkl}} = \frac{4}{3}\left(\frac{h^2+hk+k^2}{a^2}\right) + \frac{l^2}{c^2}$$

where d_{hkl} is distance between planes corresponding to (hkl). The calculated lattice constants are presented in Table 2. It can be seen from the table that the increase in sonication duration causes the lattice shrinkage.

Table 2. The calculated lattice constants, volume, Zn-O bond length and angles, strain and stress values for the produced ZnO films.

Parameter	ZnO-0	ZnO-1	ZnO-5	ZnO-15
a (Å)	3.2521	3.2511	3.2497	3.2491
c (Å)	5.2108	5.2106	5.2103	5.2100
V (Å^3)	47.73	47.70	47.65	47.63
L (nm)	1.9792	1.9788	1.9782	1.9779
α (degrees)	108.45	108.47	108.49	108.49
β (degrees)	110.54	110.52	110.50	110.50
ϵ_z (x10^{-4})	7.95	7.67	7.11	6.54
σ_c (x10^8 Nm^{-2})	-1.80	-1.74	-1.61	-1.48

Wurtzite structure has basic hexagonal symmetry, and a schematic illustration of this structure for ZnO is displayed in Fig. 4. Each unit cell in the structure have four atoms. The positions of these atoms in Cartesian coordinates are (0,0,0), (0,0,uc), $a\left(\frac{1}{2},\frac{\sqrt{3}}{6},\frac{c}{2a}\right)$, and $a\left(\frac{1}{2},\frac{\sqrt{3}}{6},\frac{(u+0.5)c}{a}\right)$. The parameter of u is related to crystal structure, and for wurtzite structure, it is expressed as [40]

$$u = \frac{a^2}{3c^2} + 0.25$$

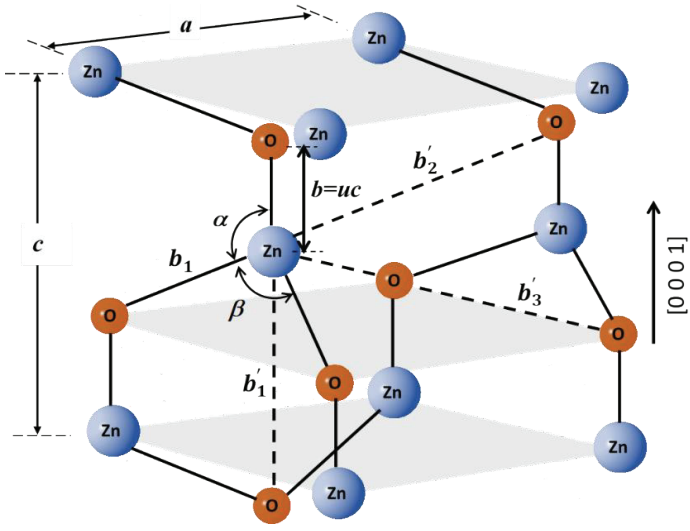

Figure 4. Schematic illustration of a wurtzitic ZnO structure with lattice constants, the nearest-neighbor distance, O-Zn-O bond dihedral angles.

The nearest-neighbor bond length (L) between Zn and O is calculated using the below equation [41, 42]:

$$L = \left(\frac{a^2}{3} + (0.5 - u)^2 c^2\right)^{1/2}$$

the L values decreased with increasing sonication duration.

The bond angles, which are α and β, are given by [2]

$$\alpha = 0.5\,\pi + \arccos\left(\left[\sqrt{1 + 3(c/a)^2(0.5 - u)^2}\right]^{-1}\right)$$

and

$$\beta = 2\arcsin\left(\left[\sqrt{4/3 + 4(c/a)^2(0.5 - u)^2}\right]^{-1}\right)$$

These angles are 109.47° in ideal crystal for a wurtzitic ZnO structure. The calculated values of the produced ZnO films are tabulated in Table 2. These values are varied from 108.45° to 110.54°.

The volume of the unit cell for the hexagonal structure can be calculated using the below equation [2]

$$V = \frac{\sqrt{3}}{2}\, a^2\, c$$

The calculated V values for the produced ZnO films (seen in Table 2) indicates that the volume of the unit cell reduces as the sonication duration increases.

Strain, which is deformation in crystalline structure, is given by the following expression [43].

$$\epsilon_z = \frac{d - d_0}{d_0}$$

where d_0 is the distance between the standard planes of the bulk material (d_{002}=2.60332 Å for ZnO). To calculate ϵ_z values for (*002*) plane of the ZnO films, Eq. (7) was used, and the calculated values are given in Table 2. It is clearly seen from this table that the ϵ_z values increases with increasing the sonication duration.

For hexagonal structure, stress parallel to the crystal surface is expressed as follows [44]:

$$\sigma_c = \left(C_{13} - \frac{C_{33}\,(C_{11} + C_{12})}{2C_{13}}\right)\epsilon_z$$

where C_{11}, C_{12}, C_{13} and C_{14} are elasticity constants, which are $2.097x10^{11}$ Nm^{-2}, $1.211x10^{11}$ Nm^{-2}, $1.051x10^{11}$ Nm^{-2} and $2.109x10^{11}$ Nm^{-2}, respectively [45]. If these elasticity constants are replaced in Eq. (9), the stress can be written as follows:

$$\sigma_c = -2.268x10^{11}\,\epsilon_z$$

σ_c values of the produced ZnO films were found using the calculated the ϵ_z values. The calculated σ_c values are given in Table 2. As seen from this table, the stress on the all films has the negative sign. This implies that *c* lattice constant of the produced ZnO films elongated along the growth direction [46].

The peak broadening in XRD patterns was used to evaluate average crystallite size (D_{ave}) by the use of the Scherrer formula [47],

$$D_{ave} = \frac{0.94\,\lambda}{\gamma\,cos\theta}$$

where λ, γ and θ are the X-ray wavelength (CuK_{α}=1.54059 nm), the full width half maximum (FWHM) peak breadth and the Bragg angle, respectively. Crystalline defects (dislocation) depend on the morphological properties of the material surface and the formation and size of the particles; directly affect the strength, hardness and ductility of the material [48]. To determine the amount of these defects, dislocation density given below is used the expression [49]:

$$\delta = \frac{1}{D_{ave}}$$

The calculated D_{ave} and δ values of the produced ZnO films are tabulated in Table 1.

Morphological Parameters

Surface morphology and degree of roughness is an important factor affecting film properties and their use in technological applications. The surface topography of the produced ZnO films were determined by AFM. Fig. 5 shows the 3x3 μm^2 three-dimensional AFM micrographs of the produced ZnO films. The surfaces of the produced ZnO films are almost homogeneous, continues and dense. There are not the defect or void formation on the surface of these films. In some regions on the surfaces, it can be seen that there are clusters with having different heights and sizes. The light colours on the surface indicate the places where atoms prefer to grow, whereas the dark ones indicate where there are fewer film formations. The clusters formed on the surface of the film during te layer-

by-layer film formation may be due to the surface properties of the used substrates.

The calculation of surface roughness is one of the most used parameter for investigation of changes in surface topography. In order to characterize the surface roughness, peak-valley (R_{pv}), root-mean-square (R_q) and average surface roughness (R_a) values were calculated for each ZnO film using the XEI version 1.7.1 software. The roughness values of the produced ZnO films are given in Table 3. It is clearly seen that change of sonication duration affected the roughness values. These values have the same trend with each other. When the sonication duration increased, the surface roughness of the produced ZnO films first increased. As the sonication duration increased further, the surface roughness of these films decreased.

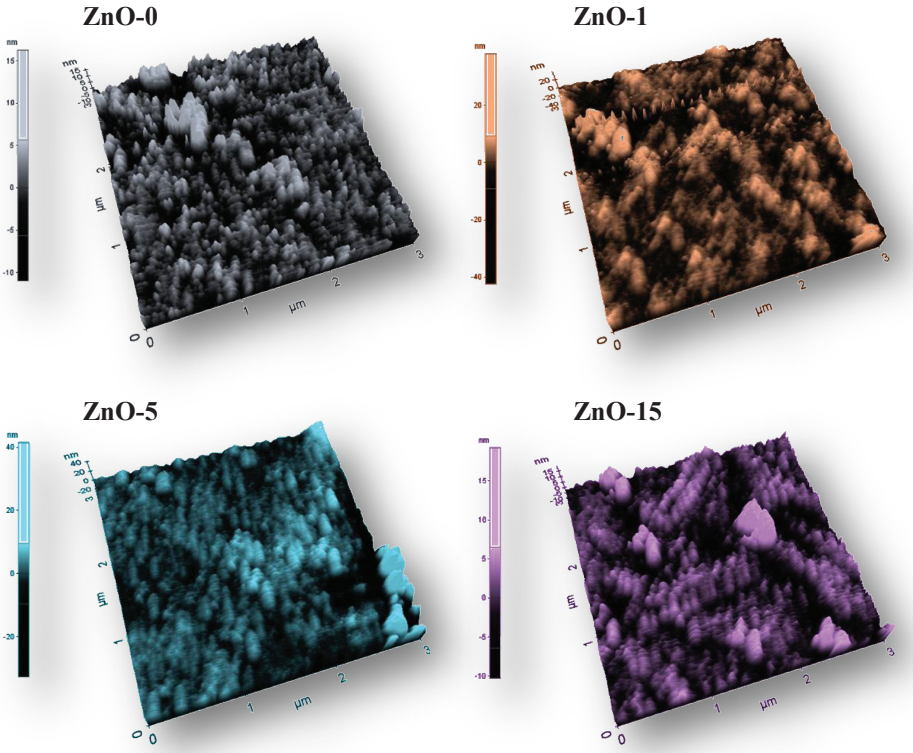

Figure 5. Three dimensional AFM micrographs and histograms of the produced ZnO films.

Table 3. Roughness parameters, Skewness and Kurtosis values of the produced ZnO films.

Parameter	ZnO-0	ZnO-1	ZnO-5	ZnO-15
R_{pv} (nm)	27.27	80.31	74.11	29.52
R_q (nm)	2.89	4.72	4.89	3.31
R_a (nm)	2.19	3.59	3.20	2.46
R_{sk}	-0.451	-0.312	-0.907	-0.888
R_{ku}	4.448	5.233	14.066	5.880

Fig. 6 presents height distribution histograms of the produced ZnO films. The statistical analysis of AFM data for the produced ZnO films was performed using the height distributions. The height asymmetry can be defined by statistical parameters of surface Skewness (R_{sk}) and Kurtosis (R_{ku}) [50]. The R_{sk} parameter represents a measure of the asymmetry of the distribution of heights [51]. The R_{sk} values of all the films are the negative, and given in Table 3. Negative R_{sk} means that the surface is planar and the surface has more valleys than peaks [52]. So, the negative sign of R_{sk} for all the produced films indicates that the surface morphology is a rough surface with planar regions and a high density of valleys. The R_{ku} parameter is useful in characterization of surfaces because of being a measure of the sharpness of the height distribution. In case of high R_{ku} value (>3, leptokurtic), the surface has with a spiky surface. That is, relatively the surface has a lot numbers both many high peaks and low valleys [53]. The R_{ku} values of all the produced ZnO films have the higher than 3 (Table 3). The fact that the height distributions have stronger and sharper peaks means that the surface of the film consists of several very deep valleys or very high summits. It was reported that metal surfaces with negative Skewness and higher Kurtosis values trend to decrease friction [54, 55].

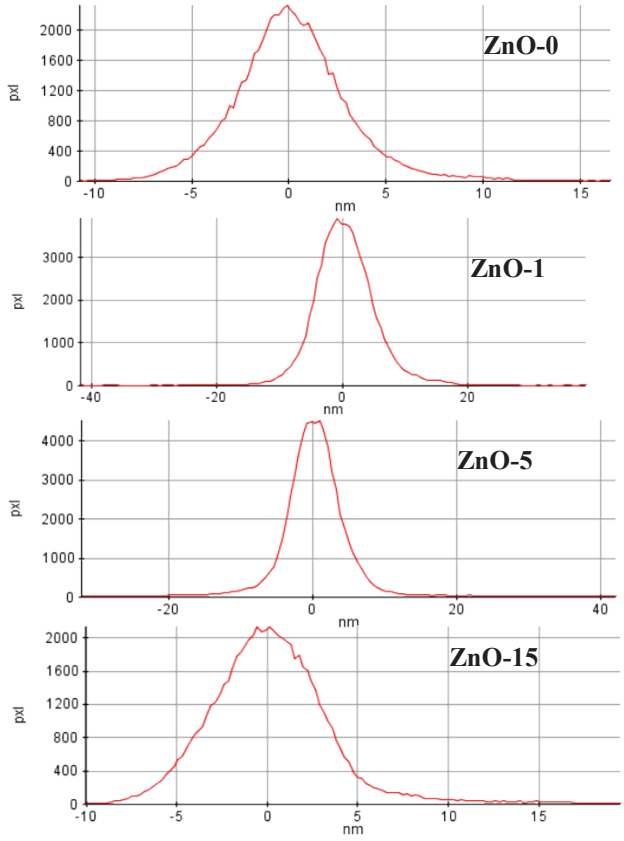

Figure 6. Height distribution histograms for the produced ZnO films.

Optical Parameters

Fig. 7 show the transmittance (T) and diffuse reflectance (R) spectra of the produced ZnO films. The T_{ave} values in the visible region of these films are higher than 85%, the R_{ave} values of them are lower than 14%. The fundamental absorption edge of the films is related to electron transitions between valence band and conduction band. To calculate the optical band gap of the films, this edge can be used. Tauc plot for the direct transition is expressed by [56]

$$(\alpha h\upsilon) = A'\left(h\upsilon - E_g\right)^{1/2}$$

where α, $h\upsilon$, A' and E_g denote absorption coefficient, photon energy, a constant and direct band gap, respectively. The E_g values of the produced ZnO films were calculated from Tauc plots of $(\alpha h\upsilon)^2$ versus $h\upsilon$ (Fig. 8) and are given in Table 4. As seen, the values of E_g first decreased with sonication duration and then increased.

It can be an exponential part called the Urbach tail that extends inward from the edge of the optical band. This exponential tail is associate with the disordered materials because such materials have localized states, which elongated in the optical band gap. Urbach empirical relation with $h\nu$ photon energy and α absorption coefficient is given the following [57].

$$\alpha = \alpha_0 \exp\left(\frac{h\upsilon}{E_U}\right)$$

where α_0 is a constant. E_U is called Urbach energy and corresponds the energy of the band tail. If the logarithm of both sides of the Eq. (14) is taken, a straight line equation can be obtained as follows:

$$ln\alpha = ln\alpha_0 + \frac{h\upsilon}{E_U}$$

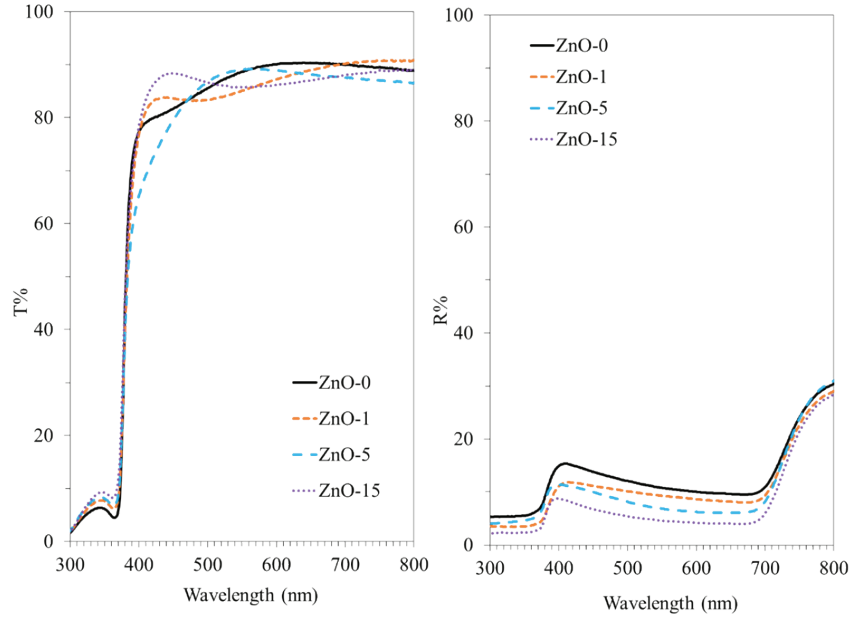

Figure 7. The transmittance and diffuse reflectance spectra of the produced ZnO films.

Table 4. Optical and dispersion parameters of the produced ZnO films.

Parameter	ZnO-0	ZnO-1	ZnO-5	ZnO-15
E_g (eV)	3.282	3.275	3.273	3.275
E_U (meV)	91	104	149	114
σ	0.27	0.24	0.17	0.22
E_d (eV)	14.531	11.148	10.244	–
E_o (eV)	5.214	5.185	5.165	–
M_{-1}	2.787	2.150	1.983	–
M_{-3} (eV)$^{-2}$	0.103	0.080	0.074	–
E_0/E_g	1.59	1.58	1.58	–

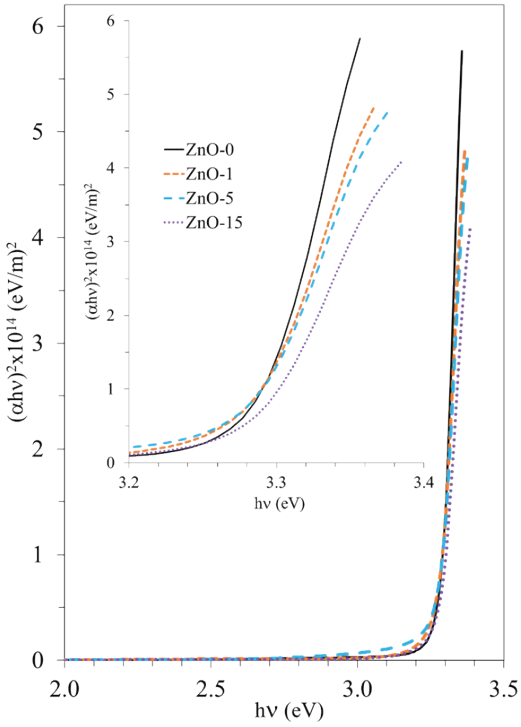

Figure 8. Tauc plots of the produced ZnO films.

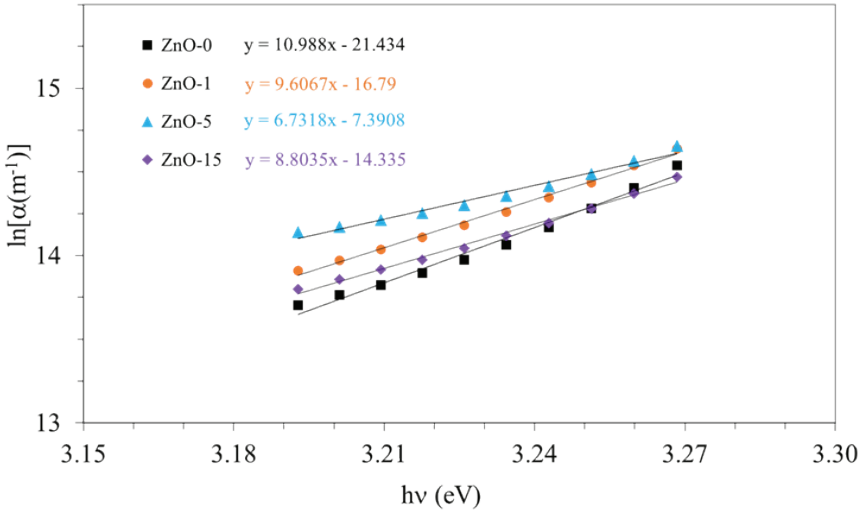

Figure 9. ln(α) vs. $h\nu$ plots of the produced ZnO films.

The plots of $ln\alpha$ versus $h\nu$ for the films are given in Fig. 9. The E_U values were determined from the inverse of the slope of these plots, and tabulated in Table 4. The increase of E_U values for the produced ZnO films suggests that the atomic structural disorder increases with sonication duration. The E_U and E_g values change inversely. The absorption edge broaden resulting of the electron–phonon or exciton–phonon interactions. This broadening is characterized by the steepness parameter (σ), and calculated by following relation [58]

$$\sigma = \frac{kT}{E_U}$$

The σ values of the produced ZnO films were calculated using Eq. (16) (for T=300 K). The calculated values are given in Table 4. The values of σ indicate that the absorption edge varies with sonication duration, and they are in same trend with E_g values.
The refractive index (n) is a considerable parameter for optical materials and their in potential applications, and can be determined using following equation [59].

$$n = \left[\frac{1+R}{1-R}\right] + \sqrt{\frac{4R}{(1-R)^2} - k^2}$$

where k is extinction coefficient, and expressed by

$$k = \frac{\alpha\lambda}{4\pi}$$

Fig. 10 shows a plot of the calculated n and k values as a function of wavelength. As seen, the values of n decrease with increasing sonication duration, and is almost constant in the range of 400-700 nm.

The real (ε_1) and imaginary (ε_2) parts of the dielectric constant depend on the values of n and k. The values of ε_1 and ε_2 are calculated using the following equations [60]:

$$\varepsilon_1 = n^2 - k^2$$

$$\varepsilon_2 = 2nk$$

For the produced ZnO films, variation of the dielectric constants as a function of wavelength are given in Fig. 11. The values of ε_1 are higher than the values of ε_2.

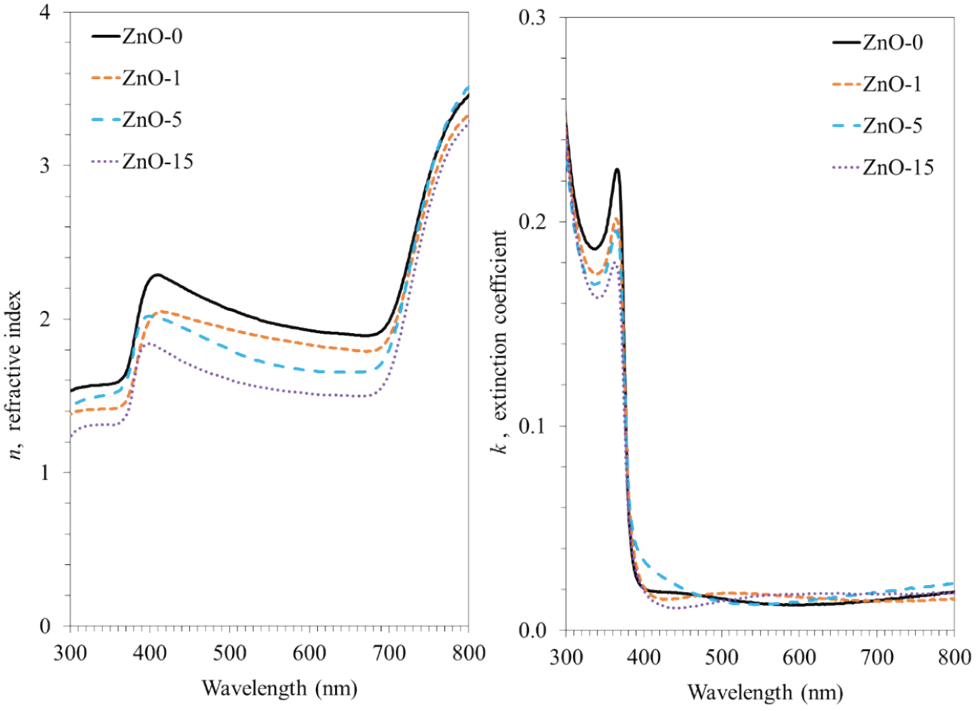

Figure 10. The variations of n and k values of the produced ZnO films as a function of wavelength.

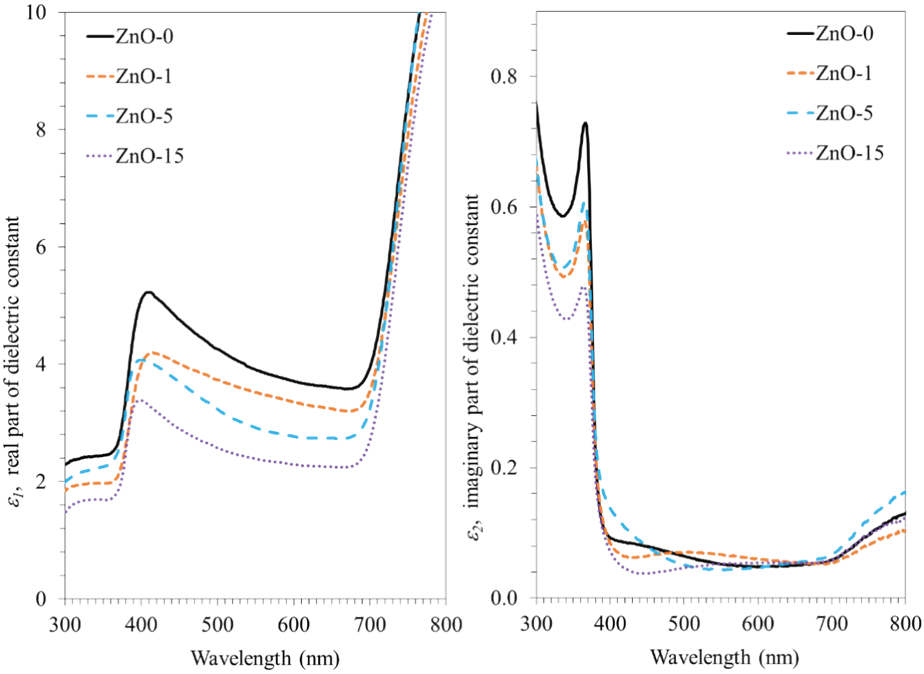

Figure 11. The variations of ε_1 and ε_2 values of the produced ZnO films as a function of wavelength.

The real (σ_1) and imaginary (σ_2) parts of the optical conductivity related to the dielectric constants. The σ_1 and σ_2 are calculated using the following equations [60]:

$$\sigma_1 = 2\pi c\varepsilon_0 \frac{\varepsilon_2}{\lambda}$$

$$\sigma_2 = 2\pi c\varepsilon_0 \frac{\varepsilon_1}{\lambda}$$

where c and ε_0 are the speed of light and the free space dielectric constant, respectively. For the produced ZnO films, optical conductivity spectra are given in Fig. 12. The values of σ_2 are higher than the values of σ_1.

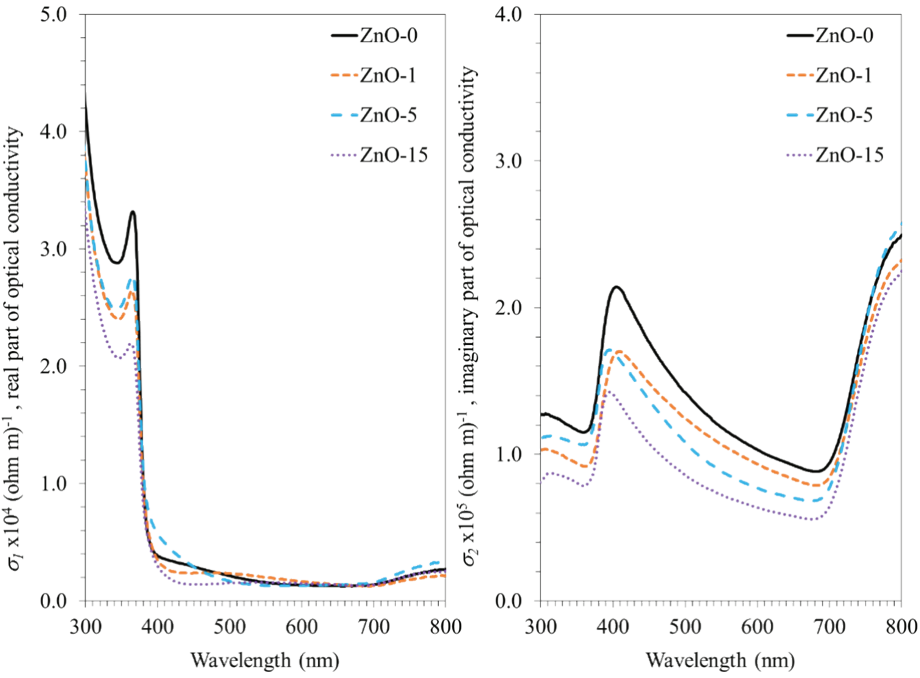

Figure 12. The variations of σ_1 and σ_2 values of the produced ZnO films as a function of wavelength.

Dispersion Parameters

The dispersion acts a significant role in the investigation of optical materials due to its importance in designing optical devices for spectral dispersion. The dispersion parameters (E_0 and E_d) are determined in view of Wemple–DiDomenico model according to the equation [61]

$$n^2 = 1 + \frac{E_0 E_d}{E_0^2 - (h\nu)^2}$$

where E_0 is oscillation energy and E_d is dispersion energy. The graphs $(n^2\text{-}1)^{-1}$ against the $(h\nu)^2$ of the produced ZnO films were drawn, and dispersion parameters were extracted from slopes and intercepts of these plots using Eq. (23). The calculated dispersion parameters are given in Table 4. The produced ZnO films except for the ZnO-15 film obeyed the single-oscillator model. The calculated E_o and E_g values are agreement with the reported values for ZnO [62, 63].

CONCLUSIONS

In present study, ZnO films were successfully produced by low-cost spin-coating technique using un-sonicated/sonicated solutions. XRD patterns, AFM images, transmittance and diffuse reflectance spectra of these films were analyzed, and determined some physical parameters. The XRD results showed that the produced ZnO films are of polycrystalline nature with hexagonal wurtzite structure. They exhibit a Zincite-type structure with the c-axis preferred orientation. The structural parameters were calculated using XRD data of the produced ZnO films. To determine of the surface morphology and degree of roughness of the films, AFM images were taken. The roughness parameters, Skewness and Kurtosis were determined. AFM measurement results showed increased roughness of the produced ZnO film because of the increased grain size. The optical band gap, Urbach energies and optical constants of the ZnO films were calculated using the transmittance and diffuse reflectance spectra. The values of optical band gap decreased and then increased with increasing sonication duration. The ZnO-5 film has a minimum optical band gap value. The dispersion parameters were calculated by Wemple−DiDomenico model. It was observed that the produced ZnO films (except ZnO-15) obeyed this model.

REFERENCES

[1] Ü. Özgür, H. Morkoç, Optical properties of ZnO and related alloys, in: C. Jagadish, S. Pearton (Eds.), Zinc Oxide Bulk, Thin Films and Nanostructures Processing, Properties and Applications, Elsevier Science, New York, 2006, pp.175–239.

[2] H. Morkoç, Ü. Özgür, Zinc Oxide: Fundamentals, Materials and Device Technology, Wiley Company, Germany, 2009.

[3] H. Lu, Y. Wang, X. Lin, Structures, varistor properties, and electrical stability of ZnO thin films, Mater. Lett. 63 (2009) 2321–2323.

[4] S. Chala, N. Sengouga, F. Yakuphanoğlu, S. Rahmane, M. Bdirina, İ. Karteri, Extraction of ZnO thin film parameters for modeling a ZnO/Si solar cell, Energy 164 (2018) 871–880.

[5] J. Cai, Z. Chen, S. Li, S. Dong, C. Wei, F. Li, Y. Peng, X. Jia, W. Zhang, A novel hierarchical ZnO-nanosheet-nanorod-structured film for quantum-dot-sensitized solar cells, Electrochim. Acta 274 (2018) 326–333.

[6] S. Ozturk, N. Kilinc, Z.Z. Ozturk, The effects of annealing on gas sensing properties of ZnO nanorod sensors coated with Pd and Pt, Procedia Eng. 47 (2012) 434–437.

[7] T. Ates, C. Tatar, F. Yakuphanoglu, Preparation of semiconductor ZnO powders by sol–gel method: Humidity sensors, Sensor. Actuat. A Phys. 190 (2013) 153–160.

[8] W. Li, Y.J. Guo, Q.B. Tang, X.T. Zu, J.Y. Ma, L. Wang, K. Tao, H. Torun, Y.Q. Fu, Highly sensitive ultraviolet sensor based on ZnO nanorod film deposited on ST-cut quartz surface acoustic wave devices, Surf. Coat. Tech. 363 (2019) 419–425.

[9] F. Yakuphanoglu, Y. Caglar, M. Caglar, S. Ilican, ZnO/p-Si heterojunction photodiode by sol–gel deposition of nanostructure n-ZnO film on p-Si substrate, Mat. Sci. Semicon. Proc. 13 (2010) 137–140.

[10] Z. A. Alahmed, F. Yakuphanoglu, The effects of microfibers on electrical characteristics of zinc oxide thin film transistor, Microelectron. Eng. 110 (2013) 25–28.

[11] Z. Onuk, N. Rujisamphan, R. Murray, M. Bah, M. Tomakin, S.I. Shah, Controllable growth and characterization of highly aligned ZnO nanocolumnar thin films, Appl. Surf. Sci. 396 (2017) 1458–1465.

[12] M.S. Kim, S. Kim, G. Nam, D.-Y. Lee, J.-Y. Leem, Effects of growth temperature for buffer layers on properties of ZnO thin films grown on porous silicon by plasma-assisted molecular beam epitaxy, Opt. Mater. 34 (2012) 1543–1548.

[13] V.K. Kaushik, C. Mukherjee, T. Ganguli, P.K. Sen, Electrical and optical characteristics of aerosol assisted CVD grown ZnO based thin film diode and transistor, J. Alloy. Compd. 696 (2017) 727–735.

[14] A. Arslan, E. Hür, S. Ilican, Y. Caglar, M. Caglar, Controlled growth of c-axis oriented ZnO nanorod array films by electrodeposition method and characterization, Spectrochim. Acta A 128 (2014) 716–723.

[15] B. Ergin, E. Ketenci, F. Atay, Characterization of ZnO films obtained by ultrasonic spray pyrolysis technique, Int. J. Hydrog. Energ. 34 (2009) 5249–5254.

[16] Z. Zheng, J. Lin, X. Song, Z. Lin, Optical properties of ZnO nanorod films prepared by CBD method, Chem. Phys. Lett. 712 (2018) 155–159.

[17] Y. Caglar, S. Ilican, M. Caglar, F. Yakuphanoglu, J. Wu, K. Gao, P. Lu, D. Xue, Influence of heat treatment on the nanocrystalline structure of ZnO film deposited on p-Si, J. Alloy. Compd. 481 (2009) 885–889.

[18] K. Muthukrishnan, M. Vanaraja, S. Boomadevi, R. K. Karn, V. Singh, P. K. Singh, K. Pandiyan, Studies on acetone sensing characteristics of ZnO thin film prepared by sol-gel dip coating, J. Alloy. Compd. 673 (2016) 138–143.

[19] I.I. Odokienko, S.M. Solonin, O.S. Nichiporenko, Use of ultrasound for the refining of atomized metal powders, Powder Metall. Met. Ceram. 15 (1976) 333–336.

[20] R.H. Smith, A.N. Meyer, Rodent control methods: non-chemical and non-lethal chemical, with special reference to food stores, in: A. Buckle, R. Smith (Eds.), Rodent Pests and Their Control, second ed., CAB International, Boston, 2015, pp.101–122.

[21] S. Kentish, T.J. Wooster, M. Ashokkumar, S. Balachandran, R. Mawson, L. Simons, The use of ultrasonics for nanoemulsion preparation, Innov. Food Sci. Emerg. Technol. 9 (2008) 170–175.

[22] G. Musielak, D. Mierzwa, J. Kroehnke, Food drying enhancement by ultrasound–A review, Trends Food Sci. Technol. 56 (2016) 126–141.

[23] K.G. Rashmi, A.S. Warrier, Non-thermal processing of dairy foods, in: J. Minj, V.A. Sudhakaran, A. Kumari (Eds.), Dairy Processing: Advanced Research to Applications, Springer, Singapore, 2020, pp.25–49.

[24] D. Liu, X. Ma, W. Wang, M. Zou, D. Wang, J. Ling, Research progress on power ultrasound technology, in: J. Jia, D. Liu, H. Ma (Eds.), Advances in Food Processing Technology, Springer, Singapore, 2019, pp.149–187.

[25] M.A. Daccache, M. Koubaa, D. Salameh, R.G. Maroun, N. Louka, E. Vorobiev, Ultrasound-assisted fermentation for cider production from Lebanese apples, Ultrason. Sonochem. 63 (2020) 104952.
[26] T.J. Mason, L. Paniwnyk, J.P. Lorimer, The uses of ultrasound in food technology. Ultrason. Sonochem. 3 (1996) 253–260.
[27] F. Got, J. Culioli, P. Berge, X. Vignon, T. Astruc, J.M. Quideau, M. Lethiecq, Effects of high-intensity high frequency ultrasound on ageing rate, ultrastructure and some physico-chemical properties of beef. Meat Sci. 51 (1999) 35–42.
[28] D. Knorr, M. Zenker, V. Heinz, D.-U. Lee, Applications and potential of ultrasonics in food processing. Trends Food Sci. Tech. 15 (2004) 261–266.
[29] G. Ilgu, Y. Caglar, S. Ilican, M. Caglar, S. Ruzgar, The effect of sol concentration on the structural and electrical parameters of nanostructure ZnO films by sol gel dip coating. J. Nanoelectron. Optoe. 9(5) (2014) 618–623.
[30] D. Aryanto, W.N. Jannah, Masturi, T. Sudiro, A.S. Wismogroho, P. Sebayang, Sugianto, P. Marwoto, Preparation and structural characterization of ZnO thin films by sol-gel method. J. Phys. Conf. Ser. 817 (2017) 012025.
[31] D. Nesheva, V. Dzhurkov, I. Stambolova, V. Blaskov, I. Bineva, J.M.C. Moreno, S. Preda, M. Gartner, T. H.-Vasileva, M. Shipochka, Surface modification and chemical sensitivity of sol gel deposited nanocrystalline ZnO films, Mater. Chem. Phy. 209 (2018) 165–171.
[32] K. Ghosh, R.K. Pandey, Annealing time induced roughening in ZnO thin films: A fractal and multifractal assessment, Mat. Sci. Semicon. Proc. 106 (2020) 104771.
[33] M.H. Mamat, Z. Khusaimi, M.Z. Musa, M.Z. Sahdan, M. Rusop, Novel synthesis of aligned Zinc oxide nanorods on a glass substrate by sonicated sol–gel immersion, Mater. Lett. 64 (2010) 1211–1214.
[34] M.F. Malek, M.H. Mamat, Z. Khusaimi, M.Z. Sahdan, M.Z. Musa, A.R. Zainun, A.B. Suriani, N.D. Md Sin, S.B. Abd Hamid, M. Rusop, Sonicated sol–gel preparation of nanoparticulate ZnO thin films with various deposition speeds: The highly preferred c-axis (002) orientation enhances the final properties, J. Alloy. Compd. 582 (2014) 12–21.
[35] M. Heshmat, H Abdizadeh, M. R. Golobostanfard, Sonochemical assisted synthesis of ZnO nanostructured thin films prepared by sol-gel method, Procedia Mater. Sci. 11 (2015) 486–490.
[36] A.S. Ismail, M.H. Mamat, N.D. Md. Sin, M.F. Malek, A.S. Zoolfakar, A.B. Suriani, A. Mohamed, M.K. Ahmad, M. Rusop, Fabrication of hierarchical Sn-doped ZnO nanorod arrays through

sonicated sol–gel immersion for room temperature, resistive-type humidity sensor applications, Ceram. Int. 42 (2016) 9785–9795.
[37] N. Sarip, C.A. Nurhidayah, S.A. Kamaruddin, F. Mahmud, S.N.M. Tawil, M.Z. Sahdan, Synthesis and characterization of zinc oxide nanostructures by different sonication period, Adv. Mater. Res. 925 (2014) 110-114.
[38] B.D. Cullity, S.R. Stock, Elements of X-Ray Diffraction, third ed., Pearson, United States of America, 2014.
[39] C. Kittel, Introduction to Solid State Physics, eighth ed., John Wiley and Sons. Inc., United States of America, 2005.
[40] Ü. Özgür, Ya.I. Alivov, C. Liu, A. Teke, M.A. Reshchikov, S. Doğan, V. Avrutin, S.-J. Cho, H. Morkoç, A comprehensive review of ZnO materials and devices, J. Appl. Phys. 98 (2005) 041301.
[41] S.J. Pearton, D.P. Norton, I.Y. Heo, T. Steiner, Recent advances in processing of ZnO, J. Vac. Sci. Technol. B 22 (2004) 932–948.
[42] C.S. Barret, F.B. Massalski, Structure of Metals, third ed., Pergamon Press, Oxford, 1980.
[43] M.E. Fitzpatrick, A.T. Fry, P. Holdway, F.A. Kandil, J. Shackleton, L. Suominen, Determination of residual stresses by X-ray diffraction, National Physical Laboratory, Teddington, UK, 2005.
[44] H. Hong, J. Huang, H. He, Z. Fan, J. Shao, Influence of different post-treatments on the structure and optical properties of zinc oxide thin films. Appl. Surf. Sci. 242 (2005) 346–352.
[45] T. B. Bateman, Elastic moduli of single-crystal zinc oxide, J. Appl. Phys. 33 (1962) 3309–3312.
[46] J. Singh, S. Ranwa, J. Akhtar, M. Kumar, Growth of residual stress-free ZnO films on SiO_2/Si substrate at room temperature for MEMS devices, AIP ADVANCES 5, 067140 (2015).
[47] P. Scherrer, Bestimmung der Grösse und der inneren Struktur von Kolloidteilchen mittels Röntgenstrahlen, Nachr. Ges. Wiss. 1918 (1918) 98–100.
[48] A.S. Hassanien, A.A. Akl, A.H. Sáaedi, Synthesis, crystallography, microstructure, crystal defects, and morphology of $Bi_xZn_{1-x}O$ nanoparticles prepared by sol–gel technique, Cryst. Eng. Comm. 20 (2018) 1716–1730.
[49] G.K. Williamson, R.E. Smallman, Dislocation densities in some annealed and cold-worked metals from measurements on the X-Ray Debye-Scherrer spectrum, Philos. Mag. 1 (1956) 34–45.
[50] B.R. Kumar, T.S. Rao, AFM studies on surface morphology, topography and texture of nanostructured zinc aluminum oxide thin films, Digest Journal of Nanomaterials and Biostructures, 7, 2012, 1881-1889.

[51] P. Eaton, P. West, Atomic Force Microscopy, first. ed., Oxford University Press, United States, 2010.
[52] A.K. Bajpai, R. Bhatt, R. Katare, Atomic force microscopy enabled roughness analysis of nanostructured poly (diaminonaphthalene) doped poly (vinyl alcohol) conducting polymer thin films, Micron 90 (2016) 12–17.
[53] L.R. Silva, D.A. Couto, F.V. Santo, F.J. Duarte, R.S. Mazzaro, G.V. Veloso, Evaluation of machined surface of the hardened AISI 4340 steel through roughness and residual stress parameters in turning and grinding, The International Journal of Advanced Manufacturing Technology (2020) 107:791–803.
[54] M. Sedlacek, B. Podgornik, J. Vizintin, Correlation between standard roughness parameters skewness and kurtosis and tribological behavior of contact surfaces, Tribology International 48 (2012) 102–112.
[55] N. Tayebi, A.A. Polycarpou, Modeling the effect of skewness and kurtosis on the static friction coefficient of rough surfaces, Tribology International, 37 (2004) 491–505.
[56] J.I. Pankove, Optical Processes in Semiconductors, first ed., Princeton Press, New Jersey, 1971.
[57] K. Boubaker, A physical explanation to the controversial Urbach tailing universality. Eur. Phys. J. Plus, 126 (2011) 1–4.
[58] S. Kasap, H. Ruda, Y. Boucher, Cambridge Illustrated Handbook of Optoelectronics and Photonics, first ed., Cambridge University Press, United Kingdom, 2009.
[59] F. Abeles, Optical Properties of Solids, North-Holland, Publishing Company, London, UK, 1972.
[60] S.B. Chen, Z.Y. Zhong, Optical and dielectric characteristics of photoactive layer thin films for organic photovoltaic cells, Applied Mechanics and Materials, 217-219 (2012) 695-698.
[61] J. Mistrik, S. Kasap, H.E. Ruda, C. Koughia, J. Singh, Optical properties of electronic materials: Fundamentals and Characterization, Chapter 3, pp.47-84. in S. Kasap, P.Capper (Eds.), Springer Handbook of Electronic and Photonic Materials, second ed., Springer International Publishing AG, Trento, Italy, 2017.
[62] Y. Caglar, S. Ilican, M. Caglar, F. Yakuphanoglu, Influence of Mn incorporation on the structural and optical properties of sol gel derived ZnO film, J. Sol-Gel Sci. Technol. 53 (2010) 372–377.
[63] S.H. Wemple, M. DiDomenico, Optical dispersion and the structure of solids, Phys. Rev. Lett., 23 (1969) 1156–1160.

Chapter 3

MAHLER COEFFICIENTS OF SOME *P*-ADIC ELEMENTARY FUNCTIONS

Hamza MENKEN[1]

Suna ÇIÇEK[2]

1 Mersin University, Science and Letters Faculty, Mathematcis Depatrment, Turkey, E-mail:hmenken@mersin.edu.tr

2 Mersin University, Graduate School of Natural and Applied Sciences, Mersin, Turkey, E-mail: sunacicek459@gmail.com

1. Introduction

In scientific studies and in daily life we generally use the rational numbers field $\mathbb{Q}$. The rational numbers field $\mathbb{Q}$ is complete field only according to the trivial norm, and by completing the rational numbers field $\mathbb{Q}$ according to the usual absolute value, we obtain the real numbers field $\mathbb{R}$. According the Ostrowski Theorem, each norm on $\mathbb{Q}$ is either equivalent to the usual absolute value norm or to the *p*-adic norm, where *p* is a prime number [1]. Now, let us briefly introduce the *p*-adic norm. Let *p* be an arbitrary prime number. For any rational number different from zero $x \in \mathbb{Q}, x \neq 0$, there exist $a, b, \alpha \in$ □ ɜ

$$x = p^{\alpha}.\frac{a}{b}, \qquad p \nmid a.b$$

Here, $\alpha \in \mathbb{Z}$ is uniquely determined by prime *p*. Hence, the function $|.|_p : \square \to [0,\infty)$ is defined by formula

$$|x|_p = p^{-\alpha}$$

If $x = 0$, then we take $|0|_p = 0$. In fact, the function $|\cdot|_p$ is a norm and it is called *p-adic norm.* It holds the *ultra-metric triangle inequality* which is more strongly than triangle inequality

$$|x + y|_p \leq \max\{|x|_p, |y|_p\}$$

A norm that satisfies the ultrametric triangle inequality is called a *non Archimedean norm*, and the analysis performed with such this norm is called *non Archimedean Analysis*.

For a given prime *p*, the *p*-adic numbers field $\mathbb{Q}_p$is the completion of the rational numbers with respect to p-adic norm . The *p*-adic numbers field was first described by Kurt Hensel in 1897, in a certain period of time; these numbers were used only in one area of number theory [2]. It

began to question why only real numbers were used in physics, and in 1968, two theoretical mathematicians had used *p*-adic numbers in physics. In 1984 two theoretical physicists had applied the *p*-adic numbers successfully to string theory, then it has begun to be used *p*-adic numbers in applied fields [3]. Moreover, fields such as *p*-adic quantum theory, the *p*-adic universe model, *p*-adic string theory have emerged in physics.

Studies made using *p*-adic numbers in mathematics were collected in a field called *p*-adic analysis. Concepts made with real numbers have begun to be redefined and interpreted by using *p*-adic numbers [3-4].

By $\mathbb{C}_p$ we denote the completion of the algebraic closure of *p*-adic numbers field $\mathbb{Q}_p$. Let $\mathbb{Z}_p = \left\{ x \in \mathbb{C}_p \,\middle|\, |x|_p \leq 1 \right\}$. It is well known from the Kaplansky's theorem that each function *f* from $C(\mathbb{Z}_p \to \mathbb{C}_{p)}$ can be uniformly approximated by polynomials [5]. For any $x \in \mathbb{Z}_p$ the binomial coefficient polynomial $\binom{x}{n}$ is defined by $\binom{x}{0} = 1$ and

$$\binom{x}{k} = \frac{x.(x-1)\ldots(x-k+1)}{k!} \ (k>0\ ).$$

Hence, $\binom{x}{k}$ is a polynomial of degree *k*.

The set of polynomial functions $\left\{ x \to \binom{x}{k} : x \in \mathbb{Z}_p, k \in \mathbb{N} \right\}$ constitutes an orthonormal basis for the space $C\left(\mathbb{Z}_p \to \mathbb{C}_p\right)$ according to the supremum norm. In the other words, for each function $f \in C\left(\mathbb{Z}_p \to \mathbb{C}_p\right)$, there exist unique numbers $a_0, a_1, a_2, \ldots \in \mathbb{C}_p$ ∋

$$f(y) = \sum_{k=0}^{\infty} a_n \binom{y}{k}$$

The set $\left\{\binom{*}{n}: k \in \mathbb{N}\right\}$ is called the *Mahler* basis of the space $C\left(\mathbb{Z}_p \to \mathbb{C}_p\right)$, and the element of $\{a_k: k \in \mathbb{N}\}$ in

$$f(y) = \sum a_k \binom{y}{k}$$

are called the *Mahler coefficients* of $f \in C\left(\mathbb{Z}_p \to \mathbb{C}_p\right)$ (see [6]) .

In the present study, we investigate the Mahler expansions and Mahler coefficients of some p-adic trigonometric functions. Also, we give their Volkenborn integral related some special numbers.

The Volkenborn integral of any function f from $C^1\left(\mathbb{Z}_p \to \mathbb{C}_p\right)$ is defined by the formula

$$\int_{\mathbb{Z}_p} f(x)dx = \lim_{k\to\infty} \frac{1}{p^k} \sum_{j=0}^{p^k-1} f(j)$$

If $f(x) = c$, then

$$\int_{\mathbb{Z}_p} f(x)dx = c$$

Also, the property holds

$$\int_{\mathbb{Z}_p} f(x+1)dx - \int_{\mathbb{Z}_p} f(x)dx = f'(0)$$

In addition, if the function f in the form of

$$f(x) = \sum_{n=0}^{\infty} a_n \binom{x}{n} \in C^1(\mathbb{Z}_p \to \mathbb{C}_p)$$

then, its Volkenborn integral is

$$\int_{\mathbb{Z}_p} f(x)dx = \sum_{n=0}^{\infty} a_n \frac{(-1)^n}{n+1}$$

(For details see [5-7]). We note that the Volkenborn integral was first defined by A. Volkenborn in his twin papers [8], [9]. By the agency of *p*-adic Volkenborn integrals and their extensions, very important studies have done on some special numbers, polynomials and functions such as Bernoulli, Euler, Changhee, Daehee, Bernstein and their extensions. ([10]-[24]). In fact, almost all special numbers and polynomial mentioned above are described by *p*-adic Volkenborn integrals and their extensions.

We note that an infinite series $\sum_{n=0}^{\infty} a_n$ with $a_n \in \mathbb{C}_p$ convergences if and only if $|a_n|_p \to 0$. In *p*-adic content the elementary functions as logarithmic, exponential and trigonometric functions are described by their usual power series but, their regions of convergence are absolutely different from the complex cases. Here, we recall only few ones of them.

The power series

$$\sum_{n=1}^{\infty} \frac{(-1)^{n+1}.x^n}{n}$$

converges for $|x|_p < 1$, and it is denoted by $\log_p(1+x)$. So, the *p*-adic logarithmic function is defined by

$$\log_p x = \sum_{n=1}^{\infty} \frac{(-1)^{n+1}.(x-1)^n}{n},$$

and it converges for $|x-1|_p < 1$.

The exponential function in *p*-adic content is defined by formula

$$\exp_p x = \sum_{n=0}^{\infty} \frac{x^n}{n!}$$

and its convergence domain is the set $E = \{x \in \mathbb{C}_p : |x|_p < p^{\frac{1}{1-p}}\}$.

In p-adic content all trigonometric functions are defined by their power series in real case. Here, we give few examples. The p-adic sine and cosine functions are defined by the usual power series, respectively,

$$\sin_p x = \sum_{n=0}^{\infty} \frac{(-1)^n x^{2n+1}}{(2n+1)!},$$

$$\cos_p x = \sum_{n=0}^{\infty} \frac{(-1)^n x^{2n}}{(2n)!},$$

and they converge for all $x \in E$. The p-adic sine and cosine hyperbolic functions are defined by the power series, respectively,

$$\sinh_p x = \sum_{n=0}^{\infty} \frac{(-1)^n x^{2n+1}}{(2n+1)!},$$

$$\cosh_p x = \sum_{n=0}^{\infty} \frac{(-1)^n x^{2n}}{(2n)!},$$

and they converge for all $x \in E$. The p-adic tangent and cotangent are described similarly and their convergence domain is $\mathbb{Z}_p$.

For any $x \in \mathbb{Z}_p$ ve $m \in \mathbb{N} \cup \{0\}$, let us consider the equality

$$x^m = \sum_{n=0}^{\infty} a_{n,m} \binom{x}{n}.$$

The numbers $a_{n,m}$ which are determined by the equality above are called the *Stirling numbers of second type*.

Lemma 1.1([5]) The Stirling numbers of second type $a_{n,m}$ hold the relations for , $m \in \{0,1,2,\dots\}$:

$i)$ $a_{0,0} = 1$; $a_{0,m} = a_{0,n} = 0$ $(m,n) \neq 0$; $a_{n,m} = 0$ $(n > m)$,

$ii)\ a_{n,m} = \sum_{j=0}^{n} (-1)^{n-j} \binom{n}{j} j^m$,

$iii)$ $a_{n,m}$ is an integer and divided by $n!$

$iv)$ $Let\ f_{n,m}(x) = (x\frac{d}{dx})^m (x-1)^n \quad (x \in \mathbb{Z}_p)$. Then,

$$a_{n,m} = f_{n,m}(1)$$

$v)$ $a_{n,m+1} = n\left(a_{n,m} + a_{n-1,m}\right) \quad (n \geq 1)$

$vi)$ $a_{n+1,m} = \sum_{j=0}^{m-1} \binom{m}{j} a_{n,j} \quad (m \geq 1)$

Lemma 1.2 [[5]) Let p is a prime, $p > 2, a \in p\mathbb{Z}_p$ and

$$\sin_p(ax) = \sum_{n=0}^{\infty} a_n \binom{x}{n},$$

$$\cos_p(ax) = \sum_{n=0}^{\infty} b_n \binom{x}{n} ,$$

Then, for all *n* the relations hold:

$$a_{2n} = (-1)^n 2^{2n} (\sin_p \tfrac{1}{2}a)^{2n} \sin_p(na),$$

$$a_{2n+1} = (-1)^n 2^{2n+1} (\sin_p \tfrac{1}{2}a)^{2n+1} \cos_p(\mathrm{n} + \tfrac{1}{2})a,$$

$$b_{2n} = (-1)^n 2^{2n} (\sin_p \tfrac{1}{2}a)^{2n} \cos_p(na),$$

$$b_{2n+1} = (-1)^n 2^{2n+1} (\sin_p \tfrac{1}{2}a)^{2n+1} \sin_p(\mathrm{n} + \tfrac{1}{2})a.$$

2. Main Results

In the present study we study some p-adic elementary functions. We investigate the Mahler expansions and Mahler coefficients of some p-adic elementary functions. Also, we compute their Volkenborn integrals related the Stirling numbers of second type.

For the Mahler expansion of p −adic hyperbolic sine function, the next theorem holds:

Theorem 2.1: Let p is a prime, $p > 2, a \in p\mathbb{Z}_p$ and

$$\sinh_p(ax) = \sum_{n=0}^{\infty} a_n \binom{x}{n} \quad (x \in \mathbb{Z}_p).$$

Then, the coefficients a_n satisfy the formulas for all n

$$a_{2n} = \frac{1}{2}\frac{(\exp_p a - 1)^{2n}.[(\exp_p a)^{2n} - 1]}{(\exp_p a)^{2n}}$$

$$a_{2n+1} = \frac{1}{2}\frac{(\exp_p a - 1)^{2n+1}.[(\exp_p a)^{2n+1} + 1]}{(\exp_p a)^{2n+1}}$$

Proof: It is well known that

$$\sinh_p(ax) = \frac{\exp_p(ax) - \exp_p(-ax)}{2}.$$

Hence, we write

$$\sinh_p(ax) = \frac{1}{2}\exp_p(ax) - \frac{1}{2}\exp_p(-ax)$$

$$= \frac{1}{2}\sum_{n=0}^{\infty}(\exp_p(a)-1)^n\binom{x}{n} - \frac{1}{2}\sum_{n=0}^{\infty}(\exp_p(-a)-1)^n\binom{x}{n}$$

$$= \sum_{n=0}^{\infty}\frac{1}{2}\left[(\exp_p(a)-1)^n-(\exp_p(-a)-1)^n\right]\binom{x}{n}$$

Now, we can determine the coefficients a_n as

$$a_n = \frac{1}{2}(\exp_p(a)-1)^n - \frac{1}{2}(\exp_p(-a)-1)^n$$

$$= \frac{1}{2}\left[(\exp_p(a)-1)^n - \left(\frac{1}{\exp_p(a)}-1\right)^n\right]$$

$$= \frac{1}{2}\left[(\exp_p(a)-1)^n - \frac{(1-\exp_p(a))^n}{(\exp_p(a))^n}\right]$$

$$a_n = \frac{1}{2}\frac{(\exp_p(a)-1)^n.(\exp_p(a))^n-(1-\exp_p(a))^n}{(\exp_p(a))^n}$$

So, we obtain the relations

$$a_{2n} = \frac{1}{2}\frac{(\exp_p(a)-1)^{2n}.[(\exp_p(a))^{2n}-1]}{(\exp_p(a))^{2n}},$$

and

$$a_{2n+1} = \frac{1}{2}\frac{(\exp_p(a)-1)^{2n+1}.[(\exp_p(a))^{2n+1}+1]}{(\exp_p(a))^{2n+1}}.$$

Teorem 2.2: The Mahler coefficients a_m of $\sinh_p(ax)$ are

$$a_m = \frac{a^{2m+1}}{(2m+1)!} \sum_{n=2m+1}^{\infty} a_{n,2m+1}.$$

Here, $a_{m,n}$ are the Stirling numbers of second type.

Proof: Let $a \in E$. Assume that

$$\sinh_p(ax) = \sum_{n=0}^{\infty} a_n \binom{x}{n}.$$

Let us determine the coefficients a_m.

By the definition of $\sinh_p(ax)$ we write

$$\sinh_p(ax) = \sum_{m=0}^{\infty} \frac{a^{2m+1}}{(2m+1)!} x^{2m+1}$$

By the definition of Striling number of second type we know that

$$x^m = \sum_{n=0}^{\infty} a_{n,m} \binom{x}{n}$$

If $j < j$ then $a_{j,i}$=0 , and so, we obtain that

$$\sinh_p(ax) = \sum_{m=0}^{\infty} \left(\sum_{n=2m+1}^{\infty} \frac{a^{2m+1}}{(2m+1)!} a_{n,2m+1} \right) \binom{x}{n}$$

Hence, we obtain the Mahler coefficients a_n of $\sinh_p(ax)$ as

$$a_m = \frac{a^{2m+1}}{(2m+1)!} \sum_{n=2m+1}^{\infty} a_{n,2m+1}.$$

Now we give the Mahler expansions and Mahler coefficients of p-adic cosine hyperbolic function.

Theorem 2.3: Let p be a prime number, $p > 2$, $a \in p\mathbb{Z}_p$, $x \in \mathbb{Z}_p$ and

$$\cosh_p(ax) = \sum_{n=0}^{\infty} c_n \binom{x}{n}.$$

Then, the relations hold:

$$c_{2n} = \frac{1}{2}\frac{(e\ \exp_p a-1)^{2n}[(\ \exp_p a)^{2n}+1]}{(\ \exp_p a)^{2n}},$$

$$c_{2n+1} = \frac{1}{2}\frac{(\ \exp_p a-1)^{2n+1}[(\ \exp_p a)^{2n+1}-1]}{(\ \exp_p a)^{2n+1}}.$$

Proof: We know that

$$\cosh_p(ax) = \frac{\exp_p(ax) + \exp_p(-ax)}{2}.$$

By the Mahler expansion of exponential function we write

$$\cosh_p(ax) = \frac{1}{2}\exp_p(ax)(ax) + \frac{1}{2}\exp_p(ax)(-ax).$$

Using the equalities

$$\exp_p(ax) = \sum_{n=0}^{\infty}(\ \exp_p(a) - 1)^n \binom{x}{n},$$

$$\exp_p(-ax) = \sum_{n=0}^{\infty}(\ \exp_p(-a) - 1)^n \binom{x}{n}$$

we obtain that

$$\cosh_p(ax) = \sum_{n=0}^{\infty}\frac{1}{2}\left[(\ \exp_p(a) - 1)^n + (\ \exp_p(-a) - 1)^n\right]\binom{x}{n}$$

Let us write the Mahler coefficients c_n in more obvious form. It is clear that

$$c_n = \frac{1}{2}\left[(\ \exp_p(a) - 1)^n + (\ \exp_p(-a) - 1)^n\right]$$

$$= \frac{1}{2}\left[(\exp_p(a) - 1)^n + \left(\frac{1}{\exp_p a} - 1\right)^n\right]$$

$$= \frac{1}{2}\left[(\exp_p(a) - 1)^n + \left(\frac{1 - \exp_p a}{\exp_p a}\right)^n\right]$$

or

$$c_n = \frac{1}{2}\frac{(\exp_p a - 1)^n((\exp_p a)^n + (1 - \exp_p a)^n)}{(\exp_p a)^n}.$$

So, we have the desire equalities:

$$c_{2n} = \frac{1}{2}\frac{(\exp_p a - 1)^{2n}[(\exp_p a)^{2n} + 1]}{(\exp_p a)^{2n}},$$

$$c_{2n+1} = \frac{1}{2}\frac{(\exp_p a - 1)^{2n+1}[(\exp_p a)^{2n+1} - 1]}{(\exp_p a)^{2n+1}}.$$

The Mahler coefficients of $\cosh_p(ax)$ in term of Stirling number of second type are given below:

Theorem 2.4: The coefficients c_m of $cosh_p(ax)$ have the form of

$$c_m = \frac{a^{2m}}{(2m)!}\sum_{n=2m}^{\infty} a_{n,2m}$$

where $a_{m,n}$ are the Stirling numbers of second type.

Proof: Let $a \in E$ and

$$\cosh_p(ax) = \sum_{n=0}^{\infty} c_n \binom{x}{n}.$$

By the definition of $\cosh(ax)$ we write

$$\cosh_p(ax) = \sum_{n=0}^{\infty} \frac{a^{2n}}{(2n)!} x^{2n}.$$

If $i < j$ then $a_{j,i}$=0. So we have

$$\cosh_p(ax) = \sum_{m=0}^{\infty} \left(\sum_{n=2m}^{\infty} \frac{a^{2n}}{(2n)!} a_{m,n} \right) \binom{x}{m}$$

Hence, we obtain the Mahler coefficients c_n in the form of

$$c_n = \frac{a^{2n}}{(2n)!} \sum_{n=2m}^{\infty} a_{m,n}$$

Theorem 2.5. If $a \in p\mathbb{Z}_p, x \in \mathbb{Z}_p$, then

$$\int_{\mathbb{Z}_p} \sin_p(ax)\, dx = \sum_{n=1}^{\infty} a_n \frac{(-1)^n}{n+1}.$$

Here, a_n are the Mahler coefficients of $\sin_p(ax)$ which are given in Lemma 1.2.

Proof . Let $a \in p\mathbb{Z}_p, x \in \mathbb{Z}_p$. By Lemma 1.2 we write

$$\sin_p(ax) = \sum_{n=0}^{\infty} a_n \binom{x}{n}$$

Taking Volkenborn integral we write

$$\int_{\mathbb{Z}_p} \sin_p(ax)\, dx = \int_{\mathbb{Z}_p} \left(\sum_{n=0}^{\infty} a_n \binom{x}{n} \right) dx$$

or

$$\int_{\mathbb{Z}_p} \sin_p(ax)\, dx = \sum_{n=0}^{\infty} a_n \int_{\mathbb{Z}_p} \binom{x}{n} dx$$

By the property

$$\int_{\mathbb{Z}_p} \binom{x}{n} dx = \frac{(-1)^n}{n+1}$$

We obtain

$$\int_{\mathbb{Z}_p} \sin_p(ax)\, dx = \sum_{n=1}^{\infty} a_n \frac{(-1)^n}{n+1}$$

Corollary 2.1: If $a \in p\mathbb{Z}_p, x \in \mathbb{Z}_p$ and the numbers a_n are the Mahler coefficients of $\sin_p(ax)$, then the equality holds

$$\sum_{n=1}^{\infty} a_n \frac{(-1)^n}{n+1} = -\frac{a}{2}$$

Proof: It is trivial from Lemma 1.2 and Theorem 2.5.

Theorem 2.6. If $a \in p\mathbb{Z}_p, x \in \mathbb{Z}_p$, then

$$\int_{\mathbb{Z}_p} \cos_p(ax)\, dx = \sum_{n=1}^{\infty} b_n \frac{(-1)^n}{n+1}$$

Here, b_n are the Mahler coefficients of $\cos_p(ax)$ which are given in Lemma 1.2.

Proof: Let

$$\cos_p(ax) = \sum_{n=1}^{\infty} b_n \binom{x}{n}$$

Taking Volkonborn integral we have

$$\int_{\mathbb{Z}_p} \cos_p(ax)\,dx = \int_{\mathbb{Z}_p} \left(\sum_{n=0}^{\infty} b_n \binom{x}{n} \right) dx$$

or

$$\int_{\mathbb{Z}_p} \cos_p(ax)\,dx = \sum_{n=0}^{\infty} b_n \int_{\mathbb{Z}_p} \binom{x}{n} dx$$

By the property

$$\int_{\mathbb{Z}_p} \binom{x}{n} dx = \frac{(-1)^n}{n+1}$$

We obtain that

$$\int_{\mathbb{Z}_p} \cos_p(ax)\,dx = \sum_{n=1}^{\infty} b_n \frac{(-1)^n}{n+1}$$

Corollary 2.2: If $a \in p\mathbb{Z}_p, x \in \mathbb{Z}_p$ and the numbers b_n are the Mahler coefficients of $\cos_p(ax)$, then the equality holds

$$\sum_{n=1}^{\infty} b_n \frac{(-1)^n}{n+1} = -\frac{a}{2}$$

Theorem 2.7: If $a \in E, x \in \mathbb{Z}_p$.then

$$\int_{\mathbb{Z}_p} \sinh_p(ax)\,dx = \sum_{n=1}^{\infty} a_n \frac{(-1)^n}{n+1}$$

where (a_n) are the Mahler coefficients of $\sinh_p(ax)$ which are given in Theorem 2.1.

Proof: By Theorem 2.1, we write

$$\sinh_p(ax) = \sum_{n=1}^{\infty} a_n \binom{x}{n}$$

Hence, we have

$$\int_{\mathbb{Z}_p} \sinh_p(ax)\, dx = \int_{\mathbb{Z}_p} \left(\sum_{n=1}^{\infty} a_n \frac{(-1)^n}{n+1} \right) dx$$

or

$$\int_{\mathbb{Z}_p} \sinh_p(ax)\, dx = \sum_{n=1}^{\infty} a_n \int_{\mathbb{Z}_p} \binom{x}{n} dx$$

By the relation

$$\int_{\mathbb{Z}_p} \binom{x}{n} dx = \frac{(-1)^n}{n+1},$$

we obtain that

$$\int_{\mathbb{Z}_p} \sinh_p(ax)\, dx = \sum_{n=1}^{\infty} a_n \frac{(-1)^n}{n+1}.$$

References

[1]. Gouvêa, Fernando Q., *p*-adic numbers. An introduction. Second edition, Universitext., *Springer-Verlag, Berlin,* 1997.

[2]. Dragovich, B., Khrennikov, A. Y., Kozyrev, S. V . Volovich, I.V. On *p*-adic mathematical physics. *p-Adic Numbers .Ultrametric Anal. Appl.,*1.(2009), no.1, 1-17.

[3]. Vladimirov, V. S. and Volovich, I. V. , Differential calculus, Theor. Math. Phys., **59**, 317–335 (1984)

[4]. Vladimirov, V. S.; Volovich, I. V.; Zelenov, E. I. p-adic analysis and mathematical physics. Series on Soviet and East European Mathematics, 1. *World Scientific Publishing Co., Inc., River Edge, NJ,* 1994.

[5]. Schikhof, W. H., Ultrametric calculus. An introduction to p-adic analysis.Cambridge Studies in Advanced Mathematics, 4. *Cambridge University Press, Cambridge,* 1984.

[6]. Mahler, K.., An interpolation series for continuous functions of a p-adic variable. *J. Reine Angew. Math.* **199** 1958 23–34.

[7]. Robert, Alain M, .A course in p-adic analysis. Graduate Texts in Mathematics, 198. *Springer-Verlag, New York,* 2000.

[8]. Volkenborn, A. E., P-adisches Integral und seine Anwendungen. I. (German) *Manuscripta Math.* **7** (1972), 341–373.

[9]. Volkenborn, A. E., *p*-adisches Integral und seine Anwendungen. II. (German) *Manuscripta Math.* **12** (1974), 17–46.

[10]. Kim, T., q-Volkenborn integration. *Russ. J. Math. Phys.* 9 (2002), No. 3, 288–299.

[11]. Kim, T., A note on *q*-Volkenborn integration. *Proc. Jangjeon Math. Soc.* 8(2005), no. 1, 13-17.

[12]. Kim, T., An invariant *p*-adic q-integral on Zp. *Appl. Math. Lett.* 21 (2008),no. 2, 105–108.

[13]. Kim, T., On *p*-adic iterpolating function for *q*-Euler numbers and its derivates, *Journal of Nonlinear Mathematical Physics*, 14:1(2008)., 15-27.

[14]. Kim, T.; Choi, J.; Kim, Y. H.; Ryoo, C. S., On the fermionic *p*-adic integral representation of Bernstein polynomials associated with Euler numbers and polynomials. *J. Inequal. Appl.* 2010, Art. ID 864247, 12 pp.

[15]. Araci, S.; Erdal, D.; Seo, J. J., A study on the fermionic p-adic q-integral representation on Zp associated with weighted q-Bernstein and q-Genocchi polynomials. *Abstr. Appl. Anal.* 2011, Art. ID 649248, 10 pp.

[16]. Kim, T.,, On the analogs of Euler numbers and polynomials associated with *p*-adic q-integral on Zp at q=−1. *J. Math. Anal. Appl.* 331 (2007), no. 2, 779–792.

[17] Kim, D.S. and Kim, T., Some *p*-Adic Integrals on Zp Associated with Trigonometric Functions, Russian Journal of Mathematical Physics, Vol. 25, no.3(2018), 300-308.

[18] Havare, Ö.Ç. and Menken, H., The Volkenborn integral of the p-adic gamma function, Int. J. Adv. Appl. Funct 5 (2), 56-59

[19] Havare, Ö.Ç. and Menken, H., A note on the p-adic gamma function and q-Changhee polynomials, J. Math. Computer Sci., 18 (2018), 11–17

[20] Havare, Ö.Ç. and Menken,, H., On the Volkenborn integral of the q-extension of the p-adic gamma function, Journal of Mathematical Analysis,Volume 8 Issue 2 (2017), Pages 64-72.

[21] Duran, U. and Açikgöz, M., On p-adic gamma function related to q-Daehee polynomials and numbers, Proyecciones, Vol. 38, No4 (2019), 799-810.

[22] Duran, U. and Açikgöz, M., ,On applications for Mahler expansion associated with *p*-adic *q*-integrals, International Journal of Number Theory, Vol. 15, No. 01, pp. 67-84 (2019)

[23] Duran, U. and Açikgöz, M., Multifarious correlations for *p*-adic gamma function and weighted *q*-Daehee polynomials Maejo Int. J. Sci. Technol. 2019, 13(03), 209-216.

[24] Duran, U. and Dutta, H., A Survey on *p*-Adic Integrals, Current Trends in Mathematical Analysis and Its Interdisciplinary Applications,Birkhäuser, 2019, 855-884

Chapter 4

A STUDY ON CATALYST USED IN MANNICH REACTION TO OBTAIN β-AMINO CARBONYL COMPOUNDS IN RECENT YEARS

Hasniye YAŞA[1]

1 Istanbul University-Cerrahpaşa, Engineering Faculty, Chemistry Department. Organic Chemistry Division, 34320 Avcılar-İstanbul/TURKEY

The Mannich reaction, an effective method used in reactions such as the synthesis of various biologically important β-amino carbonyl compounds, as well as the preparation of multi-functional synthetic building blocks containing excess nitrogen atoms, is constantly evolving. Various catalysts are used in the synthesis of β-amino carbonyl compounds in the Mannich reaction. Catalysis is considerable in diverse implementation of organic chemistry.

Sabahat et al. reported that they synthesized amino carbonyl compounds with high yields by using camphorsulfonate-based PILs in a shorter reaction time at ambient temperature directly in a one- pot Mannich condensation (Sabahat et al., 2020).

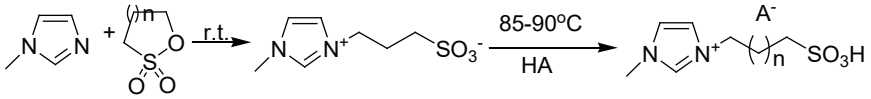

A^-= Cl^-, CF_3COO^-, HSO_4^-, $H_2PO_4^-$,$CH_3SO_3^-$, $CF_3SO_3^-$, p-TS^-,CS^-

n= 1 or 2

Figure 1. Synthesis of ionic liquids

L. Satish et al. demonstrated a simple chemical synthesis route for the synthesis of phosphate functional graphene oxide modified with copper oxide nanoparticles (CuO/PGO). The obtained nanocatalyst was used as an potent and active applicant for the synthesis of β-amino carbonyl compounds in a green synthetic ultrasonic way (L. Satish et al., 2020).

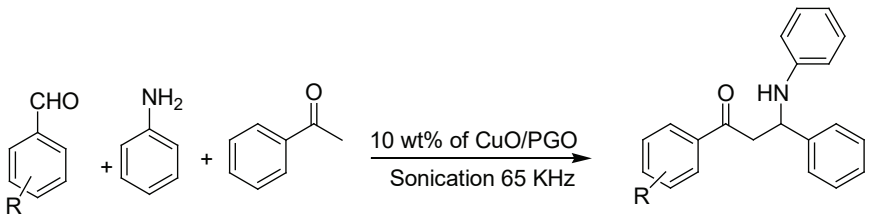

Figure 2. A model of Mannich reaction by CuO/PGO

Bhupinder et al. report that manganese perchlorate hexahydrate, a dry, odorless, pink crystalline solid, is an efficient and promising catalyst for the synthesis of organic compounds. They reported an ultrasound-assisted one-pot approach to the Mannich reaction of aromatic aldehydes, amines and ketones in ethanol catalyzed by manganese perchlorate hexahydrate at room temperature (Bhupinder et al., 2020).

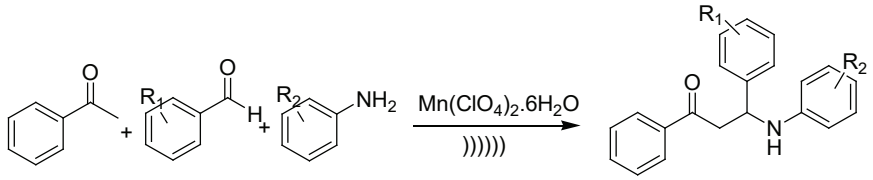

Figure 3. Three-component Mannich reactions by Mn(ClO4)2.6H2O

Hasniye et al. reported a soft, useful, efficient, one-pot Mannich reaction for obtaining β-amino carbonyl compounds from ketones, aromatic aldehydes and aromatic amines using molecular iodine as a catalyst at room temperature (Hasniye et al., 2019).

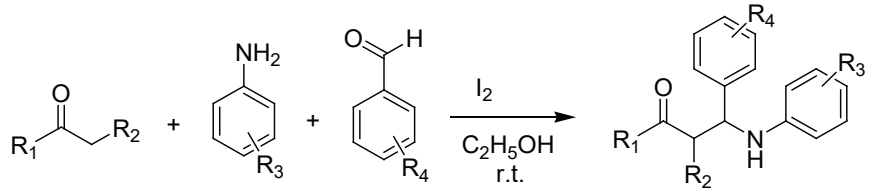

Figure 4. Iodine-catalyzed Mannich reaction

Hasniye and Kübra reported a rapid synthesis of β-aminocarbonyl compounds in the presence of Bi (NO3)3.5H2O (BN) as it is non-toxic, stable in air, and cheaper (Hasniye and Kübra 2019, Jaspreet Rajput, 2013).

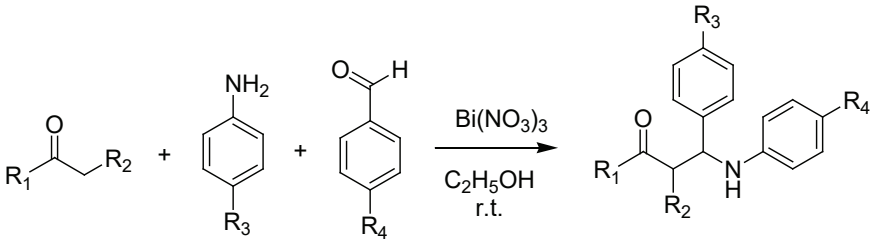

Figure 5. Mannich reaction by Bi(NO3)3

Ali et al. presented a new catalytic protocol for the efficient synthesis of β-amino ketone derivatives with a firmly bound styrene-divinylbenzene copolymer/TiCl4 complex as a reusable polymeric Lewis acid catalyst in ethanol medium. They reported that the catalyst not only showed high catalytic activity, but also had many advantages such as thermal stability and recyclability (Ali et al. 2019).

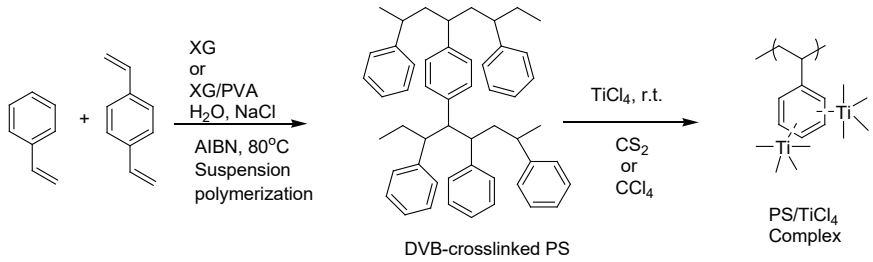

Figure 6. The synthesis of polymeric carrier and its titanium tetrachloride complex

Ali Maleki et al. reported a appropriate and potent method for synthesis of β-amino carbonyl compounds via the condensation of aniline, aldehyde and ketone compound in the presence of PEG-SO3H-functionalized Fe3O4 as a superparamagnetic heterogeneous nanocatalyst at room temperature in high yields (Ali Maleki et al., 2018).

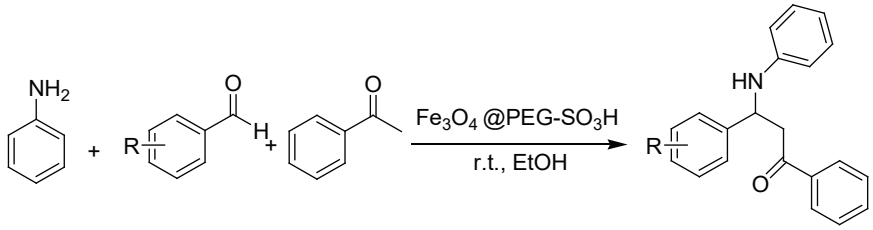

Figure 7. β-amino carbonyl compounds synthesis byFe3O4@PEG-SO3H catalyst

Farhad et al. reported that they prepared a easy, potent and environmentally friendly solid acid catalyst by fixing a propyl sulfonic acid to the surface of silica-coated magnetic nanoparticles with low-cost precursors (Farhad et al., 2017).

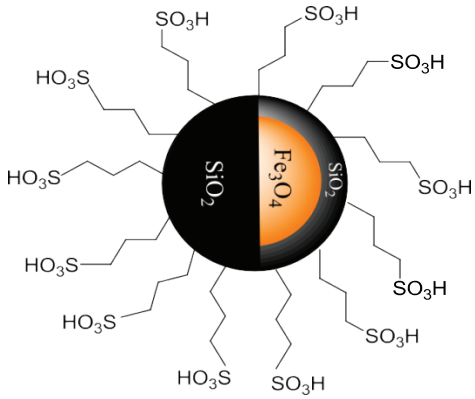

Figure 8. *Sulfonated core-shell magnetic nanoparticles (SMNPs)*

Manmeet & Satya report an efficient protocol for the synthesis of coumarins via the Pechmann reaction and β-amino carbonyl compounds via the aza-Michael reaction using a catalytic amount of solid Lewis acid catalyst, C@TiO_2-O_3-$SbCl_2$. They prepared six different catalysts by covalently immobilizing homogeneous Lewis acids on amorphous carbon and nano-titania derived ulfone carbon titania composite. Among the various catalysts tested, C@TiO_2-O_3-$SbCl_2$ reported superior catalytic activity (Manmeet & Satya 2017).

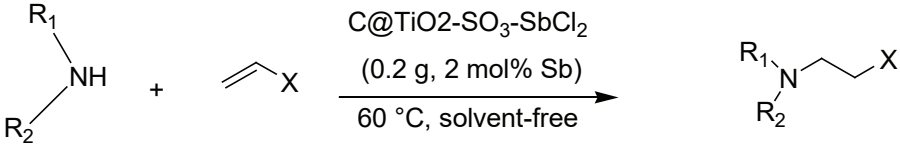

Figure 9. *C@TiO_2-O_3-$SbCl_2$ catalyzed one-pot synthesis of β-amino carbonyl compounds via aza-Michael reaction*

Susmita et al reported that they synthesized a new series of 1,3-disulfoimidazolium transition metal chloride systems: $[Dsim]_2[ZnCl_4]$, [Dsim][FeCl4] and $[Dsim]_2[NiCl_4]$ Brönsted - Lewis acidic solid material. They found that all three materials were reusable catalysts for the synthesis of one-chamber three-component Mannich-type amino carbonyl compounds (Susmita et al., 2016).

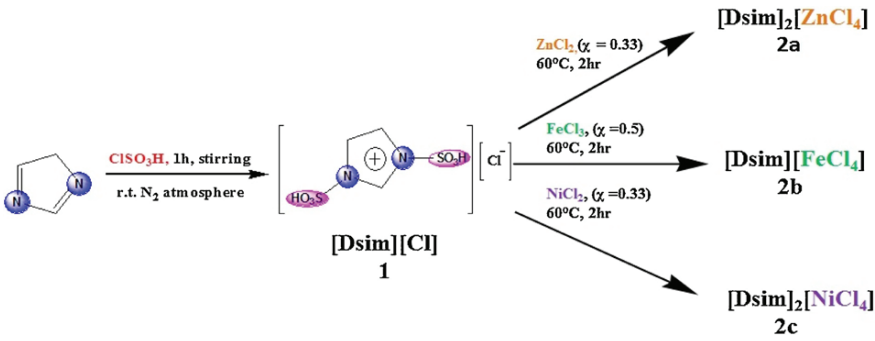

Figure 10. *Synthesis of 1,3-disulfoimidazolium chlorometallate ionic liquids [Dsim]2[ZnCl4] 2a, [Dsim][FeCl$_4$] 2b and [Dsim]$_2$[NiCl$_4$] 2c*

Hua et al., using the acidic IL catalyst under ultrasonic irradiation, they obtained a suitable procedure for the Mannich reaction, less reaction time and high efficiency (Hua et al.,2016).

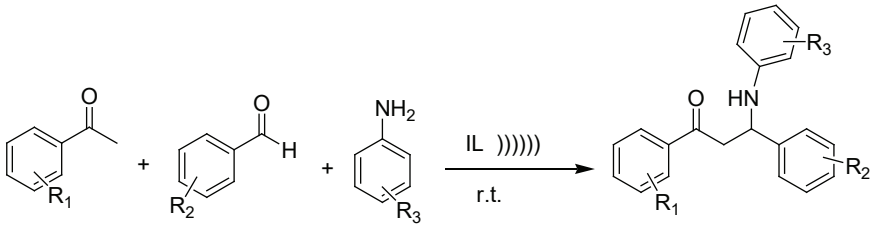

Figure 11. *Mannich reaction catalyzed by IL's under ultrasonic irradiation*

Amel et al. synthesized various β-amino carbonyl derivatives of aniline, acetophenone and aromatic aldehydes at room temperature with high yields in a shorter time using PEG-600 as a safer catalyst in solvent-free conditions. This synthetic route is extremely easy and avoids the use of toxic catalysts (Amel et al., 2016).

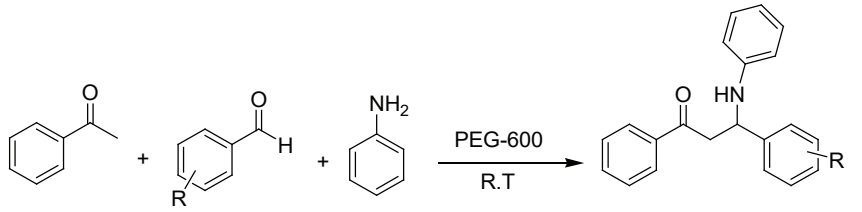

Figure 12. *Synthesis β-amino carbonyl derivatives*

Zahra et al. developed an easy synthesis method of magnetically separable heteropoly acid ($CuFe_2O_4$-SiO_2-NH_2-$H_3PW_{12}O_{40}$) consisting of immobilized phosphotungstic acid ($H_3PW_{12}O_{40}$) on amine functionalized

silica coated magnetic copper-ferrite nanoparticles ($CuFe_2O_4$-SiO_2-NH_2). The immobilized phosphotungstic acid has been used as an efficient heterogeneous catalyst for the synthesis of β-aminocarbonyl compounds using a one-pot three-component coupling reaction of aldehydes, amines and ketones at room temperature and under solvent-free conditions (Zahra et al., 2016).

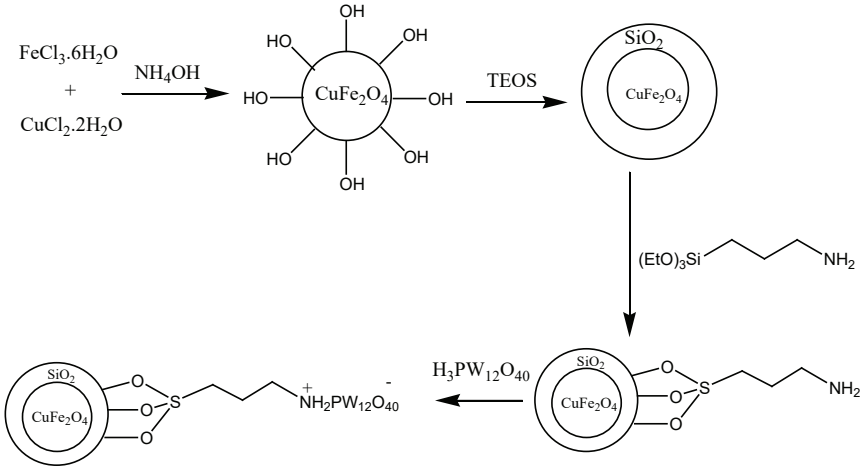

Figure 13. *Synthetic pathways of ($CuFe_2O_4$-SiO_2-NH_2-$H_3PW_{12}O_{40}$)*

Vishvanath et al. prepared silica supported $Co(ClO_4)_2$ catalyst and found that it is thermally stable over a long temperature range. They reported that it is an efficient, recyclable and heterogeneous catalyst for the synthesis of both 5-unsubstituted 3,4-dihydropyrimidinones and β-amino carbonyl compounds under solvent-free conditions (Vishvanath et al., 2016).

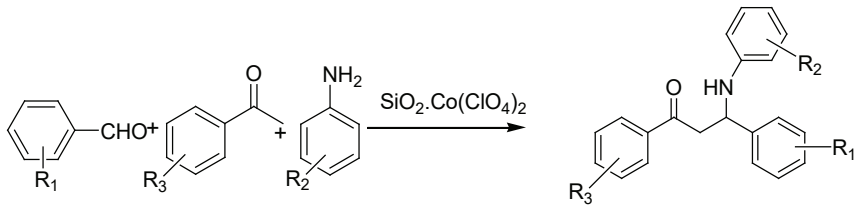

Figure 14. *β-amino carbonyl compounds using silica supported $Co(ClO_4)_2$ as catalyst under solvent free condition.*

Parishmita et al. They prepared three efficient heterogeneous organocatalysts from three non-recyclable carboxylic acids. They found that the remarkable advantages of these catalysts were high catalytic

activity in mild conditions, easy operation procedure combined with simple operation, recyclability and low cost (Parishmita et al., 2015).

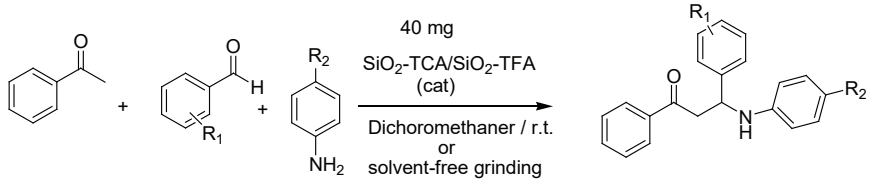

Figure 15. *Mannich-type reactions catalyzed by silica-supported organic acids*

Di Liu et al. developed a simple and efficient method for the synthesis of β-amino carbonyl compounds using PPA/SiO_2 as catalyst, which provides short reaction time, mild reaction terms, reusable catalyst (Di Liu et al., 2015).

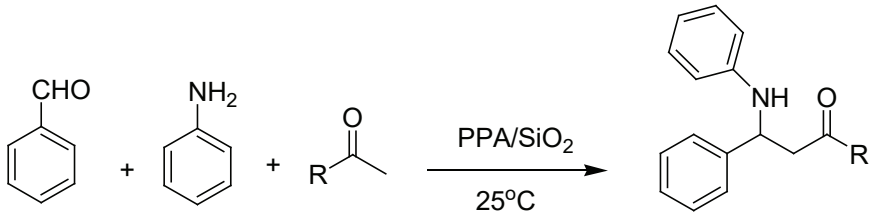

Figure 16. *the synthesis of β-amino carbonyl compounds using PPA / SiO_2 as catalyst*

Divya et al. synthesized mesoporous silica-polymer nanocomposites (SBA/PS) by wet impregnation method, functionalized with light polyphosphoric acid (PPA) for catalytic applications (Divya et al., 2015).

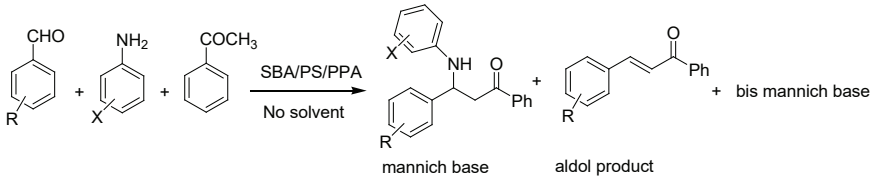

Figure 17. *The synthesis of β-amino carbonyl compounds*

Pathakota et al. Synthesized β-amino carbonyl compounds from aromatic ketones, aldehydes and amines by the Mannich reaction in the presence of amberlyst-15 as a reusable heterogeneous catalyst at room temperature under solvent-free conditions (Pathakota et al., 2015).

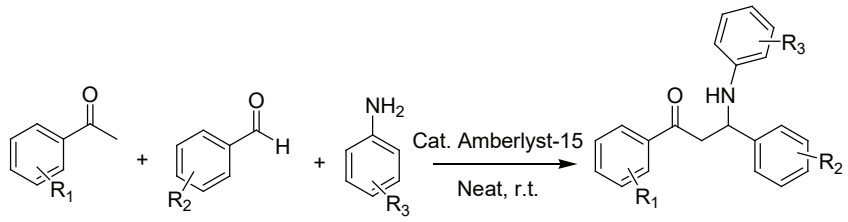

Figure 18. *Synthesis of β-amino carbonyl compounds by Amberlyst-15*

Javad Abedini et al. used PPh_3 as an efficient catalyst for the one-pot three-component Mannich reactions under solvent-free conditions at room temperature. They reported that this method provides a novel and improved method for obtaining β-amino carbonyl compounds in the lack of acidic catalyst in good yield (Javad Abedini et al.2015).

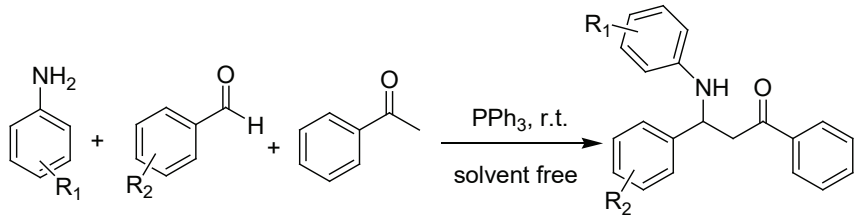

Figure 19. *Mannich reaction via PPh_3*

Ram Singh et al.were reported to synthesis of β-amino carbonyl compounds by $FeCl_3$-silica gel G catalyst and an efficient and time-saving one-pot the three-component Mannich reaction (Ram Singh et al., 2014).

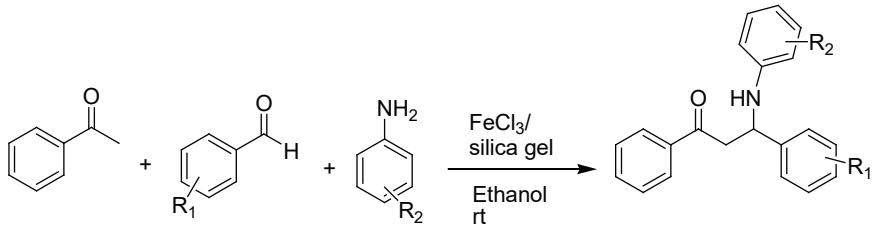

Figure 20. *Mannich reaction with $FeCl_3$/silica gel*

Sathesh Venkatesan et al. developed a novel one-pot three-component Mannich reaction involving CDD, aniline, and benzaldehyde in the presence of NH_4OAc. They synthesized anti-β-amino-carbonyl compound as the predominant one. When the ammonium acetate was used as

catalyst were obtained a mixture of anti and syn-products. There are many advantages that mild reaction condition, easy work up procedure, and high yield of using ammonium acetate as a catalyst (Sathesh Venkatesan et al., 2014).

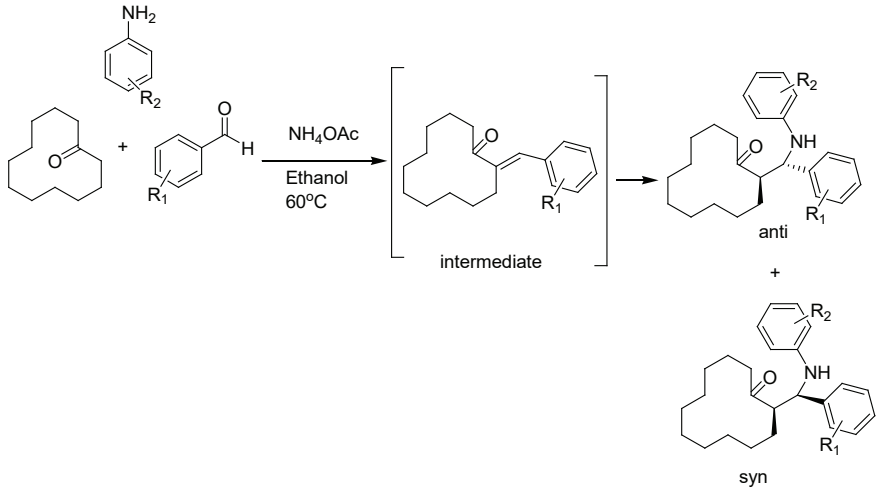

Figure 21. *Ammonium acetate catalyzed Mannich reaction*

Yi Luan et al. recorded that diazo compounds, boranes, and acyl imines undergo a three-component Mannich reaction under catalyst-free conditions to give the anti β-amino carbonyl compounds in high diastereoselectivity. They found that the obtained β-amino carbonyl compounds can be transformed to many potential bioactive molecules (Yi Luan et al., 2014).

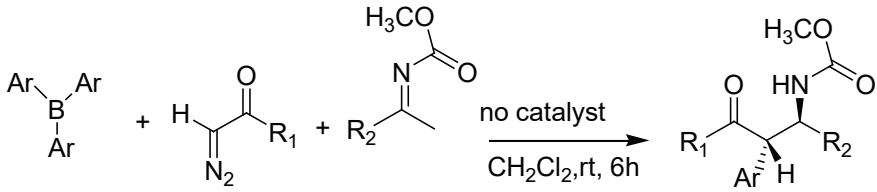

Figure 22. *Mannich reaction no catalyst*

Chao Huang et al. introduced an effective and eco-friendly work for the synthesis of β-amino carbonyl compoundsin this paper. They reported that the oxanorbornene b-amino esters and β-enamine esters were successfully arranged from oxabornene and amines by using solvent-free aza-Michael addition reaction in the absence of any catalyst (Chao Huang et al. 2014).

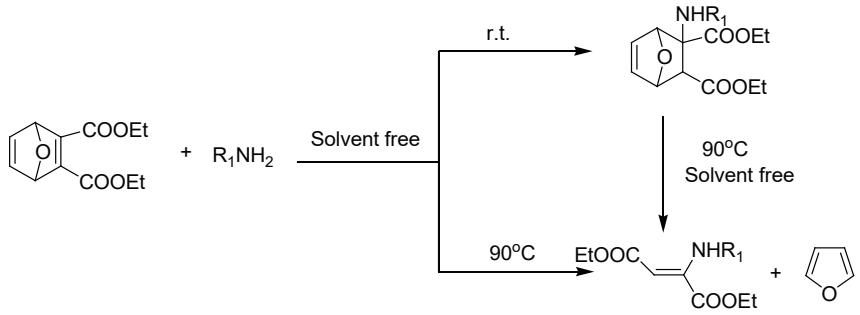

Figure 23. *Synthesis of β-amino carbonyl compounds*

Santosh et al. have developed an efficient method for the synthesis of β-amino carbonyl compounds using phenylboronic acid as catalyst via one-pot three-component Mannich reaction. Excellent yields, mild reaction condition, and simple experimental work-up procedure are some of the advantages of this method (Santosh et al., 2013).

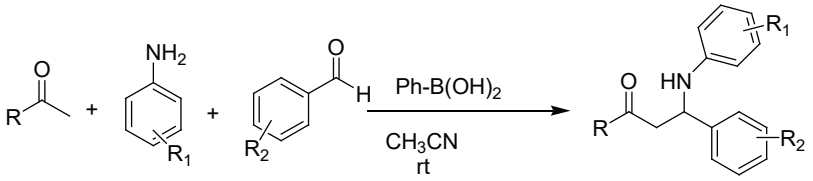

Figure 24. *Synthesis of Mannich Bases*

Xi Cun Wang et al. developed for the synthesis of β-amino carbonyl compounds via the Mannich reaction using recyclable sulfuric acid-modified polyethylene glycol 6000 (PEG-OSO3H). they declared that the reactions were completed in short times and mild reaction conditions with good yields (Xi Cun Wang et al., 2012).

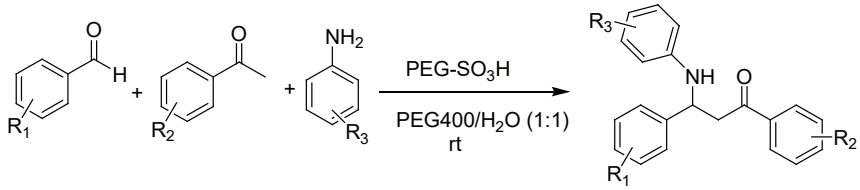

Figure 25. *Mannich reaction catalyzed by PEGOSO$_3$H*

Santosh Kamble et al. reported ultrasound promoted synthesis of β-amino carbonyl compounds in aqueous hydrotropic medium at ambient temperature. The exceptional features of the new procedure are shorter

reaction time, good yields in aqueous medium (Santosh Kamble et al., 2012).

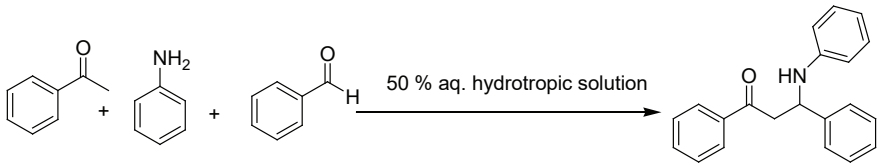

Figure 26. *Screening of synthesis of β-amino carbonyl compound.*

Polyaniline/SiO_2 catalyzed one-pot mannich reaction are carried out in ethanol to obtained diverse β-amino ketones. The various wt% of polyaniline were supported on pure silica synthesized. This record has few advantages such as good yield, non-toxic, clean, simple method, easy recovery and reusability of the catalyst (Ajeet A. Yelwande et al., 2011).

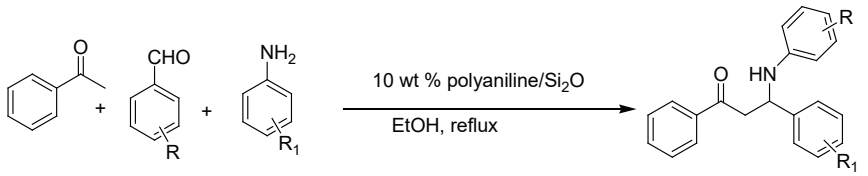

Figure 27. *Synthesis of β-amino carbonyl compounds*

ZSM-5-SO_3H efficiently catalyzed the one-pot three-component Mannich reaction and β- aminocarbonyl compounds were obtained in fair yields and excellent stereoselectivities. Simple experimental requirements and product isolation process makes this report possible for the development of environment-friendly strategy for the synthesis of β-amino-ketones (Ahmad Reza Massah, et al., 2011).

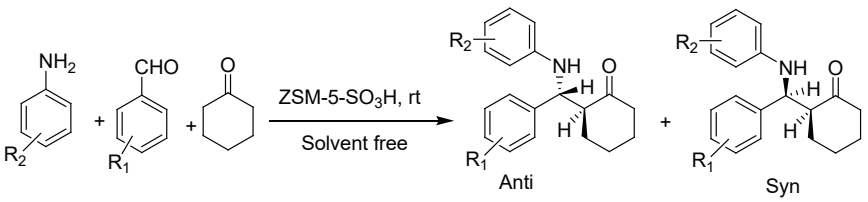

Figure 28. *Direct Mannich reactions by ZSM-5-SO_3H*

Abolghasem Davoodnia et al. reported that a simple and efficient method for the synthesis of β-amino carbonyl compounds by one-pot three-component Mannich reaction using a carbon-based solid acid (CBSA), as an effective and reusable catalyst, is described. The present procedure proposals few advantages such as simple method with an easy work-up,

shorter reaction times, and excelent yields (Abolghasem Davoodnia et al. 2011).

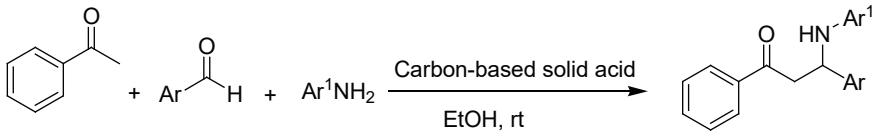

Figure 29. *Mannich reaction catalyzed by CBSA*

Hossein Eshghi et al. reported that $Fe(HSO_4)_3$-catalyzed three-component one-pot Mannich reaction of acetophenone with different aromatic aldehydes and aromatic amines in ethanol at ambient temperature. Short reaction time, good yield, easy work-up technique, and finally reusability of the catalyst show the worth of this paper (Hossein Eshghi et al. 2011).

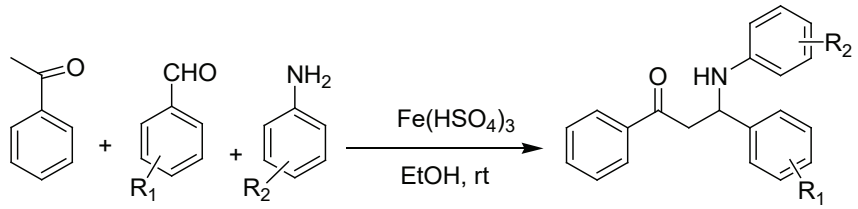

Figure 30. *β-aminocarbonyl compounds using ferric hydrogensulfate*

Mantu Rajbangshi et al. declared that iodine-alumina was employed as a catalyst in the coupling reactions under microwave irradiation to afford β-amino carbonyl compounds in excellent yields. This environmentally friendly methodology was possessed mild reaction conditions and less reaction time (Mantu Rajbangshi et al. 2011).

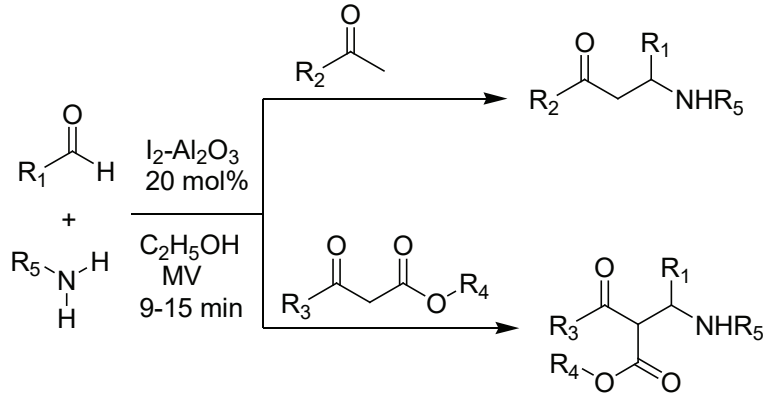

Figure 31. *One-pot three-component condensation*

Min Wang et al. published that an efficient three-component, one-pot synthesis of β-amino carbonyl compounds were described using tin tetrachloride at room temperature in ethanol. The advantages of the process are excellent yields, simple method, and cheap catalyst (Min Wang et al. 2011).

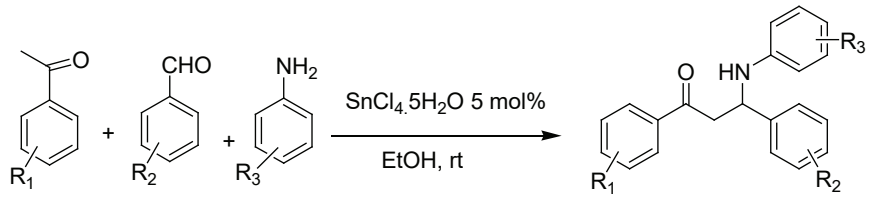

Figure 32. *Mannich reaction by $SnCl_4.5H_2O$*

Firouzeh Nemati et al. reported that three-component Mannich-type reaction of acetophenon, aromatic aldehydes, and aromatic amines is catalyzed by 2,4,6- trichloro[1,3,5]triazine at ambient temperature in EtOH and solvent-free conditions. The important properties of this procedure are good yield, use of cheap and non-hazardous catalyst, and simple procedure (Firouzeh Nemati et al.. 2010).

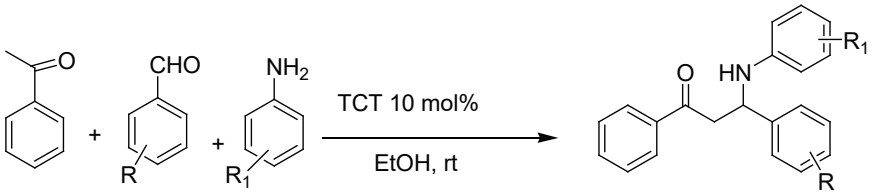

Figure 33. *Mannich reaction via TCT*

Deepak. M. Nagrik et al. declared that effective three-component condensation in the existence of MgO/ZrO_2 as an cheap and potent catalyst for the synthesis of β-amino carbonyl compounds by Mannich reaction was explained. The present methodology proposed several advantages, like good yields, short reaction times and a recyclable catalyst (Deepak. M. Nagrik et al. 2010).

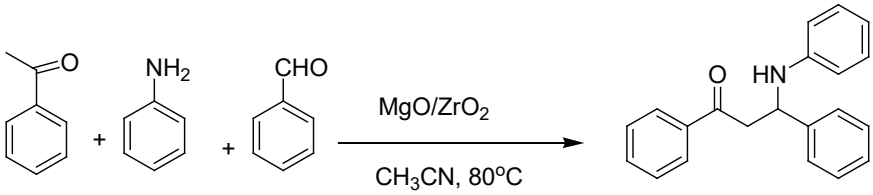

Figure 34. *Synthesis of β-amino carbonyl compounds*

REFERENCES

Abolghasem Davoodnia, Afsaneh Tavakoli-Nishaburi, and Niloofar Tavakoli-Hoseini (2011). Carbon-based Solid Acid Catalyzed One-pot Mannich Reaction: A Facile Synthesis of β Amino Carbonyl Compounds. *Bull. Korean Chem. Soc*. 32, 2, 635-638.

Ahmad Reza Massah, Roozbeh Javad Kalbasi, and Neda Samah (2011). Highly Selective Synthesis of β-Amino Carbonyl Compounds over ZSM-5-SO_3H under Solvent-free Conditions. *Bull. Korean Chem. Soc.* 32, 5, 1703-1708.

Ajeet A. Yelwande, Balasaheb R. Arbad, and Machhindra K. Lande (2011). Polyaniline/SiO_2 Catalyzed One-pot Mannich Reaction: An Efficient Synthesis of β-amino Carbonyl Compounds. *Journal of the Korean Chemical Society,* 55, 4, 644-649.

Ali Rahmatpour, Reza Eeimen and Niloofar Goodarzi (2019). Titanium tetrachloride incorporated crosslinked polystyrene copolymer as an efficient and recyclable polymeric Lewis acid catalyst for the synthesis of β-amino carbonyl compounds at room temperature. *Synthetic Communications*, 49, 21, 2915–2930.

Ali Maleki, Pedram Zand, Zahra Mohseni and Razieh Firouzi-Haji (2018). Green composite nanostructure (Fe_3O_4@PEG-SO_3H): Preparation, characterization and catalytic performance in the efficient synthesis of β-amino carbonyl compounds at room temperature. *Nano Structures & Nano-Objects,* 16, 31–37.

Amel Zetchi, Boudjemaa Boumoud, Taoues Boumoud and Abdelmadjid Debache (2016). PEG Mediated Eco-Friendly One Pot Synthesis of β-Amino Carbonyl Compounds under Ambient Temperature Conditions. *Der Pharma Chemica*, 8, 12, 84-87.

Bhupinder Kaur and Harish Kumar (2020). Ultrasound-Promoted One-Pot Three-Component Synthesis of β–Amino Carbonyl Compounds Using Manganese Perchlorate. *Organic Preparations and Procedures International*, 52, 5, 474–477.

Chao Huang, Yanqing Yin, Jiahui Guo, Jiong Wang, Baomin Fana and Lijuan Yang (2014). A facile synthesis of β-amino carbonyl compounds through an aza-Michael addition reaction under solvent-free conditions. *RSC Adv*., 4, 10188.

Deepak.M. Nagrik, D.M.Ambhore and Manoj.B. Gawande (2010). One-pot Preparation of β–amino Carbonyl Compounds by Mannich Reaction Using MgO/ZrO_2 as Effective and Reusable Catalyst. *International Journal of Chemistry,* 2, 2, 98-101.

Di Liu, Jingwei Zhang, Chi Zhang and Xiaoyan Kou (2015). One-pot synthesis of β-amino carbonyl compounds catalyzed silica supported phenylphosphinic acid. *Green Process Synth*.,4, 11–15.

Divya Sachdev, Amit Dubey, G. Robin Wilson and Ankita Sharma (2015). Mesoporous silica polymer nanocomposites encapsulated with polyphosphoric acid for the synthesis of β-amino carbonyl compounds under environmental benign conditions. *New J. Chem.*, 39, 2633.

Farhad Kabiri Esfahani, Daryoush Zareyee, Ali Shokuhi Rad andSima Taher-Bahrami (2017). Sulfonic acid supported on magnetic nanoparticle as an eco-friendly, durable and robust catalyst for the synthesis of β-amino carbonyl compounds through solvent free Mannich reaction. *Appl Organometal Chem.*31:e3865.

Firouzeh Nemati, Mohammad A. Bigdeli, Gholam Hossein Mahdavinia and Hossein Kian (2010). 2,4,6-trichloro[1,3,5]triazine (TCT)-catalyzed one-pot Mannich-type reaction. Three component synthesis of β-amino carbonyl compounds. *Green Chemistry Letters and Reviews,* 3, 2, 89-92.

Hasniye Yasa, Belma Hasdemir, Ozge Erken (2019). β-Amino Carbonyl Compounds from Iodine Catalyzed Three Component Mannich Reactions and Evaluation of Their Antioxidant Activity. *Organic Preparations and Procedures International*, 51, 6, 537-546.

Hasniye Yaşa and Kübra Demir (2019). $Bi(NO_3)_3{\cdot}5H_2O$-catalyzed Mannich Reaction: A Potent Catalyst for Synthesis of β-Aminocarbonyl Compounds. *JOTCSA*., 6, 3, 433-438.

Hossein Eshghi, Afsaneh Alipour, and Saman Damavandi (2011). Highly Efficient $Fe(HSO_4)_3$- Catalyzed One-Pot Mannich-Type Reactions: Three Component Synthesis of β-amino Carbonyl Compounds. *Synthesis and Reactivity in Inorganic, Metal-Organic, and Nano- Metal Chemistry*, 41, 3, 266-271.

Hua Qian, Wang Kai and Juejie Zhen (2016). Ultrasound-Promoted Synthesis of β-Amino Carbonyl Compounds via a Mannich Reaction Catalyzed by Ionic Liquids. *Letters in Organic Chemistry*, 13(2), 143-147.

Jaspreet Kaur Rajput, Gagandeep Kaur (2013). Bi(NO3)3·5H2O: an efficient and green catalyst for synthesis of 1,5-benzodiazepines and β-amino carbonyl compounds. *Asian Journal of Chemistry*, 25, 12, 6545-6549.

Javad Abedini-Torghabeh, Hossein Eshghi, Mehdi Bakavoli, Mohammad Rahimizadeh (2015). PPh_3-catalyzed Mannich reaction: a facile one-pot synthesis of b-amino carbonyl compounds under solvent-free conditions at room temperature. *Res Chem Intermed*, 41, 3649–3658.

Xi Cun Wang, Li Jia Zhang, Zhang Zhang, Zheng Jun Quan (2012). PEG-OSO_3H as an efficient and recyclable catalyst for the synthesis of b-amino carbonyl

compounds via the Mannich reaction in PEG–H_2O. *Chinese Chemical Letters,* 23, 423–426.

L. Satish K. Achary, Pratap S. Nayaka, Bapun Barik, Aniket Kumar, Priyabrat Dash (2020). Ultrasonic-assisted green synthes is of β-amino carbonyl compounds by copper oxide nanoparticles decorated phosphate functionalized graphene oxide via Mannich reaction. *Catalyst Today,*348,137-147.

Manmeet Kour & Satya Paul (2017). A green and convenient approach for the one-pot solvent-free synthesis of coumarins and b-amino carbonyl compounds using Lewis acid grafted sulfonated carbon@titania composite. Monatsh Chem., 148:327–337.

Mantu Rajbangshi, Md. Rumum Rohman, Icydora Kharkongor, Hormi Mecadon, and Bekington Myrboh (2011). Synthesis of β-Amino Carbonyl Compounds via the Iodine-Alumina Catalyzed Three-Component Coupling Reaction under Microwave Irradiation. *Organic Chemistry International,* 514620, 7 pp.

Min Wang, Zhiguo Song, and Yan Liang (2011). $SnCl_4.5H_2O$-Catalyzed Synthesis of β-Amino Carbonyl Compounds via a Direct Mannich-Type Reaction. *Preparative Biochemistry & Biotechnology (2011), 41(1), 1-6.*.

Pathakota Venkata Ramana, Kunda Uma Maheswara Rao, Balam Satheesh Krishna, Soora Harinath Jayaprakash, Shaik Ahammed Kabeer, Kaveti Sudheer and Cirandur Suresh Reddy (2015). Amberlyst-15: An Efficient and reusable heterogeneous catalyst for the synthesis of β-amino carbonyl compounds. *Org. Commun*. 8:4, 90-97.

Ram Singh, Geetika Bhasin, Geetanjali and Richa Srivastava (2014). An improved synthesis of β-amino carbonyl compounds using $FeCl_3$-silica gel. *J. Chem. Pharm. Res*., 6, 11, 776-781.

Sabahat Sardar, Erum Jabeen, Cecilia Devi Wilfred, Ahmad Sazali Hamzah, Jean-Marc Leveque (2020). Mechanistic studies on counter-ionic effects of camphorsulfonate-based ionic liquids on kinetics, thermodynamics and stereoselectivity of β-amino carbonyl compounds. Journal of *Molecular Liquids,* 320, 114370.

Santosh V. Goswami, Prashant B. Thorat, Avinash V. Chakrawar, Sudhakar R. Bhusare (2013). A mild and efficient one-pot synthesis of β-amino carbonyl compounds via Mannich reaction under ambient temperature condition. *Mol Divers,* 17, 33–40.

Santosh Kamble, Arjun Kumbhar, Gajanan Rashinkar, Madhuri Barge, Rajashri Salunkhe (2012). Ultrasound promoted efficient and green synthesis of β-amino carbonyl compounds in aqueous hydrotropic medium. *Ultrasonics Sonochemistry,* 19, 4, 812-815.

Sathesh Venkatesan, Natesan Sundaramoorthy Karthikeyan, Ravindranath S. Rathore, Periyasamy Giridharan, Kulathu Iyer Sathiyanarayanan (2014).

A mild and efficient one-pot three- component synthesis of anti-β-amino-carbonyl compounds catalyzed by NH_4OAc and their anticancer activities. *Medicinal Chemistry Research,* 23, 12, 5086-5101.

Susmita Saikia, Pinky Gogoi, Arup Kumar Dutta, Parishmita Sarma, Ruli Borah (2016). Design of multifaceted acidic 1,3-disulfoimidazolium chlorometallate ionic systems as heterogeneous catalysts for the preparation of -amino carbonyl compounds. *Journal of Molecular Catalysis A: Chemical,* 416, 63–72.

Vishvanath D. Patil, Nagesh R. Sutar and Ketan P. Patil (2016). Synthesıs of β-Amino Carbonyl Compounds and 5-Unsubstituted 3, 4-Dihydropyrimidinones Using Solid Supported $Co(ClO_4)_2$ Under Solvent Free Condition. *Acta Chim. Pharm. Indica*: 6(3), 72-79.

Yi Luan, Jie Yu, Xiaowei Zhang, Scott E. Schaus and Ge Wang (2014). Diastereoselective Three- Component Synthesis of β-Amino Carbonyl Compounds Using Diazo Compounds, Boranes, and Acyl Imines under Catalyst-Free Conditions. *J. Org. Chem*., 79, 4694−4698.

Zahra Maleki, Nahid Rasouli, Maryam Movahedi, Zahra Sadeghi (2016). An efficient and magnetically separable heteropoly acid catalyst for the synthesis of β-amino carbonyl compounds under solvent-free conditions. *Journal of Scientific and Engineering Research*, 3, 5, 192-202.

Chapter 5

NEW CHARACTERIZATIONS FOR THE SLANT HELICES OF A TIMELIKE CURVE DUE TO N-BISHOP ALTERNATIVE MODIFIED FRAME

Hatice KUŞAK SAMANCI[1]

Ayhan YILDIZ[2]

1 Doç.Dr.Hatice KUŞAK SAMANCI, Bitlis Eren Üniversitesi Fen Edebiyat Fakültesi Matematik Bölümü

2 Ayhan Yıldız, Bitlis Eren Üniversitesi Lisansüstü Eğitim Enstitüsü, Matematik ABD.

INTRODUCTION

In differential geometry, many types of alternative frames have been produced to examine the properties of the curves. One of these alternative frames is the Bishop frame which was constructed by Bishop in 1975. The Bishop frame which is parallel to the tangent vector is a more useful frame than the Serret-Frenet frame without the need for a second derivative, [1]. Also, if the principal normal vector field of the curve makes a constant angle with a fixed straight line, then the curve is called as a slant helix which was firstly defined by Izumiya and Takeuchi in 2004, [2]. The slant helix has important applications in many branches of science such as DNA structure and has also been used very widely in differential geometry. For example, Kula et al. analyzed some features of slant helix and spherical indicators in 2005 and 2010, [3,4]. In 2009, Bükçü and colleagues introduced slant helix due to Bishop frame, [5]. In 2008, Bükçü and Karacan studied some properties of slant helix due to Bishop frame in Minkowski space, [6, 7]. Bekar et al. worked on the slant helix and their acceleration centers in Euclidean and Minkowski space [8,9]. Moreover, Koçyiğit et al. worked on the Bishop Darboux vector for the timelike curves, and calculated some of their characterizations, [10]. For the first time, S. Yilmaz and his colleagues obtained a new alternative frame called type-2 Bishop frame in 2010 [11]. The authors also defined a type-2 Bishop frame in Minkowski space [11,12]. Furthermore, numerous articles have been published in the literature related to the type-2 Bishop frame, S.Kızıltuğ et al. studied some characterizations of the slant helix due to the type-2 Bishop frame in 2013, [13]. Firstly, Scofield introduced a new frame which includes the the vectors $\left\{\vec{N},\ \vec{C}=\vec{N}'\middle/\left\|\vec{N}'\right\|,\ \vec{W}=\tau\vec{T}+\kappa\vec{B}\middle/\left\|\kappa^2+\tau^2\right\|\right\}$, in 1995, [14]. Then, Uzunoğlu et al. defined a new slant helix called C-slant helix in 2016 [15]. Keskin et al. described a new alternative frame called N-Bishop frame based by modified frame $\left\{\vec{N},\vec{C},\vec{W}\right\}$, [16]. Then Samancı et al. developed the N-Bishop Darboux vector of a timelike curve, [17]. In this article, we examined some properties of the slant helices due to the N-Bishop frame of a timelike curve in the Minkowski-3 space. Some necessary and sufficient conditions to have a slant helix relative to the N-Bishop frame were given.

MATERIAL AND METHOD

A curve is said to be a helix if its unit tangent vector field makes a constant angle with a fixed direction. Similarly, a slant helix is a kind of helix in which the unit principal normal vector makes a constant angle with the fixed unit vector. In 1802, Lancret proved that a curve called a general helix when the ratio of curvature to torsion is constant. In 1975, Bishop found out a new alternative frame named Bishop frame which is relatively

parallel to the unit tangent field $\vec{T}$. The Bishop frame's derivative vector fields are

$$\vec{T}'(s)=k_1\vec{N}_1(s)+k_2\vec{N}_2(s),\quad \vec{N}_1'(s)=-k_1\vec{T}(s),\quad \vec{N}_2'(s)=-k_2\vec{T}(s)$$

where k_1 and k_2 are the first and second curvatures of the Bishop frame [1]. Moreover, the derivation vector fields of the Bishop frame for a timelike curve in Minkowski 3-space is $\vec{T}'=k_1\vec{N}_1+k_2\vec{N}_2$, $\vec{N}_1'=k_1\vec{T}$, $\vec{N}_2'=k_2\vec{T}$ where k_1 and k_2 are curvatures [5-7]. Yılmaz et al. introduced another Bishop frame called Type-2 Bishop frame in 2010. Type-2 Bishop frame is parallel to the binormal vector field, and the differentiation formulas of Type-2 Bishop frame are identified by

$$\vec{N}_1'(s)=-k_1\vec{B}(s),\quad \vec{N}_2'(s)=-k_2\vec{B}(s),\quad \vec{B}'(s)=k_1\vec{N}_1(s)+k_2\vec{N}_2(s)$$

where k_1 and k_2 are curvatures, [11,12]. Another alternative moving frame

$$\left\{\vec{N},\vec{C}=\vec{N}'\Big/\left\|\vec{N}'\right\|,\vec{W}=\tau\vec{T}+\kappa\vec{B}\Big/\left\|\kappa^2+\tau^2\right\|\right\}$$

which is parallel to the normal vector field is introduced by Scofield in 1995, [14]. The derivation formulas of the alternative moving frame $\left\{\vec{N},\vec{C},\vec{W}\right\}$ are computed by Uzunoğlu et al. as $\vec{N}'=f\vec{C}$, $\vec{C}'=-f\vec{N}+g\vec{W}$, $\vec{W}'=-g\vec{C}$ where the functions $f=\sqrt{\kappa^2+\tau^2}$ and $g=\kappa^2\left(\frac{\tau}{\kappa}\right)'\Big/\left(\kappa^2+\tau^2\right)=\sigma f$ are the differentiable, [15]. As a new alternative frame N-Bishop frame were first introduced by Keskin and Yaylı in 2017, [16]. The derivative vector fields of the N-Bishop frame is given by $\vec{N}'=k_1\vec{N}_1+k_2\vec{N}_2$, $\vec{N}_1'=-k_1\vec{N}$, $\vec{N}_2'=-k_2\vec{N}$. Furthermore, the N-Bishop frame of a timelike curve in Minkowski 3-space is studied on by Kusak Samancı. The derivative vector fields of the curve are

$$\vec{N}'=k_1\vec{N}_1-k_2\vec{N}_2,\ \vec{N}_1'=k_1\vec{N},\ \vec{N}_2'=k_2\vec{N},\qquad (2.1)$$

and its transition equations was given by

$$\vec{N},\ \vec{C}=\cosh\psi\vec{N}_1+\sinh\psi\vec{N}_2,\ \vec{W}=\sinh\psi\vec{N}_1+\cosh\psi\vec{N}_2$$

where $f=\sqrt{\kappa^2+\tau^2}=\sqrt{\left|k_2^2-k_1^2\right|}$ and $\psi(s)=\int_{s_0}^{s}\left(-g(t)\right)dt=-\tanh^{-1}\left(k_2/k_1\right)$. Since a curve α is a timelike curve, then T is timelike, N and B are spacelike, whereas $\left\langle\vec{T},\vec{T}\right\rangle_L=-1,\left\langle\vec{N},\vec{N}\right\rangle_L=1,\left\langle\vec{B},\vec{B}\right\rangle_L=1$. For the adapted N-Bishop frame

of the timelike curve $\vec{N}$, $\vec{N}_1$, $\vec{N}_2$ are spacelike, timelike and spacelike, respectively. Furthermore, the vectors satisfy the following equations $\left\langle \vec{N}, \vec{N} \right\rangle_L = 1, \left\langle \vec{N}_1, \vec{N}_1 \right\rangle_L = -1, \left\langle \vec{N}_2, \vec{N}_2 \right\rangle_L = 1$ and

$\vec{N} \times_L \vec{N}_1 = \vec{N}_2, \vec{N}_1 \times_L \vec{N}_2 = \vec{N}, \vec{N}_2 \times_L \vec{N} = -\vec{N}_1$, [17].

MAIN RESULTS

Definition 3.1. Let a curve $\xi : \mathrm{I} \to \mathrm{E}_1^3$ be a unit speed timelike curve in Minkowski 3-space with $\xi \neq 0$. If the vector field $\vec{N}_1$ makes a constant angle φ with a fixed certain direction u in Minkowski 3-space, then ξ is called a timelike slant helix due to N-Bishop frame $\left\{ \vec{N}, \vec{N}_1, \vec{N}_2 \right\}$, that is $\langle \vec{N}_1(s), \vec{u} \rangle = \cosh \varphi$.

Theorem 3.2. Suppose that $\xi : \mathrm{I} \to \mathrm{E}_1^3$ is a slant helix of a unit speed timelike curve. The timelike curve ξ is a timelike slant helix necessary and sufficient condition if the ratio of the curvatures k_1 and k_2 satisfy the condition k_1 / k_2 is constant.

Proof. Let the timelike curve ξ be a timelike slant helix of a in E_1^3. Then $\vec{N}_1$ holds the condition $\langle \vec{N}_1, \vec{u} \rangle = \cosh \varphi$ (const), where φ is constant angle for $\forall s \in \mathrm{I}$. Calculating the derivation of $\langle \vec{N}_1, \vec{u} \rangle = \cosh \varphi$, we obtain $\langle \vec{N}, \vec{u} \rangle = 0$. Now if the derivation of $\langle \vec{N}, \vec{u} \rangle = 0$ is calculated, we found also the equation $\langle \vec{N}', \vec{u} \rangle = 0$. By substituting the Eq. (2.1) in this equation, we get the $\langle k_1 \vec{N}_1 - k_2 \vec{N}_2, \vec{u} \rangle = 0$ and $k_1 / k_2 = \tanh \varphi \ (const.)$. If $\langle \vec{N}, \vec{u} \rangle = 0$, then the vector $\vec{u} \in s_p \left\{ \vec{N}_1, \vec{N}_2 \right\}$ is written with a linear combination of a timelike vector $\vec{N}_1$ and spacelike vector $\vec{N}_2$ as

$$\vec{u} = (-\cosh \varphi) \vec{N}_1 + (\sinh \varphi) \vec{N}_2. \tag{3.1}$$

By differentiation of the Equation (3.1), we get

$$\vec{u}' = (-\cosh \varphi) \vec{N}_1' + (\sinh \varphi) \vec{N}_2' = \left[-k_1 (\cosh \varphi) + k_2 (\sinh \varphi) \right] \vec{N} = 0.$$

If the derivation is obtain zero, then $\vec{u}$ is a constant vector.

Conversely, assume that k_1/k_2 is constant. So that the ratio can be rewritten as $k_1/k_2=\lambda$ where the coefficient can be taken as $\lambda=\tanh\varphi$. Thanks to this equation, we have $k_1/k_2=\tanh\varphi$, $k_1(\cosh\varphi)-k_2(\sinh\varphi)=0$. Then from Eq.(3.1), it is shown that the vector $\vec{u}$ is constant and the inner product $\langle\vec{N}_1,\vec{u}\rangle$ is constant. From Eq.(3.1), we get $\langle\vec{N}_1,\vec{u}\rangle=\cosh\varphi.$ Then one can easily see that ξ is a timelike slant helix. Finally, the theorem is proven.

Theorem 3.3. Assume that $\xi:\mathrm{I}\to\mathrm{E}_1^3$ be a unit speed timelike curve due to the N-Bishop frame with the curvatures k_1 and k_2. The curve ξ is a slant helix necessary and sufficient condition $\det\left(\vec{N}_1',\vec{N}_1'',\vec{N}_1'''\right)=0$.

Proof. Assume that the curve ξ is a slant helix of a timelike curve in Minkowski 3-space. Thus the ratio k_1/k_2 is constant. Taking the derivation of $\vec{N}_1$ in the Eq. (2.1), we have $\vec{N}_1''=k_1'\vec{N}+k_1^{\,2}\vec{N}_1-k_1k_2\vec{N}_2$ and the third derivative of $\vec{N}_1$ is obtained by

$$\begin{aligned}\vec{N}_1'''&=2k_1k_1'\vec{N}_1+k_1^{\,2}(k_1\vec{N})+k_1''\vec{N}+k_1'(k_1\vec{N}_1-k_2\vec{N}_2)\\&\quad-k_1'k_2\vec{N}_2-k_2'k_1\vec{N}_2-k_1k_2(k_2\vec{N})\\&=(k_1^{\,3}+k_1''-k_1k_2^{\,2})\vec{N}+(3k_1k_1')\vec{N}_1+(-2k_1'k_2-k_2'k_1)\vec{N}_2.\end{aligned}$$

In this way, the equation is calculated as $\det\left(\vec{N}_1',\vec{N}_1'',\vec{N}_1'''\right)=k_1^{\,3}k_2^{\,2}\left[k_1/k_2\right]'$. It is well known that if ξ is a slant helix, then the ratio of curvatures k_1/k_2 is constant. So we have $\left[k_1/k_2\right]'=0$. Hereby, the outcome is obtained as $\det\left(\vec{N}_1',\vec{N}_1'',\vec{N}_1'''\right)=0.$ Otherwise, suppose that $\det\left(\vec{N}_1',\vec{N}_1'',\vec{N}_1'''\right)=0$. Since the determination can be written as $\det\left(\vec{N}_1',\vec{N}_1'',\vec{N}_1'''\right)=k_1^{\,3}k_2^{\,2}\left[k_1/k_2\right]'=0$ where $k_1\neq0$ and $k_2\neq0$, by the simplification of this equation we obtain $\left[k_1/k_2\right]'=0$ and $k_1/k_2=\text{const.}$ Therefore the timelike curve ξ is a slant helix.

Theorem 3.4. Suppose that the curve $\xi : \mathrm{I} \to \mathrm{E}^3$ is a unit speed timelike curve in Minkowski 3-space. The curve ξ is timelike a slant helix if and only if $\det\left(\vec{N}_2', \vec{N}_2'', \vec{N}_2'''\right) = 0.$

Proof. The proof is analogous to the proof of Theorem 3.3.

Theorem 3.5. Let the unit speed curve $\xi : \mathrm{I} \to \mathrm{E}^3$ be a timelike curve in Minkowski 3-space. The timelike curve ξ is a slant helix necessary and sufficient condition is $\det\left(\vec{N}', \vec{N}'', \vec{N}'''\right) = 0$.

Proof. Let ξ be a timelike slant helix in Minkowski 3-space. The first, second and third differentiations of N in Eq. (2.1) are

$$\vec{N}' = k_1\vec{N}_1 - k_2\vec{N}_2, \quad \vec{N}'' = (k_1^2 - k_2^2)\vec{N} + k_1'\vec{N}_1 - k_2'\vec{N}_2,$$

$$\vec{N}''' = (3k_1k_1' - 3k_2k_2')\vec{N} + (k_1'' + k_1^3 - k_1k_2^2)\vec{N}_1 + (-k_2'' - k_1^2k_2 + k_2^3)\vec{N}_2.$$

The determinant of the first, second and third differentiations can be

$$\det\left(\vec{N}', \vec{N}'', \vec{N}'''\right) = \left(3k_1k_2^2k_1' - 3k_2^3k_2'\right)\left(\frac{k_1}{k_2}\right)'$$

compute by

$$-\left[\left(\frac{k_1}{k_2}\right)^2 - 1\right]\left[\left(\frac{k_1}{k_2}\right)'' k_2^4 + 2k_2^3k_2'\left(\frac{k_1}{k_2}\right)'\right].$$

(3.2)

As we know that ξ is a timelike slant helix, then the ratio of the curvatures is constant. Therefore, we get $\left[k_1/k_2\right]' = 0$. Also it is seen that from the Eq. (3.2) is zero. Otherwise, suppose that $\det\left(\vec{N}', \vec{N}'', \vec{N}'''\right) = 0$. Then, using the above equation, we have $\left[k_1/k_2\right]' = 0$ and $k_1/k_2 = \text{const.}$ Then it is said to be ξ is a timelike slant helix. Then the proof is finished. Now, assume that ξ is a slant helix parameterized by the unit speed parameter on a Minkowski space. N-Bishop frame's covariant differentiation due to the tangent vector $\alpha'(s) = T$ is computed by

$$D_T\vec{N} = k_1\vec{N}_1 - k_2\vec{N}_2, D_T\vec{N}_1 = k_1\vec{N}, D_T\vec{N}_2 = k_2\vec{N}. \qquad (3.3)$$

where $\vec{N}_1(s)$ and $\vec{N}_2(s)$ are two N-Bishop vector fields, k_1 and

k_2 are the curvature functions of the curve with each $s \in \mathrm{I}$ parameters.

Theorem 3.6. Assume that the curve $\xi : \mathrm{I} \to \mathrm{E}_1^3$ is a unit speed timelike curve in Minkowski 3-space and the N-Bishop frame curvatures of the curve are denoted by k_1 and k_2. The curve ξ is a timelike slant helix if and only if the following equation is provided

$$D_T(D_T D_T \vec{N}_1) = D_T \vec{N}_1 (\frac{k_1''}{k_1} - k_2^2 + k_1^2) + 3k_1' D_T \vec{N}. \tag{3.4}$$

Proof. If the curve ξ is taken as a slant helix, using the Eq. (3.4) and (3.3) the covariant differentiation of $D_T \vec{N}_1$ is obtained by

$$D_T(D_T \vec{N}_1) = D_T(k_1 \vec{N}) = k_1' \vec{N} + k_1^2 \vec{N}_1 - k_1 k_2 \vec{N}_2, \tag{3.5}$$

Also the covariant derivatation of above equation is computed by

$$\begin{aligned} D_T(D_T D_T \vec{N}_1) &= D_T(k_1' \vec{N} + k_1^2 \vec{N}_1 - k_1 k_2 \vec{N}_2), \\ &= k_1'' \vec{N} + k_1' D_T \vec{N} + 2k_1 k_1' \vec{N}_1 - (k_1' k_2 + k_1 k_2') \vec{N}_2 \\ &\quad - k_1 k_2 (k_2 \vec{N}) + k_1^2 D_T \vec{N}_1. \end{aligned} \tag{3.6}$$

From the Eq.(3.6), it is easy to say that the ratio k_1/k_2 is constant. From the equation $(k_1/k_2)' = 0$, we have $k_1' k_2 = k_1 k_2'$. Moreover, from the Eq. (3.3), the equation $N = \frac{1}{k_1} D_T \vec{N}_1$ is found. Now, by substituting these equations in the Eq.(3.6), then the third covariant differentiation of $\vec{N}_1$ is obtained by

$$D_T(D_T D_T \vec{N}_1) = k_1'' \vec{N} - k_1 k_2^2 \vec{N} + k_1' D_T \vec{N} + 2k_1' \left(\underbrace{k_1 \vec{N}_1 - k_2 \vec{N}_2}_{D_T \vec{N}} \right) + k_1^2 D_T \vec{N}_1,$$

$$= D_T \vec{N}_1 (\frac{k_1''}{k_1} - k_2^2 + k_1^2) + 3k_1' D_T \vec{N}.$$

On the other hand, let's suppose that the equality is satisfied in (3.4). Now, we will prove that ξ is a timelike slant helix. From the first and second covariant derivation of (3.8), we get

$$D_T \vec{N} = -\frac{k_1'}{k_1^2} D_T \vec{N}_1 + \frac{1}{k_1} D_T D_T \vec{N}_1.$$

$$D_T D_T \vec{N} = -\left(\frac{k_1'}{k_1^2}\right)' D_T \vec{N}_1 - \frac{k_1'}{k_1^2} D_T D_T \vec{N}_1 - \frac{k_1'}{k_1^2} D_T D_T \vec{N}_1 + \frac{1}{k_1} D_T D_T D_T \vec{N}_1. \quad (3.7)$$

By substituting (3.4) in (3.7), the covariant derivative can also be computed by

$$\begin{aligned} D_T D_T \vec{N} &= -\left(\frac{k_1'}{k_1^2}\right)' D_T \vec{N}_1 - \frac{k_1'}{k_1^2} D_T D_T \vec{N}_1 - \frac{k_1'}{k_1^2} D_T D_T \vec{N}_1 \\ &\quad + \frac{1}{k_1}\left(D_T \vec{N}_1 \left(\frac{k_1''}{k_1} - k_2^2 + {k_1}^2\right) + 3k_1' D_T \vec{N} \right) \\ &= \left(-\left(\frac{k_1'}{k_1^2}\right)' + \frac{k_1''}{k_1^2} - \frac{k_2^2}{k_1} + k_1 \right) D_T \vec{N}_1 \\ &\quad - \frac{2k_1'}{k_1^2} D_T D_T \vec{N}_1 + \frac{3k_1'}{k_1} D_T \vec{N}. \end{aligned}$$

By replacing the Eq (3.5) and Eq.(3.3) in the above equation and make the necessary arrangements, then we have

$$\begin{aligned} D_T D_T \vec{N} &= \left(-\left(\frac{k_1'}{k_1^2}\right)' + \frac{k_1''}{k_1^2} - \frac{k_2^2}{k_1} + k_1 \right) D_T \vec{N}_1 \\ &\quad - \frac{2k_1'}{k_1^2}\left(k_1' \vec{N} + {k_1}^2 \vec{N}_1 - k_1 k_2 \vec{N}_2 \right) + \frac{3k_1'}{k_1}\left(k_1 \vec{N}_1 - k_2 \vec{N}_2 \right) \\ &= \left(-\left(\frac{k_1'}{k_1^2}\right)' + \frac{k_1''}{k_1^2} - \frac{k_2^2}{k_1} + k_1 \right) D_T \vec{N}_1 + k_1' \vec{N}_1 - \frac{k_1' k_2}{k_1} \vec{N}_2 - \frac{2(k_1')^2}{k_1^2} \vec{N}. \end{aligned} \quad (3.8)$$

Otherwise, using the Eq.(3.3), the second covariant derivative $D_T D_T \vec{N}$ can also be found by

$$D_T D_T \vec{N} = k_1' \vec{N}_1 + k_1 D_T \vec{N}_1 - k_2' \vec{N}_2 - k_2^2 \vec{N}. \quad (3.9)$$

Now, by equating (3.8) and (3.9), we get $\frac{k_1' k_2}{k_1} = k_2'$. Then after some arrangements, we get $\left(k_1/k_2\right)' = 0$. This result shows that k_1/k_2 is constant. Therefore the curve ξ is a timelike slant helix.

Theorem 3.7. Assume that $\xi : \mathrm{I} \to \mathrm{E}_1^3$ is a unit speed timelike curve

in a Minkowski 3-space. The timelike curve ξ is a slant helix neccessary and sufficient condition is

$$D_T(D_T D_T \vec{N}_2) = D_T \vec{N}_2 (\frac{k_2''}{k_2} - k_2^2 + k_1^{\,2}) - 3k_2' D_T \vec{N}.$$

Proof. Let ξ be a slant helix of a timelike curve in Minkowski 3-space. Using Eq.(3.3), the second covariant differentiation of $\vec{N}_2$ is obtained $D_T(D_T \vec{N}_2) = k_2{}' \vec{N} + k_1 k_2 \vec{N}_1 - k_2^2 \vec{N}_2$. Moreover, the third covariant derivatation is obtained by

$$\begin{aligned} D_T(D_T D_T \vec{N}_2) &= D_T(k_2{}' \vec{N} + k_1 k_2 \vec{N}_1 - k_2^2 \vec{N}_2) \\ &= k_2{}'' \vec{N} + k_1^2 k_2 \vec{N} + k_2{}' D_T \vec{N} + 2k_2' \underbrace{(k_1 \vec{N}_1 - k_2 \vec{N}_2)}_{D_T \vec{N}} - k_2^2 D_T \vec{N}_2 \\ &= (k_2'' + k_1^2 k_2)\vec{N} - k_2^2 D_T \vec{N}_2 + 3k_2' D_T \vec{N}. \end{aligned}$$

Using the equation $N = \frac{1}{k_2} D_T \vec{N}_2$, the third covariant derivatation can be written as

$$\begin{aligned} D_T(D_T D_T \vec{N}_2) &= (k_2'' + k_1^2 k_2)(\frac{1}{k_2} D_T \vec{N}_2) - k_2^2 D_T \vec{N}_2 + 3k_2' D_T \vec{N} \\ &= D_T \vec{N}_2 (\frac{k_2''}{k_2} - k_2^2 + k_1^{\,2}) - 3k_2' D_T \vec{N}. \end{aligned}$$

Therefore the theorem is proven. Moreover, the sufficient condition can be similarly proven.

Theorem 3.8. Let $\xi : \mathrm{I} \to \mathrm{E}_1^3$ be a unit speed timelike curve in Minkowski 3-space. The curve ξ is a slant helix if and only if the equalities

i. $D_T(D_T D_T \vec{N}) = D_T \vec{N} \left(\frac{k_1''}{k_1} + k_1^2 - k_2^2 \right) + 3k_1' D_T \vec{N}_1 - 3k_2' D_T \vec{N}_2$

ii. $D_T(D_T D_T \vec{N}) = D_T \vec{N} \left(\frac{k_2''}{k_2} + k_1^2 - k_2^2 \right) + 3k_1' D_T \vec{N}_1 - 3k_2' D_T \vec{N}_2$

iii.

$$D_T(D_T D_T \vec{N}) = D_T \vec{N} \left(\frac{k_1''}{2k_1} + \frac{k_2''}{2k_2} + k_1^2 - k_2^2 \right) + 3k_1' D_T \vec{N}_1 - 3k_2' D_T \vec{N}_2$$

are separately provided.

Proof. Let ξ be a timelike slant helix in Minkowski 3-space. By substituting the covariant differentiation of $\vec{N}$ in Eq.(3.3), we found the equation as

$$\begin{aligned} D_T(D_T\vec{N}) &= D_T(k_1\vec{N}_1 - k_2\vec{N}_2) \\ &= k_1'\vec{N}_1 + k_1 D_T\vec{N}_1 - k_2'\vec{N}_2 - k_2 D_T\vec{N}_2 \\ &= k_1^2\vec{N} - k_2^2\vec{N} + k_1'\vec{N}_1 - k_2'\vec{N}_2. \end{aligned}$$

Differentiating the Eq.(3.3) again, we get

$$\begin{aligned} D_T(D_T D_T\vec{N}) &= D_T(k_1^2\vec{N} - k_2^2\vec{N} + k_1'\vec{N}_1 - k_2'\vec{N}_2) \\ &= 3k_1' D_T\vec{N}_1 - 3k_2' D_T\vec{N}_2 + D_T\vec{N}(k_1^2 - k_2^2) + k_1''\vec{N}_1 - k_2''\vec{N}_2. \end{aligned}$$

It is known that if ξ is slant helix, then the fraction k_1/k_2 is constant. Thus we get $\left(k_1/k_2\right)' = 0$ and then $k_1'/k_2' = k_1/k_2$. Because k_1/k_2 is constant, then k_1'/k_2' is constant. Also the properties $k_1''k_2' = k_1'k_2''$ and $k_1''/k_2'' = k_1'/k_2'$ can be obtained from the differentiation. As a result, $k_1''/k_2'' = k_1'/k_2' = k_1/k_2$ and $k_1''/k_1 = k_2''/k_2 = a$ are computed. Moreover, the phrase $k_1''\vec{N}_1 - k_2''\vec{N}_2$ can be denoted by

$$\begin{aligned} k_1''\vec{N}_1 - k_2''\vec{N}_2 &= \frac{k_1''}{k_1}k_1\vec{N}_1 - \frac{k_2''}{k_2}k_2\vec{N}_2 \\ &= a(k_1\vec{N}_1 - k_2\vec{N}_2) \\ &= aD_T\vec{N}. \end{aligned}$$

Consequently, the results are found as $k_1''\vec{N}_1 - k_2''\vec{N}_2 = \frac{k_1''}{k_1}D_T\vec{N}$ or $k_1''\vec{N}_1 - k_2''\vec{N}_2 = \frac{k_2''}{k_2}D_T\vec{N}$. Another characterizations can be also calculated by

$$\begin{aligned} D_T(D_T D_T\vec{N}) &= D_T\vec{N}(k_1^2 - k_2^2) + \frac{k_1''}{k_1}D_T\vec{N} + 3k_1' D_T\vec{N}_1 - 3k_2' D_T\vec{N}_2 \\ &= D_T\vec{N}\left(\frac{k_1''}{k_1} + k_1^2 - k_2^2\right) + 3k_1' D_T\vec{N}_1 - 3k_2' D_T\vec{N}_2, \end{aligned}$$

and also can be written by

$$D_T(D_T D_T \vec{N}) = D_T \vec{N}(k_1^2 - k_2^2) + \frac{k_2''}{k_2} D_T \vec{N} + 3k_1' D_T \vec{N}_1 - 3k_2' D_T \vec{N}_2$$

$$= D_T \vec{N}\left(\frac{k_2''}{k_2} + k_1^2 - k_2^2 \right) + 3k_1' D_T \vec{N}_1 - 3k_2' D_T \vec{N}_2.$$

On the other hand, using the equality of

$k_1'' \vec{N}_1 - k_2'' \vec{N}_2 = D_T \vec{N}\left(\frac{k_1''}{2k_1} + \frac{k_2''}{2k_2} \right)$ we can get following characterization

$$D_T(D_T D_T \vec{N}) = D_T \vec{N}(k_1^2 - k_2^2) + D_T \vec{N}\left(\frac{k_1''}{2k_1} + \frac{k_2''}{2k_2} \right) + 3k_1' D_T \vec{N}_1 - 3k_2' D_T \vec{N}_2$$

$$= D_T \vec{N}\left(\frac{k_1''}{2k_1} + \frac{k_2''}{2k_2} + k_1^2 - k_2^2 \right) + 3k_1' D_T \vec{N}_1 - 3k_2' D_T \vec{N}_2.$$

The sufficent condition can be proven similarly.

Acknowledgement

A short part of the paper has been presented the conference 16th International Geometry Symposium in Turkey. Furthermore, the manuscript is included in the master thesis of the second author supervisied by the first author. The authors thank to the referee for the precious comments and suggestions.

REFERENCES

1. R.L. Bishop, “There is more than one way to frame a curve”, The American Mathematical Monthly, 82(3), 246-251,1975.
2. S. Izumiya and N. Takeuchi, “New special curves and developable surfaces”, Turkish Journal of Mathematics, 28(2), 153-164, 2004.
3. L. Kula, N. Ekmekci, Y. Yaylı and K. İlarslan, “Characterizations of slant helices in Euclidean 3-space”, Turkish Journal of Mathematics, 34(2), 261-274, 2010.
4. L. Kula and Y. Yaylı, “On slant helix and its spherical indicatrix”, Applied Mathematics and Computation, 169(1), 600-607, 2005.
5. B. Bükcü and M.K. Karacan, “The slant helices according to Bishop frame”, International Journal of Computational and Mathematical Sciences, 3(2), 67-70, 2009.
6. B. Bükcü and M.K. Karacan, “Bishop frame of the spacelike curve with a spacelike principal normal in Minkowski 3-space”, Commun. Fac. Sci. Univ. Ank. Sér. A1 Math. Stat., 57(1), 13-22, 2008.
7. M.K. Karacan, “Bishop frame of the timelike curve in Minkowski 3-space”, SDÜ Fen Edebiyat Fakültesi Fen Dergisi, 3(1), 2008.
8. M. Bekar and Y. Yaylı, “Slant helix curves and acceleration centers in Minkowski 3-Space E_3^1”, Journal of Advanced Physics, 6(1), 133-141, 2017.
9. M. Bekar, and Y. Yaylı, “Slant helix curves and acceleration centers”, Gazi University Journal of Science, 32(1), 256-271, 2019.
10. H. Kocayiğit, A. Özdemir, M. Çetin and S.Ö. Asartepe, “Characterizations of timelike curves according to the Bishop Darboux vector in Minkowski 3-Space”, 3. International Mathematical Forum, (8)19, 903-911, 2013.
11. S. Yılmaz, E. Özyılmaz, and M. Turgut, “New spherical indicatrices and their characterizations”, An. St. Univ. Ovidius Constanta, 18(2), 337-354, 2010.
12. S. Yilmaz, and Y. Ünlütürk, “A note on spacelike curves according to type-2 Bishop frame in Minkowski 3-space E_3^1”, Int. J. Pure Appl Math, 103(2), 321-332, 2015.
13. S. Kızıltuğ, S. Kaya and Ö. Tarakçı, “Slant helices according to type-2 Bishop frame in Euclidean 3-space”, Int. Journal of Pure and Applied Mathematics, 85, 211-222, 2013.
14. P.D. Scofield, “Curves of constant precession”, The American Mathematical Monthly, 102(6), 531-537, 1995.
15. B. Uzunoğlu, İ. Gök and Y. Yaylı, “A new approach on curves of constant precession”, Applied Mathematics and Computation, 275, 317-323, 2016.
16. O. Keskin and Y. Yaylı, “An application of N-Bishop frame to spherical

images for direction curves", International Journal of Geometric Methods in Modern Physics, 14(11), 1750162, 2017.
17. H. Kuşak Samancı, "N-Bishop Darboux Vector of a Timelike curve in Minkowski 3-space", Journal of Science and Arts, 3(52), 2020.

Chapter 6

ON NEW SPINOR EQUATIONS

Nevin GÜRBÜZ[1]

1 Prof. Dr. Eskişehir Osmangazi University, Mathematics- Computer Department, ngurbuz@ogu.edu.tr

INTRODUCTION

Spinors are used in many fields of mathematics and physics . In physics, spinors are used to describe the intrinsic angular momentum or spin of electron and fermision.

The relation between spinors and the Lorentz groups has been presented by Dirac (Dirac, 1974). Recently many authors studied spinor equations for diverse frames (Castillo, 2004; Ünal et al., 2013; Kişi and Tosun, 2015; Ketenci et al., 2015; Erisir et al., 2015; Balci et al., 2015)

Some concepts relation to this chapter are presented :

Minkowski 3-space R_1^3 is given with the metric as the following:

$$\langle , \rangle = dx_1^2 + dx_2^2 - dx_3^2 .$$

For any vector $x = (x_1, x_2, x_3)$ in R_1^3 ,

if $\langle x, x \rangle > 0$, x is spacelike vector, if $\langle x, x \rangle < 0$, x is timelike vector. Spacelike or timelike curves are called as nonnull curves (O'Neill, 1983).

The derivative formulas of Frenet frame $\{T, n, b\}$ for $\beta : I \subset R \to R_1^3$ nonnull curve are

$$\begin{pmatrix} T_s \\ n_s \\ b_s \end{pmatrix} = \begin{pmatrix} 0 & \varepsilon_2 \kappa & 0 \\ -\varepsilon_1 \kappa & 0 & \varepsilon_3 b \\ 0 & -\varepsilon_2 \tau & 0 \end{pmatrix} \begin{pmatrix} T \\ n \\ b \end{pmatrix} \qquad (1)$$

where s is arclength parameter. Also

$$\langle T, T \rangle = \varepsilon_1 = \pm 1, \quad \langle n, n \rangle = \varepsilon_2 = \pm 1, \quad \langle b, b \rangle = \varepsilon_3 = \pm 1.$$

respectively, the tangent, normal and binormal vector fields are T , n and b .

Let $\{T, Q, N\}$ be the Darboux frame on oriented nonnull surface M in R_1^3 . T is the tangent vector field, N is the unit normal vector of non-nonnull curve β on nonnull surface M. The binormal vector field B is

given by $B = \varepsilon_2 T \times N$. The Frenet formulas of Darboux frame $\{T, Q, N\}$ are given by

$$\begin{pmatrix} T_s \\ Q_s \\ N_s \end{pmatrix} = \begin{pmatrix} 0 & \varepsilon_2 k_g & \varepsilon_3 k_n \\ -\varepsilon_1 k_g & 0 & \varepsilon_3 \tau_g \\ -\varepsilon_1 k_n & -\varepsilon_2 \tau_g & 0 \end{pmatrix} \begin{pmatrix} T \\ Q \\ N \end{pmatrix} \tag{2}$$

where

$$T \times Q = \varepsilon_3 N,\ Q \times N = \varepsilon_1 T, N \times T = \varepsilon_2 Q,$$

$$\langle T, T \rangle = \varepsilon_1 = \pm 1, \quad \langle Q, Q \rangle = \varepsilon_2 = \pm 1, \quad \langle N, N \rangle = \varepsilon_3 = \pm 1.$$

Consider the Bishop frame $\{T, N_1, N_2\}$ of a pseudo null curve β in R_1^3 satisfying (Grbovic and Nesovic, 2018):

$$\langle T_1, T_1 \rangle = \langle N_1, N_2 \rangle = 1, \quad \langle N_1, N_1 \rangle = \langle N_2, N_2 \rangle = \langle T_1, N_1 \rangle = \langle T_1, N_2 \rangle = 0 \tag{3}$$

where T_1 is the unit tangent vector field, N_1 and N_2 are two relatively parallel null normal vector fields. Connection between the Bishop frame $\{T, N_1, N_2\}$ and the Frenet frame $\{T, n, b\}$ of pseudo null curve are given by

$$\begin{pmatrix} T_1 \\ N_1 \\ N_2 \end{pmatrix} = \begin{pmatrix} 1 & 0 & 0 \\ 0 & \dfrac{1}{k_1} & 0 \\ 0 & 0 & k_2 \end{pmatrix} \begin{pmatrix} T \\ n \\ b \end{pmatrix} \tag{4}$$

The Frenet equations of the Bishop frame $\{T, N_1, N_2\}$ are given by

$$\begin{pmatrix} T_{1s} \\ N_{1s} \\ N_{2s} \end{pmatrix} = \begin{pmatrix} 0 & k_2 & k_2 \\ -k_1 & 0 & 0 \\ -k_2 & 0 & 0 \end{pmatrix} \begin{pmatrix} T_1 \\ N_1 \\ N_2 \end{pmatrix} \tag{5}$$

where s is pseudo arclength parameter, k_1 and k_2 are curvatures of $\{T, N_1, N_2\}$ frame (Grbovic and Nesovic, 2018).

Let $\{\mathcal{T},\mathcal{N},\mathcal{B}\}$ be the Frenet frame in pseudo-Galilean 3-space satisfying

. $$\mathcal{T} = \rho T\,,\quad \mathcal{N} = \rho n\,,\quad \mathcal{B} = \rho b$$

where ρ is the radius of the curve β. The equiform curvature and torsion are

$$\widetilde{\kappa} = \rho, \qquad \widetilde{\tau} = \rho\tau = \frac{\tau}{\kappa}.$$

The Frenet formulas in the equiform geometry of pseudo Galilean 3-space G_1^3 are presented as the following (Erjavec and Dvjak, 2008):

$$\begin{pmatrix}\mathcal{T}_\sigma\\ \mathcal{N}_\sigma\\ \mathcal{B}_\sigma\end{pmatrix}=\begin{pmatrix}\tilde{\kappa} & 1 & 0\\ 0 & \tilde{\kappa} & \tilde{\tau}\\ 0 & \tilde{\tau} & \tilde{\kappa}\end{pmatrix}\begin{pmatrix}\mathcal{T}\\ \mathcal{N}\\ \mathcal{B}\end{pmatrix} \tag{6}$$

where σ is an equiform invariant parameter.

The equiform diferential geometry of the simple isotropic space $I_3^{(1)}$ has been studied by Pavkovic (Pavkovic, 1986). The derivative formulas of Frenet frame $\{\mathcal{T},\mathcal{N},\mathcal{B}\}$ according to equiform geometry of $I_3^{(1)}$ have the following form

$$\begin{pmatrix}\mathcal{T}_\sigma\\ \mathcal{N}_\sigma\\ \mathcal{B}_\sigma\end{pmatrix}=\begin{pmatrix}\tilde{\kappa} & 1 & 0\\ -1 & \tilde{\kappa} & \tilde{\tau}\\ 0 & 0 & \tilde{\kappa}\end{pmatrix}\begin{pmatrix}\mathcal{T}\\ \mathcal{N}\\ \mathcal{B}\end{pmatrix} \tag{7}$$

where σ is an equiform invariant parameter defined by $\sigma = \int \frac{ds}{\rho}$.

The derivative formulas of Frenet frame $\{\mathcal{T},\mathcal{N},\mathcal{B}\}$ of the double isotropic space $I_3^{(2)}$ have the following form (Pavkovic, 1986) :

$$\begin{pmatrix} \mathcal{T}_\sigma \\ \mathcal{N}_\sigma \\ \mathcal{B}_\sigma \end{pmatrix} = \begin{pmatrix} \tilde{\kappa} & 1 & 0 \\ 0 & \tilde{\kappa} & \tilde{\tau} \\ 0 & 0 & \tilde{\kappa} \end{pmatrix} \begin{pmatrix} \mathcal{T} \\ \mathcal{N} \\ \mathcal{B} \end{pmatrix} \tag{8}$$

The vector $\eta = (\eta_1, \eta_2, \eta_3)$ consisting of hyperbolic symmetric matrices is given by (Pauli,1927)

$$\eta_1 = \begin{pmatrix} 1 & 0 \\ 0 & -1 \end{pmatrix}, \ \eta_2 = \begin{pmatrix} j & 0 \\ 0 & j \end{pmatrix}, \ \eta_3 = \begin{pmatrix} 0 & -1 \\ -1 & 0 \end{pmatrix},$$

$$\hat{\psi} = -\begin{pmatrix} 0 & 1 \\ -1 & 0 \end{pmatrix}\overline{\psi},$$

$$\hat{\hat{\psi}} = -\psi,$$

A hyperbolic spinor in Minkowski 3-space can be given by $\psi = \begin{pmatrix} \psi_1 \\ \psi_2 \end{pmatrix}$, where $\psi_1, \psi_2 \in H$ (Ketenci et al. , 2015).

For a, b $\in R_1^3$, $a + jb = (z_1, z_2, z_3)$

$z_1^2 + z_2^2 - z_3^2 = 0$, $a + jb \neq 0$

$$a + jb = \psi^t \sigma \psi = (\psi_1^2 - \psi_2^2, \ j(\psi_1^2 + \psi_2^2), -2\psi_1\psi_2), \tag{9}$$

$$c = -\hat{\psi}^t \sigma \psi = \overline{\psi}^t P \psi \tag{10}$$

$$= (\psi_1\overline{\psi}_2 + \overline{\psi}_1\psi_2, \ j(\psi_1\overline{\psi}_2 - \psi_2\overline{\psi}_1), \ |\psi_1|^2 - |\psi_2|^2)$$

where the mutually orthogonal vectors. The superscript t denotes transposition (Ketenci et al. , 2015). $\overline{\psi}$ is complex of conjugation of ψ and $\hat{\psi}$ is the mate of ψ .

For $U \in SU(2; R)$,

$$\overline{\psi}'^t \psi' = \psi^t \psi$$
$$\psi' = U\psi$$

1. NEW SPINOR FRENET EQUATIONS IN R_1^3

In this part new spinor Frenet equations are introduced.

Theorem 1.1. If two-component second hyperbolic spinor ϕ yields the Frenet triad $\{n, T, b\}$ with timelike curve with spacelike binormal in R_1^3, the Frenet equations are given by second hyperbolic spinor equation:

$$\frac{d\phi}{ds} = \frac{j\kappa}{2}\phi - \frac{\tau}{2}\hat{\phi}.$$

Proof. If the second hyperbolic spinor ϕ denotes the Frenet triad $\{n, T, b\}$, using (9) and (10) it can be written by

$$n + jT = \phi^t \eta \phi \qquad b = -\hat{\phi}^t \eta \phi \tag{11}$$

with $\bar{\phi}^t \phi = 1$. Also

$$\frac{d\phi}{ds} = \gamma_1 \phi + \gamma_2 \hat{\phi} \tag{12}$$

where γ_1 and γ_2 are functions and $\phi \neq 0$. Via (1) and diferentiating of (11) according to s, we have

$$\kappa T + \tau b + j\kappa n = \frac{d\phi^t}{ds}\eta\phi + \phi^t \eta \frac{d\phi}{ds} \tag{13}$$

Using (11) and (12) in (13),

$$\kappa T + \tau b + j\kappa n = 2\gamma_1 (n + jT) - 2\gamma_2 b \tag{14}$$

From (14), it can be obtained

$$\gamma_1 = \frac{j\kappa}{2}, \quad \gamma_2 = -\frac{\tau}{2} \tag{15}$$

Using (15) in (12), it can be obtained:

$$\frac{d\phi}{ds} = \frac{j\kappa}{2}\phi - \frac{\tau}{2}\hat{\phi}.$$

Theorem 1.2. If new second spinor ϕ represents the Frenet triad $\{n, T, b\}$ for spacelike curve with timelike principal normal in R_1^3, the Frenet equations are presented as the following:

$$\frac{d\phi}{ds} = -\frac{j\kappa}{2}\phi - \frac{\tau}{2}\hat{\phi}.$$

Proof. It is obvious from Theorem 1.1.

Theorem 1.3. If the third hyperbolic spinor Ω represents the Frenet triad $\{T, b, n\}$ of spacelike curve with timelike normal, the Frenet equations are given by third hyperbolic spinor equation, such that

$$\frac{d\Omega}{ds} = \left(\frac{\kappa - j\tau}{2}\right)\hat{\Omega}.$$

Proof. If the third hyperbolic spinor Ω denotes the Frenet triad $\{T, b, n\}$ via (9) and (10) the followings are derived

$$T + jb = \Omega^t \eta \Omega \qquad n = -\hat{\Omega}^t \eta \Omega \tag{16}$$

with $\overline{\Omega}^t \Omega = 1$.

$\{\Omega, \hat{\Omega}\}$ is a basis two-component third hyperbolic spinors, such that

$$\frac{d\Omega}{ds} = \nu_1 \Omega + \nu_2 \hat{\Omega} \tag{17}$$

where ν_1 and ν_2 are functions. Using (1) and diferentiating of (16) the followings are obtained:

$$-\kappa n + j\tau n = \frac{d\Omega^t}{ds}\eta\Omega + \Omega^t \eta \frac{d\Omega}{ds} \tag{18}$$

Using (16) and (17) in (18), it can be written by

$$n(j\tau - \kappa) = 2\nu_1 (T + jb) - 2\nu_2 n \tag{19}$$

From (19), it can be obtained

$$\nu_1 = 0, \qquad \nu_2 = \frac{\kappa - j\tau}{2} \tag{20}$$

Using (20) in (17), the third hyperbolic spinor representation of Frenet frame is obtained as following

$$\frac{d\Omega}{ds} = (\frac{\kappa - j\tau}{2})\hat{\Omega}\,.$$

2. NEW SPINOR DARBOUX EQUATIONS IN MINKOWSKI SPACE

In this part, second and third spinor formulations for Darboux equations in Minkowski 3-space R_1^3 are obtained via various theorems.

Theorem 2.1. If second spinor ψ represents the Darboux triad $\{T, Q, N\}$ of timelike curve β on timelike surface M in Minkowski 3-space, the Darboux equations have second spinor equation

$$\frac{d\psi}{ds} = -\frac{jk_g}{2}\psi + (\frac{k_n + j\tau_g}{2})\hat{\psi}$$

Proof. If second hyperbolic spinor ψ denotes Darboux triad $\{T, Q, N\}$ with first case, then from (9) and (10)

$$T + j\,Q = \psi^t \eta \psi\,, \qquad N = -\hat{\psi}^t \eta \psi \tag{21}$$

with $\overline{\psi}^t \psi = 1$.

Since $\{\psi, \hat{\psi}\}$ is basis two-component second hyperbolic spinor, then

$$\frac{d\psi}{ds} = \phi_1 \psi + \phi_2 \hat{\psi} \tag{22}$$

where ϕ_1 and ϕ_2 are functions. From (2) and (22), it can be written by

$$jk_g T + k_g Q + (k_n + j\tau_g)N = \frac{d\psi^t}{ds}\eta\psi + \psi^t \eta \frac{d\psi^t}{ds} \tag{23}$$

Using (21) in (23), it can be found

$$jk_gT + k_gQ + (k_n + j\tau_g)N = 2\varphi_1(T + jQ) - 2\varphi_2 N \tag{24}$$

From (24), the followings are derived

$$\phi_1 = \frac{k_g j}{2}, \qquad \phi_2 = -\frac{k_n + j\tau_g}{2} \tag{25}$$

Using (25) in (22) it can be obtained:

$$\frac{d\psi}{ds} = \frac{k_g j}{2}\psi - \left(\frac{k_n + j\tau_g}{2}\right)\hat{\psi}.$$

Theorem 2.2. If second spinor represents the Darboux triad $\{T, Q, N\}$ of spacelike curve β on timelike surface M in Minkowski 3-space according to (21), the Darboux equations have second spinor equation

$$\frac{d\psi}{ds} = -\frac{jk_g}{2}\psi - \left(\frac{k_n + j\tau_g}{2}\right)\hat{\psi}.$$

Proof is clear from Theorem 2.1.

Theorem 2.3. If the third hyperbolic spinor γ represents third Darboux triad $\{T, Q, N\}$ of a spacelike curve on spacelike surface in R_1^3, then Darboux equations are equivalent third hyperbolic spinor equation

$$\frac{d\gamma}{ds} = -\frac{jk_n}{2}\gamma + \left(\frac{\tau_g j - k_n}{2}\right)\hat{\gamma}.$$

Proof. If the third hyperbolic spinor γ represents the Darboux triad $\{T, Q, N\}$ with spacelike curve on spacelike surface M, then there exists

$$T + jN = \gamma^t \eta\gamma, \qquad N = -\hat{\gamma}^t \eta\gamma \tag{26}$$

with $\bar{\gamma}^t\gamma = 1$.

Since $\{\gamma, \hat{\gamma}\}$ is a basis for third two-component spinor, it can be obtained:

$$\frac{d\gamma}{ds} = \lambda_1 \gamma + \lambda_2 \hat{\gamma} \tag{27}$$

where λ_1 and λ_2 are functions. From (2) and (27), it can be derived:

$$-jk_n T + Q(k_g - j\tau_g) - k_n N = \frac{d\gamma^t}{ds}\eta\gamma + \gamma^t \eta \frac{d\gamma}{ds}$$

$$= 2\lambda_1 (T + jN) - 2\lambda_2 Q \tag{28}$$

From (28), it can be written by

$$\lambda_1 = -\frac{jk_n}{2}, \qquad \lambda_2 = \frac{\tau_g j - k_g}{2} \tag{29}$$

Using (29) in (27), the followings are derived:

$$\frac{d\gamma}{ds} = -\frac{jk_n}{2}\gamma + \left(\frac{\tau_g j - k_g}{2}\right)\hat{\gamma}.$$

Theorem 2.4. If the third hyperbolic spinor γ represents third Darboux triad $\{T, Q, N\}$ of a timelike curve on timelike surface M, then Darboux equations are equivalent to third hyperbolic spinor equation

$$\frac{d\gamma}{ds} = \frac{jk_n}{2}\gamma + \left(\frac{\tau_g j + k_g}{2}\right)\hat{\gamma}.$$

Proof. From Theorem 2.3 proof is obvious.

3. SPINOR BISHOP EQUATIONS OF PSEUDO NULL CURVE

In this part spinor Frenet equations according to Bishop frame of pseudo-null curve β are discussed.

Theorem 3.1. If two-component hyperbolic spinor denotes the Bishop triad $\{N_1, N_2, T\}$ of pseudo null curve β, then the Frenet equations of Bishop frame of the curve β are given by the single hyperbolic spinor equation :

$$\frac{d\Gamma}{ds} = \frac{jk}{2}\Gamma + \frac{\tau}{2}\hat{\Gamma}.$$

Proof. Let $\beta : I \subset R \to R_1^3$ be a pseudo null curve with pseudo arc length s. If the hyperbolic spinor Γ represents the Bishop triad $\{N_1, N_2, T\}$ of pseudo null curve, then there exists the hyperbolic spinor Γ such that

$$N_1 + jN_2 = \Gamma^t \eta \Gamma \qquad T = -\hat{\Gamma}^t \eta \Gamma \tag{30}$$

with $\overline{\Gamma}^t \Gamma = 1$.

Since $\{\Gamma, \hat{\Gamma}\}$ is a basis two-component second hyperbolic spinors, it can be written by

$$\frac{d\Gamma}{ds} = p_1\Gamma + p_2\hat{\Gamma} \tag{31}$$

where p_1 and p_2 are functions and $\Gamma \neq 0$. From (5), (31) and differentiating of (30) according to s, it can be written by

$$-(k_1 + jk_2)T = 2p_1(N_1 + jN_2) - 2p_2 T \tag{32}$$

From (19), it can be found

$$p_1 = 0, \qquad p_2 = \frac{k_1 + jk_2}{2} \tag{33}$$

Substituting (33) in (31), the single hyperbolic spinor representation of Bishop frame of pseudo null curve is derived as

$$\frac{d\Gamma}{ds} = \left(\frac{k_1 + jk_2}{2}\right)\hat{\Gamma}.$$

4. SPINOR FRENET EQUATIONS IN THE EQUIFORM GEOMETRY OF G_1^3 AND $I_3^{(1)}$, $I_3^{(2)}$

In this part spinor Frenet equations according to the equiform geometry of the simple isotropic space space $I_3^{(1)}$, the double isotropic space $I_3^{(2)}$ and pseudo-Galilean 3-space G_1^3 are studied.

Theorem 4.1. If two-component spinor Θ denotes the Frenet triad $\{\mathcal{T},\mathcal{B},\mathcal{N}\}$ of the simple isotropic space $I_3^{(1)}$, the Frenet equations are given by the single hyperbolic spinor equation

$$\frac{d\Theta}{d\sigma}=\frac{j\kappa}{2}\Theta+\frac{\tau}{2}\hat{\Theta}.$$

Proof. If spinor Θ represents the Frenet triad $\{\mathcal{T},\mathcal{B},\mathcal{N}\}$, it can be obtained

$$\mathcal{T}+j\mathcal{B}=\Theta^t\eta\Theta,\qquad \mathcal{N}=-\hat{\Theta}^t\eta\Theta \tag{34}$$

with $\overline{\Theta}^t\Theta=1$. Also

$$\frac{d\Theta}{d\sigma}=\varsigma_1\Theta+\varsigma_2\hat{\Theta} \tag{35}$$

Here ς_1 and ς_2 are functions. From (7), (34) and differentiating of (35) according to σ it can be obtained

$$\tilde{\kappa}\mathcal{T}+\mathcal{N}+j\tilde{\kappa}\mathcal{B}=2\varsigma_1\mathcal{T}+2\varsigma_1\mathcal{B}-2\varsigma_2\mathcal{N} \tag{36}$$

From (36) it can be derived

$$\varsigma_1=\frac{\widetilde{\kappa}}{2},\ \varsigma_2=-\frac{1}{2} \tag{37}$$

Using (37) in (31), it can be obtained

$$\frac{d\Theta}{d\sigma}=\frac{\widetilde{\kappa}}{2}\Theta+\frac{1}{2}\hat{\Theta}.$$

Theorem 4.2. If two-component spinor represents the Frenet triad $\{\mathcal{T},\mathcal{B},\mathcal{N}\}$ in the equiform geometry of double isotropic space $I_3^{(2)}$ then the Frenet equations are written by

$$\frac{d\varsigma}{d\sigma}=\frac{\widetilde{\kappa}}{2}\varsigma-\frac{1}{2}\hat{\varsigma}$$

Proof. If the spinor ς represents with the Frenet triad $\{\mathcal{T},\mathcal{B},\mathcal{N}\}$, then

$$\mathcal{T} + j\mathcal{B} = \varsigma^t \eta \varsigma \qquad \mathcal{N} = -\hat{\varsigma}^t \eta \varsigma \tag{38}$$

with $\bar{\varsigma}^t \varsigma = 1$. Then

$$\frac{d\varsigma}{d\sigma} = q_1 \varsigma + q_2 \hat{\varsigma} \tag{39}$$

Here q_1 and q_2 are functions. Using (38) and differentiating of (39) according to σ, it can be obtained

$$\tilde{\kappa}\mathcal{T} + \mathcal{N} + j\tilde{\kappa}\mathcal{B} = 2q_1\mathcal{T} + 2jq_1\mathcal{B} - 2q_2\mathcal{N} \tag{40}$$

From (40) the followings are found

$$q_1 = \frac{\tilde{\kappa}}{2}, \quad q_2 = -\frac{1}{2} \tag{41}$$

Using (41) in (39), spinor Frenet representation in the double isotropic space is given by

$$\frac{d\varsigma}{d\sigma} = \frac{\tilde{\kappa}}{2}\varsigma - \frac{1}{2}\hat{\varsigma}$$

Theorem 4.3. If the spinor ξ represents the Frenet triad $\{\mathcal{T}, \mathcal{B}, \mathcal{N}\}$ of the equiform geometry in the pseudo Galilean space, then the Frenet equations are expressed by

$$\frac{d\xi}{d\sigma} = \frac{\tilde{\kappa}}{2}\xi - \frac{(j\tilde{\tau} + 1)}{2}\hat{\xi}$$

Proof. If the spinor ξ represents the Frenet triad $\{\mathcal{T}, \mathcal{B}, \mathcal{N}\}$, there exists the spinor ς, such that

$$\mathcal{T} + j\mathcal{B} = \xi^t \eta \xi, \qquad \mathcal{N} = -\hat{\xi}^t \eta \xi \tag{42}$$

with $\bar{\xi}^t \xi = 1$. Thus

$$\frac{d\xi}{d\sigma} = \delta_1 \xi + \delta_2 \hat{\xi} \tag{43}$$

Here δ_1 and δ_2 are functions. Using (6), (42) and differentiating of (43) according to σ it is obtained

$$\tilde{\kappa}\mathcal{T}+(1+j\tilde{\tau})\mathcal{N}+j\tilde{\kappa}\mathcal{B}=2\delta_1\mathcal{T}+2j\delta_1\mathcal{B}-2\delta_2\mathcal{N} \tag{44}$$

From (44) the followings are derived

$$\delta_1=\frac{\tilde{\kappa}}{2}\ ,\quad \delta_2=-\frac{(j\tilde{\tau}+1)}{2} \tag{45}$$

Using (45) in (43), spinor Frenet representation in the equiform geometry of G_1^3 is presented as the following

$$\frac{d\xi}{d\sigma}=\frac{\tilde{\kappa}}{2}\xi-\frac{(j\tilde{\tau}+1)}{2}\hat{\xi}$$

Theorem 4.4. If the spinor χ represent the Frenet triad $\{\mathcal{N},\mathcal{B},\mathcal{T}\}$ $\{\mathcal{N},\mathcal{B},\mathcal{T}\}$ according to the equiform geometry of pseudo Galilean space, the Frenet equations are given by

$$\frac{d\chi}{d\sigma}=\frac{\tilde{\kappa}+j\tilde{\tau}}{2}\chi$$

Proof. If the spinor χ represents the Frenet triad $\{\mathcal{N},\mathcal{B},\mathcal{T}\}$ in the equiform geometry of pseudo Galilean 3-space. There is exists

$$\mathcal{N}+j\mathcal{B}=\chi^t\eta\chi\ ,\quad \mathcal{T}=-\hat{\chi}^t\eta\chi \tag{46}$$

with $\overline{\chi}^t\chi=1$. $\{\chi,\hat{\chi}\}$ is a basis for two-component spinors, such that

$$\frac{d\chi}{d\sigma}=\omega_1\chi+\omega_2\hat{\chi} \tag{47}$$

where ω_1 and ω_2 are functions and $\chi\neq 0$. Using (46) and differentiating of (47) according to σ, it can be derived

$$(\tilde{\kappa}\mathcal{N}+\tilde{\tau}\mathcal{B})+j(\tilde{\tau}\mathcal{N}+\tilde{\kappa}\mathcal{B})=-2\omega_2\mathcal{T}+2\omega_1\mathcal{N}+2\omega_1 j\mathcal{B} \tag{48}$$

From (48) it is found

$$\omega_1 = \frac{\widetilde{\kappa} + j\widetilde{\tau}}{2}, \quad \omega_2 = 0 \tag{49}$$

Using (49) in (47), second spinor Frenet representation is given by

$$\frac{d\chi}{d\sigma} = \frac{\widetilde{\kappa} + j\widetilde{\tau}}{2}\chi .$$

CONCLUSIONS

In this chapter spinor Bishop equations of pseudo null curve, spinor Frenet equations in the equiform geometry of simple isotropic space $I_3^{(1)}$ and double isotropic space $I_3^{(2)}$ and spinor equations in the equiform geometry of the pseudo Galilean 3-space have been presented.

REFERENCES

BALCI, Y. (2015) Hyperbolic spinor Darboux equations of spacelike curves in Minkowski 3-space*, Journal of the Chungcheong Mathematical Society* (28) 525-535.

CASTILLO, G. F.T. (2003) *3-D Spinors, Spin-Weighted Functions and their applications*, Birkhauser, Boston.

CASTILLO, G. F. T and BARRALES G. S (2004) Spinor formulation of the diferential geometry of curves, *Revista Colombiana de Matematicas* (38) 27-34.

DIRAC, P.A.M (1974) *Spinors in Hilbert Space*. Plenum Press, New York.

DIVJAK B. (1997) Geometrija pseudogalilejevih prostora, Ph. D. Thesis, University of Zagreb.

ERJAVEC, B.& DIVJAK, B. (2008) Equiform Diferential Geometry of Curves in the Pseudo Galilean Space, *Mathematical Communications* (13) 321-332.

ERİŞİR, T. ; GÜNGÖR M.A. ; TOSUN, M. (2015) Geometry of the Hyperbolic Spinors Corresponding to Alternative Frame, *Adv. in Appl. Clifford Algebra*. (25) 799-810.

GRBOVIC M. & NESOVIC E. (2018) On the Bishop frames of pseudo null and null Cartan curves in Minkowski 3-space, *J. Math. Anal. Appl.* (2018) 219-233.

KETENCİ Z.; ERİŞİR T.; GÜNGÖR M.A (2015) A construction of hyperbolic spinors according to Frenet frame in Minkowski space. *Journal of Dynamical Systems and Geometric Theories* (13) 179-193.

KİŞİ, İ. and TOSUN, M. (2015) Spinor Darboux Equations of Curves in Euclidean 3-Space. *Math. Morav*. (19) 87-93.

SATTINGER, D.H and WEAVER, O.L (1986) *Lie Groups and Algebras* with Applications to Physics, *Geometry and Mechanics*, Springer-Verlag, New York.

O'NEILL, B. (1983) *Semi-Riemannian Geometry, with Applications to Relativity.* Academic Press, New York.

ÜNAL, D. ; KİŞİ, İ. ; TOSUN, M (2013) Spinor Bishop equation of curves in Euclidean 3-space. *Adv. Appl. Clifford Algebras* (23) 757-765.

PAVKOVIC, B. J. (1986) Equiform Geometry of Curves in the isotropic Spaces $I_3^{(2)}$ and $I_3^{(1)}$ *Rad JAZU* , 39-44.

PAULI, W. (1927) *Zur Quantenmechanik des magnetischen Elektrons, Zeitschrift Physik* (43) 601-632.

Chapter 7

EFFECTIVE ATOMIC NUMBER AND ELECTRON DENSITY DETERMINATION OF CE AND SOME SELECTED CE COMPOUNDS

Ahmet TURŞUCU[1]

1 Department of Electric-Electronic Engineering, Sirnak University, 73000, Sirnak, Turkey.

1. Introduction

One of the most fundamental events that physics must explain is the interactions between fundamental particles and fields. As an example of this interaction, the observation and understanding of the scattering of photons from free electrons is of great importance in the development of quantum mechanics. The scattering events of X or gamma rays are occurring in different types. Inmedical and biological applications Rayleigh and the Compton scattering is important than the photoelectric effects of X or gamma rays [1].The Compton scattering is occurring in the collision of X or gamma rays with free electrons. The main objective of this study is the implementation of the Compton scattering in the determination of the effective atomic number.

The elements are represented by their unique atomic numbers. However, there is no specialized description method for compounds and mixtures. For this purpose, the atomic numbers of compounds consisting of two or more elements are referred to as the effective atomic number. The scientists have engaged in different studies to determine the effective atomic number of compounds. Some of them were examined the effective atomic number by mass absorption method. In recent years, it has become common to determine the effective atomic number by scattering method. Both determination techniques are non-destructive and used in X-ray fluorescence spectroscopy investigation experiments. The X-ray fluorescence spectroscopy experiments are useful in the non-destructive determination of atomic properties of biological, environmental, agricultural materials.

This experimental study was dedicated on the effective atomic number and electron density determination of Ce and selected Ce compounds. The target samples cerium is a lanthanide element and most abundant in nature. The Ce is found in monazite and bastnaesite mineral

composition. The usage of Ce element is very common, and the cerium oxide is widely used in commercial transactions. Cerium replaces other metal oxides used in high-quality optical surfaces. Cerium compounds are one of the components sought in lighting systems. It is an important substance used in iron alloys and widely used to increase the high temperature oxidation resistance of superalloys. Cerium, an important component for phosphors used in television screens and fluorescent lamps, prevents the formation of polymers in pigments exposed to sunlight. Some areas and products using cerium, its compounds and alloys are as follows; glass polish, catalytic converters, pigments, television glass plates, jet engines alloys, carbon arc lamps, porcelain coatings, energy saving bulbs, projectors, magnets, stainless steel, incandescent lamps, magnetic optical compact discs, chrome finishes, spectacles, self-cleaning surfaces of furnaces. Also, Ce was used in superconductor applications in different compositions. Although not as widely used as MgB_2, it is possible to find Ce-doped superconductors.There are also many studies on MgB_2 superconductors. These are usually about investigating their electrical properties and effects resulting from different doping. [2-3]

Important studies have been included in this field by many researchers. Hosamani and Badiger [4]have been determined the effective atomic number of composite materials by using the backscattered photons that were emitted from ^{127}Cs radioactive isotope. The backscattered photons were detected via ″2x2″NaI(Tl) scintillation gamma ray spectrometer that was coupled with 16 K multi-channel analyzer. The effective atomic number of target samples has been determined by knowing the saturation thicknesses of pure samples. Then, the saturation thickness of pure materials was used to measure the effective atomic number determination of composite materials. Babu and Badiger[5] have

been measured the stopping power, cross section and the effective atomic number of amino acids. The interaction between electron and sample was called narrow beam effect. They have used the narrow beam geometry setup that was coupled with Si(Li) semiconductor detector and 8K multichannel analyzer. Singh et al. [6] have been determined the effective atomic number of target samples by using the scattered gamma photons that were emitted from ^{203}Hg radioisotope. The emitted gamma photons from the source have 279 keV energy. Rayleigh to Compton scattering intensity ratio of incident gamma photons was used in determination of brass, bronze, soldering material, Perspex and bakelite composite samples. Similar studies were performed from several researchers by using different samples. [7-8-9-10]

This recent work hasadopted to the scattering intensity ratio of 59.54 keV gamma rays that were emitted from ^{241}Am radioisotope. Because of the scientific and commercial importance, the Ce and some selected compounds have been selected as a target. The determined values of the effective atomic number and the electron densities of samples have been in good accordance with calculated theoretical values.

2. Theory

The effective atomic number and the electron densities of pure and composite samples have been determined by using scattering intensity ratios of incident radiation in recent years. The scattering intensity ratio measurements were carried out by using the Rayleigh (coherent) and Compton scattered peaks of target samples. The usage of this technique was containing the probabilities of related scattering. In Rayleigh (coherent) scattering event, the incident beam has collided from the target sample with no energy and wavelength change. The Rayleigh (coherent) scattering has been called elastic collision and, in this collision, no energy

change has been observed. The Rayleigh scattering probability has been formulized by the following equation,

$$\frac{d\sigma_R}{d\Omega} = \frac{r_0^2}{2}(1 + cos^2\theta)|F(q,Z)|^2 \quad (1)$$

In this equation, the atomic form factor, the transferred momentum to the electron,the classical electron radius and the scattering angle is representing by $F(q,Z)$, q,$r_0(= 2{,}8179x10^{-15}m)$, θrespectively.

Compton scattering is a phenomenon where a high energy photon interacts with an electron and emits a low frequency scattered electron and a low energy photon.This situation shown that the Compton scattering experiment is evidence of the particle structure of electromagnetic radiation. Different from the Rayleigh scattering, the Compton scattering cross section was calculated by using Klein-Nishina equation,

$$(\frac{d_\sigma}{d_\Omega})_{KN} = \frac{1}{2}r_0^2\left(\frac{E}{E_0}\right)^2(\frac{E_0}{E} + \frac{E}{E_0} - sin^2\theta) \quad (2)$$

the scattered and incident photon energies was represented by$E$andE_0respectively. In Compton scattering events, the momentum of photon has been transferred to the electron. This transportation value has been affectedthe incoherent scattering function ($S(q,Z)$). In some cases, the momentum transportation has been large values and the incoherent scattering function have been equals to the atomic electrons. If otherwise, the transferred momentum to the electron very low, approaches to the zero, the incoherent scattering function becomes zero. So, the calculation of the effective atomic number has been carried out by using the ratio of elastic and inelastic scattering cross sections. The cross-section ratio (R) equation was given below,

$$R = (\frac{d\sigma}{d\Omega})_R/(\frac{d\sigma}{d\Omega})_{aC} \propto \frac{|F(q,Z)|^2}{S(q,Z)} \quad (3)$$

The atomic Compton scattering cross-section parameter was symbolized by using$(d\sigma/d\Omega)_{aC}$equation. The atomic Compton

scattering has occurred from bound atomic electrons. The atomic Compton scattering cross-section given as,

$$(\frac{d\sigma}{d\Omega})_{aC} = S(q,Z)(\frac{d\sigma}{d\Omega})_{KN} \quad (4)$$

The calculated value of R has been proportional to the atomic number of investigated materials. The equation parameters$F(q,Z)$and $S(q,Z)$that was used in the calculation of Rayleigh to Compton scattering cross-section has been created by Hubbel *et al.*[11].

The weighted atomic percentages of target samples were used in calculation of the Rvalue. The R value has been directly related with the atomic number of target samples and calculated by using following equation,

$$R = (\frac{d\sigma}{d\Omega})_R / (\frac{d\sigma}{d\Omega})_{aC} \propto \frac{\sum_{j=1}^{n} a_j^{at} |F(q,Z_j)|^2}{\sum_{j=1}^{n} a_j^{at} S(q,Z_j)} \quad (5)$$

In equation (5), the atomic percentage was represented by a_j^{at} term. The a_j^{at} term has been calculated via following equation,

$$a_j^{at} = \frac{(W_j/A_j)}{\sum_j (W_j/A_j)} (6)$$

where the atomic percentages have been represented by $W_j$and the atomic mass of the Jth element have been represented $A_j$respectively.

3. Experimental setup and present measurements

The present experimental study was focused on the effective atomic number determination of pure and some selected Ce compounds. For this purpose, 59,54 keV gamma photons were directed to the samples and scattered photons were detected and analyzed. The effective atomic number determination of rare earth element Ce and selected compounds were widely used in radiation shielding applications, lasers, neutron capturing, medical physics, and many other technological applications.

Target materials scattered the incident gamma photons that were emitted from the source, and also, the scattered photons were detected from the HPGe semiconductor detector.The specific feature of the detector was given in Table 1. Besides, Fig. 1 and Fig. 2 has been represented the schematic structure of the experimental setup used in this work. In this work, we have studied pure Ce and some selected Ce compounds ($CeCl_3$,$Ce(NO_3)_3$,CeF_3, $Ce(SO_4)_3$,Ce_2O_3). Canberra (AccuSpec) Pc-based multichannel analyzer card was used in the processing of the scattered spectrum of samples. Besides, Ortec 472 model amplifier was used for obtaining the best counting rates from the detector. The time constant of the amplifier was set to 6 μs. All these parameters were gained by using the Genie-2000 computer program. The Compton and coherently scattered photons were collected by MCA in 1024 channels. In addition to the collecting process, all these data were analyzed by the Origin 7.5 software program.

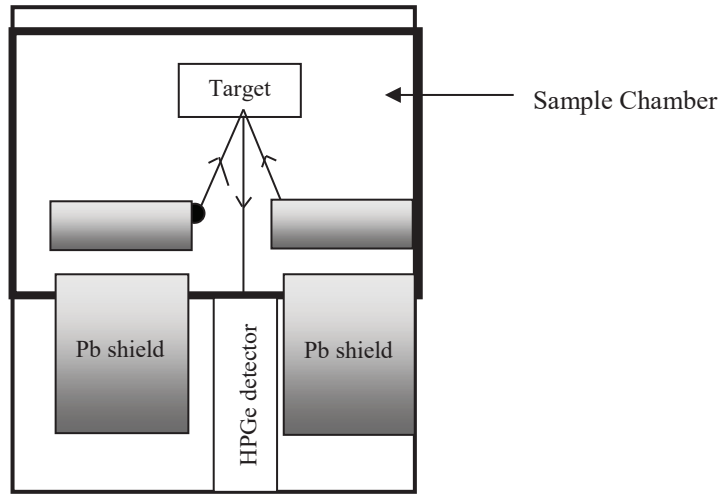

Figure 1. Experimental setup (radius of collimator is 0.53 cm). This figure is only a schematic diagram of experimental setup.

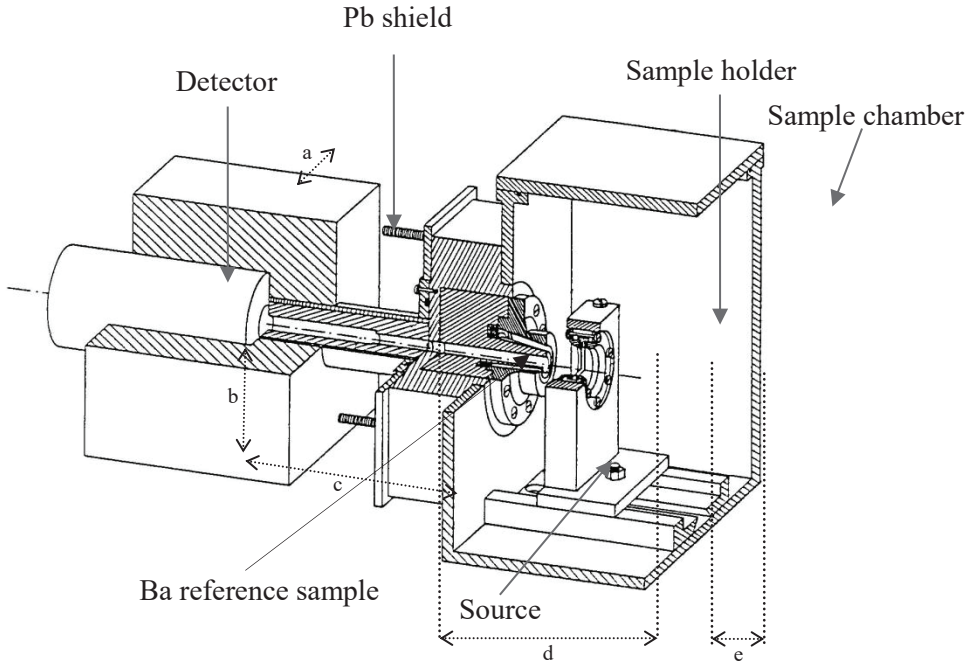

Figure 2. Sample chamber (a=6.5 cm, b=6.3 cm, c=13.5 cm, d=11 cm, e=5 cm).

Table 1. The characteristics specifications of HPGe detector.

Active Diameter	16 mm
Active Area	200 mm^2
Sensitive Detector Depth	10 mm
Distance From Window	5 mm
Beryllium window thickness	0.12 mm
Supply Voltage	-1500 V
Resolution (5,9-122 keV)	182-488 eV

Table 2. The effective atomic number values of Ce and selected samples.

Target Samples	R/C Ratio	Experimental	Theoretical
Ce			5,80E+01
$CeCl_3$	9,34E-01	5,35E+01	5,36E+01
CeF_3	1,01E+00	5,53E+01	5,56E+01
$Ce(NO_3)_3$	1,12E+00	5,89E+01	5,88E+01
$Ce_2(SO_4)_3$	8,41E-01	5,19E+01	5,18E+01
Ce_2O_3	1,05E+00	5,66E+01	5,68E+01

4. Conclusion

Effective atomic number values obtained by the present study, other experimental values available in the literature, and density ratios of Rayleigh scattering to Compton scattering are given in Table 2. In addition, the theoretical effective atomic numbers of the samples used in the experiment are given in Table 2. Experimental error factors and

uncertainties arising from different factors caused errors in the evaluation of characteristic signals at 1.64-3.51%, target sample mass thicknesses at 1.37-3.18%, photopic efficiency at 1.10-2.04%, and statistical errors less than 1%. It has been determined that all parameters affecting the experimental values have values between 2.68% and 5.40%. Molecular and solid-state effects were not taken into account in the calculation of theoretical values. Also, the XCOM [12] database ignores the interaction between atoms, the coulomb interaction between photoelectron, and positively charged ions. In addition, the XCOM database does not calculate energy absorption components. This situation causes an inconsistency between theoretical and experimental values.

It is seen that there is a good harmony between experimental values and theoretical values. This has shown that the present experimental technique is a usable method for effective atomic number calculation. It is clear that more experimental data must be obtained. Especially, more precise results can be obtained with experiments with compounds having different scattering angles and chemical compositions.

5. References

[1]Rao, D. V., Yuasa, T., Akatsuka, T., Tromba, G., Takeda, T., Cesareo, R., ... &Gigante, G. E. (2007). Whole-atom Compton scattering cross-sections and individual shell cross-sections for the biological elements in the energy region from 1 to 4 keV. *Nuclear Instruments and Methods in Physics Research Section B: Beam Interactions with Materials and Atoms*, *261*(1-2), 193-196.

[2]Ulgen, A.,T.(2019). The Cobalt Diffusion in MgB_2Superconductors During Heat Treatment. Research & ReviewsIn ScienceAnd Mathematics,ISBN:978-605-7631-45-9, Pages:125 -136.

[3]Ulgen, A., T. (2019). Comparison Of Diffusion Coefficients With Different Transition Metal Coatings In MgB_2superconductor. Academic Studies In Mathematic and Natural Sciences,ISBN:978-9940-540-72-2, Pages: 11-22.

[4]Hosamani, M. M., &Badiger, N. M. (2018). Determination of effective atomic number of composite materials using backscattered gamma photons–a novel method. *Chemical Physics Letters*, *695*, 94-98.

[5]Babu, S. R., &Badiger, N. M. (2019). Determination of mass stopping power, stopping cross section and effective atomic number of standard amino acids for relativistic electron interactions. *Radiation Physics and Chemistry*, *156*, 210-215.

[6]Singh, M. P., Sandhu, B. S., & Singh, B. (2007). Measurement of the effective atomic number of composite materials using Rayleigh to Compton scattering of 279 keV gamma rays. *Physica Scripta*, *76*(4), 281.

[7]Oto, B., Gulebaglan, S. E., Madak, Z., &Kavaz, E. (2019). Effective atomic numbers, electron densities and gamma rays buildup factors of inorganic metal halide cubic perovskites CsBX3 (B= Sn, Ge; X= I, Br, Cl). *Radiation Physics and Chemistry*, *159*, 195-206.

[8]Agar, O., Khattari, Z. Y., Sayyed, M. I., Tekin, H. O., Al-Omari, S., Maghrabi, M., ... &Kityk, I. V. (2019). Evaluation of the shielding parameters of alkaline earth-based phosphate glasses using MCNPX code. *Results in Physics*, *12*, 101-106.

[9]Dong, M. G., Agar, O., Tekin, H. O., Kilicoglu, O., Kaky, K. M., & Sayyed, M. I. (2019). A comparative study on gamma photon shielding

features of various germanate glass systems. *Composites Part B: Engineering*, *165*, 636-647.

[10]Baltas, H. A. S. A. N., Sirin, M. U. R. A. T., Celik, A., Ustabas, İ. L. K. E. R., & El-Khayatt, A. M. (2019). Radiation shielding properties of mortars with minerals and ores additives. *Cement and Concrete Composites*, *97*, 268-278.

[11]Hubbell, J. H., Veigele, W. J., Briggs, E. A., Brown, R. T., Cromer, D. T., & Howerton, D. R. (1975). Atomic form factors, incoherent scattering functions, and photon scattering cross sections. *Journal of physical and chemical reference data*, *4*(3), 471-538.

[12]Gerward, L., Guilbert, N., Jensen, K. B., &Leving, H. (2004). WinXCom–a program for calculating X-ray attenuation coefficients. *Radiation physics and chemistry*, *71*, 653-654.

Chapter 8

EVALUATION OF MAGNETO-RESISTIVITY PERFORMANCES AND FLUX PINNING CENTERS WITH VANADIUM ADDITION IN BI-2223 MAIN MATRIX

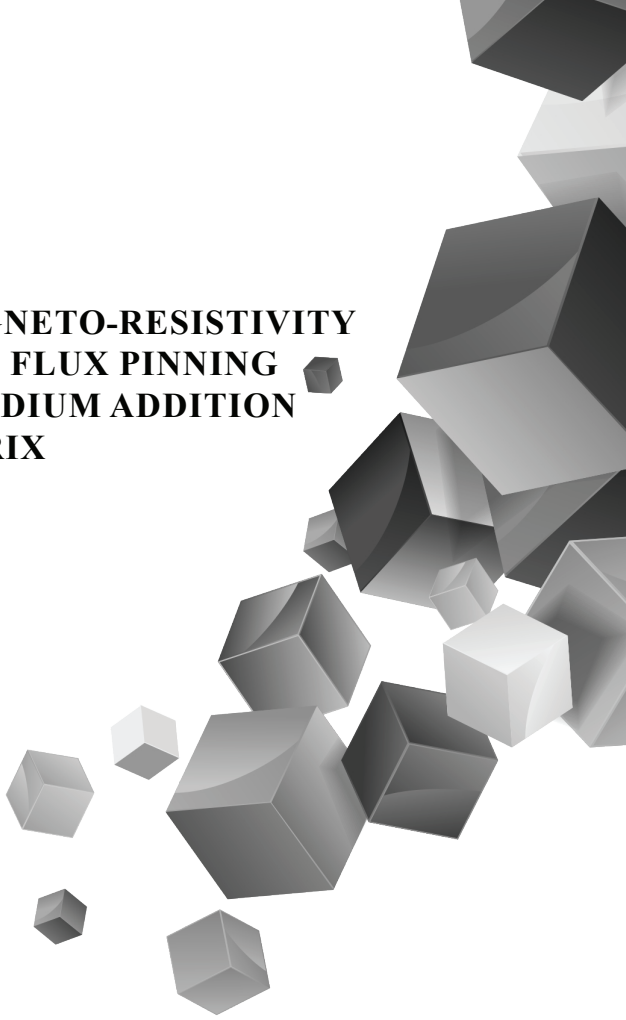

Mustafa Burak TÜRKÖZ
Muhammed OZ
Tahsin TURGAY
Gürcan YILDIRIM

1. INTRODUCTION

Materials science takes an important place in daily life of people. The history of science points out that there appear a number of turning points for the materials sciences and technology application fields. Especially, in the year of 1911 H. Kamerlingh Onnes discovered the superconducting phenomenon in the mercury heavy-metal element at temperature of 4.2 K [1]. Those years made a lot of positive effects in the scientific world, and the superconductivity has widely attracted the remarkable interest of research community. In the following years, the researchers have discovered new superconducting phases and materials such as metals, semi-metals, metal or semi-metal-based compounds, alloys, carbon-containing compounds, materials with heavy fermions, organic compounds, A-15 inorganic samples, rare-earth borocarbide materials, rutheno-cuprate samples, compounds with chevrel phase, chalcogens and related compounds, silicon-containing materials, pyrochlore oxides, magnesium diboride with two-gap superconductivity and distorted oxygen deficient multi-layered perovskite structures (Tl-, Bi- and Hg-containing high-Tc superconducting compounds) [2]. Thus, the superconducting compounds have a chance to take much more places in the application-oriented materials science, innovative energy infrastructure, advanced engineering, electro-optics, medicine, industry, and different energy sectors [3–5]. This is because, the superconducting compounds exhibit extremely larger magnetic field and especially current carrying capability, much smaller power consumption, energy losses and dissipations in the crystal system [6–8]. In particular, among the parents of cuprate-layered perovskite superconducting materials the bismuth-based copper oxides show relatively high critical temperature (up to about 110 K), critical current density ($\approx 10^7 A/cm^2$) and upper critical magnetic field (≈100 T). Moreover, the Bi-based copper oxides are easily prepared with the simple chemical composition and production procedure. Similarly, the easy and fast phase formations, easy availability of chemicals, low-cost efficiency, and environmental benefits can be mentioned for the other superior properties for the preparation of Bi-containing superconducting compounds. At the same time, the bi-based superconducting parents phase has great attracted attention of many researchers as a consequence of their highly thermodynamic stability, compositional and oxygen stability, (in the atmospheric pressure without any gas atmospheres/high-pressure environments) and resistant towards to

the water/humid atmosphere under rather higher sintering temperature values [9–12].

As for the crystal structure of the materials, all the family members are crystallized in perovskite structures within the homologous series of $Bi_2Sr_2Ca_{n-1}Cu_nO_{4+2n+x}$ and composed of the active and effective short-range-ordered antiferromagnetic Cu-O_2 sheets of adjacent superconductive layers [13–15]. The parents consist of three different participants depending on the conducting Cu-O_2 plane numbers (observed by number of *n*) in the unit cell: Bi-2201 (very low phase), Bi-2212 (low phase) and Bi-2223 (high phase). Accordingly, in the tetragonal structure of superconducting systems, the Ca-site forms a layer within the interior of Cu-O_2 layers for the low and high phase whereas no Ca layer takes place in the very low phase [16]. Likewise, the *n* value is directly related to the number of Cu-O_2 planes in the crystal system. To illustrate, the Bi-2201 superconducting phase possesses a Cu-O_2 plane in the structure while the low phase has two Cu-O_2 planes as against three Cu-O_2 planes for the Bi-2223 phases [17, 18]. Besides, the Cu atom takes the different positions in the coordination of superconducting system. Throughout the Bi-2201 superconducting phase the octahedral coordination formation of a Cu atom with the oxygen atoms is observed in the crystal structure. On the other hand, the five oxygen atoms surround a Cu atom in a pyramidal arrangement for the Bi-2212 superconducting phase while in case of Bi-2223 phase the Cu atoms obtain two different coordination types with regard to the oxygen atoms: (I) one Cu atom is bonded by four oxygen atoms to configure in the square planar molecular geometry; and (II) another Cu atom is coordinated by five oxygen atoms to be arranged in a pyramidal molecular geometry [9, 17–19]. Moreover, it is directly received that the number of *n* plays an important role on the fundamental characteristics such as the normal-state resistivity, residual resistivities, offset/onset critical transition temperatures, degree of broadening parameters and flux pinning ability of Bi-based superconducting parents [20].

It is to be strongly stressed here that the parents have some problematic faults that prevent seriously the materials to use in some specific application fields of new industrial and technological application fields [21, 22]. At the beginning of these faults, the structural layers, grain interaction coupling problems, grain alignment distributions, operating temperature range problems, low charge carrier (hole)

densities, brittleness nature, extremely sensitivity towards the external magnetic field and current, tremendously large penetration depths and short coherence lengths can be mentioned.In the present study, we try to improve the restrictions given above with the vanadium dopant in bulk Bi-2223 phase (for *n* number of 3) so that we can enhance the usage areas in newly, novel and feasible application fields (especially future heavy-industrial technology, application-oriented materials science, advanced engineering, electro-optics, innovative energy infrastructure and energy-related sectors) of Bi-2223 superconducting materials. On this basis, we investigate the fundamental differentiations in the magneto-resistivity performance and related scientific quantities as regards the active and dynamic electron-phonon couplings throughout the intra-grain regions, flux pinning abilities for two-dimensional pancake vortices, energy barriers for vortices motions, recoupling line-like mechanism, lattice period for the vortices, interplane interaction energy, movement of vortices to neighboring state length throughout pinning regions, dynamic nucleation centers in the superconducting system with the addition of different vanadium concentration (between 0.0 and 0.3 molar ratio) in the Bi-2223 superconducting crystal lattice with the assistant of magnetic field measurements exerted at external magnetic fields varying from zero T to five T.

2. EXPERIMENTAL PROCEDURES FOR VANADIUM ADDED SOLID Bi-2223 CERAMIC MATERIALS

This present study is a continuation of methodical characterization searches and focuses sensitively on the critical influence of V addition into the high phase superconducting ceramic compounds on the lattice period for the vortices, energy barriers for vortices motions, formation of the active and dynamic electron-phonon couplings throughout the intra-grain regions, flux pinning abilities for two-dimensional pancake vortices, interplane interaction energy for Josephson coupling lengths, pinning center sizes, recoupling line-like mechanism, dynamic nucleation centers in the superconducting system with the aid of magneto transport measurements performed the external magnetic fields intervals 0–5T. One can see some fundamental characteristic properties, viz. the temperature-dependent resistivity values at room temperature, dc electrical resistivity at the value of 115 K, residual resistivity, residual resistivity ratio, ρ_{norm} and $\Delta\rho$ and superconducting features of onset-offset

critical transition temperature and broadening transition width parameters in Ref. [23-26]. Besides, we examined the powder X-ray diffraction results and illustrated differentiation of texturing, phase volume fractions, crystal structure qualities, lattice constant parameters (*a* and *c*-axis length), grain alignment distributions, grain size parameters, coupling problems for grain boundary and connectivity quality intra and inter-grain regions depending on the vanadium concentration level. Similarly, we determined the coherence and bulk genuine temperatures related to the critical characteristic temperatures of solid $Bi_{1.8}Sr_{2.0}Ca_{2.2}Cu_{3.0}V_xO_y$ within $0.00 \leq x \leq 0.30$ molar ratio in the scientific paper published in Ref. [23,26]. It was obtained that the presence of vanadium in the Bi-2223 superconducting crystal structure damages dramatically the general characteristic properties mentioned above. Furthermore, we endeavor to find the possible maximum critical transition (onset and offset) temperatures with empirical model including defects and disorders for bulk Bi-2223 superconducting crystal system added with vanadium ions. One can see the production of Bi-2223 superconductors and vanadium addition procedure, also. However, we remind roughly the general production procedure of materials in this part of paper. All the superconducting materials including pure and vanadium added bulk Bi-2223 superconducting materials with the chemical formula of $Bi_{1.8}Sr_{2.0}Ca_{2.2}Cu_{3.0}V_xO_y$ are experimentally prepared by the standard solid-state reaction method [27]. On this basis, the powder of chemicals (oxide and carbonate) including the high purity materials (%99.99) of Bi_2O_3, CuO, $SrCO_3$, $CaCO_3$ and V_2O_5 purchased from Alfa Aesar exclusive distributor is used for the production of main superconducting materials. Firstly, we weigh the chemicals with respect to the stoichiometric ratios of $Bi_{1.8}Sr_{2.0}Ca_{2.2}Cu_{3.0}V_xO_y$ ($0.00 \leq x \leq 0.30$) by use of the electronic balance and mix all the chemicals using the grinding machine for nine hours in the medium of air at the constant temperature of room temperature. We, hence, obtain much more homogenous chemical mixture within the desired particle sizes of powders. For the calcination procedure, the annealing ambient combination is preferred to be 800 °C temperature and 36 hours annealing period in the furnace under the atmospheric air pressure condition. Both the heating and cooling rates are adjusted as 5 °C/min. After the calcination process, we remove the homogenous powder of chemicals (the last color of powders turns into the blackish) from the furnace. We ground the blackish powder for 30 minutes in the medium of air in an agate by a pestle. The last (milled) powder of chemicals is exposed

to pelletize into the rectangular bars with the volume of 1.5x0.5x0.2 cm^3 at the load strength of 300 MPa in air atmosphere conditions. The different vanadium added bulk samples are annealed at 850 °C for 24 h. All the materials exposed to different vanadium addition level such as x=0.01, 0.03, 0.05, 0.07, 0.10 and 0.30 will thereafter be shown to be pure, V-01, V-03, V-05, V-07, V-1 and V-3, respectively. In the current work the magneto transport measurements are done in the cryostat system for 5 different applied magnetic fields varying from 0 to 5T. The experimental signals are gathered in the temperatures between 5 K and 130 K at 5mA current.

3. RESULTS AND DISCUSSION

In the current work, the influence of vanadium addition within the different molar ratios of 0.0-0.3 on the fundamental magnetic performance features, viz. the active and dynamic electron-phonon couplings throughout the intra-grain regions, flux pinning abilities for two-dimensional pancake vortices, energy barriers for vortices motions, recoupling line-like mechanism, lattice period for the vortices, interplane interaction energy, movement of vortices to neighboring state length throughout pinning regions, dynamic nucleation centers in the superconducting system, recoupling line-like mechanism, pinning center sizes, interplane interaction energy for Josephson coupling lengths of Bi-2223 system is investigated by the magneto transport measurement tests performed in various external magnetic fields (abbreviated as $\mu_0 H$) differing between 0T and 5T. We give all the measurement magneto resistivity results for the pure and V-doped bulk Bi-2223 samples in the whole vanadium dopant concentration ranges in Figs. 1-3. Prior to the numerical values, we will discuss the general trend in the magneto resistivity curves with the vanadium addition. We give the curves in three different figures since the vanadium added Bi-2223 superconducting compounds exhibit three different mechanism because of their own the crystallinity problems and the induced the pair-breaking mechanism (to be discussed in the following section in detail) in the superconducting system. It is visible form Fig. 1 that the superconductivity for the pure, V-01, V-03, V-05 superconducting compounds cannot be destroyed totally up to the maximum external magnetic field strength of 5 T. However, from higher vanadium concentration value of x=0.05 onwards we could not determine the offset critical transition temperature values for the bulk

V-07, V-1 and V-3 ceramic samples (See Fig. 2 and 3). The V-07 superconducting compound can carry the maximum 3 T applied magnetic field whereas the V-1 and V-3 sample can carry the magnetic field strength of only 1 T. It is clear that the excess vanadium causes the impurity in the superconducting system, thus, the Bi-2223 material with excess vanadium dopant cannot carry much more magnetic field strength.

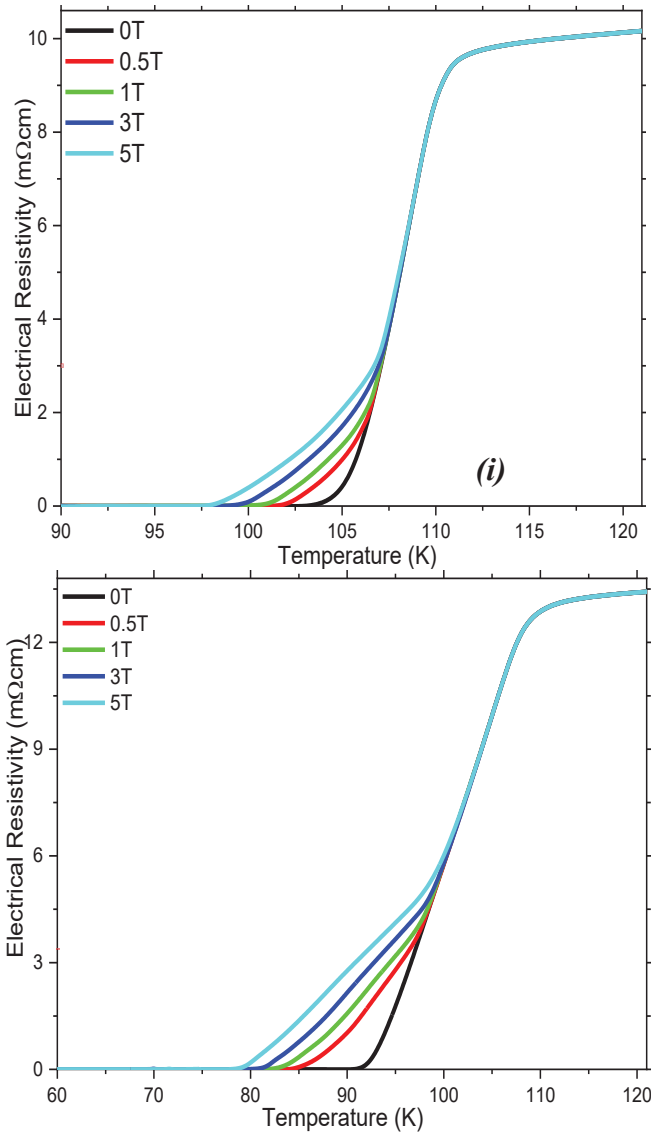

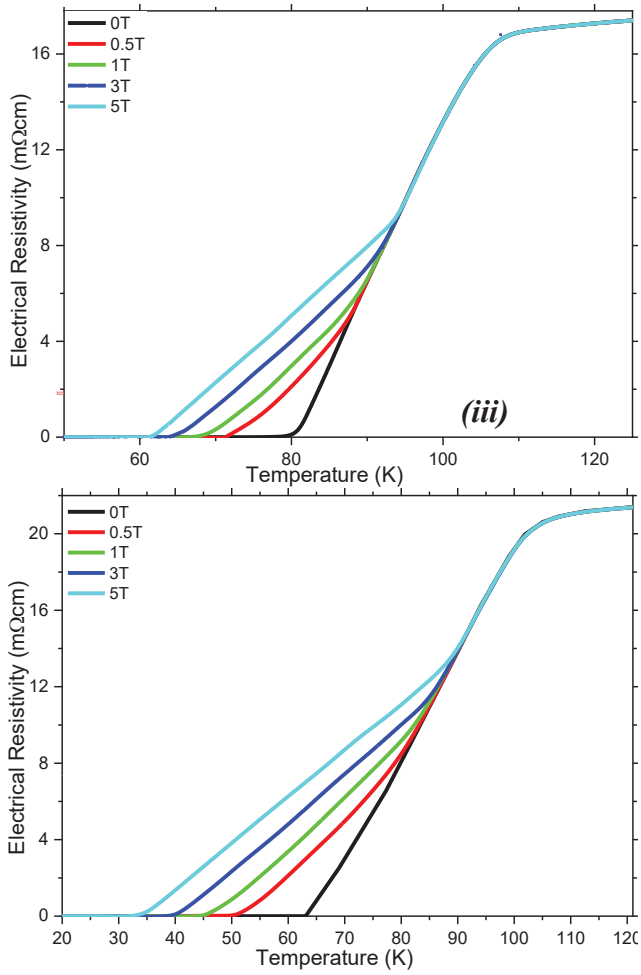

Figure 1 Variation of magneto resistivity curves against temperature at various applied field strengths for (i) virgin, (ii) V-01, (iii) V-03 and (iv) V-05 ceramic compounds.

In more detail, it is apparent from the curves that the magneto resistivity performance of Bi-2223 superconducting system is found to depend strongly on both the external magnetic field strength and vanadium addition content level. As well known that under the applied magnetic field two main mechanisms lead to damage the superconductivity phenomenon. The first of them is Pauli paramagnetic effect or spin effect due to the appearance of Zeeman splitting for the

spin-singlet pairing under the applied magnetic field strength. Diamagnetic effect or orbital limit effect is the second reason and is related to the increment of kinetic energy due to the fact that the applied magnetic field is excluded by the orbital current. Among them, the diamagnetic effect predominantly takes place at relatively higher temperature loser to the critical transition temperature. Thus, the pair-breaking mechanism (meaning: there appears an interaction between the conduction electron spins and quantum spin number (S) of vanadium impurities) is realized by the diamagnetic effect under the applied magnetic field strength. On the other hand, the Pauli paramagnetic effect is encountered at the low temperature regime and higher applied magnetic field strength. Accordingly, the superconducting characteristic features of Bi-based superconducting ceramic materials can seriously be damaged under the applications of current density and external magnetic field. Moreover, with the assistant of magneto resistivity graphics gathered in Fig. 1 we define the fundamental superconducting characteristic parameters of offset and onset (T_c^{offset} and T_c^{onset}) critical transition temperature values. It is emphasized here that the value between the offset and onset critical transition temperatures is known to be the broadening transition width (namely, it can be shortened to be $\Delta T_c = T_c^{onset} - T_c^{offset}$. We infer every parameter (T_c^{offset}, T_c^{onset} and related ΔT_c) from the magneto resistivity curves and display in Table 1 for emphasizing the influence of vanadium inclusions in the Bi-2223 crystal system. It is found that both the T_c^{offset} and T_c^{onset} parameters are dramatically affected (especially former one) by ascending amount of vanadium impurity concentration in the host superconducting crystal structure and external magnetic fields applied. It is to be stressed here that the T_c^{offset} parameter is connected to inter-granular component in the crystal structure, and is affected by the density of states distribution at Fermi energy level in the superconducting system. As to the T_c^{onset} parameter for the superconducting materials, the parameter is related to electrical transition of intra granular regions throughout the crystal structure into the superconducting state. That is why; the T_c^{onset} value is determined by the capability of active and dynamic electron-phonon couplings in the superconducting system [28–30]. According to measurement results provided, the reduction of critical transition

temperatures with ascending the vanadium addition in the crystal lattice of superconducting system results dominantly from the dramatic enhancement in the crystallinity problems arranged as porosity, defects and related flaws in the Bi-2223 ceramic compounds [31, 32]. Another possible mechanism being in charge of the degradation of T_c^{onset} and T_c^{offset} values is related to the reduction of localization phenomenon for the density of states distribution at Fermi energy level in the superconducting system [33, 34].

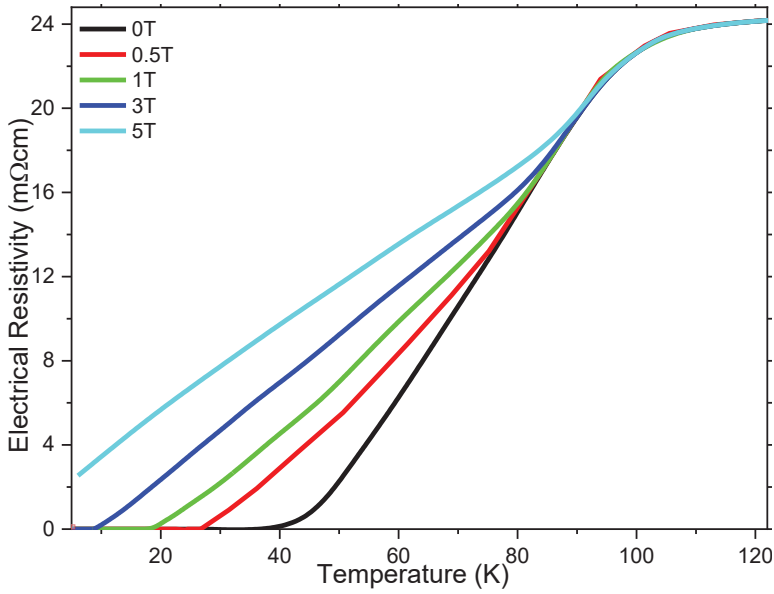

Figure 2 Magneto resistivity performances for V-07 superconducting material under applied magnetic fields.

In this regard, we can easily claim that the increment of V-ions addition in the Bi-2223 system causes to degrade of flux pinning abilities for 2D pancake vortex and dynamic nucleation centers in the superconducting system. In other words, the presence of vanadium impurities leads to truncate the active and dynamic electron-phonon couplings throughout the intra-grain regions, energy barriers for vortices motions, recoupling line-like mechanism, lattice period for the vortices, interplane interaction energy, movement of vortices to neighboring state length throughout pinning regions, interplane interaction energy for

Josephson coupling lengths and pinning center sizes in bulk Bi-2223 superconductor. Similarly, the augmentation level of V-ions concentration in the system results in much more induced recoupling line-like mechanism in the Bi-2223 crystal lattices. Moreover, based on the T_c^{offset} and T_c^{onset} values in Table 1 it is seen that the applied magnetic field is obtained to much more affect the T_c^{offset} parameters as compared to the T_c^{onset} parameters.

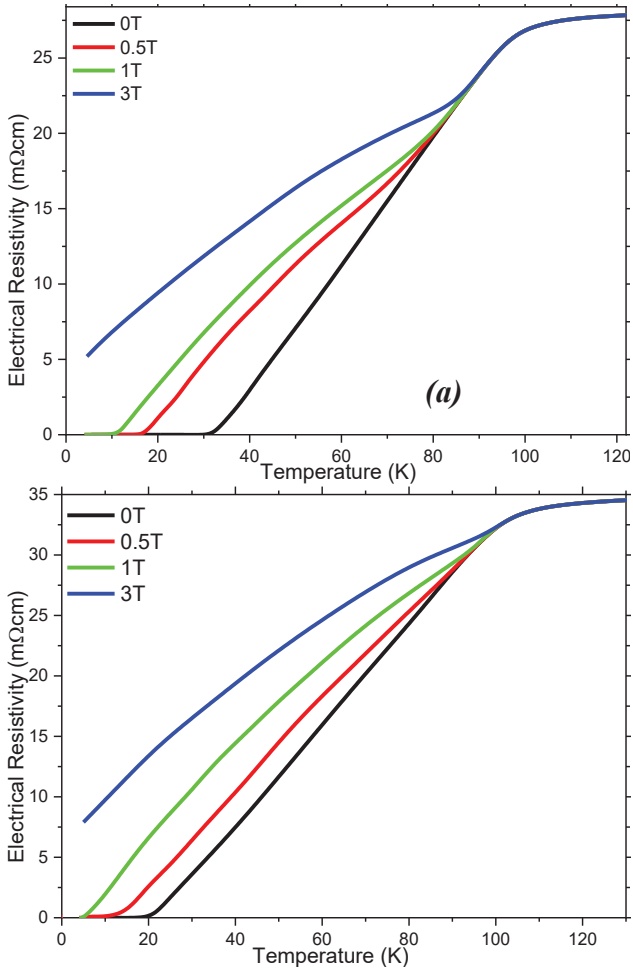

Figure 3 Differentiation in magneto resistivity curves as a function of temperature at various external magnetic fields for bulk V-1 and V-3 superconducting materials.

As for the numerical values for the T_c^{offset} and T_c^{onset} values, the T_c^{offset} parameters are recorded as about 103.17 K, 91.11 K, 79.42 K, 56.68 K, 38.07 K, 30.29 K and 18.38 K for the virgin sample, V-01, V-03, V-05, V-07, V-1 and V-3 samples, respectively, without any external field. With the increment in the applied magnetic field, it is, of course, that the T_c^{offset} values degrade rapidly. In this respect, the T_c^{offset} value for the pristine compound decreases towards to 98.06 K temperature under the maximum applied field of 5T. Similarly, the V-01 superconducting sample exhibits the T_c^{offset} value of 78.93 K at 5 T applied field. The T_c^{offset} values (deduced from Figure 1) are found to be about 61.43 K and 33.36 K for the V-03 and V-05 ceramic compounds, respectively. As for the second group (the bulk V-07 superconducting material), we only determine the T_c^{offset} values for the maximum external field of 3 T. On this basis, the material presents the T_c^{offset} value of 8.52 K. Finally, the last superconducting materials including the solid V-1 and V-3 superconductors show the T_c^{offset} values of 10.57 K and about 4.91 K at only 1 T external magnetic field strength. In this regard, it is to be emphasized here that the increase in V-ions impurity level degrades harshly the T_c^{offset} values. Namely the sensitivity (strength) to applied magnetic field is found to tend to enhance regularly with the increase in the vanadium addition level. Consequently, the bulk V-3 sample(highest dopant level) displays the most response to the applied field. This evidence is verified with the differentiation in the broadening transition width (ΔT_c) values, also. In more detail, the smallest value (assigned as the best sample) of 5.11 K is attributed to pristine material, on the other hand the bulk V-05 superconducting ceramic compound with the ΔT_c value of 26.32 K is received to be the worst material for the first group. It is to be mentioned here that we could not determine the ΔT_c value for 5 T (in fact for 3 T) applied magnetic field.

Table 1 Experimental findings depending on magneto resistivity measurements for pure and vanadium added ceramic materials under magnetic fields

Samples	T_c^{onset} *(K)*	T_c^{offset} *(K)*					ΔT_c
		0T	*0.5T*	*1T*	*3T*	*5T*	
Pure	110.92	103.17	101.85	100.87	99.60	98.06	5.11
V-01	109.48	91.11	84.67	82.81	81.15	78.93	12.18
V-03	106.95	79.42	71.33	68.04	64.15	61.43	17.99
V-05	103.94	59.68	50.27	44.64	39.43	33.36	26.32
V-07	99.21	38.07	26.72	17.81	8.52	----	----
V-1	98.98	30.29	16.39	10.57	----	----	----
V-3	97.45	18.38	11.96	4.91	----	----	----

As for the T_c^{onset} parameters, the compounds (pure, V-01, V-03, V-05, V-07, V-1 and V-3) present the values of about 110.92 K, 109.48 K, 106.95 K, 103.94 K, 99.21 K, 98.98 K and 97.45 K respectively (see Table 1). Based on the values observed, the T_c^{onset} parameters are noticed to reduce systematically with increasing the vanadium impurity addition level because of the augmented defects and disorders in the bulk Bi-2223 system. Conversely, the magnetic field cannot change the T_c^{onset} parameters for all the samples since the external field applied cannot harm on the capability of active and dynamic electron-phonon couplings in the Bi-2223 superconducting system

4. CONCLUSION

In the present study, we scrutinize the crucial variation of fundamental magneto-resistivity performance parameters and ability/formation of effective and active flux pinning centers in the Bi-2223 crystal system by use of the magneto-transport measurements conducted in the applied magnetic fields intervals 0–5T with the

vanadium concentration level (Bi-2223+V_x, where x is between 0.00 and 0.30). Besides, the influence of V-ions on the grain boundary coupling problems, ability/strength of vortex lattice period and elasticity of thermal fluxons in the correlated two-dimension (2D) pancake vortices. The solid compounds are prepared by the standard solid-state reaction route in the room temperature conditions at the atmospheric pressure. The magneto-resistivity curves are taken from the temperature intervals 15 K-125 K at a closed-cycle cryogenic refrigeration system. Besides, the discussions are determined from the fundamental quantitates as regards the offset (T_c^{offset}), onset (T_c^{onset}) critical transition temperature and broadening transition width ($\Delta T_c = T_c^{onset} - T_c^{offset}$) parameters. Based on the experimental measurement findings deduced from the magneto-transport curves, the presence of V-ions concentration in solid Bi-2223 crystal structure significantly diminishes the magneto-resistivity performances because of the rapid decrement (augmentation) in the formation of dynamic flux pinning centers (random distribution of artificial pinning centers) in the crystal lattice and the ability/strength of vortex lattice period and elasticity (the grain boundary coupling problems). Similarly, the vanadium concentration leads to degrade the energy barriers of flux lines between the copper-oxide consecutively stacked layers for the pinning ability so that the flux lines can easily jump to the neighboring states due to the appearance of recoupling linelike nature in the Cu-O_2 consecutively stacked layers. Finally, we examine the change in the hole localization problems for the density of states distribution at Fermi energy level in the Bi-2223 superconducting system. Numerically, the T_c^{onset} parameters are found to be about 110.92 K, 109.48 K, 106.95 K, 103.94 K, 99.21 K, 98.98 K and 97.45 K for the pure, V-01, V-03, V-05, V-07, V-1 and V-3 superconducting compounds, respectively. As for the T_c^{offset} values, the pure sample has the maximum offset critical transition temperature of 103.17 K whereas the minimum T_c^{offset} value is observed for the V-3 superconducting material. Under the maximum external magnetic field of 5 T the T_c^{offset} degrades towards to the value of 98.06 K, 78.93 K, 61.43 K and 33.36 K for the pure, V-01, V-03 and V-05 ceramic compounds (the first group), respectively. However, we could not define the T_c^{offset} value at 5 T applied field for the other bulk materials prepared in this work. In this regard, in the first group samples the pure sample

(best material) possesses the smallest ΔT_c value of 5.11 K. All in all, the pure sample is recorded as the least response to applied field. On the other hand, the V-3 compound is found to be rather more sensitive to the applied field.

REFERENCES

[1] H.K. Onnes, Further experiments with Liquid Helium. D. On the change of Electrical Resistance of Pure Metals at very low Temperatures, etc. V. The Disappearance of the resistance of mercury, Koninklijke Nederlandsche Akademie van Wetenschappen Proceedings, 14 (1911) 113-115.

[2] S.B. Guner, Y. Zalaoglu, T. Turgay, O. Ozyurt, A.T. Ulgen, M. Dogruer, G. Yildirim, A detailed research for determination of Bi/Ga partial substitution effect in Bi-2212 superconducting matrix on crucial characteristic features, J. Alloy. Compd. 772 (2019) 388–398.

[3] T.A. Coombs, A finite element model of magnetization of superconducting bulks using a solid-state flux pump, IEEE T. Appl. Supercond. 21 (2011) 3581–3586.

[4] A.T. Ulgen, Evaluation of Superconducting Properties and Diffusion Behavior of Ex Situ and In Situ Bulk MgB2 Materials with Ni Coating, Journal of Superconductivity and Novel Magnetism, 2019, 32(8), pp. 2383–2389

[5] A.T. Ulgen, F. Karaboga, M. Karakaya, R. Podila, A.M. Rao, I. Belenli, Improved transport properties of MgB2 superconducting round wires via minute addition of gold nanoparticles, Ceramics International, Volume 45, Issue 1, January 2019, Pages 1031-1036

[6] S.Y. Oh, H.R. Kim, Y.H. Jeong, O.B. Hyun, C.J. Kim, Joining of Bi-2212 high-T-c superconductors and metals using indium solders, Physica C 463–465 (2007) 464–467.

[7] A.T. Ulgen, I. Belenli, Time-Dependent Diffusion Coefficient of Fe in MgB2 Superconductors, Journal of Superconductivity and Novel Magnetism Volume: 30 Issue: 12 Pages: 3367-3375 Published: DEC 2017

[8] M. Chen, W. Paul, M. Lakner, L. Donzel, M. Hoidis, P. Unternaehrer, R. Weder, M. Mendik, 6.4 MVA resitive fault current limiter based on Bi-2212 superconductor, Physica C 372 (2002) 1657–1663.

[9] C.J. Poole, H.A. Farach, R. Creswick, Superconductivity, Academic Press, San Diego, 1995.

[10] M.E. Takayama, High-pressure synthesis of homologous series of high critical temperature (T_c) superconductors, Chem. Mater. 10 (1998) 2686–2698.

[11] J. Karpinski, G.I. Meijer, H. Schwer, R. Molinski, E. Kopnin, K. Conder, M. Angst, J. Jun, S. Kazakov, A. Wisniewski, P. Puzniak, J. Hofer, V. Alyoshin, A. Sin, High-Pressure Synthesis, Crystal Growth, Phase Diagrams, Structural and Magnetic Properties of $Y_{(2)}Ba_{(4)}Cu_{(N)}O_{2(2n+X)}$, $HgBa_2Ca_{n-1}Cu_nO_{2n+2+y}$ and Quasi-One-Dimensional Cuprates, Supercond. Sci. Technol. 12 (1999) R153–181.
[12] H. Yamauchi, M. Karppinen, Application of High-Pressure Techniques: Stabilization And Oxidation-State Control of Novel Superconductive and Related Multi-Layered Copper Oxides, Supercond. Sci. Techol. 13 (2000) R33–R52.
[13] W. Buckel, R. Kleiner, Superconductivity: Fundamentals and Applications, 2nd ed., Wiley-VCH Verlag, Weinheim, (2004).
[14] A.M. Luiz, Applications of High-Tc Superconductivity, Janeza Trdine, India, (2011)
[15] J.D. Hodge, H. Muller, D.S. Applegate, Q. Huang, A resistive fault current limiter based on high temperature superconductors, Appl. Supercond. 3 (1995) 469–482.
[16] A.V. Narlikar, Superconductors, Oxford Press, 2014, 1st Ed.
[17] R. Wesche, Physical Properties of High-Temperature Superconductors, (Wiley Series in Materials for Electronic & Optoelectronic Applications) 1st Edition, Kindle Edition, 516 pages
[18] M. Cyrot, D. Pavuna, Introduction to Superconductivity and High-Tc Materials, World Scientific Publishing Company, 1992.
[19] T.P. Sheahen, Introduction to High-temperature Superconductivity, 1st ed., Kluwer Academic Publishers, New York, Boston, 2002
[20] A.M. Hermann, J.V. Yakhmi, eds. Thallium-Based High-Temperature Superconductors, Marcel Dekker, 1994.
[21] H. Miao, M. Meinesz, B. Czabai, J. Parrell, S. Hong, Microstructure and Jc improvements in multifilamentary Bi-2212/Ag wires for high field magnet applications, AIP Conference Proceedings 986 (2008) 423–430.
[22] K. Koyama, S. Kanno, S. Noguchi, Electrical, Magnetic and superconducting properties of the quenched Bi2Sr2Ca1-XNdXCu2O8+y system, Jpn. J. Appl. Phys. 29 (1990) L53–L56.
[23] Ulgen, A.T., Erdem, U., Zalaoglu, Y., Turgay, T., Yildirim, G. Effect of vanadium addition on fundamental electrical quantities of Bi-2223 crystal structure and semi-empirical model on structural disorders-defects, Journal of Materials Science: Materials in Electronics, 2020, 31(16), pp. 13765–13777.
[24] M.B. Turkoz, U. Erdem, (2020). Investigation of the Electrical and

Structural Effects of Li Dopping on YBCO Ceramic Superconducting Materials Prepared with Nitrate Compounds. International Journal of Engineering Research and Development, 12, 210-216.
[25] Yaşar, E., Erdem, U., Tuna, M. A., Armağan, O., & Kırındı, T. (2018). The Effect of Ti Content on α'Martensite Phase Transformation, and Magnetic Properties by Mössbauer Spectroscopy in Fe-30% Ni-x% Ti (wt%) Alloys. Acta Physica Polonica A, 133(5), 1165-1169.
[26] Y. Zalaoglu, T. Turgay, A.T. Ulgen, U. Erdem, M.B. Turkoz, G. Yildirim, (2020). A novel research on the subject of the load-independent microhardness performances of Sr/Ti partial displacement in Bi-2212 ceramics. Journal of Materials Science: Materials in Electronics, doi: https://doi.org/10.1007/s10854-020-04724-6
[27] A.T. Ulgen, I. Belenli, The Effect of Fe Diffusion on Some Physical and Superconducting Properties of MgB2 JOURNAL OF SUPERCONDUCTIVITY AND NOVEL MAGNETISM Volume: 30 Issue: 4 Pages: 1089-1095 Published: APR 2017
[28] R. Shabna, P.M. Sarun, S. Vinu, U. Syamaprasad, Charge carrier localization and metal to insulator transition in cerium substituted (Bi,Pb)-2212 superconductor, J. Alloy. Compd. 493 (2010) 11–16.
[29] D.M. Newns, P.C. Pattnaik, C.C. Tsuei, Role of vanhove singularity in high-temperature superconductors - Mean field, Phys. Rev. B 43 (1991) 3075–3084.
[30] S. Martin, M. Gurvitch, C.E. Rice, A.F. Hebard, P.L. Gammel, R.M. Fleming, A.T. Fiory, Nonlinear temperature-dependence of the normal-state resistivity in $YBa_2Cu_4O_{8\gamma}$ films, Phys. Rev. B 39 (1989) 9611–9613.
[31] S. Martin, M. Gurvitch, C.E. Rice, A.F. Hebard, P.L. Gammel, R.M. Fleming, A.T. Fiory, Nonlinear Temperature-Dependence of the Normal-State Resistivity in $YBa_2Cu_4O_{8+-y}$ Films, Phys. Rev. B 39 (1989) 9611–9613.
[32] D.M. Newns, P.C. Pattnaik, C.C. Tsuei, Role of Vanhove Singularity in High-Temperature Superconductors-Mean field, Phys. Rev. B 43 (1991) 3075–3084.
[33] G. Yildirim, Beginning Point of Metal to Insulator Transition for Bi-2223 Superconducting Matrix Doped with Eu Nanoparticles, J. Alloy. Compd. 578 (2013) 526–535.
[34] H. Eskes, G.A. Sawatzky, Tendency Towards Local Spin Compensation of Holes in the High-T_c Copper-Compounds, Phys. Rev. Lett. 61 (1988) 1415–1418.

Chapter 9

ON MP ITERATIVE METHOD FOR ACM IN BANACH SPACES

Kadri DOGAN[1]

1 Kadri DOĞAN, Department of Computer Engineering, Artvin Çoruh University, Artvin, Turkey, Email: dogankadri@hotmail.com

1 Introduction and Preliminaries

Let C be a nonempty closed convex subset of a Banach space X and S be a self map of C. Suppose $s_0 \in C$ and $s_{n+1} = f(S, s_n)$ defines an iterative procedure which yields a sequence of points $\{s_n\}_{n=0}^{\infty}$ in C. For example, $s_{n+1} = f(S, s_n) = Ss_n$. Suppose $\{y_n\}_{n=0}^{\infty} \subset C$ and $\{\epsilon_n\}_{n=0}^{\infty} \subset \mathbb{R}^+$ are two sequences given by $\epsilon_n = \|y_{n+1} - f(S, y_n)\|$ and $F(S)$ is the set of fixed points of S such that $F(S) = \{s^* \in C: Ss^* = s^*\}$ with $\{s_n\}_{n=0}^{\infty}$ converges strongly to $s^* \in F(S)$. If $\lim_{n\to\infty} \epsilon_n = 0$ implies that $\lim_{n\to\infty} y_n = s^*$, then the iterative method $\{s_n\}_{n=0}^{\infty}$ is said to be S-stable or stable with respect to S

In the last fifty years, many researchers have demonstrated an effort to identify a new iterative process and they have been successful in this area. The most famous of these iterative processes are defined as follows:

In 1890, the Picard iterative process [1] was defined by Picard as follows:

$$p_{n+1} = Sp_n,\ n \in \mathbb{N} \tag{1}$$

and is used to approximate fixed point of contraction mappings satisfying the following condition

$$d(Sx, Sy) \leq \gamma d(x, y), \forall x, y \in B \text{and} \gamma \in [0,1). \tag{2}$$

In 1953, the Mann iterative process [2] was defined by Mann as follows:

$$w_{n+1} = (1 - \alpha_n)w_n + \alpha_n Sw_n, foralln \in \mathbb{N} and \alpha_n \in [0,1]. \tag{3}$$

In 1974, the Ishikawa iterative process [3] was defined by Ishikawa as follows:

$$\begin{cases} I_1 \in C \\ I_{n+1} = (1 - a_n)I_n + a_n Sh_n \\ h_n = (1 - b_n)I_n + b_n SI_n, \end{cases} \tag{4}$$

where, $\{a_n\}_{n\in\mathbb{N}}$ and $\{b_n\}_{n\in\mathbb{N}} \subset [0,1]$.

In 2013, the Picard-Mann iterative process [4] defined by Khan, as follows:

$$\begin{cases} k_1 \in C \\ k_{n+1} = St_n \\ t_n = (1 - c_n)k_n + c_n Sk_n,\ foralln \in \mathbb{N}, \end{cases} \tag{5}$$

where, $\{c_n\}_{n\in\mathbb{N}} \in (0,1)$.

When defining an iteration process, two important criteria should be considered. These criteria are speed and simplicity. For this reason, the Picard- Mann iteration process is important. Considering the Picard-Mann and some others iterative procedures in the current literature, we introduce a new iterative procedure is called Mann-Picard iterative process. Our iterative process defined by $\{\pi_n\}_{n\in\mathbb{N}}$ as follows:

$$\begin{cases}\pi_1 \in C \\ \pi_{n+1} = (1-\varphi_n)\rho_n + \varphi_n S\rho_n \\ \rho_n = S\pi_n, \quad \forall n \in \mathbb{N},\end{cases} \tag{6}$$

where $\{\varphi_n\}_{n\in\mathbb{N}} \in [0,1]$.

In the sequel, we will prove that iterative process (6) converges to the unique fixed point of ACM satisfying (8). We also prove that iterative process (1.6) is equivalent to Mann iterative process and faster than all Picard, Mann and Ishikawa iterative processes when all converge to the fixed point of ACM (8). Finally, using iterative process (6), we prove a data dependence result for the fixed of point of ACM satisfying (8).

To prove our main results, we need to the following Theorems, Lemmas and Definitions.

Definition 1.1 [5] If the operator $T: C \to C$ is almost-contraction mapping (ACM), then, for all $x, y \in B$, the following conditions are performed

$$(i) L \geq 0 \; and \; \delta \in (0,1),$$
$$(ii) \|Sx - Sy\| \leq \delta\|x - y\| + L\|y - Sx\|. \tag{7}$$

Theorem 1.2 [5] Let (X, d) be a complete metric space and $T: X \to X$ be an ACM for which there exist $\delta \in (0,1)$ and some $L_1 \geq 0$ such that

$$\|Tx - Ty\| \leq \delta\|x - y\| + L_1\|x - Tx\|. \tag{8}$$

Then, T has a unique fixed point.

Theorem 1.3 [5] Let X be a Banach space and C be a nonempty closed convex subset of X. Assume that the map $S: C \to C$ is satisfies all of the conditions of ACM (8). Then $F(S) \neq \emptyset$.

Definition 1.4 Let $\{\omega_n\}_{n\in\mathbb{N}}$ and $\{\varpi_n\}_{n\in\mathbb{N}}$ be two sequences and $\{\omega_n\}_{n\in\mathbb{N}}$ and $\{\varpi_n\}_{n\in\mathbb{N}}$ be converging to the same fixed point p of S. Suppose that

$$\lim_{n\to\infty} \frac{\|\omega_n - s^*\|}{\|\varpi_n - s^*\|},$$

then, it said that $\{\omega_n\}_{n\in\mathbb{N}}$ converges faster than $\{\varpi_n\}_{n\in\mathbb{N}}$ to s^*.

Definition 1.5 [5] Let $\{\omega_n\}_{n\in\mathbb{N}}$ and $\{\varpi_n\}_{n\in\mathbb{N}}$ be two sequences both converging to the same fixed point s^*, the error estimates

$$\|\omega_n - s^*\| \leq a_n, \forall n \in \mathbb{N}$$
$$\|\varpi_n - s^*\| \leq b_n, \forall n \in \mathbb{N}$$

are valiable where the sequences $\{a_n\}_{n\in\mathbb{N}}$ and $\{b_n\}_{n\in\mathbb{N}}$ converge to zero. Suppose that

$$\lim_{n\to\infty} \frac{a_n}{b_n} = p$$

(1) If $p = 0$, then $\{a_n\}_{n\in\mathbb{N}}$ converges faster than $\{b_n\}_{n\in\mathbb{N}}$.

(2) If $0 < p < \infty$, then $\{a_n\}_{n\in\mathbb{N}}$ and $\{b_n\}_{n\in\mathbb{N}}$ have equal

convergence

(3) If $p = \infty$, then $\{b_n\}_{n\in\mathbb{N}}$ converges faster than $\{a_n\}_{n\in\mathbb{N}}$.

So, if $\{a_n\}_{n\in\mathbb{N}}$ converges faster than $\{b_n\}_{n\in\mathbb{N}}$ then $\{\omega_n\}_{n\in\mathbb{N}}$ converges faster than $\{\varpi_n\}_{n\in\mathbb{N}}$.

Definition 1.6 [17] Let S, $S^o: C \to C$ be two operators satisfying the ACM. $\forall p \in C$ and $\epsilon > 0$ a fixed real number, if the following condition is performed such that

$$\|S - S^o\| \leq \epsilon,$$

then the operator S is said to be an approximate operator of S^o.

Lemma 1.7 [18] Let $\{s_n\}_{n\in\mathbb{N}}$ and $\{\tau_n\}_{n\in\mathbb{N}}$ be two nonnegative sequences satisfiying inequality:

$$s_{n+1} \leq (1 - \varsigma_n)s_n + \varsigma_n\tau_n,$$

where $\forall n \in \mathbb{N}$, $\tau_n \in (0,1)$ and $\sum_{n=1}^{\infty}\varsigma_n = \infty$. Then the following inequality holds

$$0 \leq \limsup_{n\to\infty} s_n \leq \limsup_{n\to\infty} \tau_n,$$

it is implies that $\lim_{n\to\infty} s_n = 0$.

Lemma 1.8 [19] Let $\{s_n\}_{n\in\mathbb{N}}$ and $\{\tau_n\}_{n\in\mathbb{N}}$ be two nonnegative sequences satisfying inequality:

$$s_{n+1} \leq (1 - \varsigma_n)s_n + \tau_n,$$

where $\forall n \in \mathbb{N}$, $\tau_n \in (0,1)$, $\sum_{n=1}^{\infty}\varsigma_n = \infty$ and $\lim_{n\to\infty}\frac{\tau_n}{\varsigma_n} = 0$. Then $\lim_{n\to\infty} s_n = 0$.

2 Main results

Theorem 2.1 Let $S: C \to C$ be an operator satisfying the condition of ACM (8) with $F(S) \neq \emptyset$ and the sequence $\{\pi_n\}_{n\in\mathbb{N}}$ defined by (6) with $\{\varphi_n\}_{n\in\mathbb{N}} \in [0,1]$ such that $\sum_{n=1}^{\infty}\varphi_n = \infty$. Then the sequence $\{\pi_n\}_{n\in\mathbb{N}}$ converges to the unique fixed point s^* of S.

Proof. From Theorems 1.2 and 1.3, we have uniqueness and existence of fixed point $s^* \in F(S)$.

By (6) and (8), we obtain

$$\begin{aligned}\|\pi_{n+1} - s^*\| &= \|(1 - \varphi_n)\rho_n + \varphi_n S\rho_n - s^*\| \\ &\leq (1 - \varphi_n)\|\rho_n - s^*\| + \varphi_n\|S\rho_n - s^*\| \\ &\leq (1 - \varphi_n)\|\rho_n - s^*\| + \varphi_n\delta\|\rho_n - s^*\| + \\ \varphi_n L\|s^* - Ss^*\| \quad &(9) \\ &= \big(1 - \varphi_n(1 - \delta)\big)\|\rho_n - s^*\| + \varphi_n L\|s^* - Ss^*\|.\end{aligned}$$

Again

$$\|\rho_n - s^*\| = \|S\pi_n - s^*\|$$

$$\leq \delta\|\pi_n - s^*\| + L\|s^* - Ss^*\|.$$

Substituting (10) in (9) yields that

$$\|\pi_{n+1} - s^*\| \leq \delta\big(1 - \varphi_n(1-\delta)\big)\|\rho_n - s^*\| + \big(1 - \varphi_n(1-\delta)\big)L\|s^* - Ss^*\| + \varphi_n L\|s^* - Ss^*\|$$
$$\leq \big(1 - \varphi_n(1-\delta)\big)\|\rho_n - s^*\| + (1 + \varphi_n\delta)L\|s^* - Ss^*\|.$$

Since $\|s^* - Ss^*\| = 0$, we have

$$\|\pi_{n+1} - s^*\| \leq \big(1 - \varphi_n(1-\delta)\big)\|\rho_n - s^*\|.$$

By induction assumption, we obtain

$$\|\pi_{n+1} - s^*\| \leq \big(1 - \varphi_n(1-\delta)\big)\|\rho_n - s^*\|$$
$$\|\pi_n - s^*\| \leq \big(1 - \varphi_{n-1}(1-\delta)\big)\|\rho_{n-1} - s^*\|$$
$$\|\pi_{n-1} - s^*\| \leq \big(1 - \varphi_{n-2}(1-\delta)\big)\|\rho_{n-2} - s^*\|$$
$$\vdots$$
$$\|\pi_1 - s^*\| \leq \big(1 - \varphi_0(1-\delta)\big)\|\rho_0 - s^*\|, \text{for all} n \in \mathbb{N}.$$

Hence

$$\|\pi_{n+1} - s^*\| \leq_{i=0}^{n} \big(1 - \varphi_i(1-\delta)\big)\|\rho_0 - s^*\|$$
$$\leq \|\rho_0 - s^*\| e^{(-(1-\delta)\sum_{n=1}^{\infty}\varphi_n)}.$$

Since $\delta \in (0,1)$ and $\sum_{n=1}^{\infty}\varphi_n$, we have

$$\lim_{n\to\infty}\|\pi_{n+1} - s^*\| = 0,$$

and it implies that $\lim_{n\to\infty}\pi_n = s^*$.

Theorem 2.2 Let $S: C \to C$ be an operator satisfying the condition of ACM (8) with $F(S) \neq \emptyset$ and two sequences $\{\pi_n\}_{n\in\mathbb{N}}$ and $\{w_n\}_{n\in\mathbb{N}}$ defined by (6) and (3) (respectively) with $\{\varphi_n\}_{n\in\mathbb{N}} \in [0,1]$ such that $\sum_{n=1}^{\infty}\varphi_n = \infty$. Also, if the initial values are the same, then $\{\pi_n\}_{n\in\mathbb{N}}$ and $\{w_n\}_{n\in\mathbb{N}}$ are equivalent when they convergence to the fixed point s^* of S.

Proof. Under assumption $\pi_n \to s^*$ as $n \to \infty$, we shall show that $w_n \to s^*$ as $n \to \infty$.
Using (1), (6) and (3), we obtain

$$\|\pi_{n+1} - w_{n+1}\| = \|(1-\varphi_n)\rho_n + \varphi_n S\rho_n - (1-\varphi_n)w_n + \varphi_n Sw_n\|$$
$$\leq (1-\varphi_n)\|\rho_n - w_n\| + \varphi_n\|S\rho_n - Sw_n\|$$
$$\leq (1-\varphi_n)\|\rho_n - w_n\| + \varphi_n\delta\|\rho_n - w_n\| + \varphi_n L\|\rho_n - S\rho_n\|$$

$$\leq \big(1-\varphi_n(1-\delta)\big)\|\rho_n - w_n\| + +\varphi_n L\|\rho_n - S\rho_n\|.$$

Again, from (6), we obtain

$$\|\rho_n - w_n\| = \|S\pi_n - w_n\|$$
$$\leq \|S\pi_n - \pi_n\| + \|\pi_n - w_n\|$$

Substituting (12) in (11), we have

$$\|\pi_{n+1} - w_{n+1}\| \leq \big(1-\varphi_n(1-\delta)\big)\|\pi_n - w_n\| + \|\pi_n - S\pi_n\| + \varphi_n L\|\rho_n - S\rho_n\|$$
$$= \big(1-\varphi_n(1-\delta)\big)\|\pi_n - w_n\| + \big(1-\varphi_n(1-\delta)\big)\|\pi_n - S\pi_n\| + L\varphi_n\|\rho_n - S\rho_n\|.$$

Let

$$s_n = \|\pi_n - w_n\|,$$
$$\varsigma_n = \varphi_n(1-\delta),$$
$$\tau_n = \big(1-\varphi_n(1-\delta)\big)\|\pi_n - S\pi_n\| + L\varphi_n\|\rho_n - S\rho_n\|.$$

Since $\pi_n \to s^*$ as $n \to \infty$ it follows that

$$\|\pi_n - S\pi_n\| \leq \|\pi_n - s^*\| + \|Ss^* - S\pi_n\|$$
$$\leq \|\pi_n - s^*\| + \delta\|s^* - \pi_n\| + L\|s^* - Ss^*\|$$
$$= (1+\delta)\|\pi_n - s^*\| \to 0, \text{forall} n \in \mathbb{N},$$

and

$$\|\rho_n - S\rho_n\| \leq \|\rho_n - s^*\| + \|Ss^* - S\rho_n\|$$
$$\leq \|\rho_n - s^*\| + \delta\|s^* - \rho_n\| + L\|s^* - Ss^*\|$$
$$= (1+\delta)\|\rho_n - s^*\| + L\|s^* - Ss^*\|$$
$$= (1+\delta)\|\rho_n - s^*\|$$
$$\leq (1+\delta)\delta\|\pi_n - s^*\| + L(1+\delta)\|s^* - Ss^*\|$$
$$= (1+\delta)\delta\|\pi_n - s^*\| \to 0, \text{ forall} n \in \mathbb{N},$$

and therefore, $\lim_{n\to\infty}\|\rho_n - S\rho_n\| = \lim_{n\to\infty}\|\pi_n - S\pi_n\| = 0$, that is, $\lim_{n\to\infty}\frac{\tau_n}{\varsigma_n} = 0$. It follows from Lemma 1.8 that $\lim_{n\to\infty}\|\pi_n - w_n\| = 0$.
Also, we have

$$\|w_n - s^*\| \leq \|w_n - \pi_n\| + \|\pi_n - s^*\|,$$

it implies that $\lim_{n\to\infty}\|w_n - s^*\| = 0$.
Conversely, let $w_n \to s^*$ as $n \to \infty$, we shall show that $\pi_n \to s^*$ as $n \to \infty$.
Using (1), (6) and (3), we obtain

$$\|w_{n+1} - \pi_{n+1}\| = \|(1-\varphi_n)w_n + \varphi_n Sw_n -$$
$$(1-\varphi_n)\rho_n + \varphi_n S\rho_n\|$$
$$\leq (1-\varphi_n)\|w_n - \rho_n\| + \varphi_n\|Sw_n - S\rho_n\|$$
$$\leq (1-\varphi_n)\|w_n - \rho_n\| + \varphi_n\delta\|w_n - \rho_n\| +$$

$$\varphi_n L\|w_n - Sw_n\|$$
$$\leq \big(1-\varphi_n(1-\delta)\big)\|w_n-\rho_n\| + \varphi_n L\|w_n - Sw_n\|.$$

Again, from (6), we obtain

$$\|w_n-\rho_n\| = \|w_n - S\pi_n\|$$
$$\leq \|w_n - Sw_n\| + \|Sw_n - S\pi_n\|$$
$$\leq \|w_n - Sw_n\| + \delta\|w_n-\pi_n\| + L\|w_n - Sw_n\|$$
$$= \delta\|w_n-\pi_n\| + (1+L)\|w_n - Sw_n\|.$$

Substituting (15) in (14), we have

$$\|w_{n+1}-\pi_{n+1}\| \leq \big(1-\varphi_n(1-\delta)\big)\|w_n-\pi_n\| + \big[\big(1-\varphi_n(1-\delta)\big)(1+L) + \varphi_n L\big]\|w_n - Sw_n\|.$$

Set

$$s_n = \|w_n-\pi_n\|,$$
$$\varsigma_n = \varphi_n(1-\delta),$$
$$\tau_n = \big[\big(1-\varphi_n(1-\delta)\big)(1+L) + \varphi_n L\big]\|w_n - Sw_n\|.$$

Since $\lim_{n\to\infty} w_n = s^*$ and $Ss^* = s^*$, it is clear that $\lim_{n\to\infty}\|w_n - Sw_n\|$.
Therefore, all the conditions of Lemma 1.8 are provided, yield

$$\lim_{n\to\infty}\|w_n-\pi_n\| = 0.$$

Since $\lim_{n\to\infty}\|\pi_n - s^*\| = 0$, we obtain

$$\|\pi_n - s^*\| \leq \|\pi_n - w_n\| + \|w_n - s^*\| \to 0. \text{ as} n\to\infty.$$

this completes the proof.

Keeping in mind the results in Gürsoy [23], Soltuz [24]-[25] and Chugh and Kumar [26], we can give the following corollary:

Corollary 2.3 Let $S: C \to C$ be an operator satisfying the condition of ACM (8) with $F(S) \neq \emptyset$. Also, if the initial values is the same, then the followings are equivalent:

1. The iterative process (1) converges to $s^* \in F_T$;
2. The iterative process (3) converges to $s^* \in F_T$;
3. The iterative process (4) converges to $s^* \in F_T$;
4. The iterative process (6) converges to $s^* \in F_T$.

Theorem 2.4 Let $S: C \to C$ be an operator satisfying the condition of ACM (8) with $F(S) \neq \emptyset$ and $\tilde{S}$ is approximate operator of S. Let $\{\pi_n\}_{n\in\mathbb{N}}$ be a sequence generated by (6) with respect to S and $\{\tilde{\pi}_n\}_{n\in\mathbb{N}}$ be a sequence generated by

$$\begin{cases} \pi_1 \in C \\ \tilde{\pi}_{n+1} = (1-\varphi_n)\tilde{\rho}_n + \varphi_n \tilde{S}\tilde{\rho}_n \\ \tilde{\rho}_n = \tilde{S}\tilde{\pi}_n, \qquad \forall n \in \mathbb{N}, \end{cases} \tag{16}$$

where $\{\varphi_n\}_{n\in\mathbb{N}} \in [0,1]$ is a real sequence satisfying the following conditions:

(i) $1-\varphi_n \leq \varphi_n$,
(ii) $\sum_{n=1}^{\infty} \varphi_n = \infty$.
If $\tilde{s}^* \in F(\tilde{S})$ such that $\lim_{n\to\infty}\tilde{\pi}_n = \tilde{s}^*$, then we obtain

$$\|s^* - \tilde{s}^*\| \leq \frac{2\epsilon}{1-\delta}.$$

Proof. From (16) and (6), we have

$$\pi_{n+1} - \tilde{\pi}_{n+1} = (1-\varphi_n)(\rho_n - \check{\rho}_n) + \varphi_n\big(S\rho_n - \check{S}\check{\rho}_n\big).$$

Thus

$$\|\pi_{n+1} - \tilde{\pi}_{n+1}\| = \big\|(1-\varphi_n)(\rho_n - \check{\rho}_n) + \varphi_n\big(S\rho_n - \check{S}\check{\rho}_n\big)\big\|$$

$$\leq (1-\varphi_n)\|\rho_n - \check{\rho}_n\| + \varphi_n\big\|S\rho_n - \check{S}\check{\rho}_n\big\|$$

$$\leq (1-\varphi_n)\|\rho_n - \check{\rho}_n\| + \varphi_n\big[\|S\rho_n - S\check{\rho}_n\| + \big\|S\check{\rho}_n - \check{S}\check{\rho}_n\big\|\big] \tag{17}$$

$$\leq (1-\varphi_n)\|\rho_n - \check{\rho}_n\| + \varphi_n\delta\|\rho_n - \check{\rho}_n\| + \varphi_n L\|\rho_n - S\rho_n\| + \varphi_n\epsilon$$

$$= \big(1-\varphi_n(1-\delta)\big)\|\rho_n - \check{\rho}_n\| + \varphi_n L\|\rho_n - S\rho_n\| + \varphi_n\epsilon.$$

By using (16), (6) and (8), we obtain

$$\|\rho_n - \check{\rho}_n\| = \big\|S\pi_n - \check{S}\tilde{\pi}_n\big\|$$
$$\leq \|S\pi_n - S\tilde{\pi}_n\| + \big\|S\tilde{\pi}_n - \check{S}\tilde{\pi}_n\big\|$$
$$\leq \delta\|\pi_n - \tilde{\pi}_n\| + L\|\pi_n - S\pi_n\| + \epsilon.$$

Substituting (18) in (17), we get

$$\|\pi_{n+1} - \tilde{\pi}_{n+1}\| \leq \big(1-\varphi_n(1-\delta)\big)\delta\|\pi_n - \tilde{\pi}_n\| + \big(1-\varphi_n(1-\delta)\big)\epsilon$$
$$+\big(1-\varphi_n(1-\delta)\big)L\|\pi_n - S\pi_n\| + \varphi_n L\|\rho_n - S\rho_n\| + \varphi_n\epsilon.$$

Since $1-\varphi_n \leq \varphi_n$, we have

$$\|\pi_{n+1} - \tilde{\pi}_{n+1}\| \leq \big(1-\varphi_n(1-\delta)\big)\|\pi_n - \tilde{\pi}_n\| +$$

$$\varphi_n[(1-\delta)\epsilon + (1-\delta)L\|\pi_n - S\pi_n\| + L\|\rho_n - S\rho_n\| + \epsilon] \leq \big(1-\varphi_n(1-\delta)\big)\|\pi_n - \tilde{\pi}_n\| + \varphi_n(1-\delta)\frac{[L\|\pi_n - S\pi_n\| + L\|\rho_n - S\rho_n\| + 2\epsilon]}{(1-\delta)}.$$

we define

$$s_n = \|\pi_n - \tilde{\pi}_n\|,$$
$$\varsigma_n = \varphi_n(1-\delta),$$
$$\tau_n = \frac{[L\|\pi_n - S\pi_n\| + L\|\rho_n - S\rho_n\| + 2\epsilon]}{(1-\delta)}.$$

By Theorem 2.1, we note that $\lim_{n\to\infty}\|\pi_n - S\pi_n\| = \lim_{n\to\infty}\|\rho_n - S\rho_n\| = 0$. Because, both $\{\pi_n\}_{n\in\mathbb{N}}$ and $\{\rho_n\}_{n\in\mathbb{N}}$ converge to the fixed point of S.

Then, it follows from Lemma 1.7 that

$$0 \leq \limsup_{n\to\infty}\|\pi_n - \tilde{\pi}_n\| \leq \limsup_{n\to\infty}\frac{[L\|\pi_n - S\pi_n\| + L\|\rho_n - S\rho_n\| + 2\epsilon]}{(1-\delta)}. \quad (19)$$

So, the inequality (19) implies that

$$\|s^* - \tilde{s}^*\| \leq \frac{2\epsilon}{1-\delta}.$$

Theorem 2.5 Let $S: C \to C$ be an operator satisfying the condition of ACM (8) with $F(S) \neq \emptyset$ and the sequence $\{\pi_n\}_{n\in\mathbb{N}}$ defined by (6) with $\{\varphi_n\}_{n\in\mathbb{N}} \in [0,1]$ such that $\sum_{n=1}^{\infty}\varphi_n = \infty$. Then, the iterative procedure $\{\pi_n\}_{n\in\mathbb{N}}$ is S-stable.

Proof. Suppose that $\lim_{n\to\infty}\epsilon_n = 0$. Then, we shall establish that $\lim_{n\to\infty} y_n = s^*$. In view of ACM (8) and the fact that $\|Sy_n - s^*\| = \|Sy_n - Ss^*\|$,

$$\begin{aligned}\|y_{n+1} - s^*\| &= \big\|y_{n+1} - \big((1-\varphi_n)\rho_n + \varphi_n S\rho_n\big)\big\| \\ &\quad + \|(1-\varphi_n)\rho_n + \varphi_n S\rho_n - s^*\| \\ &\leq \epsilon_n + (1-\varphi_n)\|\rho_n - s^*\| + \varphi_n\|S\rho_n - s^*\| \\ &\leq \epsilon_n + (1-\varphi_n)\|\rho_n - s^*\| + \varphi_n\delta\|\rho_n - s^*\| + \\ &\quad L\varphi_n\|Ss^* - s^*\| \\ &\leq \epsilon_n + \big(1-\varphi_n(1-\delta)\big)\|\rho_n - s^*\| + L\varphi_n\|Ss^* - s^*\| \end{aligned} \quad (20)$$

$$\begin{aligned}\|\rho_n - s^*\| &= \|Sy_n - s^*\| \\ &\leq \delta\|y_n - s^*\| + L\|Ss^* - s^*\| \end{aligned} \quad (21)$$

Substituting (21) in (20), we have

$$\|y_{n+1} - s^*\| \leq \epsilon_n + \big(1 - \varphi_n(1-\delta)\big)(\delta\|y_n - s^*\| + L\|Ss^* - s^*\|) + L\varphi_n\|Ss^* - s^*\|$$

$$\leq \epsilon_n + \big(1 - \varphi_n(1-\delta)\big)\delta\|y_n - s^*\| + L\big(\varphi_n + \big(1 - \varphi_n(1-\delta)\big)L\big)\|Ss^* - s^*\|$$

Since $\|Ss^* - s^*\| = 0$, we obtain

$$\|y_{n+1} - s^*\| \leq \epsilon_n + \big(1 - \varphi_n(1-\delta)\big)\delta\|y_n - s^*\|.$$

Also, since $0 < \big(1 - \varphi_n(1-\delta)\big)\delta < 1$ and using Lemma 1.8, we obtain $\lim_{n\to\infty} y_n = s^*$.

Conversely, letting $\lim_{n\to\infty} y_n = s^*$, we shall establish that $\lim_{n\to\infty} \epsilon_n = 0$ as follows:

$$\epsilon_n = \big\|y_{n+1} - \big((1-\varphi_n)\rho_n + \varphi_n S\rho_n\big)\big\|$$

$$\leq \|y_{n+1} - s^*\| + \big\|s^* - \big((1-\varphi_n)\rho_n + \varphi_n S\rho_n\big)\big\|$$

$$\leq \|y_{n+1} - s^*\| + (1-\varphi_n)\|s^* - \rho_n\| + \varphi_n\|s^* - S\rho_n\|$$

$$\leq \|y_{n+1} - s^*\| + (1-\varphi_n)\|s^* - \rho_n\| + \varphi_n\delta\|s^* - \rho_n\| + \varphi_n L\|Ss^* - s^*\|$$

$$\leq \|y_{n+1} - s^*\| + \big(1 - \varphi_n(1-\delta)\big)\|s^* - \rho_n\|$$

$$\leq \|y_{n+1} - s^*\| + \big(1 - \varphi_n(1-\delta)\big)\|s^* - Sy_n\|$$

$$\leq \|y_{n+1} - s^*\| + \delta\big(1 - \varphi_n(1-\delta)\big)\|s^* - y_n\|$$

Since $\lim_{n\to\infty} y_n = s^*$, it follows that $\lim_{n\to\infty} \epsilon_n = 0$. Thus, the iterative procedure $\{\pi_n\}_{n\in\mathbb{N}}$ defined by (6) is S-stable.

Theorem 2.6 Let $S: C \to C$ be an operator satisfying the condition of ACM (8) with $F(S) \neq \emptyset$ and two sequences $\{\pi_n\}_{n\in\mathbb{N}}$ and $\{k_n\}_{n\in\mathbb{N}}$ defined by (6) and (5) (respectively) with $\{\varphi_n\}_{n\in\mathbb{N}} \in [0,1]$ such that

$\sum_{n=1}^{\infty} \varphi_n = \infty$. Also, if the initial points of $\{\pi_n\}_{n\in\mathbb{N}}$ and $\{k_n\}_{n\in\mathbb{N}}$ are equal, then the sequences $\{\pi_n\}_{n\in\mathbb{N}}$ and $\{k_n\}_{n\in\mathbb{N}}$ converge to the fixed point s^* of S with the same rate of convergence.

Proof. From Theorem 2.1, we obtain

$$\|\pi_{n+1} - s^*\| \leq \delta\big(1 - \varphi_n(1-\delta)\big)\|\pi_n - s^*\|$$

$$\|\pi_{n+1} - s^*\| \leq \delta^{n+1}\|\pi_0 - s^*\|_{i=0}^{n}\big(1 - \varphi_i(1-\delta)\big) = a_n$$

and

$$\|k_{n+1} - s^*\| \leq \delta\big(1 - \varphi_n(1-\delta)\big)\|k_n - s^*\|$$

$$\|k_{n+1} - s^*\| \leq \delta^{n+1}\|k_0 - s^*\|_{i=0}^{n}\big(1 - \varphi_i(1-\delta)\big) = b_n$$

for all n∈ ℕ.

By using Definition 1.4, we have

$$\lim_{n\to\infty} \frac{\|a_n - 0\|}{\|b_n - 0\|} = \lim_{n\to\infty} \frac{a_n}{b_n}$$
$$= \lim_{n\to\infty} \frac{\delta^{n+1}\|\pi_0 - s^*\|_{i=0}^{n}\big(1-\varphi_i(1-\delta)\big)}{\delta^{n+1}\|k_0 - s^*\|_{i=0}^{n}\big(1-\varphi_i(1-\delta)\big)}$$
$$= 1.$$

By (2) in the Definition 1.4, The MP (6) and PM (5) iterative schemes have the same rate of convergence.

Example 2.7 [16] Let $S\colon [0,2] \to [0,2]$ be a mapping such that $S = (x+2)^{\frac{1}{3}}$ and $\varphi_n = \frac{3}{4}$ for all $n \geq 15$ otherwise $\varphi_n = 0$. It is easy to see that S is a ACM with $1{,}521379706804570 \in F(S)$ and the Example 2.7 satisfies for all conditions of Theorem 2.1. If $\{\pi_n\}_{n\in\mathbb{N}}$ (6) and $\{k_n\}_{n\in\mathbb{N}}$ (5) have the same initial condition, then we show that $\{\pi_n\}_{n\in\mathbb{N}}$ (6) and $\{k_n\}_{n\in\mathbb{N}}$ (5) iterative schemes have same the rate of convergene to fixed point $1{,}521379706804570$ of S.

Table 1: Comparison rate of convergence between MP and PM iteration methods

x_n	MP	PM
x_1	1,990000000000000	1,990000000000000
x_2	1,544499673873150	1,544874898372010

x_3	1,522569021765430	1,522589308040770
x_4	1,521441018705160	1,521442067123600
. . .	. . .	. . .
x_{11}	1,521379706804630	1,521379706804630
x_{12}	1,521379706804570	1,521379706804570

It is shown by Example 2.7 that iterative method MP and PM iterative schemes have the same rate of convergence.

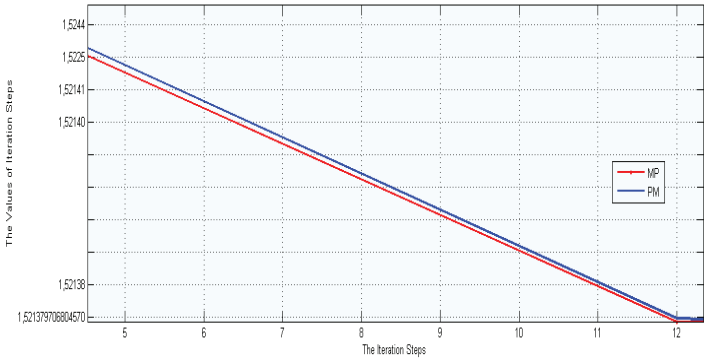

Figure 1: Convergence behavior of MP and PM iterative schemes.

Figure1 shows the rate of convergence between the MP and PM iterative schemes.

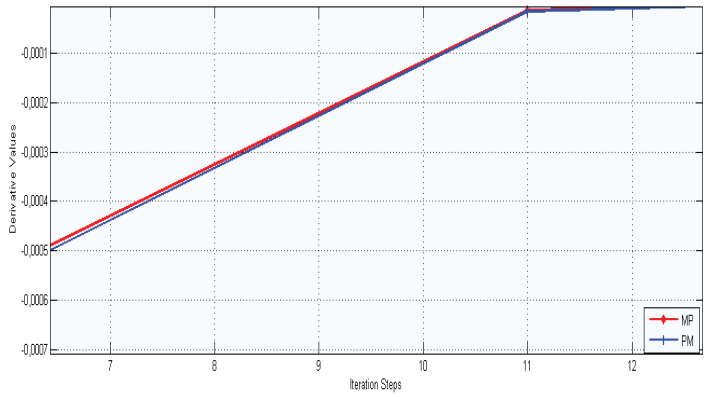

Figure 2: Derivative curves

Figure 2 is given to illustrate the changes between successive steps. A good way to show a relationship between two steps of the iteration scheme is to use Figure 2.

3. Conclusion In this study, a new iterative procedure is defined and this iteration procedure is compared with the Picard-Mann iterative procedure. It is evident that these two iterations have the same convergence rate although they are completely independent of each other. Since Picard-Mann iterative procedure is the fastest among two-step fixed point iterative schemes, the same is valid for the Mann-Picard iterative procedure.

4. References

[1] E. Picard, Memoire sur la theorie des equations aux derivees partielles et la methode des approximations successives. J. Math. Pures Appl. 6, 145-210 (1890).

[2] W.R. Mann: Mean value methods in iteration, Proc. Amer. Math. Soc., 4(1953), 506-510.

[3] S. Ishikawa: Fixed point by a new iteration method. Proc. Amer. Math. Soc. 4 (1), 147-150 (1974).

[4] SH. Khan : A Picard-Mann hybrid iterative process. Fixed Point Theory Appl. (2013). doi:10.1186/1687-1812-2013-69.

[5] V. Berinde: Picard iteration converges faster than Mann iteration for a class of quasi-contractive operators, Fixed Point Theory and Applications, vol no. 1(2004), 1-9.

[6] Zamfirescu, T. : Fix point theorems in metric spaces, Arch. Math.(Basel), 23(1972),292-298.

[7] Abbas, M. & Nazir, T. 2013. A new faster iteration process applied to constrained minimization and feasibility problems. Matematicki Vesnik, Article.

[8] V. Berinde, *O*n the approximation of fixed points of weak contractive mappings, Carpathian J. Math, **19** (2003), 7 - 22.

[9] Berinde, V. & Berinde, M. 2005. The fastest Krasnoselskij iteration for approximating fixed points of strictly pseudo-contractive mappings. Carpathian J. Math 21(1-2): 13-20.

[10] Chugh, R., Kumar, V. & Kumar, S. 2012. Strong Convergence of a new three step iterative scheme in Banach spaces. American Journal of Computational Mathematics 2: 345-357.

[11] Hussain, N., Rafiq, A., Damjanovic, B. & Lazovic, R. 2011. On rate of convergence of various iterative schemes. Fixed Point Theory and Applications 2011(1): 1-6.

[12] Karakaya, V., Doğan, K., Gürsoy, F. & Ertürk, M. 2013. Fixed Point of a New Three-Step Iteration Algorithm under Contractive-Like Operators over Normed Spaces. Abstract and Applied Analysis 2013.

[13] Phuengrattana, W. & Suantai, S. 2012. Comparison of the Rate of Convergence of Various Iterative Methods for the Class of Weak Contractions in Banach Spaces. Thai Journal of Mathematics 11(1): 217-226. 30.

[14] Popescu, O. 2007. Picard iteration converges faster than Mann iteration for a class of quasiontractive operators. Math. Commun. 12: 195-202.

[15] Xue, Z. 2008. The comparison of the convergence speed between Picard, Mann, Krasnoselskij and Ishikawa iterations in Banach spaces. Fixed Point Theory Appl. 2008.

[16] Yuan, Q. & Rhoades, B.E. 2008. Comments on the rate of convergence between Mann and Ishikawa iterations applied to Zamfirescu operators. Fixed Point Theory and Applications 2008.

[17] V. Berinde, Iterative Approximation of Fixed Points, Springer, Berlin, Germany, 2007.

[18] Soltuz, S.M. & Grosan, T. 2008. Data dependence for Ishikawa iteration when dealing with contractive like operators. Fixed Point Theory and Applications 2008: 242916(1-7).

[19] Weng, X. 1991. Fixed point iteration for local strictly pseudocontractive mapping. Proc. Amer. Math. Soc. 113: 727-731.

[20] Karakaya, V., Doğan, K., Gürsoy, F. & Ertürk, M. 2013. Fixed Point of a New Three-Step Iteration Algorithm under Contractive-Like Operators over Normed Spaces. Abstract and Applied Analysis 2013.

[21] Rhoades, B. E. & Soltuz, S. M. 2004. The equivalence between the convergences of Ishikawa and Mann iterations for an asymptotically nonexpansive in the intermediate sense and strongly successively pseudocontractive maps. Journal of mathematical analysis and applications 289(1): 266-278.

[22] Rhoades, B. & Soltuz, S.M. 2004. The equivalence between Mann–Ishikawa iterations and multistep iteration. Nonlinear Analysis: Theory, Methods & Applications 58: 219-228.

[23] F. Gürsoy, V. Karakaya, and B. E. Rhoades, "The equivalence among new multistep iteration, S-iteration and some other iterative schemes," http://arxiv.org/abs/1211.5701. In press.

[24] S. M. Soltuz, "The Equivalence of Picard, Mann and Ishikawa iterations Dealing with Quasi-Contractive Operators, Mathematical Communications, Vol. 10, 2005, pp. 81-89.

[25] S. M. Soltuz, "The Equivalence between Krasnoselskij, Mann, Ishikawa, Noor and Multistep Iterations," Mathematical Communications, Vol. 12, 2007, pp. 53-61.

[26] R. Chugh and V. Kumar, "Strong Convergence of SP Iterative Scheme for Quasi-Contractive Operators," International Journal of Computer Applications, Vol. 31, No. 5, 2011, pp. 21-27.

Chapter 10

INACTIVATION OF *E. COLI* BY SONICATION

Buket KUNDUHOGLU[1]
Senem ÇIL

1 Assoc. Prof. Dr., Department of Biology, Faculty of Science and Letters, University of Eskisehir Osmangazi, 26040-Eskişehir/ TURKEY

Introduction

Conventional thermal inactivation methods such as pasteurization and sterilization are the most common techniques currently used to inactivate microorganisms in food products. However thermal process is very effective, it degrades nutritional and sensory quality of food. For this reason, new preservation techniques are needed. One of the new approaches is combined factors for inactivation or inhibition of microorganisms in foods. This techniques uses several factors (water activity/aw, pH, temperature, inhibitors etc.) at mild level instead of one factor (such as heat) at high level to control microbial activity in foods. Some emerging factors are ultrasonic waves, pulse-electric field, pulse-light, lacto peroxidase system (LPS) and high pressure (Leistner, 1996). Although sonication is used to disintegrate cells in many microbial or cellular studies since many years, it has newly discovered as inactivation factor in food preservation. Sonication is a promising alternative technique to classical thermal process especially in inactivation of foodborne pathogens.

As an early study, Hedges et al. (1980) described mechanisms of inactivation of ultrasound on *E. coli*. In the recent years, several studies published about inactivation of microorganisms with ultrasound.

E. coli is an indicator organism for most of the foodborne pathogens and hygienic condition of foods, also many strains of this species are pathogen. These strains can contaminate raw fruit and vegetable juices and other non-thermally preserved liquid food. *E. coli* O157:H7 can contaminate apple in the garden and survive in apple cider (Stopforth et al., 2004). Other non-pasteurized fruit and vegetable juices may be contaminated in a similar way. Sonication can be a used as a altenative process to inactivate *E. coli* and similar pathogens in this kind of liquid foods. Ugarte-Romeo et al. (2006) showed that, power ultrasound treatment can provide the 5-log reduction for *E. coli* in apple cider required by the FDA and sonication may be useful as an alternative to traditional pasteurization method. They also showed that ultrasound causes holes on *E. coli* surfaces and causes cell death. Although inactivation of ultrasound at sub-lethal and lethal temperatures is well studied, effect of pH and temperature combination in the inactivation of *E. coli* and isnot investigated.

The aim of this study was to determine the effect of pH (pH 4.0 and 7.0) and non-lethal temperatures on the inactivation of *E. coli* by ultrasound.

*

Materials and methods

Test organism

The strain of *E. coli* LMG 8223 (ATCC 25922) used in this study was purchased from the Belgian Co-ordinated Collections of Microorganisms (BCCM), K. L.Ledeganckstraat, 35 B-900 Gent, BELGIUM as lyophilized culture. Lyophilized culture tube was opened aseptically and the content transferred to Nutrient Broth (NB) tube (Merck, Germany) and incubated at 37 °C for 24 h. Then NB culture transferred in to slants of Nutrient Agar (NA; Merck). NA slant cultures were stored at 4 °C until use.

Media

Tryptone-yeast extract broth (TYEB- 10 g/l tryptone, 5 g/l yeast extract, 5 g/l sodium chloride) was used for growth of culture. Violet red bile agar (Merck) was used for enumeration. Citrate–phosphate buffers at pH 4.0 and 7.0 were used as sonication medium.

Preparation of cell suspension

The culture was inoculated into 50 ml TYEB in a 500 ml flask and incubated for 24 h at 37 °C in a shaking incubator (130 rpm). The cells were harvested by centrifugation at 6000 rpm for 10 min and re-suspended and washed 3 times in 0.85% saline, than resulting suspension stored at 4 °C. The cell number of this stock suspension was determined with standard plate count technique before each replicate study.

Inactivation studies

Sonication was carried out using a VC-750 ultrasound generator Vibracell® WCX 750 model ultrasonic processor at frequency of 20 kHz. A solid probe, 13 mm diameter is used. Two AED was used as 3.0 and 7.3 W/ml in treatments. A 10-mL jacketed vessel was used to hold the samples. Temperature of the content of the vessel was controlled by a refrigerated circulating bath. After each treatment, all equipment was rinsed with sterilized distilled water and vessel and probe were sterilized before and after each replicate of study.

At the beginning each trial, 9.9 ml citrate-phosphate buffer was pipetted in to a sterile tube and left for 3 min in the water bath to bring the medium temperature to the test temperature, then inoculated with 0.1 ml of stock *E. coli* suspension, stirred on a vortex for a few seconds and poured into the vessel which has reached to the test temperature. Probe was immersed into the vessel, carefully centered and then sonication started immediately. Cell suspensions were subjected to sonication 2-6 min and sampled at predetermined intervals. The 0.5-mL portions of aliquot were taken from vessel as samples and serially diluted in sterile 0.85% saline water (1:10). Drop plate technique was used for enumeration of survival cells. Replicate

0.02 ml aliquots were taken from dilutions and plated on VRBA. Plates were incubated at 37 °C for 24 h. Viable counts were determined as same as standard plate count technique.

Experimental design

All combinations of conditions were selected from the following: temperature (20, 30 and 40 °C); pH (4.0 and 7.0); sonication (0, 3.0 and 7.3 W/ml). Each experiment was conducted in duplicate, and the experimental design was; ((two temperature × 2 pH × 2 AED) × 2).

Construction of survival curves

First order reaction kinetic was used for survival studies. Inactivation coefficients were calculated from all survival curves by linear regression. Microbiologists are familiar log transformation rather than ln transformation. For this reason logarithmic order of death of microorganisms was expressed by the fallowing equation as given by Xiong et al. (1999):

$$Log\frac{N(t)}{N_0} = -\frac{t}{D}$$

Where, t is treatment time, N_t is the number of the surviving cells after t minutes of treatment, N_0 is the number of the living cells at t=0 and D is decimal reduction time.

This equation can be referred as fallows:

$$Log(N_t) = Log(N_0) - t * \frac{1}{D}$$

"1/D" is calculated from linear regression line of survival plot.

For the Arrhenious plot, inactivation rate constants are expressed as k as follows:

$$N = N_0 \times e^{-kt} \quad \text{or} \quad \ln(N) = \ln(N_0) - kt$$

Where, N was the number of live *E. coli* cells after ultrasonic irradiation, N_0 was the initial number of the *E. coli* cells, k was the inactivation rate constant, and t was the treatment time.

Relationship between k and can be expressed as fallows:

$$k = 2.303 \times \frac{1}{D}$$

Process duration for 5D reductions of survivals were calculated from 1/D values.

Results and discussion

Inactivation of E. coli for combination of pH and temperature without sonication application

Inactivation of *E. coli* for non-sonic treatments at 20-40 °C and pH 4.0 and 7.0 were negligible (Fig. 1). Reductions in the number of the survivals were changed between from no-reduction to 0.8 log in 80-160 min of treatment durations. Average of inactivation rate constants (1/D values) of the curves of non-sonic treatments was 0.0045 ± 0.0074 min^{-1}. These coefficients imply that only 1-log reduction may be observed in population of *E. coli* at citrate buffer, pH 4.0-7.0 in 3-5 hours of incubation at 20-40 °C. This reduction is not important in magnitude for food preservation process and probably arises from lack of maintain energy in the buffer medium, so that could not be observed in food products. Temperature and pH differences were also found statistically unimportant ($p>0.05$) on the reduction in non-sonic treatment. Roering, et al. (1999) reported that *E.coli* O157:H7 reduction level was 5 log unit for pasteurized and non-pasteurized apple cider in 21 days (stored at 4 and 10 °C). The pH and the Brix of the apple cider were between 3.3 - 3.5 and 12-14 respectively. This is a slower reduction compared to our study, probably caused by protective effect of low storage temperature or adaptation of cells to lower pH. Steenstrup and Floros (2002) predicated D_{50} values to be 71 min for apple cider without additives. This result is more comparable with our non-sonic treatments.

Inactivation of E. coli with the sonications at the level of 3.0 and 7 .3 W/ml at 4.0 and 7.0 pH, and 20, 30 and 40 °C combinations

Sonication at AED of 3.0 and 7.3 W/ml resulted 3-4 log unit reduction in the initial population of *E. coli* in 2 - 6 and 1 - 2 minutes respectively. The coefficient of inactivation kinetic was calculated from survival plot by linear regression model, as Log_{10} (survival/ml) versus treatment time. Coefficients of inactivation of replicate treatments were not statistically different ($p>0.05$). Two replicate coefficients were averaged and then D value and 5D processing time were calculated. The results are presented in Table 1.

According to results, sonication was the most effective factor on the inactivation rate constant. Treatment at 20 °C and 3.0 W/ml level of sonication resulted rate constants as 0.61 and 0.89 min^{-1} for pH 4.0 and 7.0

respectively. When sonication energy was increased from 3.0 W/ml to 7.3 W/ml (243 %), reduction rate constants mostly increased more then this ratio. Raso et al. (1997) reported that resistance of *Yersinia enterecolitica* decreased exponentially when the ultrasound amplitude was increased linearly.

Even though pH and level of AED were same, in increasing temperature, inactivation also increased (Fig. 2). However in the same temperature range of inactivation in non-sonic treatments was not show any difference. Similarly, Ross et al. (2000) reported that lower temperatures reduced the rates of death at non-thermal inactivation.

According to results, pH slightly affects the inactivation rate constants. The rate constants at pH 7.0 were slightly higher at each sonication levels and each temperature combinations then those at pH 4.0. This difference was found as statistically important ($p=0.03$). This situation can be seen in Fig.3. Normally, decrease in pH increases inactivation rate constant at same temperatures in both of non-thermal treatments (Scandamis and Nychas, 2000) and thermal treatments (Steenstrup and Floros, 2002). Some authors were reported similar findings, as some *Enterobacteriaceae* were more sensitive at neutral pH then low pH to high hydrostatic pressure (HHP) treatments (Raso and Barbosa-Cánovas, 2003).

Table 1. Inactivation coefficients, D and 5D values of E. coli treated with sonication at pH 4 and 7 and 20, 30 and 40 °C.

Acoustic energy density AED (W/ml)	pH	Temperatures °C								
		20			30			40		
		C.I. (log/ min)	D (min)	5D (min)	C.I.[(1)] (log/ min)	D (min)	5D (min)	**C.I.[(1)] (log/ min)**	**D (min)**	**5D (min)**
3	4.0	0,61	1,63	8,14	0,80	1,24	6,22	1,58	0,63	3,17
	7.0	0,89	1,12	5,59	1,19	0,84	4,21	1,75	0,57	2,85
7.3	4.0	1,89	0,53	2,65	2,93	0,34	1,71	5,41	0,18	0,92
	7.0	2,15	0,46	2,32	3,22	0,31	1,55	5,78	0,17	0,87
Increase in C.I. [(1)] (%)	4.0	309%			366%			342%		
	7.0	241%			270%			330%		

[(1)]Sonication energy was increased 243 % in the second energy level.

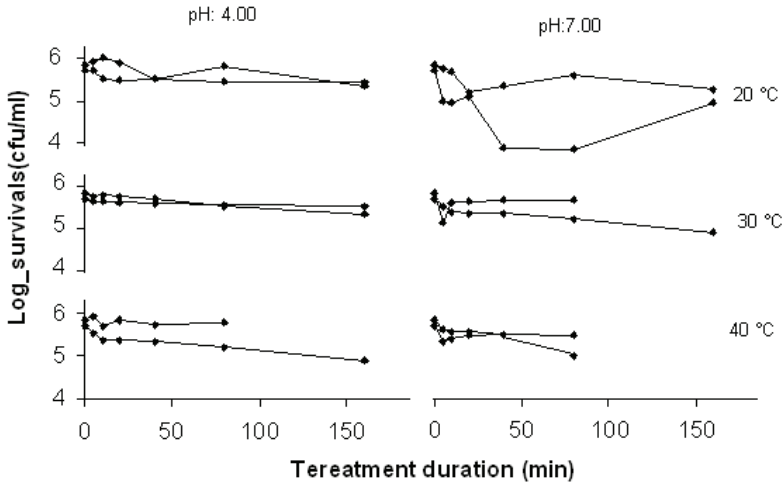

Fig.1. Inactivation of E. coli for non-sonic treatments at 20-40 °C and pH 4.0 and 7.0.

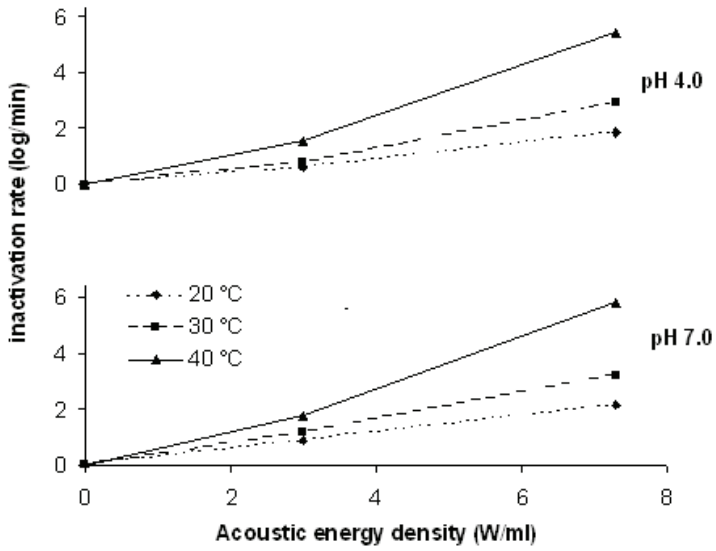

Fig. 2. Inactivation of E. coli with sonic treatments (3.0 and 7.3 W/ml AED) at different pH (4.0 and 7.0) and temperature (20, 30 and 40 °C) combinations.

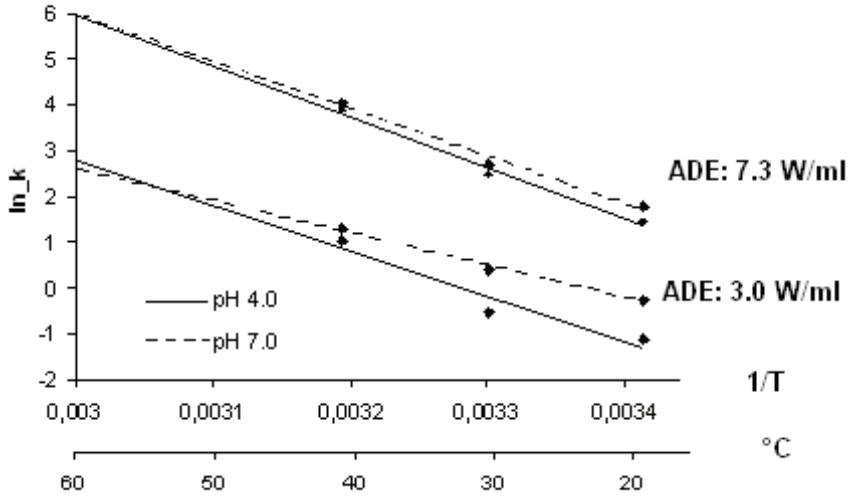

Fig. 3. Arrhenius plot of inactivation rates at pH 4.0, 7.0, AED level of 3.0, and 7.3 W/ml

Conclusion

In this study, ultrasonic inactivation of *Escherichia coli* LMG 8223 using non-thermal temperatures and non-lethal pH ranges was investigated. Death rates were measured for a combination of three temperatures (20°C, 30°C and 40°C), two pH levels (4.0 and 7.0) and two Acoustic Energy Densities, AED (3.0 and 7.3 W/ml). Inactivation of the *E. coli* cells by ultrasonic irradiation was showed first-order behavior. The inactivation rate constants calculated as log/min or 1/D. Inactivation of *E. coli* for non-sonic treatments was negligible. In the sonic treatments, inactivation rates are increased with increasing amplitude of the sonication. The maximum inactivation rate was determined as 5.78 log/min at 7.3 W/ml AED level at 40 °C for pH 7.0. According to result, treatment duration for 5D reduction of *E. coli* was 52 s for 10 ml suspension with our laboratory type equipment (750 W). Although this inactivation process is too far from industrial expectations, by increasing the thermal component of inactivation and using industrial type equipment, sonication could be an alternative food safety technique for heat sensitive food products.

References

Hedges, M., Lewis, M., Lunec, J., Cramp, W.A. 1980. The effect of ultrasound at 1.5 MHz on *Escherichia coli*. Int. J. Radiat. Biol. 37, 103-108.

Leistner, l. 1996. Principles and application of hurdle technology. In: Gould, G.W. (Ed.), New Methods of Food Preservation. Blackie Academic & Professional (Chapman & Hall), London, pp.1-21.

Raso, J., Pagán, R., Condón, S., Sala, F.J. 1997. Influence of temperature and pressure on lethality of ultrasound. Appl. Environ. Microbiol. 64, 465-471.

Roering, A.M., Luchansky, J B., Ihnot, A.M., Ansay, S.E., Kaspar ,C. W., Ingham, S. C. 1999 Comparative survival of *Salmonella typhimurium* DT 104, *Listeria monocytogenes*, and *Escherichia coli* O157:H7 in preservative-free apple cider and simulated gastric fluid. Int. J. Food Microbiol. 46, 263-269.

Raso,J., Barbosa-Cánovas, G.V. 2003 Nonthermal preservation of foods using combined processing techniques. Critical Reviews in Food Science and Nutrition. 43, 265-285.

Ross T, Dalgaard P, Trenungoon S. 2000. Predictive modeling of the growth and survival of *Listeria* in fishery products. Int. J. Food Microbiol. 62, 231-245.

Scandamis, P.N., Nychas, G.E. 2000. Development and Evaluation of a Model Predicting the Survival of *Escherichia coli* O157:H7 NCTC 12900 in Homemade Eggplant Salad at Various Temperatures, pHs, and Oregano Essential Oil Concentrations. Appl. Environ. Microbiol. 66, 1646-1653.

Steenstrup, L.L., Floros, J.D. 2002. Statistical modelling of D and z-value of *E. coli* O157:H7 and pH in apple cider containing preservatives. J. Food Sci. 7, 793-796.

Stopforth, J.D., Ikeda, J.S., Kendall, P.A., Sofos, J.N. 2004. Survival of acid-adapted or nonadapted *Escherichia coli* O157:H7 in apple wounds and surrounding tissue following chemical treatments and storage. Int. J. Food Microbiol. 90, 51-61.

Ugarte-Romeo, E., Feng, H., Martin, S.E., Cadwallader, K.R., Robinson, S.J. 2006. Inactivation of *Escherichia coli* with power ultrasound in apple cider. J. Food Sci. 71, E102-E108.

Xiong, R., Xie, G., Edmondson, A.E., Sheard, M.A. 1999. A mathematical model for bacterial inactivation. Int. J. Food Microbiol. 46, 45-55.

Chapter 11

BOTANICAL DESCRIPTION, CHEMICAL COMPOSITION AND MEDICAL USE OF *ZINGIBER OFFICINALE* (ROSCOE) (GINGER)

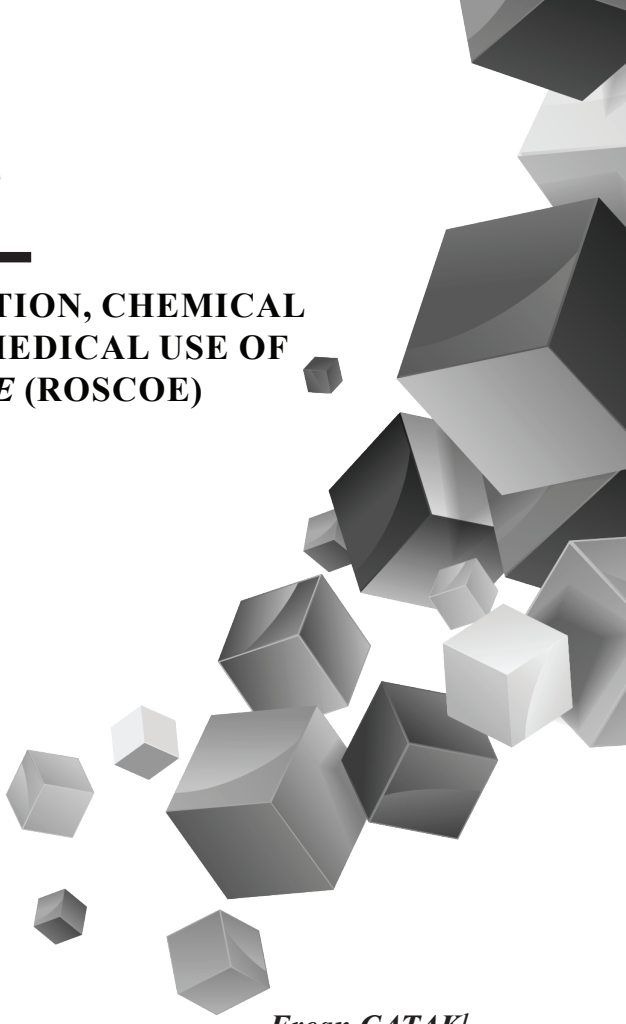

***Ercan ÇATAK*[1]**

1 Ercan ÇATAK, Eskişehir Osmangazi University, Faculty of Arts and Sciences, Department of Biology, Eskişehir, Turkey. (ORCID: 0000-0003-2680-590X)

1. Botanical Definition and Features of *Zingiber officinale* (Roscoe) (Ginger)

Based on the findings of the World Health Organization based on the studies conducted with medicinal plants in 91 countries; That number for the benefit of plants for medicinal purposes and Turkey are reported to be about 20,000 around 140 (Kaplan, 2005). On the contrary (Baytop, 1999) stated that these numbers are around 500 for our country and around 100,000 for the whole world.

One of the most recent examples of these medicinal plants, which have many uses, is ginger. It was described by the English botanist William Roscoe in 1807 and was named *Zingiber officinale* by Fostor (Fostor, 2000).

Table 1. *Scientific classification of ginger*

Scientific classification of ginger	
Regnum	*Plantae*
Phylum	*Magnoliophyta*
Clasis	*Liliopsida*
Ordo	*Zingiberales*
Familia	*Zingiberaceae*
Genus	*Zingiber*
Species	*Z. officinale*

(Rehman et al., 2011) also stated; Ginger is perennial, herbaceous and rhizome. It extends up to a height of 90 cm. Rhizomes aromatic, thick lobed, pale yellowish, simple bedding alternate distichous narrow oblong lanceolate leaves. It develops several lateral shoots in clusters; When the plant matures, it begins to dry. The leaves are long and 2 - 3 cm wide, sheath-based, with a blade gradually tapering to a point. Inflorescence solitary has oblong cylindrical spikes with lateral radical stems. Flowers are rare, rather small, calyx superior, gamosepalous, triangular, open cleavage on one side, spear-shaped double unequal rectangular greenish segments with three corollas (Kawai, 1994).

Figure 1. *Zingiber officinale root, rhizome, leaf and flower status [14].*

It is a plant that grows throughout Southeast Asia and China. It is also cultivated in some Africa countires, Austria, Japan, and Jamaica. Ginger has long been used as a spice and medicine in India and China (Sasidharan, 2010).

Throughout history, ginger has been used frequently, especially from its root and rhizome, for its high medicinal value and the flavor it adds to foods.

Figure 2. *Zingiber officinale rhizome (Rehman, et al., 2011).*

2. Chemical composition and nutritional content of ginger:

Zingiber officinale has many fat, wax, carbohydrate, vitamin and mineral content. Ginger rhizomes have an effective enzyme known as zingibain. (Connell, 1969).

As stated in the article [8,30] by (Pour et al., 2014), types of volatile oils in ginger; It consists of very small proportions bisabolene and b-sesquiphellandrene and farnesene (10%), curcumene (18%), mainly zingeberene (35%), sesquiterpene hydrocarbons. There are more than 40 different mono-terpenoid hydrocarbons with a small percentage, of which 1,8-cineol, neral, geraniol, linalol and borneol are the most abundant. According to (Pour et al., 2014), These active ingredients of ginger give it its unique aroma and taste.

As stated in [8,30], ginger contains biologically active ingredients such as zingerone, gingerol, paradoller and shogaol in its chemical content. And these create a feeling of warmth in the mouth. (Connell, 1969), on the other hand, gingerols have been defined as the main effective ingredients freshly dug out of the ground ginger rhizome. It has also been emphasized that when ginger is dried, the first prominent ingredient is shogaols. (Pour et al., 2014) stated that the paradol, which resembles gingerole, is formed by hydrogenation of the shogoal.

(Hasan et al, 2012) stated that ginger basically has the active ingredients gingerol, zingiberen, β-bisabolen, α-farnesen, shogaol, β-sesquiphellandren and α-curcumene.

Below are the formulas of some of the best known of these active ingredients.

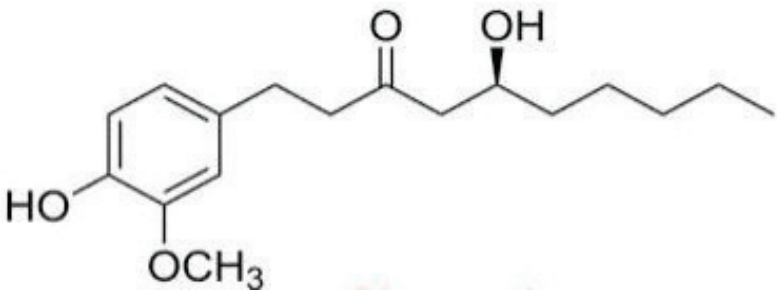

Figure 3. *Gingerol [7]*

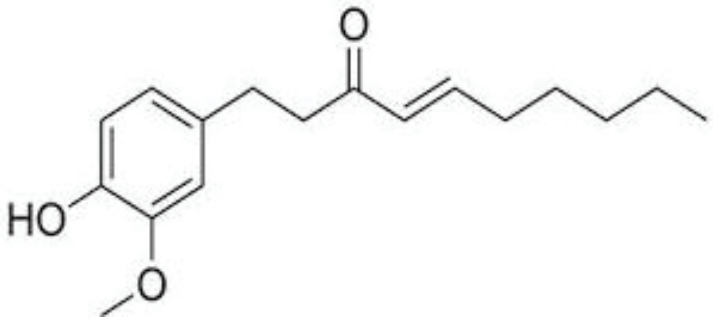

Figure 4. *Shogaol [7]*

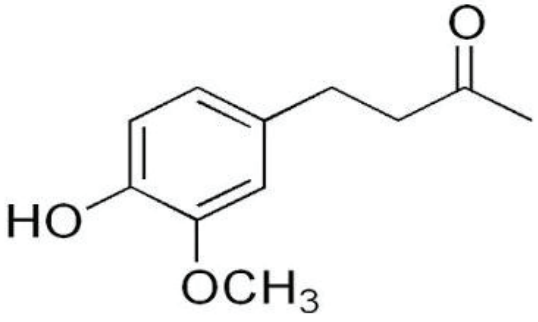

Figure 5. *Zingeron [7]*

(Adel, 2010), in their study where they revealed the chemical content of ginger, they collected the component names and quantities they obtained in the table 2 and table 3 below. Accordingly, they stated that due to the components that ginger has, It can be said to be both a good source of

antioxidants and nutrients. As it is stated in Table 2, ginger besides high amounts of protein, carbohydrate and fat; It also contains many inorganic compounds that are very important for human health such as calcium, phosphorus and iron.

Table 2. *Nutritional composition of 100 g of ginger [2].*

Component Name	Amount of	Component Name	Amount of
Protein	5,1 g/100 g	Iron	8,0 mg
Water insoluble fiber	%23,2	Phosphorus	174 mg
Water soluble fiber	%25,5	Zinc	0,9 mg
Oil	3,72 g	Calcium	88,4 mg
Moisture	%15,02	Manganese	9,13 mg
Carbohydrate	38,35 g	Chromium	70µg
Ash	3,85 g	C Vitamin	9,3 mg
		Total carotenoid	79 mg

Table 3: *Ingredients and antioxidant activity of Zingiber officinale. [2].*

Component Name	Amount of
Total Phenols	840 mg
Tanin	1,51 g
Flovanoids	2,98 g
Total antioxidant activity	73529 µmol/g

As indicated in the table below, ginger root contains many vitamins that we need for healthy growth.

Table.4 *The vitamin content of ginger [29].*

Vitamin Name	**Raw ginger (root) (in 100 g)**
Riboflavin (B2)	0,034 mg
Panthenic acid (B5)	0.203 mg
Niacin (B3)	0,75 mg
Vitamin E	0.26 mg
Vitamin B6	0.16 mg
Folate (B9)	11 µg
Thiamine (B1)	0,025 mg
C Vitamin	5 mg

Due to these high nutritional properties of ginger; Although it is consumed as a sweetener all over the world, it is widely used in the food, beverage and confectionery industries. It is especially used in pickles, chutney, marmalade, wine, ginger beer, and liqueur [28].

3. Use of Ginger in Medical Field and Its Health Effects

Although drugs developed synthetically to treat diseases are widely used today; Throughout history, medicinal plants accompanied this purpose and offered an alternative to modern medicine. Moreover, according to (Kaplan, 2005); medicinal plants increasingly; They often replace artificial compounds because they only have a single effect and have multiple side effects.

According to (Güceyü et al., 2019), *Zingiber officinale* has been widely used in the geography to eliminate bacterial infections since ancient times due to its antimicrobial activity. (Grzanna et al., 2005) stated that ginger is used in the treatment of stomach aches and asthma, especially in China and India. Because ginger has active compounds and these compounds show different effects; It has also been used in colic, swelling and indigestion, ulcer, hypercholesterolemia and burn ailments. In addition, there are documents showing its use in the treatment of depression, liver toxicity and impotence (Jahromi, 2009).

Ginger has the potential to treat diabetes, cardiovascular disorders (hypertension and atherosclerosis), digestive health (constipation, indigestion and ulcers), arthritis and rheumatic diseases, vomiting, and cancer. It also has anti-inflammatory (anti-inflammatory) and antioxidative activities that restrain aging. In addition, it is known that its antimicrobial potential may be helpful in the treatment of infectious diseases [16, 26].

The use of ginger as an anti-inflammatory, pharmacological activities, treatment of rheumatoid and osteoarthritis has been documented. Zingiberen, one of the active ingredients of ginger, increases the effect of all these. As a result, ginger has a wide use in medicine, both as a single medicine and as a combined medicine. [23].

According to (Mashhadi et al., 2013); Medicinally important additives of ginger are now well-known. Ginger has therapeutic effects in a variety of ways, such as immuno-nutritional and anti-inflammatory. With its anti-inflammatory properties, ginger can reduce muscle pain after movement. Likewise, the cancer-preventing effect of ginger has been demonstrated by scientific studies; Active components of ginger, such as gingerol, shogaol and paradols, can inhibit various cancers with their effectiveness in angiogenesis and metastasis, apoptosis induction, and cell cycle progression. Ginger also continues to be used to treat cardiovascular diseases and gastrointestinal system disorders.

According to (Abdalla, 2018); In addition to the ginger rhizome being consumed as a spice and finding many uses in foods; With numerous industrial and traditional medicine research studies, the existence of antibacterial effect potential has been revealed. While 2 negative results were reported in 40 articles published on the antibacterial properties of ginger; In 38 of these studies, they were reported to respond effectively to the majority of the bacteria tested. For this reason, there is a need for advanced multidisciplinary studies to be conducted to investigate the antibacterial effectiveness of ginger and to eliminate contradictions.

Again according to (Abdalla, 2018); ginger is a popular medicinal herb. It has been confirmed to be antibacterial by many medical studies. In the study, It has been determined that ginger rhizome stops bacteria thanks to its essential oils. However, in order to reveal this efficiency much more clearly, it should be supported by multidisciplinary studies of microbiology, molecular physiology, pharmaceutical and medical sciences.

There is an interesting study by (Macit et al., 2019) on animal obesity. Accordingly, they revealed the important effects of ginger on obese animals and energy metabolism. However, unfortunately, the mechanism of action for these conditions in humans has not yet been revealed. When ginger is applied, it has been emphasized that the results of studies evaluating the effects of people on body weight are not very realistic. Because in affecting thermogenesis and respiratory coefficient; Various factors may play a role, including differences in active ingredients between studies, low levels of administration, differences in application times, and variations in the highest tolerated dose. For these reasons, consumption of ginger continuously and for long periods can affect both body weight and thermogenesis by increasing or decreasing values. It will be appropriate to re-evaluate these situations with subsequent studies. In order to reveal the relationship between obesity and energy metabolism in ginger applications; There is also a need for studies to determine and evaluate the active ingredient and supplementation time, optimum dose, and signal molecule pathways that affect the possible effects of long-term use.

(Savaşer et al., 2019) in their study to examine the effects of powdered ginger added to trout diets on their growth and immune systems as a nutritional supplement; They determined that ginger had positive effects especially on immune system parameters. The immune systems of the trout were negatively affected by the use of ginger at doses of 5.0 g / kg and above. However; They observed that after 0.5, 1.0 and 2.5 g / kg doses of ginger powder nutritional supplements, it made positive contributions to the body defense system.

In their study on laying hens (Gürbüz & Salih, 2017); when applied as a dietary supplement using a mixture of ginger powder and sumac (*Rhus*

coriaria L.); They observed that egg yolk tends to lower cholesterol levels in laying hens and stated that this mixture can be used as a feed additive.

(Akbulut, 2019) in their studies to determine the antiobesity effect using nicotine and ginger on obese rats; They observed that ginger was more effective than nicotine in treating obesity by inhibiting the glycogen increase. Thus, ginger has been shown to cause more weight loss in the treatment of obesity.

In our country, the usage areas of ginger among the people are quite many and it is widely used. Because it is a powerful anti-inflammatory, it can be used to prevent inflammation and strengthen the immune system. In addition, its anti-cold and anti-cold effect; prevention of vomiting (especially in early pregnancy and in chemotherapy to prevent nausea and vomiting) use as a natural pain reliever in severe pain; digestive effect; It has many uses in our daily lives with its many effects that reduce lipid and glucose levels.

4. Conclusion

Experiences gained from generation to generation, knowledge about which organs of medicinal plants, in what ways and proportions; They offer an alternative treatment to modern medicine in our age. In addition to the use of these plants in many areas such as food, spices, food additives; After realizing that they are also effective in treating some diseases, their use is increasing all over the world.

Plants used in the medical field are of very high economic importance all over the world. Zingiber officinale is one of these plants. Because it has both health and nutritional values. Ginger also appears as an important spice and sweetener all over the world. Heart protective, anti-inflammatory, antimicrobial, antioxidant, anticancer, etc. draws attention with its features. For these reasons, scientists need to do more scientific studies on ginger for drug production [11].

Due to the recent interest in herbal medicines, the values of medicinal plants have increased even more. Based on the historical and public use of medicinal plants, first their bioactivity and then their phytochemical evaluation are made. Mostly, some herbal medicines have a higher sales rate than their synthetic counterparts in Europe. The factor in the increasing use of medicinal plants among the public is the pharmacological studies conducted on this subject that direct their use. One of these plants is ginger, which has been used in treatments from ancient times to the present. The historical uses of ginger confirm its modern therapeutic application. In clinical and phytochemical studies, it confirms this use and reveals that ginger is a safe and effective drug [19].

The contributions of ginger to our health are emerging more and more every day. Both the increase in the frequency of use and the medical studies conducted on it; will make ginger even more popular and effective.

REFERENCES

- Abdalla, W.E., Abdallah, E.M., "Antibacterial Activity of Ginger (*Zingiber Officinale* Rosc.) Rhizome: A Mini Review" International Journal of Pharmacognosy and Chinese Medicine, Vol. 2, Issue 4, p:1-8, 2018.
- Adel, P.R., S., Prakash, J., "Chemical Composition and Antioxidant Properties of Ginger Root (*Zingiber officinale*)" Journal of Medicinal Plants Research Vol. 4(24), p:2674-2679, 2010.
- Akbulut, M.D., Evsen, H., Bozkurt, F., "The Determination of the Antiobesity Effects of Nicotine and Ginger In the Rats with Obesity Using Fish Oil", Afyon Kocatepe Üniversitesi, Fen ve Mühendislik Bilimleri Dergisi, 19, 021003, p:275-285, 2019.
- Baytop, T., "Türkiye'de Bitkiler ile Tedavi", Nobel Tıp Kitapevleri, p:3-5, Dış Ticaret Müsteşarlığı, İstanbul, 1999.
- Connell D, Sutherland M., "A Re-examination of Gingerol, Sshogaol and Zingerone, The Pungent Principles of GİnGer (*Zingiber officinale* Roscoe)", Australian Journal of Chemistry, 22, p:1033–1043, 1969.
- Fostor, S., "Ginger Your Food is Your Medicine", www.herphoto.com/ education/ monograph/ginger.html, 2000.
- Ghosh, A.K., Banerjee, S., Mullick, H.I., Banerjee, J., "*Zingiber officinale*: A Natural Gold", International Journal of Pharma and Bio Sciences, 2, p:283-294, 2011.
- Govindarajan V., "Ginger-Chemistry Technology and Quality Evaluation: Part-I CRC.", Critical Reviews in Food Science and Nutrition, 17, p:1–96, 1982.
- Grzanna, L., Lindmark, L., Frondoza, G., "Ginger-A Herbal Medicinal Product with Broad Anti-İnflammatory Actions", Journal of Medicinal Food, 8(2), p:125-132, 2005.
- Gurbuz, Y., Salih, Y.G., "Influence of Sumac (*Rhus Coriaria* L.) and Ginger (*Zingiber officinale*) on Egg Yolk Fatty Acid, Cholesterol and Blood Parameters in Laying Hens", Journal of Animal Physiology and Animal Nutrition, 101(6), p:1316-1323, 2017.
- Gupta, S.K., Sharma, A., "Medicinal properties of *Zingiber officinale* Roscoe - A Review", IOSR Journal of Pharmacy and Biological Sciences, Volume 9, Issue 5 Ver. V, p:124-129, 2014.
- Güceyü, Ç., Goncagül, G., Günaydın, E., Akpınar, P., "Zencefil'in Antibakteriyal Etkisi", Etlik Vet Mikrobiyol Dergisi, 30 (1) p:44-50, 2019.
- Hasan, H.A., Raauf, A.M.R., Razik, B.M.A., Hassan, B.A.R, "Chemical Composition and Antimicrobial Activity of the Crude Extracts Isolated

from *Zingiber officinale* by Different Solvents", Pharmaceutica Analytica Acta, 3:9, p:1-5, 2012.

- https://www.soin-et-nature.com/en/medicinal-plants/550-ginger-rhizome-root-zingiber-officinale-roscoe-iphym-herbalism.html
- Jahromi, E.A., "Ginger a Soothing Spices" Iranian Women Health Journal, p:14:36, 2009.
- Jiang, H., Xie, Z., Koo, H.J., McLaughlin, S.P., Timmermann, B.N., Gang, D.R., "Metabolic Profiling and Phylogenetic Analysis of Medicinal *Zingiber* Species: Tools for Authentication of Ginger (*Zingiber officinale* Rosc.)", Phytochemistry, 67, p:232–244, 2006.
- Kaplan, H., "Zencefilin (*Zingiber officinale* Roscoe) Bitkisel Özellikleri ve Yetiştiriciliği", Batı Akdeniz Tarımsal Araştırma Enstitüsü, Derim, Cilt 22, Sayı 2, p:1-9, Antalya, 2005.
- Kawai, T., "Anti-emetic principles of Magnolia obovata Bark and *Zingiber officinale* Rhizome", Plan Med., 60, p:17-20, 1994.
- Konuklugil, B., Özçelikay, G., "Zencefil'in (*Zingiber officinale*) Tarih Boyunca Önemi ve Günümüzdeki Kullanımı" p:173-189, Ankara.
- Macit, M.S., Sözlü, S., Kocaadam, B., Acar-Tek, N., "Evaluation of Ginger (*Zingiber officinale* Roscoe) on Energy Metabolism and Obesity: Systematic Review and Meta-Analysis", Food Reviews International, Volume 35, Issue 7, 2019.
- Mashhadi, N.S., Ghiasvand, R., Askari, G., Hariri, M., Darvishi, L., Mofid, M.R., "Anti-Oxidative and Anti-Inflammatory Effects of Ginger in Health and Physical Activity: Review of Current Evidence", Int J Prev Med, 4 (Suppl 1), p:36–42, 2013.
- Pour, H.A., Norouzzade, R., Heidari, M.R., Ogut, S., Yaman, H., Gokce, S., "Therapeutic Properties of *Zingiber officinale* Roscoe: A Review", European Journal of Medicinal Plants 4(12), p:1431-1446, 2014.
- Rehman, R., Akram, M., Akhtar, N., Jabeen, Q., Saeed, T., Ali-Shah, S.M., Ahmed, H., Shaheen, G., Asif, H.M., "*Zingiber officinale* Roscoe (Pharmacological Activity)", Journal of Medicinal Plants Research Vol. 5(3), p: 344-348, 2011.
- Sasidharan, I., Nirmala-Menon, A., "Comparative Chemical Composition and Antimicrobial Activity Fresh & Dry Ginger Oils (*Zigiber officinale* Roscoe)", International Journal of Current Pharmaceutical Research 2: p:40-43, 2010.
- Savaşer, S., Akçimen, U., Ceylan, M., Hanol-Bektaş, Z., Yener, O., Bulut, C., "Zencefil (*Zingiber officinale*)'in Gökkuşağı Alabalıklarında (*Oncorhynchus mykiss* Walbaum) İmmunostimulant ve Büyüme Destekleyici Olarak Kullanımı", LIMNOFISH-Journal of Limnology and Freshwater Fisheries Research, 5(2) p:121-135, 2019.

- Shukla, Y., Singh, M., "Cancer preventive properties of ginger: A brief review", Food Chem Toxicol, 45, p:683–90, 2007.
- Wagner, H., Hıkıno, H., Fransworth, N., "Economic and Medicinal Plant", (l), p:61- 65, Research Academic Press, Orlando, Sandiego, Tokyo, 1985.
- Wang X., Zheng Z.J., Guo X.F., Yuan J.P, Zheng C.C., "Preparative Separation of Gingerols from *Zingiber officinale* by High-Speed Counter-Current Chromatography Using Stepwise Elution", Food Chemistry 125, p:1476–1480, 2011.
- www.wikipedia.org. Ginger, Dated 15.09.2014.
- Yogeshwer S., Madhulika S., "Cancer Preventive Properties of Ginger: A Brief Review", Food and Chemical Toxicology. 45, p:683–690, 2007.

Chapter 12

ANALYSIS OF LUNG CANCER WITH MACHINE LEARNING TECHNIQUES

Sevcan AYTAÇ KORKMAZ[1]
Furkan ESMERAY[2]

1 Electronic and AutomationDepartment, Fırat University Elazığ, Turkey
sevcanaytackorkmaz@gmail.com
2 Electric and Energy Department, Munzur University, Tunceli, Turkey
furkanesmeray@munzur.edu.tr

Introduction

In this study, we aimed to better diagnosis of lung cancer with lung tomography, lung cell histopathology and light microscopy images. In addition, two types of images, good and malignant, were used. Various size reduction methods have been used to obtain optimum properties of these two types of images. These methods include Principal Component Analysis (PCA), Generalized Discriminant Analysis (GDA), and Linear Discriminant Analysis (LDA). Random Forest (RF), Decision Tree (DT) methods were used as the classifier. In addition, Maximum Stationary Extreme Regions (MSER), Speeded Up Robust Features (SURF) were added to each of these classifier methods and the status of the accuracy value was examined.Various methods have been developed for the early and accurate diagnosis of lung cancer. In this thesis, a total of 240 images were used for the methods. These images were obtained from 60 patients by taking 4 sections for each. The accuracy of each classifier, each size reduction method and each feature was compared with the images used. In addition, the methods with the highest accuracy were found. Some of the methods used were found to have 100% accuracy. Thus, the distinction between benign and malignant tumors has been achieved thanks to the methods that provide the highest accuracy. It is also aimed to increase the accuracy rate for the early diagnosis of lung cancer, which is one of the cancer types with the highest mortality rate in the world. Thus, lung images loaded into computer assisted diagnostic systems were passed through various stages in this system to obtain an accurate result.

Lung is one of the important organs of the respiratory system. Like every organ, it is found in diseases of the lung. At the beginning of these diseases is a type of cancer called lung cancer. As in our country, lung cancer is accepted as one of the main causes of cancer death in other countries (American Cancer Society,2010), (Türkiye Cumhuriyeti Sağlık Bakanlığı, 2009).

Cells in lung tissues proliferate in an uncontrolled manner, causing lung cancer. If these cells proliferate in lung tissues uncontrolled, they affect another nearby cell and if they come into contact with other tissues, an increase in the number of diseased cells occurs. Symptoms of lung cancer include cough, weight loss, and shortness of breath. However, since these symptoms are common to the symptoms of other diseases, the diagnosis can be difficult and can take a long time. Computed tomography is used to make a diagnosis of lung cancer. Biopsy is used to make a definite diagnosis. This procedure is performed by computed tomography biopsy. Detection of cancer-causing nodules in the lung by computed tomography is very important (Ceylan, 2006). Computed

tomography can be used for early detection of the disease with advanced imaging systems. Particularly, computed tomography imaging of lungs of small nodules plays an important role in early diagnosis. However, it has emerged in a complexity due to the systems used. Radiological examination of computed tomography images, which have a large number of cross-sections for each patient, takes a long time and indicates a tiring process. On the other hand, there is a difference between the diagnosis of one radiologist and the diagnosis of another radiologist. Because there are differences between the knowledge and experience according to the person to be diagnosed. Therefore, there is a need for the use of computer-aided systems to eliminate different diagnoses among people and reduce human error. Thus, computer-assisted detection / diagnostic systems have an important role in the decision-making process of the diagnosis / diagnosis of the disease (Doi, 2007). With the development of technology, new systems are needed to assist the person who will make this determination by using various systems in cancer diagnoses. The use of these systems is also needed in the diagnosis of lung cancer.

Due to advances in screening technologies, the diagnosis rate of lung cancer nodules is increasing. After the detection of nodules of lung cancer, computer assisted diagnostic systems were used to assist radiologists in this diagnostic system. There are two important points in computer aided diagnostic systems. These are the identification and classification of nodules in the lung. Thus, both faster and more accurate diagnoses are provided (Aydın Kaya, 2018).

Therefore, in this study, for early detection of lung cancer disease; Computed tomography of lung, histopathology images of lung, images taken from light microscope will be used. In addition, this study is a study obtained from the master thesis.

Theory and Method

1. Features for Lung Cancer Images

1.1. Maximum Stable Extreme Regions (MSER)

The MSER algorithm is an algorithm used to device rounds or ellipse-like figures (spots) in images. The algorithm calculates the attributes of these key points by selecting key points that take these shapes into account (Matas, 2002). An MSER area (Matas, 2004) occurs of a series of interdependented points on a particular sill value whose permanence is addicted on the changing sill value. That is, the chosen zone is a local binary form that is not bound to a set of sill values.

According to the study in Source (Güney, 2009), evidence MSER areas works similarly to the basin method. While the sill value ranges from [0-255], the areas that are connected to each other and do not change much in all scenes are defined as MSER areas In the application of the method; the image points are ranked by shine value and the points are placed in the image in rising or decreasing order. During this process, the component zones and areas found by the merge detection algorithm are kept in a list. At each stage of the silling process, by joining the two zones, the small zone is inclusive in the wide zone and the small zone is removed from the list. Sill values where zone change is minimized by increasing / decreasing the sill value are selected as sill ranges that produce maximum decisive extremal zones. Alias, the border $A_1,\ldots A_{i-1},A_i,\ldots$ of the end zones formed by the connected components at all sill values are shown as a series of adjacent zones. This array satisfies condition $A_i \subset A_{i+1}$. To select the A_i^* end zone of the array as maximum decided (Güney, 2009); A_i^* local minimum is needed at the i^* value of $f(i) = |A_i \pm \Delta|/|A_i|$. |.| specifies the area of the zone, and Δ specifies a parameter of the method. The ± mark also shows that there is a local minimum for both descending and ascending sill values. This procedure applies to all zone sequences in the extreme zone set to obtain maximum extremally stable zones (Güney, 2009). In the MSER method, attached image points having a similar color are exposed to clustering based on clustering. For clustering, color distances at four or eight adjacent points are kept in an related list. At each stage of the algorithm, the b∈[0… B] image points are stamped in stages. If the coordinate area of the image points is specified as the Ω = [1… K]x[1… M] $\subset Z^2$label set, each step is phrased as a E_b: Ω → N map. As a result of tagging, anchor points that contain the same points indicate excessive zones in the image. The distance between all neighboring points of the image extremal zone should be less than the $d_{bhr}(b)$ value, which is a sill value calculated for that step. The distance of the picture points in the color the infinite is calculated using the chi-square margin. At first, all values in the sticker image B_0 are stamped as 0. In the sticker image, all neighboring points shorter than $d_{bhr}(b)$ are stamped as the new zone and the sticker image E_{b+1} is obtained (Güney, 2009).Because of the spatial correlation between picture points, the margins of all neighboring points do not show a uniform dispersion. The spacious majority of distances have small values and very few large distances. Therefore, the threshold value is increased linearly at each step, which initially results in a very rapid label change. Thus, labels change at many points until the end of the steps (Güney, 2009). To change the sticker of an tantamount number of image points in each step, the distance between all adjacent points in the image is taken as a haphazard factor and the sill values are changed according to the sequential inverse of the cumulative distribution function

(CDF) (Güney, 2009). For color images, the chi-square CDF is calculated as in Equation 1.1, where μ is the average of the sample set.

$$H_3(c) = \sqrt{\frac{4c}{\lambda\pi}} e^{-3c/2\pi} + erf(\sqrt{3c/2\mu}) \quad (1.1)$$

As a result, Equation 1.2 is used to find the sill values after the average prediction.

$$d_{bhr}(b) = g^{-1}(\frac{b}{B})\text{b}\in [0\dots \text{B}] \quad (1.2)$$

Then, by increasing the value $d_{bhr}(b)$, the area changes of the extremal zones detected are checked at each step to determine the maximum constant. In addition, those smaller than a certain value are eliminated from the maximum consistent extremal zones (Güney, 2009).

1.2. Accelerated Robust Features(SURF)

SURF is based on the amount of two-dimensional Haar wavelets and the use of integral images. SURF determines image properties using Hessian matrices. Approximate determinants of Hessian blob sensors are calculated using Haar wavelets. The performance of the SURF method, which is an important feature, is influenced by the use of integral images (Teke, 2010a), (Viola, 2001). Integral images is the calculation of a specific rectangular area. The area images below the coordinates are also calculated by Equation 1.3 (Viola, 2001):

$$F\sum(a,b) = \sum_{c=0}^{c\leq a}\sum_{d=0}^{d\leq b} F\,(c,d) \quad (1.3)$$

When an integral image is calculated for the F image, the sum of the densities is calculated by triple addition from any pixel coordinate. As the size of the images is independent, processing time is shortened (Teke, 2010b), (Alparslan, 2013).

2. Size Reduction Methods for Lung Cancer Images

2.1. Principal Component Analysis (PCA)

Principal component analysis (PCA) is a multivariate technique that analyzes a data table in which investigations are defined by several quantitative addicted variables associated with each other. Its purpose is to extract important information from the table, to show it as a new set of orthogonal variables called actual constituents, and to show the similarity

model between the investigations and the scores on the maps (Abdi, 2010).

Actual constituent analysis is a multivariate statistical method and provides dimension reduction by explaining the variance-covariance structure of a data set consisting of variables with the help of linear combinations of these variables (Saraswat, 2013).

2.2. Generalized Discriminant Analysis (GDA)

Generalized discriminant analysis (GDA) is the extremities of the classical linear discriminant analysis (LDA) from a linear field to a nonlinear field (Zheng, 2004).Classical discriminant analysis solves the problem of self-decomposition when M_f is non-annular. For small problems, M_f is singular, since the pattern size b may be smaller than its extent c. In this chapter, we describe a new gauge F_1, where the nonsingularity of M_f is not needed. The new criterion F_1 is a natural extremities of the classical one in Eq. (2.1), where the adverse of a matrix is changed by the pseudo-inverse (Golub, 1996). While the adverse of a matrix may not exist, the pseudo-adverse of any matrix is well described. Moreover, when the matrix is reversible, its pseudo-adverse encounters with its adverse. The new criterion F_1 is needed as

$$F_1(A) = trace((M_f^L + M_b^L)) \tag{2.1}$$

The optimal mutation matrix G is calculated so that F_1(G) is maximized. Note that in the following, the matrix G in F_1(G) may be disregarded if it is clear from the ingredient. M_f total eradiate matrix, M_b between-class eradiate matrix, G transformation matrix (Ye, 2005).

2.3. Linear Discriminant Analysis (LDA)

Linear Discriminant Analysis (LDA) is a well-known technique in statistical pattern classification for improving the discrimination of a feature vector and compressing information contents (by classification) into a linear transformation. For large word phoneme-based recognizers, the reported results do not provide a clear table. Yu et al. (Yu, 1990) operated LDA to transform the feature space (before vector quantization) of the BBN BYBLOS recognizer, a system based on status-addicted discrete HMMs reproduced from three code books. They described the 50 basic phonemes as the classes to be discriminated. The discriminant analysis did not result in an overall amelioration. Wood et al. (Wood, 1991) fixing the classes with sub-phone units, so-called phonicles, which were modeled by multivariate Gaussians. They arrived advanced

identification precision by applying the IMELDA transform (Hunt, 1991). The large vocabulary conversation recognizer prefered here is different from the ones above. When employing LDA in such a framework a few design alternatives have to be aforethought, e.g. what is the best description of the classes to be discriminated (Umbach, 1992).

3. Classification Methods for Lung Cancer Images

3.1. Decision Tree (DT)

Decision tree (DT) method is generally used in the literature, but it is also used as a pattern identification algorithm. This method is used effectively because the methods used in tree formation are understandable and simple. This method consists of multi-stage and sequential approaches. It performs a gradual simple decision-making process for very complex classification problems (Safavian, 1991). A decision tree consists of three parts. These knots, leaves and branches are called. Although branches and leaves represent other elements of the tree, the knot represents a peculiarity in the tree structure. In a tree, the first part is leaf and the last part is root. The remaining part of these structures is the branch (Quinlan, 1993). Tree; data consists of a root node and branches and leaves. The principle formed in the formation of a decision tree structure by using the qualitative information of the educational data can be defined as asking questions about the data and acting quickly according to the answers obtained. In this way, the decision tree collects the answers to the questions and forms the decision rules. The decision tree collects the answers and forms the decision rules. The tree structure is created by asking questions with the classification of the data in the root node. This process continues until there are no nodes and leaves without an idle branch (Safavian, 1991). Depending on the number of variables used in tree formation, one-variable or multi-variable decision tree structures can be found (Friedl, 1997). It may be the case that each internal node of a univariate decision tree is divided into multiple subsets by testing a single attribute (Swain, 1977).In this way, the division continues until the decision tree repeatedly reaches a leaf node of the input data and the class label in the leaf is assigned to the observations. In a univariate decision tree, the specific values of the decision boundaries are estimated experimentally from the training data.In the case of continuous data, a logical evaluation a_i>b is performed in which the attribute value a_i at each internal node points to a property in the data space and b is a threshold in the observed range of a_i from the training data. Threshold b can be determined using certain conditions, such as maximizing differences or lowering similarity in landing nodes. Assuming that a data set B_1 ,B_2,...,B_n consists of several classes and F

represents class values, the probability of a class is $M_i = (B_i/|F|)$ and the entropy of classes is given in Equation 3.1.;

$$\text{Entropy(F)} = -\sum_{i=1}^{n} M_i \log_2(M_i) \quad (3.1)$$

calculated. Consider that the F class values are subdivided into F_1 , F,...,F_n according to the H attribute in the data set. The gain to be obtained as a result of dividing the F class values by using H attribute values, in Equation 3.2,

$$\text{Gain (H, F)} = \text{Entropy(F)} - \sum_{i=1}^{n} \frac{|F_i|}{|F|} \text{Entropy}(F_i) \quad (3.2)$$

is calculated by equation. Partition information is used to determine the value of the H attribute for the set F (Equation 3.3).

$$\text{Division İnformation (H)} = -\sum_{i=1}^{n} \frac{|F_i|}{|F|} \log_2^{\frac{|F_i|}{|F|}} \quad (3.3)$$

In this case, the profit rate in Equation 3.4,

$$\text{Gain Ratio} = \frac{\text{Gain (H,F)}}{\text{Division İnformation (H)}} \quad (3.4)$$

calculated. This equation gives the rate of information obtained by the separation to be used in the classification process. Using this criterion, the training set F is repeatedly separated so that the gain ratio is maximum at each node of the tree. This process is repeated until each leaf node contains observation values for only one class. If the sub-tree with a single leaf or the most used branch of this tree is to reduce the expected error rate, the tree is pruned. As the error rate on the sub-branches decreases, the error rate for the whole tree will decrease. At the end of pruning, a tree is obtained in which the error rate is minimized (Kavzoğlu, 2010).

3.3. Random Forest (RF)

Random forest (RF) is a good classifier compared to unknown and traditional pattern recognition techniques. RF provides an algorithm for estimating lost values, as well as the flexibility to perform various types of data analysis, including regression, classification, survival analysis, and unsupervised learning (Rodriguez, 2012).

RF is a type of tree classifier collection. Gini index is wasted in RF classifier. The split status is determined according to the smallest Gini index by Gini indications. To create a tree with the RF classifier, there must be two external parameters as input value. These parameters are a and B parameters. a represents the number of factors used in each node. B represents the determination of the number of trees in the best part to be developed (Pal, 2005), (Korkmaz, 2017). Initially a value should be inserted haphazard from the outside. The a values are then reduced or increased according to the overall error rate. Classification truth is understood based on error data. The new operating data K is obtained from the operating data L. The tree classifiers in the RF classifier are of type { h(F, θ_K)K = 1,…}.F shows the input data and θ_K shows the random vector. h(F, L_K) classifier was created using new study data. F and M are not present in Z_i. Random pixels are picked for a given study data. When L is set, this pixel belongs to class S_c. Therefore, the Gini index is phrased in Equation 3.5 as follows.

$$\sum\sum_{j\neq c}(f(S_c,L)/|L|)(f((S_c,L)/|L|) \quad (3.5)$$

Here, L is the training data set, S_c is the class to which a haphazard picked pixel belongs, f (S_c, L) /|L|) indicates the probability that the selected sample belongs to class S_c (Korkmaz, 2018).

Experimental Results and Discussion

Histopathology images of lung adenocarcinoma were obtained using light microscopy images. The results were obtained using appropriate methods. 240 different sections from 60 people were used. The obtained images were processed in the appropriate program. It was also compared which methods yielded better results.

TABLE 1: ACCURACY RATE BY ADDING SURF PROPERTIES OF SIZE REDUCTION METHODS AND RANDOM FOREST CLASSIFICATION METHOD USED

Number of Features Used	**Size Reduction Methods and Accuracy Rate (%)**		
	PCA (%)	**GDA(%)**	**LDA(%)**
5	95,000000	93,333333	90,833333
10	92,500000	91,666667	91,666667
15	89,166667	91,666667	89,166667
20	88,333333	91,666667	89,166667
25	89,166667	91,666667	88,333333
30	87,500000	91,666667	88,333333
35	85,000000	91,666667	86,666667
40	84,166667	91,666667	85,833333
45	86,666667	91,666667	85,000000
50	86,666667	**99,166667**	85,833333

Table 1 shows the results corresponding to the dimension reduction methods when SURF is used in the Random Forest classifier. The results are shown according to the number of features used. The highest result is 99,166667% accuracy rate and it is a result with 50 features which is used by the SEE dimension reduction method.

TABLE 2: ACCURACY RATE BY ADDING SURF PROPERTIES OF SIZE REDUCTION METHODS AND DECISION TREE CLASSIFICATION METHOD USED

Number of Features Used	**Size Reduction Methods and Accuracy Rate (%)**		
	PCA (%)	**GDA(%)**	**LDA(%)**
5	89,166667	**91,666667**	90,000000
10	89,166667	91,666667	90,000000
15	85,000000	91,666667	85,000000
20	85,000000	91,666667	85,000000
25	87,500000	91,666667	85,000000
30	87,500000	91,666667	85,000000
35	87,500000	91,666667	85,000000
40	82,500000	91,666667	85,000000
45	83,333333	91,666667	85,000000
50	83,333333	91,666667	85,000000

Table 2 shows the results corresponding to the dimension reduction methods when SURF is used in the decision tree classifier. The results are shown according to the number of features used. The highest result is 91,666667% accuracy rate and it is a result which has 5 properties number.

TABLE 3: ACCURACY RATE BY ADDING MSER PROPERTIES OF SIZE REDUCTION METHODS AND RANDOM FOREST CLASSIFICATION METHOD USED

Number of Features Used	**Size Reduction Methods and Accuracy Rate (%)**		
	PCA (%)	**GDA(%)**	**LDA(%)**
5	95,833333	96,666667	92,500000
10	95,833333	96,666667	92,500000
15	93,333333	**97,500000**	85,000000
20	92,500000	97,500000	85,000000
25	88,333333	97,500000	83,333333
30	88,333333	97,500000	84,166667
35	84,166667	97,500000	81,666667
40	85,000000	97,500000	86,666667
45	84,166667	97,500000	84,166667
50	82,500000	97,500000	82,500000

Table 3 shows the results corresponding to the dimension reduction methods when the MSER feature is used in the Random Forest classifier. The results are shown according to the number of features used. The highest result with an accuracy rate of 97,500000% is a result of 15 properties number using SEE size reduction method.

TABLE 4: ACCURACY RATE BY ADDING MSER PROPERTIES OF SIZE REDUCTION METHODS AND DECISION TREE CLASSIFICATION METHOD USED

Number of Features Used	**Size Reduction Methods and Accuracy Rate (%)**		
	PCA (%)	**GDA(%)**	**LDA(%)**
5	93,333333	69,166667	86,666667
10	91,666667	69,166667	86,666667
15	92,500000	87,500000	85,833333
20	92,500000	87,500000	86,666667
25	92,500000	87,500000	86,666667
30	92,500000	87,500000	86,666667
35	92,500000	87,500000	86,666667
40	92,500000	87,500000	78,333333
45	92,500000	87,500000	78,333333
50	**92,500000**	87,500000	78,333333

Table 4 shows the results corresponding to the dimension reduction methods when the MSER feature is used in the Random Forest classifier. The results are shown according to the number of features used. The highest result with a accuracy rate of 92,500000% is the result of the PCA size reduction method with 50 features.

When all the results are examined, when SURF feature is used in Random Forest classifier, it is the method which gives the highest accuracy according to the results corresponding to the dimension reduction methods. The highest result is 99,166667% accuracy rate and it is a result with 50 features which is used by the SEE dimension reduction

method. It is the method which gives the best degree of accuracy among the methods used.

Conclusions

According to the results of the analysis of lung cancer by machine learning techniques, the methods with the highest accuracy are shown in the tables. The value of the method which gives the highest accuracy according to the number of features for each of the methods used is shown in bold. When all tables are examined, when SURF feature is used in Random Forest classifier, it is the method that gives the highest accuracy rate according to the results corresponding to dimension reduction methods. The highest result is 99,166667% accuracy rate and it is a result with 50 features which is used by the SEE dimension reduction method. It is the method which gives the best degree of accuracy among the methods used. Among the methods used, the other methods yielded good accuracy.

Apart from the methods used, there are other methods that can give good results with this method. Classification methods such as artificial neural networks and discriminant analysis can also be used as classifiers. Local linear embedding, conservation of neighborhood migration, stochastic proximity embedding, classical multidimensional scaling can be used as dimension reduction methods. Binary robust invariable scalable key points can be used as a feature method.

References

American Cancer Society. (2010). "Cancer Facts And Figures", Atlanta.

Türkiye Cumhuriyeti Sağlık Bakanlığı. (2009). Sağlık Istatistikleri Yıllığı, Ankara.

Ceylan, M. (2006). Bilgisayar Tomografili Akciğer Görüntülerinin Değerlendirilmesinde Kompleks Değerli Yeni Bir Akıllı Sistem Tasarımı, Doktora Tezi, Selçuk Üniversitesi Fen Bilimleri Enstitüsü, Konya.

Doi K. (2007). "Computer-aided diagnosis in medical imaging: historical review, current status and future potential", Computerized Medical Imaging and Graphics, 31(4–5), 198–211.

Aydın Kaya, Ali Seydi Keçeli, Ahmet Burak Can. (2018). Examination of various classification strategies inclassification of lung nodule characteristics, *Journal of the Faculty of Engineering and Architecture ofGazi University* (2018), https://doi. or./10.17341/gazimmfd.416530

Matas, J., Chum, O., Urban, M., Pajdla, T. (2002). Robust widebaseline stereo from maximally stable extremal regions, British Machine Vision Conference, s.384-393.

J. Matas, O. Chum, M. Urban, ve T. Pajdla. (2004), "Robust widebaseline stereo from maximally stable extremal regions," Image and vision computing, Sayı 22, 761-767.

Güney M., Arıca N.(2009). " Desen Tabanlı İlgi Bölgesi Tespiti" Journal of Naval Science and Engineering 2009, Vol. 5 , No.1, pp. 94-106.

Teke, M., and A. Temizel. (2010a, August). Multi-spectral satellite image registration using scale-restricted SURF. In Pattern Recognition (ICPR), 2010 20th International Conference on (pp. 2310–13). USA: IEEE.

Viola, P., and M. Jones. (2001). Rapid object detection using a boosted cascade of simple features. In Computer Vision and Pattern Recognition, 2001. CVPR 2001. Proceedings of the 2001 IEEE Computer Society Conference on (Vol. 1, pp. I–I). USA: IEEE.

Teke, M., and A. Temizel. (2010b, April). Registration of multi-spectral satellite images with scale-restricted SURF. In Signal Processing and

Communications Applications Conference (SIU), 2010 IEEE 18th (pp. 356–59). IEEE.

Alparslan, N. (2013). New approaches to gradient based heterogeneous feature extraction methods. Turkey: Institute of Science, İnönü Üniversity.

Abdi, H., & Williams, L. J. (2010). Principal component analysis. *Wiley interdisciplinary reviews: computational statistics*, *2*(4), 433-459.

Saraswat, M., Wadhwani, A. K., Dubey, M., & Mits, R. (2013). Compression of breast cancer images by principal component analysis. *International journal of Advanced Biological and Biomedical Research*, *1*(7), 767-776.

Zheng, W., Zhao, L. ve Zou, C. (2004). Genelleştirilmiş diskriminant analizi için değiştirilmiş bir algoritma. *Sinirsel Hesaplama* , *16* (6), 1283-1297.

G. H. Golub and C. F. Van Loan. (1996). Matrix Computations. The Johns Hopkins University Press, Baltimore, MD, USA, third edition.

Ye, J. (2005). Örneklenmiş problemler üzerinde genelleştirilmiş diskriminant analizi için bir algoritma ailesinin karakterizasyonu. *Makine Öğrenimi Araştırmaları Dergisi* , *6* (Nis), 483-502.

G. Yu, W. Russell, R. Schwartz, J. Makhoul. (1990).Discriminant analysis and supervised vector quantization for continuous speech recognition, Proc. ICASSP, pp. 685-688, Albuquerque, NM.

L. Wood, D. Pearce, F. Novello. (1991). Improved vocabulary-independent sub-word HMM modelling, Proc. ICASSP, pp. 181-184, Toronto, Canada.

M.J. Hunt, S.M. Richardson, D.C. Bateman, A. Piau. (1991). An Investigation of PLP and IMELDA acoustic representations and of their potential for combination, Proc. ICASSP, pp. 881-884, Toronto, Canada, May.

Haeb-Umbach, R., & Ney, H. (1992). Gelişmiş geniş kelime sürekli konuşma tanıma için doğrusal diskriminant analizi. Gelen *[Proceedings] ICASSP-92: 1992 Akustik, Konuşma IEEE International Conference, ve sinyal işleme* (Cilt 1, sayfa 13-16.).. IEEE.

Safavian S.R., Landgrebe D. (1991). “A survey of decision tree classifier methodology”, IEEE Transactions on Systems Man and Cybernetics, 21, 660-674.

Quinlan J.R. (1993). “C4.5: Programs for Machine Learning”, Morgan Kaufmann, San Mateo, CA, 302 s.

Friedl M.A., Brodley C.E. (1997). “Decision tree classification of land cover from remotely sensed data”, Remote Sensing of Environment, 61, 399–409.

Swain P.H., Hauska H., (1977). “Decision tree classifier - design and potential”, IEEE Transactions on Geoscience and Remote Sensing, 15, 142-147.

Kavzoğlu, T.,& Çölkesen, İ. (2010). Karar ağaçları ile uydu görüntülerinin sınıflandırılması: Kocaeli örneği. *Harita Teknolojileri Elektronik Dergisi*, *2*(1), 36-45.

Rodriguez-Galiano, VF, Ghimire, B., Rogan, J., Chica-Olmo, M., ve Rigol-Sanchez, JP. (2012). Arazi örtüsü sınıflandırması için rastgele bir orman sınıflandırıcısının etkinliğinin değerlendirilmesi. *ISPRS Fotogrametri ve Uzaktan Algılama Dergisi* , *67* , 93-104.

Pal, Mahesh. (2005). "Random forest classifier for remote sensing classification." International Journal of Remote Sensing, vol. 26, no. 1, pp. 217-222, .

Korkmaz, Sevcan Aytaç, and Hamidullah Binol. (2017). "Analysis of Molecular Structure Images by using ANN, RF, LBP, HOG, and Size Reduction Methods for early Stomach Cancer Detection."Journal of Molecular Structure.

Korkmaz, SA, Esmeray, F. (2018). MSER özellikleri için Yerleşim Yerinde Teğet Yer Tespiti ve Mahalle Koruma Yerleştirme ile Rastgele Orman Tabanlı Sınıflandırma: MSER_DFT_LTSA-NPE_RF.

Chapter 13

CLUSTERING ACCORDING TO THE LEVEL OF THE ELECTRICITY GENERATION VALUES USING DIFFERENT DISTANCE METRIX AND LINKAGE METHODS

Sevcan AYTAÇ KORKMAZ[1]

1 Electronic and AutomationDepartment, Fırat University Elazığ, Turkey
sevcanaytackorkmaz@gmail.com

Introduction

The low, medium and high quantity of electricity manufactured in a power plant is very significant for today's economy. In this article, the electricity generation (MW) values obtained from Etikrom A.Ş. are clustered using different distance and different linkage methods with ClusterData clustering method. The main purpose of the cluster is to determine how much, how much, and how much of the value of the electricity generated in the company has high electricity generation. The different distance methods are euclidean, squaredeuclidean, seuclidean, mahalanobis, cityblock, minkowski, chebychev, cosine, correlation, hamming, jaccard, and spearman. Different Linkage methods are Average, Centroid, Complete, Median, Single, Ward, and Weighted. All electricity production values were clustered by cluster method using distance and linkage methods. At the end of the clustering process, it was determined that 17.67% of all electricity production amounts obtained from Etikrom A.Ş. are at small electricity generation level, 68.09% at medium electricity generation level and 14.50% at high electricity generation level. Also, the validity of the proposed method has been proven. Also, the validity of the proposed method has been proven.

Today, different types of energy production are used to meet the quantity of electricity consumed by the consumer. In order to meet the energy needs, energy types such as hydropower, solar energy and wind energy are used. In addition to these types of energy production, there is also steam generation method. Steam passes through various stages of the water, the gas from the liquid state of water is the transition into. In this article, steam is used to generate electricity by passing through various stages. In addition, electrical energy production quantities and factors affecting production amounts were examined and classified. The data on the quantity of electricity generation and the factors affecting this quantity belong to 2017. This data is recorded by the operators both for automation data recording systems and for every timer. ETİKROM A.Ş. We observed the data recorded in the cogeneration plant, classifying the quantity of electricity generation and the factors affecting the quantity of electricity generation.

In a steam generating unit; high pressure steam turbine, high pressure steam boiler, auxiliary condenser, condenser, gear box for turbine-generator connection, feed water tank, boiler, demineralization monad for supplying water to feed water tank, condenser and cooling towers for liquid vaporization in condenser and auxiliary condenser. . The

water to be manufactured in the demineralization monad must have a maximum conductivity of 0.2 μS and a minimum pH of 9.4. Water with these characteristics should be sent to the feed water tank. The temperature of the water in the feed water tank increases slightly with the rotten steam coming from the condenser. As a result of the combustion of the arc furnace used to melt the chrome at an installed capacity of 23 MW, the resulting high temperature flue gas is vacuumed with the help of ID-Fan and taken into the boiler. The water taken into the boiler with the help of pipes is circulated in the boiler. Boiler; high pressure superheater, high pressure evaporator, high pressure economizer, high pressure steam drum. When the water circulated in the boiler interacts with the high-temperature gas entering the boiler through the counter-flow principle, superheated steam is produced. The steam achieved as superheated steam in the boiler is taken to the high pressure steam drum. The pressured steam is sent from the high-pressure steam drum to the steam turbine by the adjustment of the valves controlled by the servo motor. The steam sent to the steam turbine is superheated steam. The steam with a pressure of 300 ° C and 30 bar was sent to the steam turbine with the help of the valves to adjust the quantity of steam. The rotten steam from the steam turbine is condensed in the condenser with the help of cold water from the cooling towers. With the help of the pumps at the outlet of the condenser, the water obtained from the rotten steam is pumped back into the feed water tank and the covered loop is completed. Also, the feed water tank is kept constantly hot with low pressure rotten steam. There may be harmful and suspended substances in the boiler, piping lines, feed water tank. The harmful and suspended matterss in the system are taken out by the blowdown tank. Synchronized with the steam turbine is connected to each other by a generator gearbox. The connected turbine and generator are operated together and electricity is produced. The quantity of electricity produced, the quantity of steam produced in the boiler, the temperature of the gas taken into the boiler, etc. depends on such variables. These variables are the power of the arc furnace, ie the flow and temperature of the gas coming out of the chimney, the inlet temperature of the gas entering the boiler, the total steam produced, the water temperature in the feed water tank temperature, the ID fan speed and the environmental temperature. If these factors are to be accounted, the temperature and flow rate of the gas exiting the furnace is immediately comparative to the power of the furnace. That is, when the furnace power is high, the temperature and flow rate of the gas exiting the

chimney is high. Therefore, the flue gas temperature and flow rate immediately affect the boiler inlet temperature, ie the temperature of the gas affecting the water. The higher and continuous this temperature and flow rate, the better the evaporation and the higher the quantity of vapor. It is easier to evaporate the water from the low temperature to the higher temperature, so that the water in the feed water tank is heated by preheating steam. This means that, while the temperature of the water remains constant, the steam to be generated can be manufactured more easily. Because the quantity of heat enthalpy required to evaporate cold water is higher than the quantity of heat enthalpy required to heat the hot water. As the quantity of steam manufactured increases, so does the quantity of electrical energy manufactured. The valves that adjust the turbine inlet steam quantity are directly proportional to the increase in the steam quantity. As the quantity of steam increases, the servo motor controlled valves will open more and thus the number of active states in the turbine will increase. As the number of active turbines increases, the generation of electricity in the generator connected with each other will increase. Depending on the ID-Fan speed, the suction power is influenced by the steam generation. If the ID-Fan speed is not syntonized according to the flue gas flow rate, the steam generation quantity decreases. If the gas flow is low and the ID-Fan cycle is not of adequate value and the gas passages quickly through the boiler, the flue gas is removed from the boiler without lating the heat to the water, which reduces the quantity of steam generated. Therefore, optimization should be done well. In addition, the amount of steam production affects the ambient temperature. When the outside temperature is low, the flue gas temperature in the flue gas ducts decreases. In order to prevent this, the insulation in the lines should be done well. If not done, both the gas and the steam produced will decrease, so the amount of steam produced is reduced.

On the other hand, in case of any failure of the steam turbine, generator or system, the overheated steam is taken to the auxiliary condenser. So the system will not work efficiently. Closed loop will continue with the help of auxiliary condenser so that steam production does not stop. Thus, the superheated steam will not lose its property. In addition, dust and harmful residues from the flue gas are retained by the filter bags. The conveyed dust is transported to the silo by the conveyor system. The powder taken into the silo is mixed with various chemicals and disposed of in a way that does not harm the nature. At this point, the

plant becomes an environmentally friendly facility both by not releasing the flue gas and eliminating the dust generated. In addition, because there are two arc furnaces in the cogeneration plant of Eti Krom A.Ş.

There are many works about electricity production (Ustüntaş, 2008), (Agrawal, 2008), (Grubb, 2006), (Aelterman, 2008), (Seabra, 2010), (Dastrup, 2012), (Tekiner, 2010), (Mamay, 2006). However, Elazığ Etikrom A.Ş. does not have any studies that determine the levels of electrical power generated by the electricity production values. The purpose of this article is to determine how much small, how much medium, and how much high of the electricity generation amount of the Etikrom A.Ş has electricity generation. The innovation of this study, when studies in the literature are analyzed, it is seen thatdifferent distance and different linkage methods are not used in together to determine the levels of the electricity generation amount taken from Etikrom A.Ş. Different distance and linkage methods in this article have been used in together. Also, the levels of the electricity generation amount taken from Etikrom A.Şhave been compared. The validity of the proposed method has been proven.

Theory and Method of the study are defined in Section 2. Proving results and conclusions are explained in Section 3 and Section 4, seriatim.

Theory and Method

A. Obtaining the data

Electricity generation datums in this article have been taken from Etikrom A.Ş. The electricity generation datas are current for the first four months of 2017. The data consists of total and instantaneous values per hour. At the same time, the installed capacity of the cogeneration plant was accepted as 2.2 MWe by the Ministry of Energy. However, this acceptance is temporary acceptance. The methods of obtaining the data are realized by taking the instantaneous data in the automation system and reading the meter values.

In this article, the proposed system for determining the small, medium, and high Electricity generation level from Electricity generation datas of the Elazığ Etikrom A.Ş. is shown in Fig 1.

In this article, according to figure 1, Etikrom A.Ş. (MW) values are clustered using different distance and different linkage methods. Different distance motions were euclidean, squaredeuclidean, seuclidean,

mahalanobis, cityblock, chebychev, minkowski, correlation, hamming, cosine, spearman and jaccard.

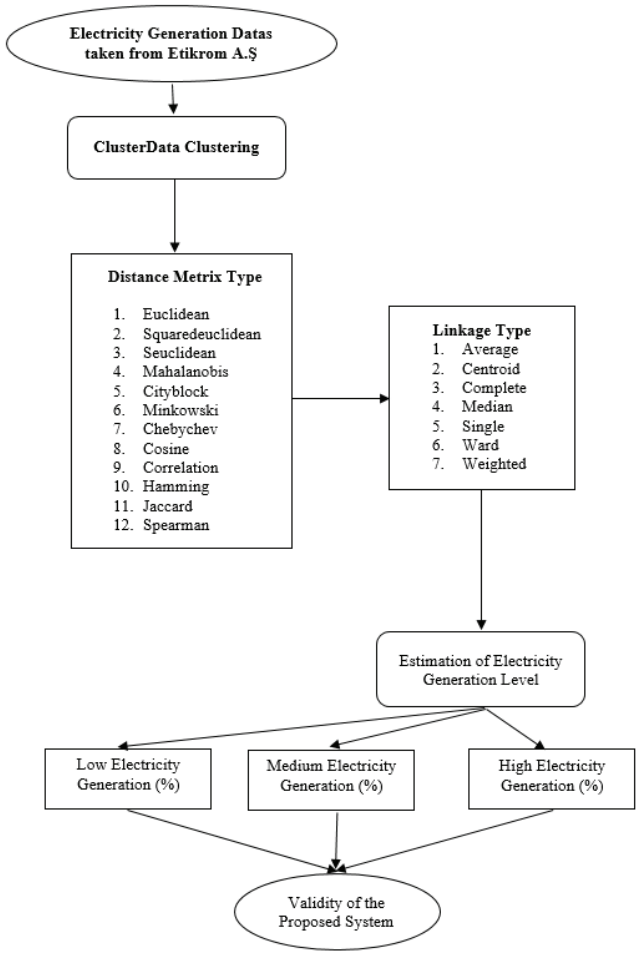

Figure 1: Propounded System

Different Linkage methods are Centroid, Average, Complete, Single, Median, Weighted and Ward. All electricity production values were clustered by cluster method using distance and linkage methods. At the end of the clustering process, it was determined that all electricity production values obtained from Etikrom A.Ş. are at low, medium and

high electricity production levels. The validity of the forward system has been proven.

B. ClusterData Clustering

Cluster Data is agglomerative clusters from data. ClusterData methods are distance Metrics and linkage.

C. Distance Metrics Methods for ClusterDataClustering

A distance metric (www.mathworks.com, cluster data, 2018), (www.mathworks.com, pdist, 2018) is a function that describes a distance between two investigations. pdist supports different distance metrics: Euclidean distance, standardized Mahalanobis distance, Euclidean distance, Minkowski distance, Chebychev distance, city block distance, correlation distance, cosine distance, Jaccard distance, Hamming distance, and Spearman distance. Given an *k*-by-*l* data matrix A, which is used as *k* (1-by-*l*) row vectors $a_1, a_2, \ldots, a_k$ the different distances between the vector $a_m$and a_n are described as follows:

1) Euclidean distance[9-10]is expressed as follows

$$d_{mn}^2 = (a_m - a_n)(a_m - a_n)'$$

The Euclidean distance is a private status of the Minkowski distance, where $p = 2$.

2) Standardized Euclidean distance (www.mathworks.com, cluster data, 2018), (www.mathworks.com, pdist, 2018) is expressed as follows

$$d_{mn}^2 = (a_m - a_n)V^{-1}(a_m - a_n)'$$

where *V* is the l-by-l diagonal matrix whose *f*th diagonal factort is $(S(f))^2$, where *S* is a vector of scaling agents for each dimension.

3)Seuclidean (www.mathworks.com, cluster data, 2018), (www.mathworks.com, pdist, 2018) is explained as follows

Seuclidean is the Standard Euclidean distance. The Seuclidean is divided into points corresponding to the standard deviation to find each coordinate difference between observations.

4) Mahalanobis distance (www.mathworks.com, cluster data, 2018), (www.mathworks.com, pdist, 2018) is expressed as follows

$$d_{mn}^2 = (a_m - a_n)C^{-1}(a_m - a_n)'$$

where *C* is the covariance matrix.

5) City block distance (www.mathworks.com, cluster data, 2018), (www.mathworks.com, pdist, 2018) is expressed as follows

$$d_{mn} = \sum_{f=-1}^{b} |a_{mf} - a_{nf}|$$

The city block distance is a private status of the Minkowski distance, where $p = 1$.

6) Minkowski distance (www.mathworks.com, cluster data, 2018), (www.mathworks.com, pdist, 2018) is expressed as follows

$$d_{mn} = \sqrt[p]{\sum_{f=-1}^{b} |a_{mf} - a_{nf}|^p}$$

For the private status of $p = 1$, the Minkowski distance delivers the city block distance. For the private status of $p = 2$, the Minkowski distance serves the Euclidean distance. For the private status of $p = \infty$, the Minkowski distance grants the Chebychev distance.

7) Chebychev distance (www.mathworks.com, cluster data, 2018), (www.mathworks.com, pdist, 2018) is expressed as follows

$$d_{mn} = max_f\{|a_{mf} - a_{nf}|\}$$

The Chebychev distance is a private status of the Minkowski distance, where $p = \infty$.

8) Cosine distance (www.mathworks.com, cluster data, 2018), (www.mathworks.com, pdist, 2018) is expressed as follows

$$d_{mn} = 1 - \frac{a_m a'_n}{\sqrt{(a_m a'_m)(a_n a'_n)}}$$

9) Correlation distance (www.mathworks.com, cluster data, 2018), (www.mathworks.com, pdist, 2018) is expressed as follows

$$d_{mn} = 1 - \frac{(a_m - \overline{a_m})(a_n - \overline{a_n})'}{\sqrt{(a_m - \overline{a_m})(a_m - \overline{a_m})'}\sqrt{(a_n - \overline{a_n})(a_n - \overline{a_n})'}}$$

where

$$\overline{a_m} = \frac{1}{b}\sum_f a_{mf} \text{ and } \overline{a_n} = \frac{1}{b}\sum_f a_{nf}$$

10) Hamming distance (www.mathworks.com, cluster data, 2018), (www.mathworks.com, pdist, 2018) is expressed as follows

$$a_{mn} = (\#(a_{mf} \neq a_{nf})/b)$$

11) Jaccard distance (www.mathworks.com, cluster data, 2018), (www.mathworks.com, pdist, 2018) is expressed as follows

$$a_{mn} = \frac{\#[(a_{mf} \neq a_{nf}) \cap ((a_{mf} \neq 0) \cup (a_{nf} \neq 0)}{\#(a_{mf} \neq 0) \cup (a_{nf} \neq 0)}$$

12) Spearman distance (www.mathworks.com, cluster data, 2018), (www.mathworks.com, pdist, 2018) is expressed as follows

$$d_{mn} = 1 - \frac{(r_m - \overline{r_m})(r_n - \overline{r_n})'}{\sqrt{(r_m - \overline{r_m})(r_m - \overline{r_m})'}\sqrt{(r_n - \overline{r_n})(r_n - \overline{r_n})'}}$$

wherer_{mf} is the grade of r_{mf} taken over $a_{1f}, a_{2f}, \ldots . a_{kf}$,as computed by tiedrank. r_m and r_n are the coordinate-wise grade vectors of a_m and a_n, i.e., $r_m = (r_{m1}, r_{m2}, \ldots . r_{mb})$.

$$\overline{r_m} = \frac{1}{b}\sum_f r_{mf} = \frac{(b+1)}{2}$$

$$\overline{r_n} = \frac{1}{b}\sum_f r_{nf} = \frac{(b+1)}{2}$$

D. Linkages for ClusterDataClustering

Linkage is agglomerative hierarchical cluster tree.The following representation is used to designate the connections used by various methods (www.mathworks.com, cluster data, 2018),

(https://www.mathworks.com, linkage, 2018): Cluster h is created from clusters b and c.n_h is the number of objects in cluster h.$a_{hj}$is the ith object in cluster h.The only link, also called the nearest neighbor, uses the smallest distance between the objects in the two coils www.mathworks.com, cluster data, 2018), (https://www.mathworks.com, linkage, 2018):

$$d(h,s) = \min\left(dist\left(a_{hi}, a_{sj}\right)\right), i \in (i, \dots., n_h), j \in (1, \dots, n_s)$$

The complex linkage (www.mathworks.com, cluster data, 2018), (https://www.mathworks.com, linkage, 2018), also called the farthest neighbor, uses the greatest distance between the objects in the two coils:

$$d(h,s) = \max\left(dist\left(a_{hi}, a_{sj}\right)\right), i \in (i, \dots., n_h), j \in (1, \dots, n_s)$$

The average link (www.mathworks.com, cluster data, 2018), (https://www.mathworks.com, linkage, 2018) accesses the average distance between all pairs of objects in both stacks:

$$d(h,s) = \frac{1}{n_h n_s} \sum_{i=1}^{n_h} \sum_{j=1}^{n_s} dist(a_{hi}, a_{sj})$$

Centroid linkage (www.mathworks.com, cluster data, 2018), (https://www.mathworks.com, linkage, 2018) accesses the Euclidean distance between the centroids of the two stacks:

$$d(h,s) = \|\overline{a_h} - \overline{a_s}\|_2$$

$$\overline{a_h} = \frac{1}{n_h} \sum_{i=1}^{n_h} a_{hi}$$

Median linkage (www.mathworks.com, cluster data, 2018), (https://www.mathworks.com, linkage, 2018) accesses the Euclidean distance between weighted centroids of the two stacks,

$$d(h,s) = \|\widetilde{a_h} - \widetilde{a_s}\|_2$$

where $\widetilde{a_h}$and $\widetilde{a_s}$ are weighted centroids for the clusters *h* and *s*. If cluster h was formed by combining clusters *b* and *c*, $\widetilde{a_h}$is defined recursively as

$$\widetilde{a_h} = \frac{1}{2}(\widetilde{a_b} + \widetilde{a_c})$$

Ward's link (www.mathworks.com, cluster data, 2018), (https://www.mathworks.com, linkage, 2018) uses increasing total amount of squares; that is, the amount of the total squares in the stack as a result of joining the two stacks. The amount of intra-frame squares is described as the amount of the squares between all objects in the co-ordinate and the center of the frame. The amount of squares plumb is tantamount to the following distance measure $d(h,s)$, which is the formula linkage uses:

$$d(h,s) = \sqrt{\frac{2n_h n_s}{n_h + n_s}} \|\overline{a_h} - \overline{a_s}\|_2$$

where

$\|\|_2$is Euclidean distance. $\overline{a_h}$and $\overline{a_s}$ are the centroids of stacks *h* and *s*. n_h and n_s are the number of elements in stacks *h* and *s*

In some references the Ward contact (www.mathworks.com, cluster data, 2018), (https://www.mathworks.com, linkage, 2018) does not use the factor of 2 increasing $n_h n_s$. The contact function uses this factor so the distance between two singleton stacks is the same as the Euclidean distance.Weighted average contact (www.mathworks.com, cluster data, 2018), (https://www.mathworks.com, linkage, 2018) uses a recursive description for the distance between two stack. If stack *h* was formed by joining stacks *b* and *c,* the distance between h and another cluster *s* is described as the average of the space between *b*and *s* and the space between *c* and *s*:

$$d(h,s) = \frac{(d(b,s) + d(c,s))}{2}$$

Experimental Results and Discussion

Produced power production values obtained from Etikrom AS have been clustered using different distance and different linkage methods.

Different distance motions were squaredeuclidean, euclidean, mahalanobis, cityblock, seuclidean, minkowski, cosine, chebychev, correlation, jaccard, hamming, and spearman. Different Linkage methods are Centroid, Average, Complete, Single, Median, Weighted, and Ward. All electricity production values were clustered by cluster method using distance and linkage methods.In [Table 1], Clustering Rates of the Small Electricity Generation found for Linkage and Distance Type have been seen.Accordingly, 3623 electricity generation data were clustered separately using all the different distance metrix and linkage methods. Averages of all the clusters were taken. According to [Table 1], on average 17.67% were found to be at small electricity generation level values.In [Table 2], Clustering Rates of the medium Electricity Generation found for Linkage and Distance Type have been seen. Accordingly, 3623 electricity generation data were clustered separately using all the different distance metrix and linkage methods. Averages of all the clusters were taken. According to [Table 2], it is determined that 68.09% of the average electricity generation level values are on average.

In [Table 3], Clustering Rates of the high Electricity Generation found for Linkage and Distance Type have been seen. According to [Table 3], it is determined that on average 14.50% of electricity production levels are at high levels. When the percentages of low, medium and high electricity production levels are examined, it is determined that the proposed method is valid. Because, the sum of the classification levels is 100%, which is 17.67%, 68.09%, and 14.50%.

According to [Table 1], [Table 2] and [Table 3], the level of electricity produced in Etikrom A.Ş. is higher than that of low and high level electricity production. However, the amount of low-level electricity production is higher than the amount of high-level electricity production.

TABLE 1: CLUSTERING RATES OF THE SMALL ELECTRICITY GENERATION FOUND FOR LINKAGE TYPE

	Clustering Rates of the Small Electricity Generation found for Linkage Type							
Distance	Average	Centroid	Complete	Median	Single	Ward	Weighted	**Average**
Euclidean	80.67	80.67	19.29	21.08	0.0552	0.0276	26.08	**32,55**
Squaredeuclidean	19.29	80.67	19.29	21.08	0.0552	73.19	19.21	**33,25**
Seuclidean	80.67	80.67	19.29	21.08	0.0552	0.0276	26.08	**32,55**
Mahalanobis	80.67	80.67	19.29	21.08	0.0552	0.0276	26.08	**32,55**
Ctyblock	80.67	80.67	19.29	21.08	0.0552	0.0276	26.08	**32,55**
Minkowski	80.67	0.027	0.027	0.027	0.0552	0.0276	26.08	**15,27**
Chebychev	80.67	80.67	19.29	21.08	0.0552	0.0276	26.08	**32,55**
Cosine	0.19	0.02	0.19	0.02	0.02	0.19	0.19	**0,117**
Correlation	0.02	0.02	0.02	0.02	0.02	0.02	0.02	**0,02**
Hamming	0.27	0.38	0.27	0.38	0.38	1.821	0.276	**0,538**
Jaccard	0.02	0.02	0.27	0.02	0.38	0.358	0.0276	**0,156**
Spearman	0.02	0.02	0.02	0.02	0.02	0.02	0.02	**0,02**
Average	**41,98**	**40,37**	**9,711**	**10,58**	**0,10**	**6,31**	**14,68**	**17,67**

TABLE 2: CLUSTERING RATES OF THE MEDIUM ELECTRICITY GENERATION FOUND FOR LINKAGE TYPE

	Clustering Rates of the Medium Electricity Generation found for Linkage Type							
Distance	Average	Centroid	Complete	Median	Single	Ward	Weighted	**Average**
Euclidean	19.29	19.29	80.67	78.88	99.91	79.60	73.88	**64,50**
Squaredeuclidean	80.67	19.29	80.67	78.88	99.91	26.77	80.76	**66,70**
Mahalanobis	19.29	19.29	80.67	78.88	99.91	79.60	73.88	**64,50**
Ctyblock	19.29	19.29	80.67	78.88	99.91	79.60	73.88	**64,50**
Minkowski	19.29	79.60	79.60	79.60	99.91	79.60	73.88	**73,06**
Chebychev	19.29	19.29	80.67	78.88	99.91	79.60	73.88	**64,50**
Cosine	6.65	6.79	6.65	6.79	6.79	6.65	6.65	**6,71**
Correlation	99.94	99.94	99.94	99.94	99.94	99.94	99.94	**99,94**
Hamming	99.42	99.33	99.42	99.33	99.33	91.33	99.42	**98,22**
Jaccard	6.79	6.79	99.42	6.79	99.33	99.33	6.79	**46,46**
Spearman	99.94	99.94	99.94	99.94	99.94	99.94	99.94	**99,94**
Average	**44,53**	**44,44**	**80,75**	**71,52**	**91,34**	**74,72**	**69,35**	**68,09**

TABLE 3: CLUSTERING RATES OF THE HIGH ELECTRICITY GENERATION FOUND FOR LINKAGE TYPE

	Clustering Rates of the High Electricity Generation found for Linkage Type							
Distance	Average	Centroid	Complete	Median	Single	Ward	Weighted	**Average**
Euclidean	0.02	0.02	0.027	0.027	0.027	20.36	0.0276	**2,92**
Squaredeuclidean	0.02	0.02	0.027	0.027	0.027	0.027	0.0276	**0,025**
Seuclidean	0.02	0.02	0.027	0.027	0.027	20.36	0.0276	**2,92**
Mahalanobis	0.02	0.02	0.027	0.027	0.027	20.36	0.0276	**2,92**
Ctyblock	0.02	0.02	0.027	0.027	0.027	20.36	0.0276	**2,92**
Minkowski	0.02	20.36	20.36	20.36	0.027	20.36	0.0276	**11,64**
Chebychev	0.02	0.02	0.027	0.0276	0.027	20.36	0.0276	**2,92**
Cosine	93.15	93.18	93.15	93.18	93.18	93.15	93.15	**93,16**
Correlation	0.02	0.02	0.02	0.02	0.02	0.02	0.02	**0,02**
Hamming	0.30	0.27	0.30	0.27	0.27	6.84	0.303	**1,22**
Jaccard	93.18	93.18	0.30	93.18	0.27	0.303	93.182	**53,37**
Spearman	0.02	0.02	0.02	0.02	0.02	0.02	0.02	**0,02**
Average	**15,56**	**17,26**	**9,52**	**17,26**	**7,82**	**18,54**	**15,57**	**14,50**

Clustering Rates of the Small Electricity Generation found for Linkage Type

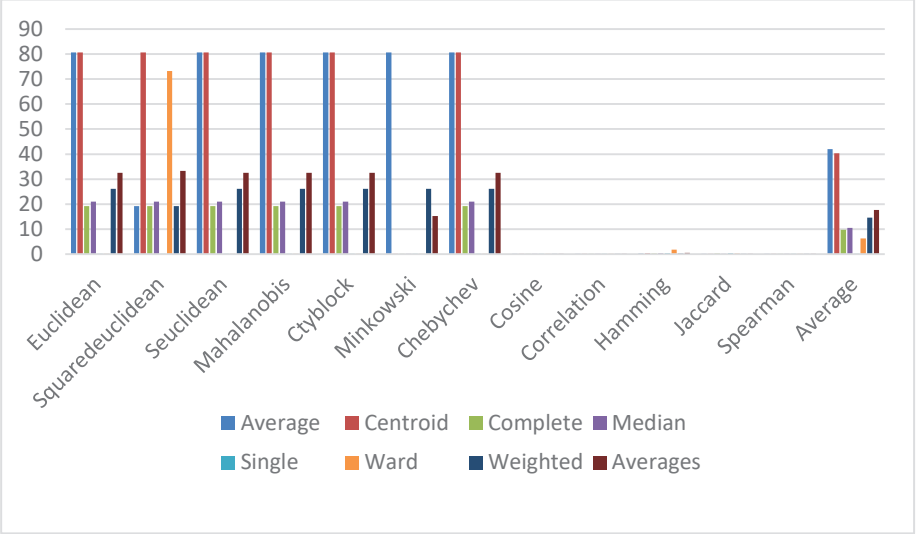

Conclusions

To date, there are many domain work for classification or clustering (Korkmaz, 2017), (KORKMAZ, 2017), (Turkoğlu, 2007), (Korkmaz, 2018), (Korkmaz, 2014), (Korkmaz, 2015), (Korkmaz, 2016), (KORKMAZ, 2017), (KORKMAZ, 2017), (Korkmaz, 2014), (Korkmaz, 2015), (KORKMAZ, 2013) energy recovery and dust collection facility. Electricity production data were obtained for the first four months of 2017. It consists of total and momentary values written by facility operators for each hour.At the same time, the installed capacity of the cogeneration plant was accepted as 2.2 MWe by the Ministry of Energy. However, this acceptance is temporary acceptance. The methods of obtaining the data are realized by taking the instantaneous data in the automation system and reading the meter values. The low, medium and high quantity of electricity manufactured in a power plant is very considerable for today's economy. In this article, the electricity generation (MW) values obtained from Etikrom A.Ş. are clustered using different distance and different linkage with ClusterData clustering

method. The main purpose of the cluster is to determine how much, how much, and how much of the value of the electricity generated in the company is in terms of high electricity generation. Different distance motions were, cityblock, euclidean squaredeuclidean, seuclidean, mahalanobis, chebychev, minkowski, hamming, correlation, cosine, spearman, and jaccard. Different Linkage methods are Average, Centroid, Complete, Median, Single, Ward, and Weighted. All electricity production values were clustered by cluster method using distance and linkage methods. At the end of the clustering process, it was determined that 17,67% of all electricity production amounts obtained from Etikrom A.Ş. are at small electricity generation level, 68.09% at medium electricity generation level and 14,50% at high electricity generation level. The amount of electricity produced at Etikrom A.Ş. at medium level is found to be higher than that of low and high level electricity production. However, it has been determined that the amount of low-level electricity generation is higher than that of high-level electricity generation. Also, the validity of the proposed method has been proven.

References

Üstüntaş, T., & Şahin, A. D. (2008). Wind turbine power curve estimation based on cluster center fuzzy logic modeling. Journal of Wind Engineering and Industrial Aerodynamics, 96(5), 611-620.

Agrawal, S., Panigrahi, B. K., & Tiwari, M. K. (2008). Multiobjective particle swarm algorithm with fuzzy clustering for electrical power dispatch. IEEE Transactions on Evolutionary Computation, 12(5), 529-541.

Grubb, M., Butler, L., & Twomey, P. (2006). Diversity and security in UK electricity generation: The influence of low-carbon objectives. Energy policy, 34(18), 4050-4062.

Aelterman, P., Versichele, M., Marzorati, M., Boon, N., & Verstraete, W. (2008). Loading rate and external resistance control the electricity generation of microbial fuel cells with different three-dimensional anodes. Bioresource technology, 99(18), 8895-8902.

Seabra, J. E., Tao, L., Chum, H. L., & Macedo, I. C. (2010). A techno-economic evaluation of the effects of centralized cellulosic ethanol and co-products refinery options with sugarcane mill clustering. Biomass and bioenergy, 34(8), 1065-1078.

Dastrup, S. R., Zivin, J. G., Costa, D. L., & Kahn, M. E. (2012). Understanding the Solar Home price premium: Electricity generation and "Green" social status. European Economic Review, 56(5), 961-973.

Tekiner, H., Coit, D. W., & Felder, F. A. (2010). Multi-period multi-objective electricity generation expansion planning problem with Monte-Carlo simulation. Electric Power Systems Research, 80(12), 1394-1405.

Marnay, C., & Venkataramanan, G. (2006, October). Microgrids in the evolving electricity generation and delivery infrastructure. In Power Engineering Society General Meeting, 2006. IEEE (pp. 5-pp). IEEE.

https://www.mathworks.com/help/stats/clusterdata.html. 22.02.2018

https://www.mathworks.com/help/stats/pdist.html.22.02.2018

https://www.mathworks.com/help/stats/linkage.html. 22.02.2018

Korkmaz, S. A., & Binol, H. (2017). Analysis of Molecular Structure Images by using ANN, RF, LBP, HOG, and Size Reduction Methods for early Stomach Cancer Detection. Journal of Molecular Structure.

KORKMAZ, Sevcan Aytaç, et al. (2017). A expert system for stomach cancer images with artificial neural network by using HOG features and linear discriminant analysis: HOG_LDA_ANN. In: Intelligent Systems and Informatics (SISY), 2017 IEEE 15th International Symposium on. IEEE, (2017):000327-000332.

Turkoglu, I. (2007). Hardware implementation of varicap diode's ANN model using PIC microcontrollers. Sensors and Actuators A: Physical, 138(2), 288-293.

Korkmaz, S. A. (2018). LBP Özelliklerine Dayanan Lokasyon Koruyan Projeksiyon (LPP) Boyut Azaltma Metodunun Farklı Sınıflandırıcılar Üzerindeki Performanslarının Karşılaştırılması. Sakarya University Journal of Science, 22(4), 1-1.

Korkmaz, S. Aytac, and Mustafa Poyraz. (2014). "A New Method Based for Diagnosis of Breast Cancer Cells from Microscopic Images: DWEE--JHT." Journal of medical systems 38.9 (2014): 1.

Korkmaz, Sevcan Aytac, and Mehmet Fatih Korkmaz. (2015). "A new method based cancer detection in mammogram textures by finding feature weights and using Kullback–Leibler measure with kernel estimation." Optik-International Journal for Light and Electron Optics 126.20 (2015): 2576-2583.

Korkmaz, Sevcan Aytac, Mehmet Fatih Korkmaz, and Mustafa Poyraz. (2016)."Diagnosis of breast cancer in light microscopic and mammographic images textures using relative entropy via kernel estimation." Medical & biological engineering & computing 54.4 (2016): 561-573.

KORKMAZ, Sevcan AYTAÇ. (2017). "DETECTING CELLS USING IMAGE SEGMENTATION OF THE CERVICAL CANCER IMAGES TAKEN FROM SCANNING ELECTRON MICROSCOPE." The Online Journal of Science and Technology-October 7.4 (2017).

KORKMAZ, Sevcan Aytaç, et al. (2017).Recognition of the stomach cancer images with probabilistic HOG feature vector histograms by using HOG features. In: Intelligent Systems and Informatics (SISY),

2017 IEEE 15th International Symposium on. IEEE, (2017). p. 000339-000342.

Korkmaz, S. A., & Poyraz, M. (2014). A New Method Based for Diagnosis of Breast Cancer Cells from Microscopic Images: DWEE—JHT. Journal of medical systems, 38(9), 92.

Chapter 14

RECENT ADVANCES IN THE SYNTHESIS AND PHARMACOLOGICAL ACTIVITIES OF 1,3-DIOXOLANES

Hatice BAŞPINAR KÜÇÜK [1]

1 Istanbul University-Cerrahpaşa, Engineering Faculty, Chemistry Department. Organic Chemistry Division, 34320 Avcılar-İstanbul/TURKEY

1.Introduction

1,3-Dioxolane (Figure 1), a five-membered, two oxygen-containing atoms at the 1,3-positions of the cyclic system heterocyclic ring, is a fully completely cyclic acetal. 1,3-dioxolane derivatives are found as center structures in a wide variety of compounds with significant pharmaceutical activities. They are very important building blocks in the substance of different drugs as antiviral, antifungal, anti-HIV and adrenoreceptor antagonists. Some examples of significant drugs containing 1,3-dioxolane ring in clinical use are given in Figure 1.

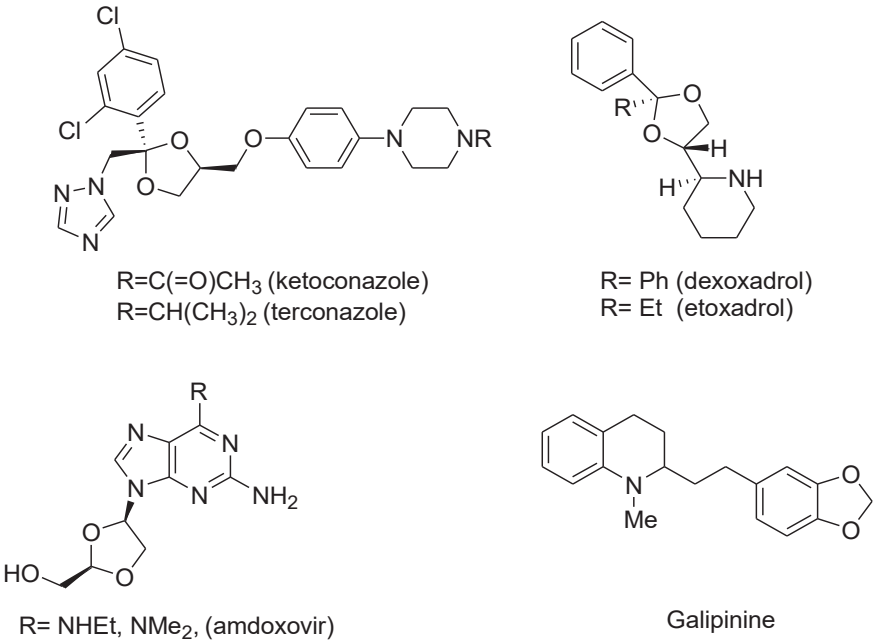

Figure 1. *Pharmaceutical drugs containing 1,3-dioxolane scaffold.*

2.Synthesis of 1,3-dioxolanes using various synthetic approaches

1,3-Dioxolanes are synthesized with the condensation of 1,3-propanediol or 1,2-ethanediol with carbonyl compounds, with a Brønsted or Lewis acid catalyst. The reaction products with 1,3-diols yield more stable products. As a catalyst, *p*-toluenesulfonic acid is used for protective means in refluxing toluene medium, therefore continuous removal of water is collected from the medium with a Dean-Stark apparatus (Greene & Wuts, 1999).

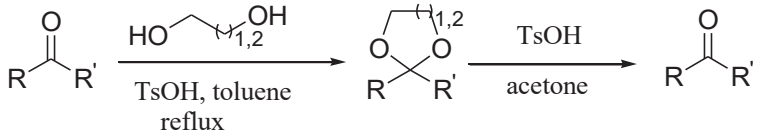

Figure 2. General methods for the synthesis of 1,3-dioxolanes

In excellent yields, a number of carbonyl compounds, give acyclic and cyclic acetals under mild reaction conditions in the presence of $(RO)_3CH$ and $Bu_4N^+ Br_3^-$ as catalyst in absolute alcohol. The presented methodology has many advantages. An aldehyde is acetalyzed chemoselectively in the presence of a ketone, an unsymmetric acetal is formed, conditions are easy to adopt, acid-sensitive protecting groups are stable in the medium, efficiencies are high, desired products are isolated easily, and the reagent is also a catalyst. (Gopinath et al., 2002).

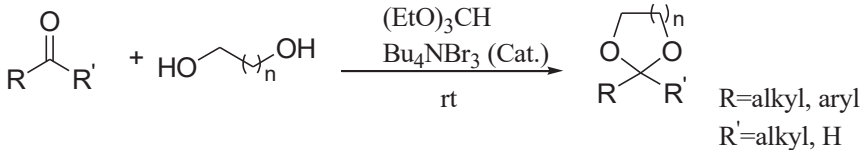

Figure 3. Tetrabutylammonium tribromide-catalyzed acetal reaction

SiO_2 or Al_2O_3, in the absence of solvent with pressure applied, is used to obtain 1,3-dioxolane with a condensation of carbonyl compounds. Oxazolidines, in a similar fashion, could be obtained with carbonyl compounds reacting with 2-amino-2-methylpropanol and having a catalyst in the form of silica gel or acid-activated clay. In these synthetic routes, no solvent is employed and pressure is applied. Glycol and aminopropanol react with the H^+(Brønsted) and Si and Al (Lewis) acidic locations on the catalysts' surface and there are reportedly many ionic intermediates (Rohand et al., 2018).

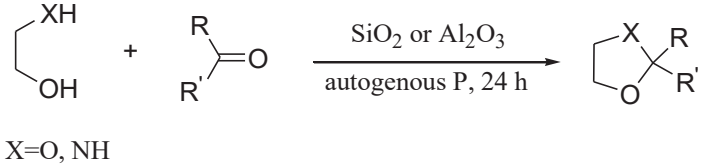

Figure 4. *Synthesis of oxazolidines compounds by SiO_2 or Al_2O_3 catalyst*

NTPA (N-triflylphosphoramide) has been an efficient Brønsted acid catalyst for 2,5-disubstituted 1,3-dioxolane-4-ones. There is no need to use azeotropic distillation nor a dehydration agent in the synthesis

where NTPA was used as a catalyst and several aldehydes were used, in high selectivity and moderate yield, to protect optically pure and racemic mandelic and lactic acid (Küçük, 2015).

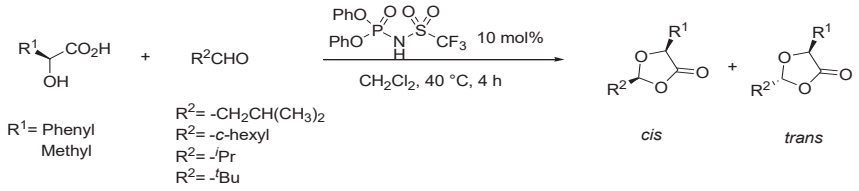

Figure 5. *Protection of (±)-mandelic acid and (±)-lactic acid with various aldehydes by NTPA*

Aryl bromides and chlorides are used in Heck coupling of electron-rich olefins and they do not need the presence of silver triflate and thallium acetate as halide scavengers. When ammonium-based additives are used, the reaction can be conducted in an imidazolium-based IL or a common molecular solvent and high yields and excellent regioselectivities are found with 1,1'-disubstituted olefins (Mo & Xiao, 2006).

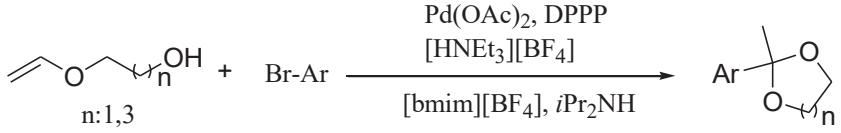

Figure 6. *Heck coupling reaction of 1,1'-disubstituted olefins*

Through a radical chain process, addition of 1,3-dioxolane to imines has been described. There were no metal nor redox-involving chemistry, and inexpensive materials are converted into a vast selection of α-amino aldehydes with yields from good to excellent and a radical precursor trace was employed. The presences of thiol and a little amount of air oxygen is very important for the success of the reaction, according to the control experiments (Zeng et al., 2018).

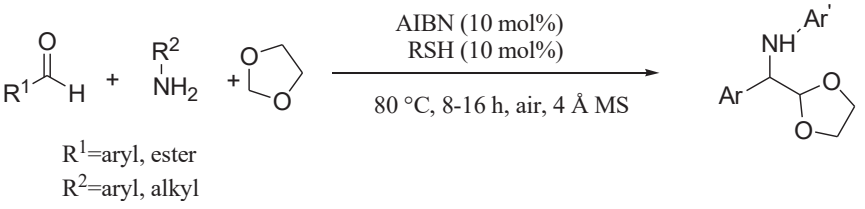

Figure 7. *A thiol-mediated radical chain reaction of 1,3-dioxolane with imines*

In the presence of Montmorillonite K10, a group of ten chiral 1,3-dioxolanes with >99% enantiomeric excess were prepared. Having long alkyl chains, aryl groups, and aryls with a single substitution, this protocol is the first example of chiral ketalization starting from ketones. The enantiomeric excess values were obtained with a chiral HPLC device on a Chiralcel OD column and ten racemic 1,3-dioxolanes were, for the first time, evaluated (Küçük & Yusufoğlu, 2012).

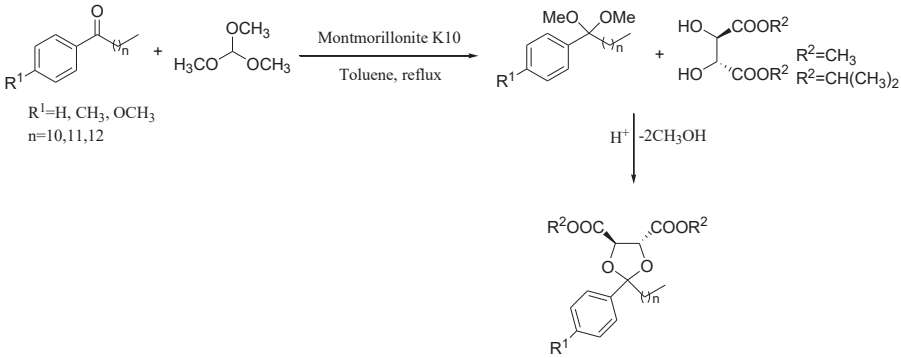

Figure 8. *Chiral ketalization reaction via Montmorillonite K10*

If one adds ethanol into the synthesis of 1,3-dioxolanes, which is prepared by the action of carbonyl compounds on vicinal diols, the reaction yield was found to be high and the reaction time was diminished. A possible explanation is that ethanol produces an adduct with carbonyl compound, which is referred to as a hemiacetal, and this proves to be an active intermediate in the synthetic effort. When aceton is ketalyzed with glycerol, a cyclic product (a ketal) is formed, while ethanol here helps transketalyzation mechanism without encountering the liberation of water (Vol'eva et al., 2012).

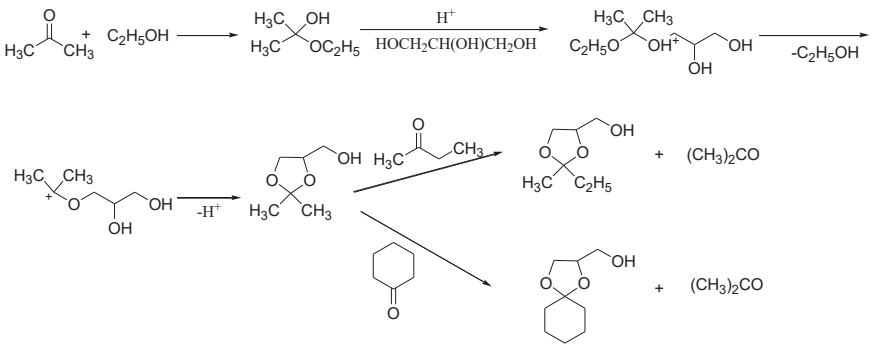

Figure 9. *The new 1,3-dioxolanes obtained in the study*

A broad group of protected aldols were synthesized, in the presence of scandium triflate at 10 mol% concentration, by the effect of bromomagnesium 2-vinyloxy ethoxide on a wide selection of aldehydes. Swern oxidation – CBS reduction sequence provided an enantioselective preparation of the aldols studied. From 2-bromocyclohexanone, the dioxolane led to the expected aldol as the anti diastereomer (diastereomer ratio > 99:1) (Quinio et al., 2016).

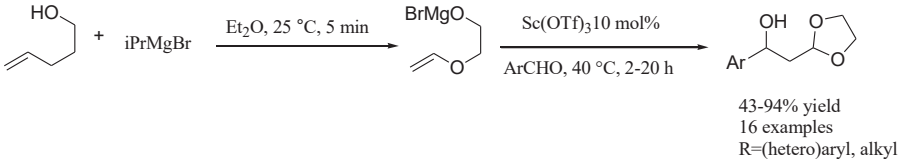

Figure 10. *Preparation of protected aldol products catalysed by Sc(OTf)$_3$*

3. Pharmacological Activities of 1,3-dioxolanes

A group of imidazole-dioxolane compounds were prepared in a hope to be novel inhibitors of heme oxygenase (HO). (2*R*,4*R*)-2-[2-(4-chlorophenyl)ethyl]-2-[(1*H*-imidazol-1-yl)methyl]-4-methyl-1,3-dioxolane hydrochloride (**1**) is the main structural motif in these compounds and they are distinct, in a structural manner, from metalloporphyrin heme oxygenase inhibitors and the aminothiophenol group of azalanstat is not present. The compounds are highly selective against heme oxygenase-1 isozyme (stress-induced) and much less inhibitory against heme oxygenase-2, which is the constitutive isozyme. These compounds, for the first time, provide isozyme-selective heme oxygenase inhibition (Vlahakis et al., 2006).

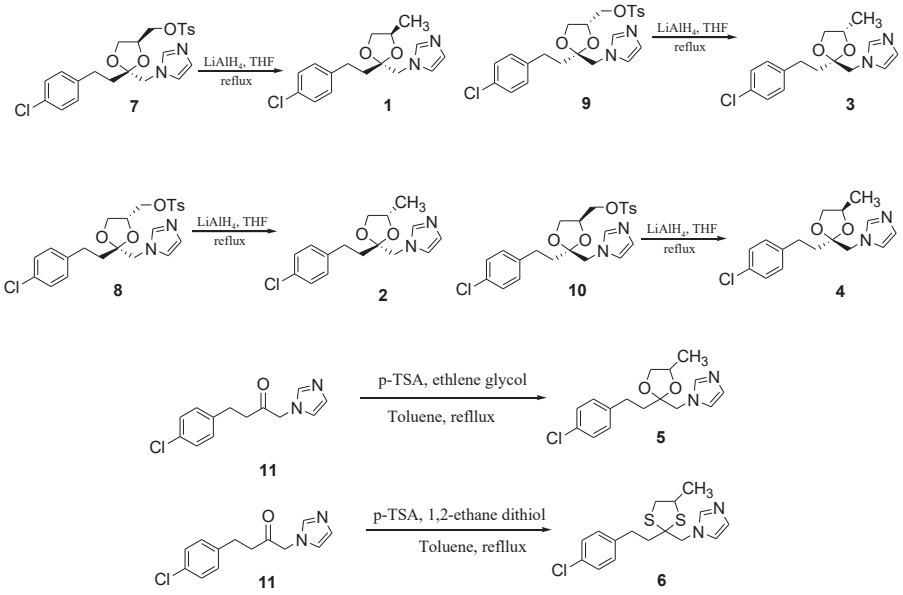

Figure 11. *Synthesis of a group of imidazole-dioxolane compounds*

As VLA-4 receptor antagonists, a successful attempt was paid to synthesize a set of 1,3-dioxolane-containing compounds as a proline bioisostere. High receptor affinities were found with three compounds. N-(2-phenyl)phenyl amide, which contains a 1,3-dioxolane moiety instead of the pyrrolidine ring in the N-acylphenylalanine of VLA-4 antagonists, was potent in the series (Rehman et al., 2010).

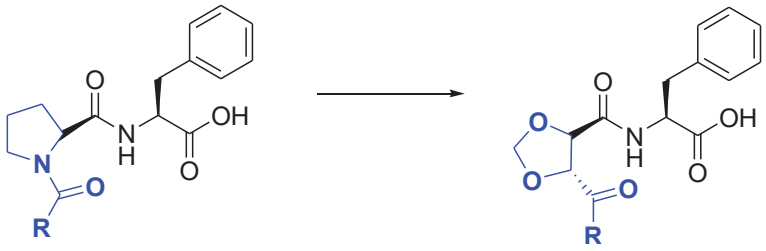

Figure 12. *New 1,3-dioxolane-containing compounds as VLA-4 receptor antagonists*

Utech et al. have prepared four aminoethyl-1,3-dioxane compounds by transacetalizing of the acetals with pentane-1,3,5-triol, tosylating the free OH moiety, then performing nucleophilic substitution. Three 3-aminopropyl derivatives were obtained by performing substitution of the tosylates with potassium cyanide and applying reduction with lithium aluminum hydride. 1,3-dioxanes, having, at the

acetalic position, a phenyl and ethyl group had the highest NMDA receptor affinity (Utech et al., 2011).

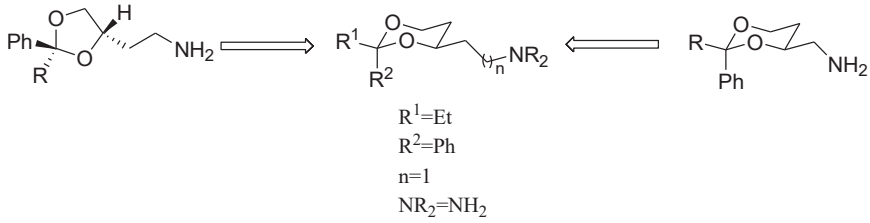

Figure 13. *Formation of aminoethyl-1,3-dioxane compounds by transacetalizing of the acetals*

A catalytic amount of Montmorillonite K10 was used in the reaction between salicylaldehyde and commercially available diols and pure by enantiomerical fashion and eight racemic 1,3-dioxolanes were prepared. The new compounds were subjected to routine analyses like elemental analysis and spectroscopic characterization. The compounds were subjected to antibacterial and antifungal activity. The results indicate that except one compound, all compounds display, against *C. albicans,* an excellent antifungal activity and significant antibacterial activity against *S. aureus, S. epidermidis, E. faecalis*, and *P. aeruginosa* by most of the compounds displayed ***(K***üçük et al., 2011).

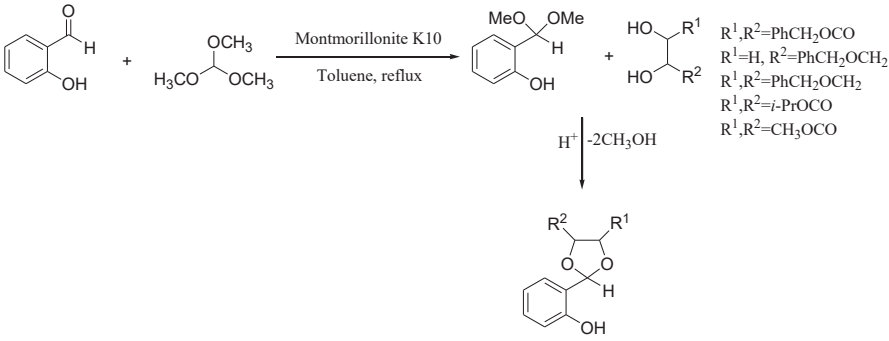

Figure 14. *Enantiomeric and racemic 1,3-dioxolanes for testing of antifungal and antibacterial activities*

Glycerol and ethylene glycol were reacted with aldehydes and ketones to obtain cyclic ketals and acetals, with substitutients at 2 and 4 on the dioxolane ring and they were shown to contain a wide range of antimicrobial activities against Gram positive and -negative bacteria. Owing to the antiradical activity of the studied compounds and the hydrophilicity – hydrophobicity balance, this activity allows for targeted

variation of the preparation of new active compounds. It is quite possible that cyclic ketals having high antimicrobial activity could be employed as antiseptic agents for the sterilization of surfaces of work and of the instruments to be used (Ovsyannikova et al., 2013).

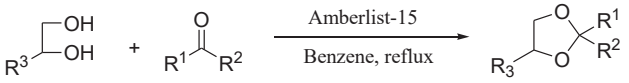

I: $R^1=R^2=CH_3$; $R^3=H$; **II**: $R^1=CH_3$; $R^2=C_2H_5$; $R^3=H$
III: $R^1=R^2=(CH_2)_5$; $R^3=H$; **IV**: $R^1=R^2=CH_3$; $R^3=CH_2OH$
V: $R^1=CH_3$;$R^2=C_2H_5$; $R^3=CH_2OH$; **VI**: $R^1=R^2=(CH_2)_5$; $R^3=CH_2OH$
VII: $R^1=H$; $R^2=CH_3$; $R^3=CH_2OH$; **VIII**: $R^1=R^2=CH_3$;
$R^3=CH_2OC_2H_5$; **IX**: $R^1=R^2=CH_3$; $R^3=CH_3COOCH_3$.

Figure 15. *The structure of cyclic ketals*

Alkylation of 6-substituted purines with a number of 2-(chloroalkyl)-2-aryl-1,3-dioxolanes and related compounds yielded new 6-substituted purines. Their inhibition of HIV reverse transcriptase activities were reported. A structure-activity relationship has been found with the molecules synthesized (Komissarov et al., 2015).

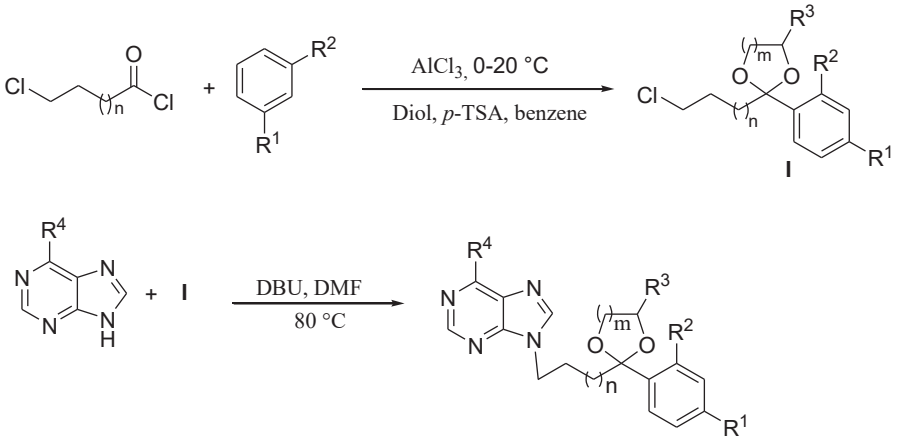

Figure 16. *Formation of 6-substituted purines from -(chloroalkyl)-2-aryl-1,3-dioxolanes*

Franchini et al. synthesized a range of compounds, spectrally characterized them, and investigated their antiviral, antibacterial, and antineoplastic chemotherapy properties. They prepared a and b anomers of the natural nucleosides and characterization was performed with NMR, HR-MS, and X-ray crystallography. Antimicrobial activity was

conducted against some pathogenic fungi, bacteria, and viruses. Antitumor activity was screened with a large number of human cancer cell lines. It was found that only one compound provided a weak inhibition of HIV-1 multiplication. Having an unnatural a configuration, two compounds displayed a residual antineoplastic activity. Examining these compounds' design, one can gain structural insight about these antiviral and antitumor agents (Franchini et al., 2017).

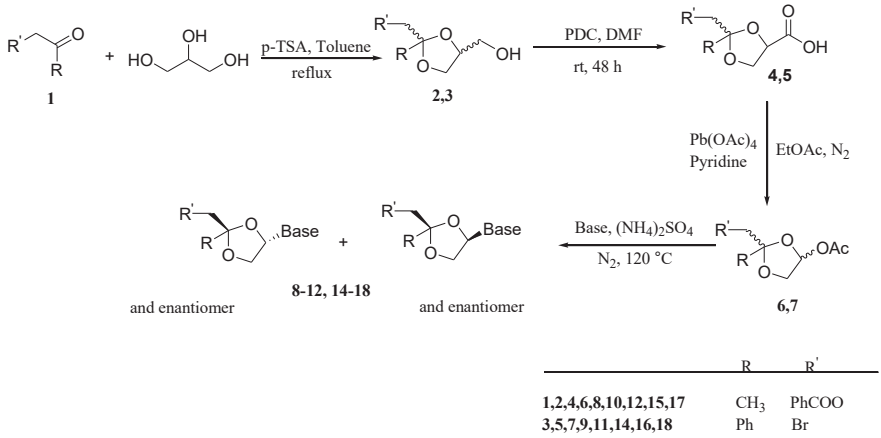

Figure 17. *Synthesis of phenyl dioxolane compounds containing pyrimidine and purine nucleosides*

Three 1,3-dioxolanes containing tellurium were prepared and assayed against *Trichomonas vaginalis*. ATCC 30236, which is an isolate of *T. vaginalis*, received six concentrations of the dioxolane compounds in an in-vitro testing. Compound 1 was 100% effective against *T. vaginalis* trophozoites, at 90 µM with IC_{50} of 60 µM (Sena-Lopes et al., 2017).

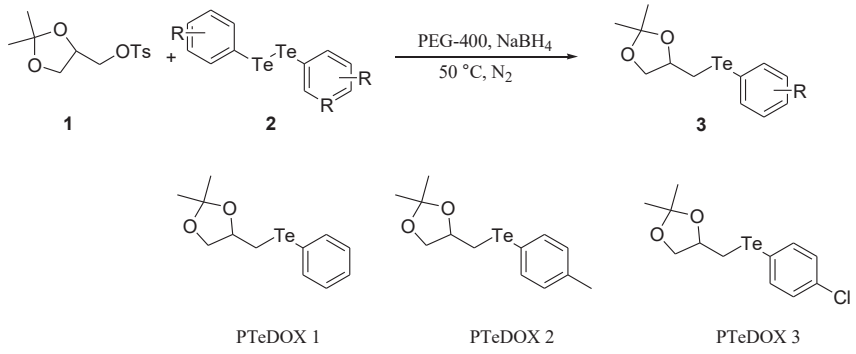

Figure 18. *Tellurium-containing 1,3-dioxolanes*

A series of 1H-imidazoles and 1,2,4-triazoles showed high fungicidal activity against six common fungal phytopathogens, including *Fusarium oxysporum* and others. These compounds were prepared by cyclization of substituted benzyl phenyl ketones or dibenzyl ketones in the presence of 3-chloro-1,2-propanediol and alkylation of 4-chloromethyl-containing 1,3-dioxolanes with sodium salts of imidazole or 1,2,4-triazole (Talismanov, Popkov, Zykova, & Karmanova, 2018).

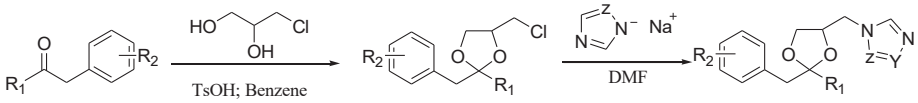

Figure 19. *1H-imidazoles and 1,2,4-triazoles with 1,3-dioxolanes*

Talismanov et al. also reported the antimycotic activity of dioxolane-containing imidazole compounds against *C. albicans* and *S. salmonicolor*, and *F. oxysporum* and *F. moniliforme* as well. The compounds were prepared with the reaction between substituted ketones and 3-chloro-1,2-propanediol. Then, they were further reacted with the sodium salts of imidazole (Talismanov, Popkov, Zykova, Karmanova, et al., 2018).

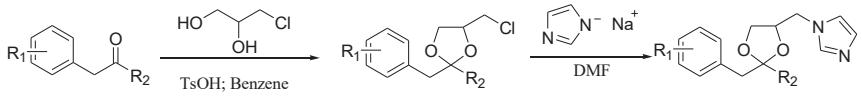

Figure 20. *Formation of dioxolane-containing imidazoles*

1,3-Dioxolane was prepared from L-tartaric acid, a commercially available, chiral substance. 1,3-dioxolane was obtained with a series of reaction in which L-tartaric acid was protected and partially hydrolyzed. A series of amides were synthesized from the aromatic amines and 1,3-dioxolane. Column chromatography was used to purify the compounds and a series of spectral analysis methods were employed for characterization. Antimicrobial activities against different strains of bacteria and fungi were reported (Fabiyi & Olanrewaju, 2019).

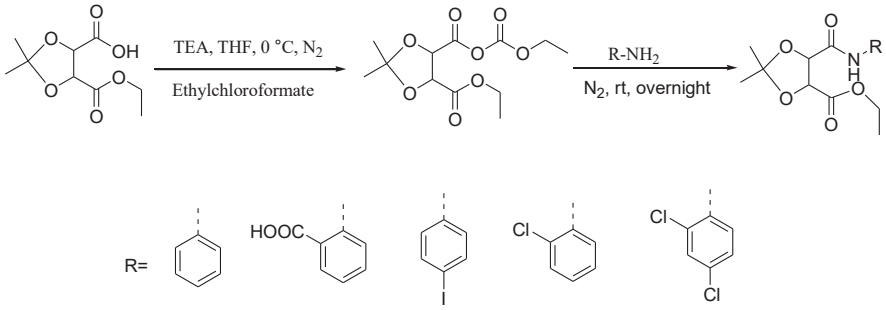

Figure 21. *Conversion of L-Tartaric acid into amides*

A dioxolan-containing isatin molecule was prepared with the reaction between isatin and a dioxolan-containing benzenesulfonate compound with a solution of sodium hydride in dry DMF at ambient temperature. Adding thiosemicarbazide yielded the corresponding thiosemicarbazone, which, underwent cyclization, with an aqueous solution of potassium carbonate to give the thione in good yield. Alkylsulfanyl derivatives were also prepared with the action of aqueous sodium hydroxide solution or sodium hydride in DMF. Proton and carbon NMR spectra showed a Z/E isomerism occurring together of some compounds. A moderate activity of the compounds against *Candida albicans* was found with clotrimazole as reference. One compound showed moderate activity against *Staphylococcus aureus*, a Gram-positive bacterium, with imipenem as the standard drug. All examined compounds were inactive against *E. coli* and *P. aeruginosa* (Ramadan et al., 2019) **.**

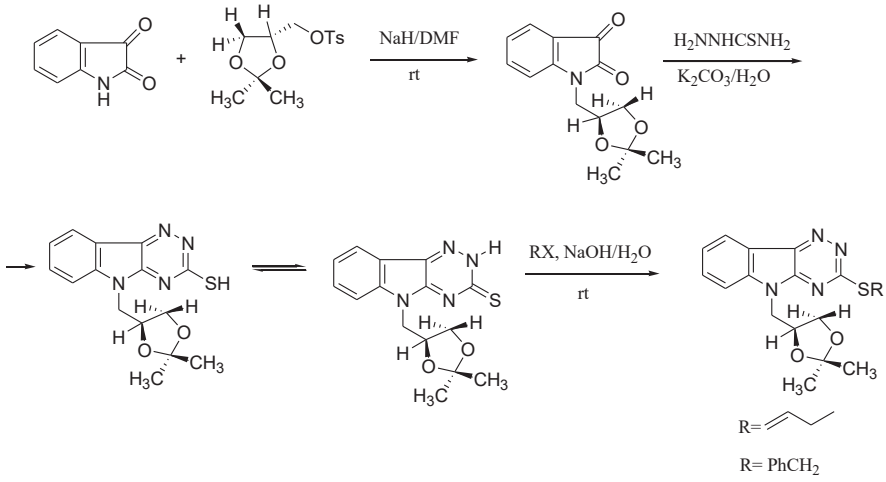

Figure 22. *Green approach of a dioxolan-containing isatin*

REFERENCES

Fabiyi, F. S., & Olanrewaju, A. A. (2019). Synthesis, Characterization, Antifungal and Antibacterial Activities of Novel Amide Derivatives of 1, 3-Dioxolane. *International Journal of Chemistry*, *11*(1), 71–78.

Franchini, S., Battisti, U. M., Sorbi, C., Tait, A., Cornia, A., Jeong, L. S., Lee, S. K., Song, J., Loddo, R., Madeddu, S., Sanna, G., & Brasili, L. (2017). Synthesis, structural characterization and biological evaluation of 4′-C-methyl- and phenyl-dioxolane pyrimidine and purine nucleosides. *Archives of Pharmacal Research*, *40*(5), 537–549. https://doi.org/10.1007/s12272-016-0825-6

Gopinath, R., Haque, Sk. J., & Patel, B. K. (2002). Tetrabutylammonium Tribromide (TBATB) as An Efficient Generator of HBr for an Efficient Chemoselective Reagent for Acetalization of Carbonyl Compounds †. *The Journal of Organic Chemistry*, *67*(16), 5842–5845. https://doi.org/10.1021/jo025701o

Greene, T. W., & Wuts, P. G. M. (1999). *Protective groups in organic synthesis* (3rd ed). Wiley.

Komissarov, V. V., Valuev-Elliston, V. T., Ivanova, O. N., Kochetkov, S. N., & Kritzyn, A. M. (2015). The synthesis of ω-(2-aryl-1,3-dioxolan-2-yl)alkyl purine derivatives and their activity towards HIV reverse transcriptase. *Russian Journal of Bioorganic Chemistry*, *41*(1), 37–45. https://doi.org/10.1134/S1068162015010069

Küçük, H. B. (2015). Practical synthesis of 2,5-disubstituted 1,3-dioxolane-4-ones and highly diastereoselective cis-2,5-disubstituted 1,3-dioxolane-4-ones from α-hydroxy acids catalyzed by N-triflylphosphoramide. *Tetrahedron Letters*, *56*(41), 5583–5586. https://doi.org/10.1016/j.tetlet.2015.08.046

Küçük, H. B., & Yusufoğlu, A. (2012). Synthesis of New Chiral and Racemic 1,3-Dioxolanes: Synthesis of New Chiral and Racemic 1,3-Dioxolanes. *Journal of Heterocyclic Chemistry*, *49*(5), 1066–1070. https://doi.org/10.1002/jhet.937

Küçük, H. B., Yusufoğlu, A., Mataracı, E., & Döşler, S. (2011). Synthesis and Biological Activity of New 1,3-Dioxolanes as Potential Antibacterial and Antifungal Compounds. *Molecules*, *16*(8), 6806–6815. https://doi.org/10.3390/molecules16086806

Mo, J., & Xiao, J. (2006). The Heck Reaction of Electron-Rich Olefins with Regiocontrol by Hydrogen-Bond Donors. *Angewandte Chemie*, *118*(25), 4258–4263. https://doi.org/10.1002/ange.200600799

Ovsyannikova, M. N., Vol'eva, V. B., Belostotskaya, I. S., Komissarova, N. L., Malkova, A. V., & Kurkovskaya, L. N. (2013). Antibacterial Activity of Substituted 1,3-Dioxolanes. *Pharmaceutical Chemistry Journal*, *47*(3), 142–145. https://doi.org/10.1007/s11094-013-0913-6

Quinio, P., Kohout, L., Roman, D., Gaar, J., Karaghiosoff, K., & Knochel, P. (2016). Sc(OTf)3-Catalyzed Addition of Bromomagnesium 2-Vinyloxy Ethoxide to Various Aldehydes Leading to Protected Aldol Products. *Synlett*, *27*(11), 1715–1719. https://doi.org/10.1055/s-0035-1561934

Ramadan, E., Rasheed, H., & El, A. (2019). Synthesis and antimicrobial screening of novel 1,3-dioxolanes linked to N-5 of 5H-[1,2,4]triazino[5,6-b]indole-3-thiol. *Journal of the Serbian Chemical Society*, *84*(1), 1–10. https://doi.org/10.2298/JSC171127067R

Rehman, A., Soni, A., Naik, K., Nair, S., Palle, V. P., Dastidar, S., Ray, A., Alam, M. S., Salman, M., Cliffe, I. A., & Sattigeri, V. (2010). Synthesis and biological activity of N-substituted aminocarbonyl-1,3-dioxolanes as VLA-4 antagonists. *Bioorganic & Medicinal Chemistry Letters*, *20*(18), 5514–5520. https://doi.org/10.1016/j.bmcl.2010.07.069

Rohand, T., Savary, J., & Markó, I. E. (2018). Synthesis of dioxolanes and oxazolidines by silica gel catalysis. *Monatshefte Für Chemie - Chemical Monthly*, *149*(8), 1429–1436. https://doi.org/10.1007/s00706-018-2198-7

Sena-Lopes, Â., das Neves, R. N., Bezerra, F. S. B., de Oliveira Silva, M. T., Nobre, P. C., Perin, G., Alves, D., Savegnago, L., Begnini, K. R., Seixas, F. K., Collares, T., & Borsuk, S. (2017). Antiparasitic activity of 1,3-dioxolanes containing tellurium in Trichomonas vaginalis. *Biomedicine & Pharmacotherapy*, *89*, 284–287. https://doi.org/10.1016/j.biopha.2017.01.173

Talismanov, V., Popkov, S., Zykova, S., & Karmanova, O. (2018). Synthesis and study of the fungicidal activity of substituted 1-[(2-benzyl-1, 3-dioxolan-4-yl) methyl]-1H-imidazoles, 1-[(2-benzyl-1, 3-dioxolan-4-yl) methyl]-1H-1, 2, 4-triazoles and 4-[(2-benzyl-1, 3-dioxolan-4-yl) methyl]-4H-1, 2, 4-triazoles. *Journal of Pharmaceutical Sciences and Research*, *10*(7), 1780–1783.

Talismanov, V., Popkov, S., Zykova, S., Karmanova, O., & Tsaplin, G. (2018). Design, synthesis and evaluation of antimycotic and fungicidal activities of novel substituted 1-[(2-benzyl-1, 3-dioxolan-4-yl) methyl]-1H-imidazoles. *Journal of Pharmaceutical Sciences and Research*, *10*(6), 1625–1628.

Utech, T., Köhler, J., & Wünsch, B. (2011). Synthesis of 4-(aminoalkyl) substituted 1,3-dioxanes as potent NMDA and σ receptor antagonists. *European Journal of Medicinal Chemistry*, *46*(6), 2157–2169. https://doi.org/10.1016/j.ejmech.2011.02.070

Vlahakis, J. Z., Kinobe, R. T., Bowers, R. J., Brien, J. F., Nakatsu, K., & Szarek, W. A. (2006). Imidazole−Dioxolane Compounds as Isozyme-Selective Heme Oxygenase Inhibitors. *Journal of Medicinal Chemistry*, *49*(14), 4437–4441. https://doi.org/10.1021/jm0511435

Vol'eva, V. B., Belostotskaya, I. S., Malkova, A. V., Komissarova, N. L., Kurkovskaya, L. N., Usachev, S. V., & Makarov, G. G. (2012). New approach to the synthesis of 1,3-dioxolanes. *Russian Journal of Organic Chemistry*, *48*(5), 638–641. https://doi.org/10.1134/S1070428012050028

Zeng, H., Yang, S., Li, H., Lu, D., Gong, Y., & Zhu, J.-T. (2018). Site-Specific Functionalization of 1,3-Dioxolane with Imines: A Radical Chain Approach to Masked α-Amino Aldehydes. *The Journal of Organic Chemistry*, *83*(9), 5256–5266. https://doi.org/10.1021/acs.joc.8b00715